Characterization of Silicon Modules and Sensors for the ATLAS Inner Tracker Strip Detector

Dissertation

zur Erlangung des Doktorgrades
an der Fakultät für Mathematik, Informatik und Naturwissenschaften
Fachbereich Physik
der Universität Hamburg

vorgelegt von

Edoardo Rossi

aus Abbiategrasso, Italien

Hamburg
2020

Gutachter der Dissertation:	Prof. Dr. Erika Garutti	Universität Hamburg
	Prof. Dr. Ingrid-Maria Gregor	DESY/Universität Bonn
Gutachter der Disputation:	Prof. Dr. Erika Garutti	Universität Hamburg
	Prof. Dr. Ingrid-Maria Gregor	DESY/Universität Bonn
	Prof. Dr. Dieter Horns	Universität Hamburg
	Prof. Dr. Bernd Kniehl	Universität Hamburg
	Dr. Christian Sander	DESY
Vorsitzender der Prüfungskommission:	Prof. Dr. Bernd Kniehl	Universität Hamburg
Datum der Disputation:		31.08.2020
Vorsitzender Fach-Promotionsausschusses PHYSIK:	Prof. Dr. Günter Hans Walter Sigl	Universität Hamburg
Leiter des Fachbereichs PHYSIK:	Prof. Dr. Wolfgang Hansen	Universität Hamburg
Dekan der Fakultät MIN:	Prof. Dr. Heinrich Graener	Universität Hamburg

Ti getteró un piccolo seme
e da quello nascerá una quercia

A mia madre

Abstract

For the High-Luminosity LHC, the ATLAS Experiment will replace the current tracking system with an all-silicon detector, the Inner Tracker (ITk), consisting of inner pixel layers and outer strip layers. The ITk Strip Detector will operate in a much harsher environment than the current strip detector, the Semiconductor Tracker (SCT). For this reason, an intense R&D campaign has been completed to develop new radiation-hard sensors and front-end chips.
In this work, test beam measurements performed to characterize ITk Strip prototype modules are presented. The performance of non-irradiated and irradiated modules is evaluated, with a focus on the hit detection efficiency, noise occupancy, and charge collection. The results prove that the current prototype modules will provide excellent performance for the entire lifetime of the High-Luminosity LHC.
Based on the test beam results with ITk Strip prototype modules, sensors with a special layout were produced. These sensors consist of five zones with different aluminum layer and strip implant widths. Non-irradiated and irradiated sensors are characterized with electrical and test beam measurements. The results show that the implementation of a wide aluminum layer and strip implant mitigates some of the detrimental effects of radiation damage.
The last part of this work deals with the Beam-Induced Background (BIB): particles generated by the interaction of the LHC beam with the surrounding environment. An online monitoring system developed to study the effects of the BIB in the SCT is described in detail.

Zusammenfassung

Das ATLAS Experiment wird das aktuelle Trackingsystem für den High-Luminosity LHC durch einen neuen, nur mit Siliziumsensoren arbeitenden Detektor ersetzen, den Inner Tracker (ITk). Die inneren Lagen des ITk werden aus Pixel-, die äußeren aus Streifendetektoren bestehen. Der ITk Streifendetektor wird unter wesentlich schärferen Bedingungen betrieben werden als der derzeitige Streifendetektor, der Semiconductor Tracker (SCT). Daher wurde ein intensives Forschungs- und Entwicklungsprogramm durchgeführt, um neue, strahlenharte Sensoren und Auslesechips zu entwickeln.
In dieser Arbeit werden Teststrahl-Messungen vorgestellt, die durchgeführt wurden, um ITk Streifendetektor-Modul Prototypen zu charakterisieren. Das Verhalten unbestrahlter und bestrahlter Module wird ausgewertet mit Schwerpunkt auf Trefferdetektionseffizienz, Rauschbelegung und Ladungssammlung. Die Ergebnisse zeigen, dass die aktuellen Modul Prototypen über die gesamte Laufzeit des High-Luminosity LHC hervorragende Leistung erbringen werden.
Ausgehend von den Teststrahl Ergebnissen mit ITk Streifendetektor-Modul Prototypen wurden Sensoren mit einem speziellen Layout entwickelt. Diese Sensoren bestehen aus fünf Zonen mit jeweils verschiedenen Aluminiumschicht- und Streifenimplantatbreiten. Unbestrahlte und bestrahlte Sensoren werden mit Hilfe von elektrischen und Teststrahlmessungen charakterisiert. Die Ergebnisse zeigen, dass eine breite Aluminiumschicht und ein breites Streifenimplantat einige schädliche Effekte der Strahlungsaussetzung reduzieren können.
Der letzte Teil dieser Arbeit beschäftigt sich mit Untergründen, die durch die Wechselwirkung des LHC Strahls mit der umliegenden (Beschleuniger-/Detektor-) Umgebung erzeugt werden (Beam-Induced Background, BIB). Ein Echtzeit-Überwachungssystem, entwickelt, um die Effekte des BIB auf den SCT zu untersuchen, wird im Detail beschrieben.

CONTENTS

LIST OF FIGURES

LIST OF TABLES

INTRODUCTION

Our interaction with the surrounding environment is determined by our response to external stimuli. Our eyes are sensitive to photons in the visible spectrum, our ears to acoustic waves, our skin to an applied pressure, and our tongue and nose to chemical elements and molecules. The information collected by the five senses is converted in electro-chemical signals which are transmitted to our brain. In this way, we can detect an external stimulus.
The use of external detectors can enhance our contact with the reality surrounding us and expand our comprehension of nature. Therefore, the study and development of new detectors is a crucial step for the progress of our scientific knowledge.

The ATLAS Experiment is located at CERN, near Geneva (Switzerland), and it is one of the largest and most innovative detectors ever built. It is designed to detect the fragments generated by collisions of two proton beams accelerated by the Large Hadron Collider (LHC). Since the beginning of its experimental program in 2009, the ATLAS Collaboration is pursuing an intense campaign to study the properties of the Standard Model of particle physics and to search for new physics phenomena, such as supersymmetry and dark matter. This campaign led to the historical discovery in 2012 of the long-sought Higgs boson, the last missing piece of the Standard Model.

Starting from 2022, the LHC will be upgraded to the High-Luminosity LHC which will provide an instantaneous luminosity about five times larger than the current luminosity and will greatly enhance the physics reach of the LHC experiments. The High-Luminosity LHC, however, will also create a very harsh environment for the LHC detectors, with unprecedented radiation levels and high pile-up. For this reason, the ATLAS Experiment will replace the current tracking system with an all-silicon detector, the Inner Tracker (ITk), consisting of inner pixel layers and outer strip layers. This thesis describes studies concerning the latter component, the ATLAS ITk Strip Detector, for which new radiation-hard sensors and front-end chips have been developed.

The first part of this thesis introduces the main topics of this work and provides the tools to understand the following Chapters.

Chapter 1 describes the LHC, the ATLAS Experiment, and their upgrades: the High-Luminosity LHC and the ATLAS Inner Tracker.
Chapter 2 discusses silicon sensors and their usage in high-energy physics.
Chapter 3 introduces test beams and the related infrastracture, such as the EUDET-type beam telescopes and the irradiation facilities exploited for the studies discussed in this thesis. A special focus is put on the EUTelescope test beam reconstruction framework, whose maintenance and development was an essential part of this work.

The second part of this thesis deals with the characterization of prototype modules and sensors for the ATLAS ITk Strip Detector.
Chapter 4 discusses the test beam campaigns performed to study the performance of ITk Strip prototype modules. The test beam analysis procedure and the observables of interest are described in detail. The threshold calibration accuracy and precision are studied using the data obtained with several non-irradiated modules. The response of a non-irradiated module to particles crossing its boundary regions is described, with a focus on the hit detection efficiency and spatial resolution. The performance of non-irradiated and irradiated ITk Strip prototype modules is discussed. The last part of this Chapter describes the effects of radiation damage on the amount of charge carriers shared between adjacent strips. Part of these results laid the basis for the studies described in the following Chapter.
Chapter 5 discusses the characterization of sensors with layouts alternative with respect to the standard ATLAS ITk Strip sensors. These sensors have five regions with different strip implant and aluminum widths. The electrical and test beam measurements performed with these sensors are described in detail. The results obtained with different layouts are compared with each other and with the specifications for the ATLAS ITk Strip sensors. The focus of this Chapter is on the understanding of the interaction between the sensor layout and the radiation damage effects.

The final Chapter of this thesis, Chapter 6, deals with the Beam-Induced Background (BIB): particles generated by the interaction of the LHC beams with the surrounding environment. The characteristics of the BIB in the current strip detector, the Semiconductor Tracker (SCT), are discussed. An online monitoring system was developed to study the BIB in the SCT and was operative during part of the ATLAS data-taking in the LHC Run 2. Example histograms produced by this online monitoring system are explained in detail.

CHAPTER

1

THE LHC, THE ATLAS EXPERIMENT, AND THEIR UPGRADES

This Chapter introduces the ATLAS Experiment and the upgrade of its tracking system, the ATLAS Inner Tracker. Section 1.1 introduces the Large Hadron Collider (LHC), the accelerator that provides the colliding beams for the ATLAS Experiment. Section 1.2 describes the ATLAS Detector and its sub-detectors with a focus on the Semiconductor Tracker, one of the main topics of Chapter 6. Section 1.2.4 discusses a few selected physics ATLAS results from the LHC Run 2, which started in 2015 and lasted until 2018. The future upgrade of the LHC, the High-Luminosity LHC, is described in Section 1.3. The ATLAS Inner Tracker upgrade is discussed in Section 1.4 and Section 1.4.1 describes in detail the ATLAS Inner Tracker Strip Detector, the main topic of this thesis. Section 1.4.2 analyzes the tracking and physics performance of the Inner Tracker and compares it with the performance of the current Inner Detector.

1.1 Large Hadron Collider

The Large Hadron Collider (LHC) [1] at CERN is currently the most powerful proton synchrotron in the world. The LHC currently provides proton-proton collisions with a collision energy of 13 TeV. It has a circumference of about 27 km and is located about 100 m underground on the outskirts of Geneva, on the border between Switzerland and France (see Figure 1.1). Its planning began in the middle of the 1980s [2] with the physics targets of probing new physics up to the TeV scale and looking for the long-sought Higgs boson, the last particle of the Standard Model yet to be observed at the time.

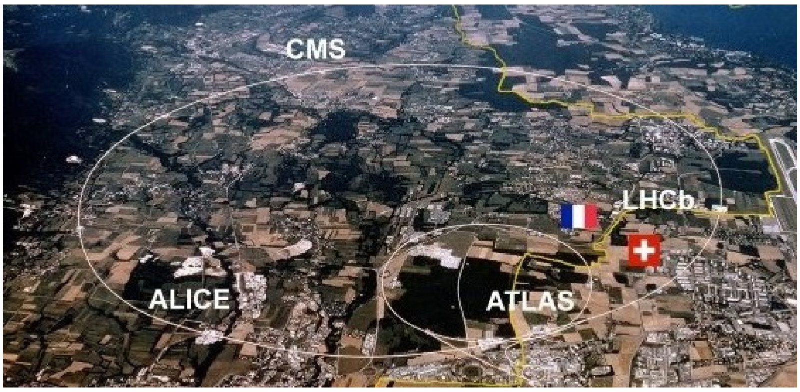

Figure 1.1: The LHC and its four major experiments on the outskirts of Geneva. The position of the SPS is also highlighted in the proximity of the ATLAS experiment.

The most innovative aspects of the LHC are its unprecedented collision energy and interaction rate. The interaction rate can be quantified using the concept of luminosity:

$$\frac{dR}{dt} = \mathscr{L} \cdot \sigma \tag{1.1}$$

where dR/dt is the rate for a given interaction, $\mathscr{L}$ is the instantaneous luminosity, and σ is the interaction cross section.
The LHC provides an instantaneous luminosity larger than $10^{34}\,\mathrm{cm}^{-2}\,\mathrm{s}^{-1}$. As a comparison, the Tevatron, a proton-antiproton collider with a collision energy of 1.96 TeV, provided a maximum instantaneous luminosity of $4.3 \times 10^{32}\,\mathrm{cm}^{-2}\,\mathrm{s}^{-1}$ [3] and the Superconducting Super Collider (SSC), a 40 TeV collider cancelled in 1993, was designed for $1 \times 10^{33}\,\mathrm{cm}^{-2}\,\mathrm{s}^{-1}$ [4]. The very high luminosity of the LHC greatly enhances its physics reach, although it posed a serious challenge for the detector design.

Several steps are necessary to prepare the beam for the injection into the LHC ring. Starting from an hydrogen molecule from a tank, protons and electrons are separated by an electric field. The protons are accelerated to an energy of 50 MeV by LINAC 2, a linear accelerator. The next step is the Proton Synchrotron Booster, a small synchrotron which reaches an energy of 1.4 GeV and then inject the protons to the Proton Synchrotron, another synchrotron which increases the energy to 26 GeV. The last pre-acceleration step is provided by the Super Proton Synchrotron, which increases the beam energy to 450 GeV and injects the protons into the LHC where the beams are accelerated to the nominal collision energy.

The LHC complex comprises four large-scale experiments: ATLAS (A Toroidal LHC ApparatuS) [5], CMS (Compact Muon Solenoid) [6], ALICE (A Large Ion Collider Experiment) [7], and LHCb (Large Hadron Collider beauty) [8]. ATLAS and CMS are general purpose detectors, meaning that they are designed to study the widest possible range of physics processes. ALICE and LHCb are detectors specialized in the study of quarkgluon plasma and bottom quark physics, respectively.

The first LHC data-taking campaign (Run 1) started in 2009 and lasted until 2013. Run 1 of the LHC set a historical milestone with the discovery of the Higgs boson at a mass of 125 GeV. The discovery was announced in July 2012 jointly by the ATLAS [9] and CMS [10] collaborations.

1.2 ATLAS Experiment

The ATLAS Experiment is one of the two general purpose detectors at the LHC [5]. The ATLAS Detector is 46 m long, has a diameter of 25 m and weighs 7000 tonnes, making it the largest detector ever built for a collider experiment. It is located in a cavern 100 m underground in Point 1 of the LHC.

The design of the ATLAS Experiment started in the early 1990s, and its assembly started in 2003 and finished in 2008. The long design and prototyping phases were motivated by the strict and unprecedented requirements imposed by the LHC environment:

- High granularity to resolve single particles and jets in a dense track environment.
- Significant radiation hardness for the detecting elements, electronics, and all the material present in the detector.
- Perfect hermeticity to minimize the number of particles escaping detection.
- Efficient triggering system to limit the data collection rate and retain the events containing interesting physics processes.
- Good momentum resolution and tracking efficiency in the tracking detector.

The final choice was a layered design centered around the interaction point, the standard choice for collider experiments. Each layer serves a different purpose and only by combining the data from all these sub-detectors the full physics reach of ATLAS is attained. Figure 1.2 shows a sketch of the ATLAS Experiment and its sub-detectors:

- The Inner Detector, composed of Pixel Detector, Semiconductor Tracker, and Transition Radiation Tracker.
- The Calorimeters, composed of Liquid Argon Calorimeter and Tile Calorimeter.
- The Muon Spectrometer.

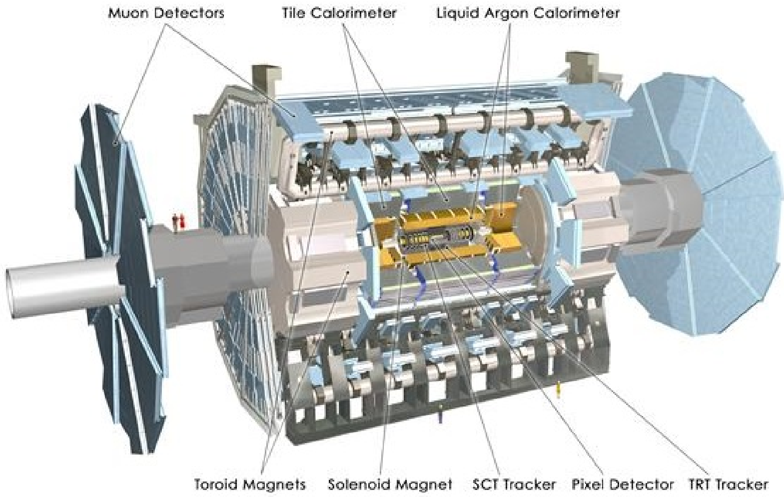

Figure 1.2: Cross-sectional view of the ATLAS Detector [11].

1.2.1 Inner Detector

The Inner Detector (ID) is the ATLAS tracking and vertexing detector and it is the sub-detector closest to the interaction point [12]. The ID measures the trajectory of charged particles close to the interaction point and its main purposes are to provide a measurement of the collision fragments momentum and to reconstruct interaction vertices. As shown in Figure1.3, the ID is divided in three components: the Pixel Detector, the Semiconductor Tracker and the Transition Radiation Tracker.

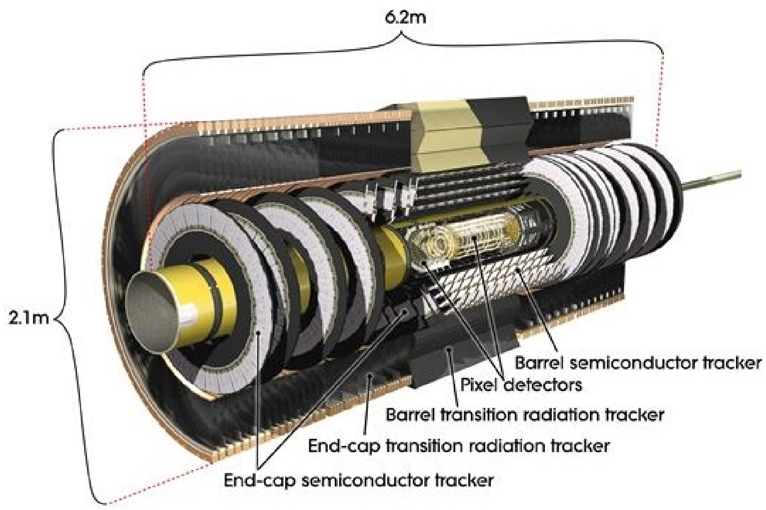

Figure 1.3: Cross-sectional view of the Inner Detector and its components: the Pixel Detector, the Semiconductor Tracker and the Transition Radiation Tracker [13].

Figure 1.4 shows the layout of the Inner Detector. The ID extends up to a radius of 1 m around the interaction point and for a length of 2.7 m in each beam direction. The ID coverage extends up to a pseudorapidity η of 2.5 [1].

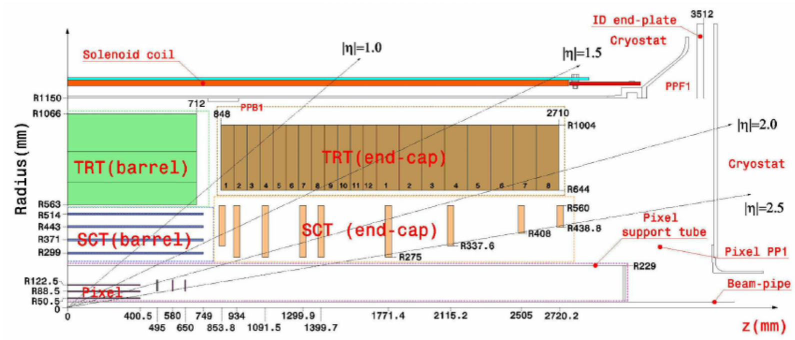

Figure 1.4: Layout of the Inner Detector and its three sub-detectors [14].

The ID is surrounded by a solenoid which generates a 2 T magnetic field parallel to the beam pipe. The magnetic field bends the tracks of charged particles by means of the Lorentz force. Having measured the curvature of a particle trajectory, its momentum can be calculated using the following formula:

$$p_{\perp} = q \cdot R \cdot B \tag{1.2}$$

Where $p_{\perp}$ is the particle transverse momentum, R is the curvature radius of its trajectory and B is the magnetic field. Additionally, the sign of the charge can be determined by the direction of the curvature. Figure 1.5 shows the tracks reconstructed in the ID in a proton-proton collision event.

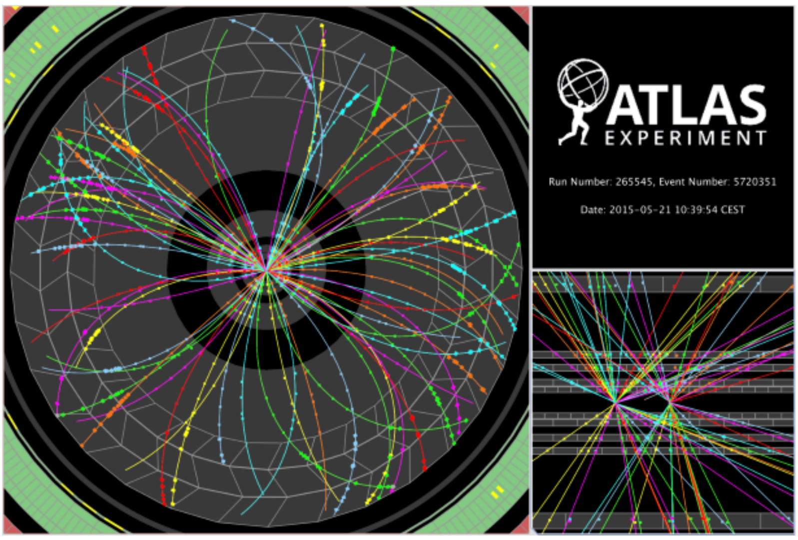

Figure 1.5: Display of the reconstructed tracks in the Inner Detector in a proton-proton collision event [15]. The hits from which the tracks are reconstructed are also shown. In the lateral view in the bottom right panel it can be seen that the tracks originated from two interaction points, indicating a pile-up event.

[1]The pseudorapidity η is related to the angle with respect to the beam pipe θ by η = -ln(θ/2)

Pixel Detector

The Pixel Detector is the innermost system in the ID. Each pixel module comprises an n^+-in-n planar silicon sensor with pixel size of 50 µm × 400 µm, which provide hits with spatial resolution of about 8 µm × 75 µm [16]. In 2014 a new innermost barrel layer was installed at a distance of 3.3 cm from the beam axis: the Insertable B-Layer (IBL) [17]. The IBL includes both planar and 3D sensors, with the latter technology chosen because of its high radiation hardness [18]. Each sensor is bump-bonded to the front-end readout electronics, FE-I3 and FE-I4B for the Insertable B-Layer.

The Pixel Detector is designed to have a very high granularity and to provide hit information with very high spatial resolution. This is crucial for the reconstruction of primary and secondary vertices and for the determination of the track impact parameter.

Beam Conditions Monitor

The Beam Conditions Monitor (BCM) is housed inside the ID and it measures the luminosity and beam conditions close to the interaction point. It provides time-of-arrival and pulse height measurements to distinguish proton-proton collisions from particles lost by the beam [19]. The BCM is also one of the two dedicated detectors to measure the luminosity bunch-by-bunch [20].

The BCM consists of two stations, upstream and downstream with respect to the interaction point. They are located in the very forward region at a distance of about 184 cm from the interaction point and at a radius of 5.5 cm (pseudorapidity of about 4.2). Each station contains four modules, which include two 1 cm × 1 cm diamond sensors. The choice of the diamond technology is driven by the high radiation hardness necessary to operate in the very forward region of the ID.

The sensor signal is processed by fast electronics which generate an output signal with about 1 ns rise time and 3 ns width [21]. Because of the fast signal it is possible to resolve single particles and to measure their time-of-arrival. This information is used to trigger on events with a significant fraction of particles out-of-time with respect to the collision fragments.

Semiconductor Tracker

The Semiconductor Tracker (SCT) is a silicon strip detector and is located outside the Pixel Detector. Figure 1.6a shows a picture of the SCT during construction. The SCT comprises four concentric barrels and two end-caps with nine disks each (Figure 1.4). The two end-caps are labeled A and C and correspond respectively to positive and negative z in the ATLAS coordinate system[2].

Figure 1.6b shows an SCT barrel module. It comprises a float-zone p-in-n silicon sensor with active thickness of 285 µm. The hybrid hosts the front-end chips, the ABCD chips, which are wire-bonded to the silicon strips. Every ABCD chip has 128 channels, each with a preamplifier and a shaper stage with a final shaping time of about 20 ns. The signal is then discriminated against a threshold of 1 fC (6250 electrons) in order to provide a binary output which is eventually transmitted to the off-detector electronics [22].

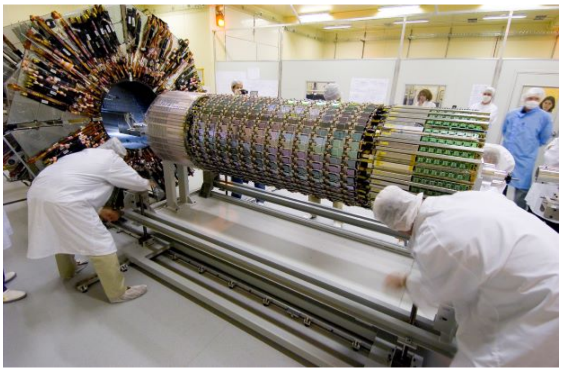

(a) The SCT during assembly [23].

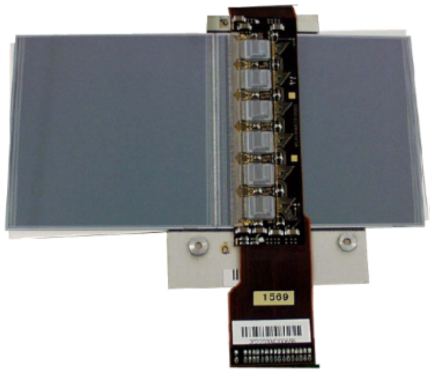

(b) An SCT barrel module [24].

Figure 1.6: The SCT during assembly and an SCT barrel module.

Every SCT barrel layer comprises rectangular silicon strip sensors with pitch of 80 µm and length of about 12 cm. End-cap disks are formed by sensors with a trapezoidal shape and a mean pitch of 80 µm. Both in the barrel and in the end-caps two identical sensors are glued back-to-back slightly tilted with respect to each other. The tilt angle, called stereo angle, has a value of 40 mrad (about 2.3°). Although hits on one sensor provide essentially a one-dimensional measurement of the track position on the sensor plane, by exploiting the stereo angle, the two hits from the back-to-back sensors can be combined to create a space point, a two-dimensional entity crucial for high precision tracking.

Figure 1.7 explains how a space point is obtained by exploiting the overlap of two strip hits. The space points provide a precision of 17 µm in the Rϕ plane. In the barrel layers they provide a precision of 580 µm in the z direction while in the end-cap disks the same precision is achieved in the R direction [25].

[2] ATLAS uses a right-handed coordinate system centered in the interaction point and with the z-axis following the beam pipe. The y-axis points upward and the x-axis points to the center of the LHC ring. The positive direction of the z-axis is determined by the directions of the x- and y-axes combined with the requirement of having a right-handed system.

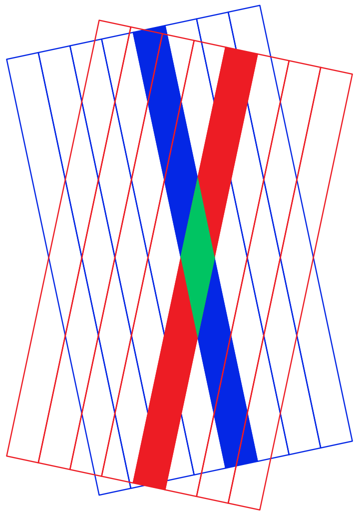

Figure 1.7: Example illustration of a space point (green) and the two strip hits used to create it (red and blue).

The SCT is read out every 25 ns (corresponding to a frequency of 40 MHz), matching the LHC bunch spacing. The hit information is sampled for three consecutive bunch crossings. The central time bin is synchronized with the signals generated by the collision fragments, with the synchronization being made during special collision runs every year. The hit information of the previous and next time bins are recorded as well. Usually the notation $X_1X_2X_3$ is used, where X can assume the values 0 and 1 depending if the amplitude of the signal exceeds the threshold at the correspondent time bin.

Before July 2016, the SCT was operated in the so-called level mode, in which all the hits with a pattern of the form X1X are transmitted to the off-detector electronics. This means that a hit is transmitted if the signal of a strip is above the threshold in the triggered bunch crossing, with no criterion set for the other time bins. Since then, the SCT is operated in the so-called edge mode, transmitting only hits with a 01X pattern. In this case, it is also required that no signal is registered at the bunch crossing before the triggered one. With the edge mode readout, long hits from earlier collision are rejected thus reducing the hit occupancy. This is the readout mode originally designed for the nominal 25 ns bunch spacing used during the LHC Run 2.

Transition Radiation Tracker

The Transition Radiation Tracker (TRT) is the outermost system in the ID. The TRT is built of straw tubes filled with noble gases. The tubes operate as drift chambers, therefore when a particle crosses the gas, it ionizes the gas molecules and generates a detectable signal. Despite the relatively large tube diameter of 4 mm [26], it is possible to exploit the drift time information obtained from the signal shape to achieve hits with a spatial resolution of about 110 μm [26].

The TRT provides a large number of hits per track (about 34) with a lever arm longer than the silicon detectors. Therefore, the TRT improves mostly the momentum resolution for high $p_\perp$ tracks (see Figure 1.8), which are almost straight tracks with small curvature [27]. An important drawback of the TRT is its saturation in the presence of a large number of interactions per bunch crossing or for large pile-up (Figure 1.9). Therefore, the TRT will not be able to operate proficiently in the High Luminosity LHC environment.

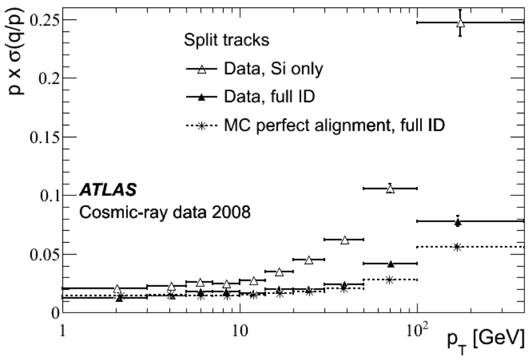

Figure 1.8: ID relative momentum resolution as a function of the transverse momentum, for full ID tracking (both data and simulation) and for only the Pixel Detector and the SCT [12].

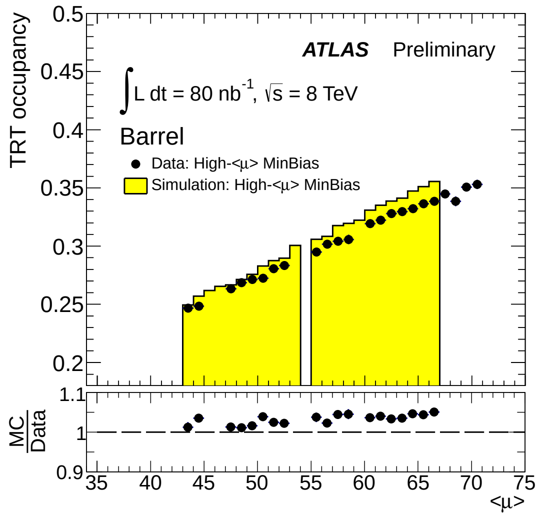

Figure 1.9: TRT occupancy as a function of the number of interactions per bunch crossing <μ> in a special run with no pile-up from adjacent bunches [26].

An important property of the TRT is the use of transition radiation for particle identification. Transition radiation consists of x-ray emitted when a charged particle crosses the boundary between two materials with different dielectric constants. The x-ray energy depends on the relativistic Lorentz factor γ of the particle. Given two particles with the same momentum, the one with the lowest rest mass will emit more high-energy x-rays. The TRT exploits this effect in order to discriminate electrons from pions, reaching an electron identification efficiency of 90%, while maintaining the pion mis-idenfication probability at 5% [28].

1.2.2 Calorimeters

The Inner Detector provides important information on the particle momentum and on the vertices associated with particle decays, but it does not fully characterize a particle.

In order to do this, the knowledge of either the particle energy or its type is necessary. Once the particle energy or type is known, the other can be then determined by using the relativistic energy-momentum equation:

$$E^2 = (pc)^2 + (m_0 c^2)^2 \tag{1.3}$$

where E is the particle energy, p its momentum, m_0 its rest mass and c the speed of light.

The ATLAS Calorimeters are detectors that measure a particle energy by absorbing it. They also measure the position and the direction of the energy release. This information, in conjunction with the momentum information from the ID, allows the particle type to be identified. While the ID can (almost) only detect charged particles, the Calorimeters are also sensitive to neutral particles as photons and neutrons. It is then possible to identify neutral particles by looking for a calorimeter hit with no corrispondent track in the ID. Additionally, the ATLAS Calorimeters provide trigger functionalities to search for high-energy electrons, photons, τ leptons, jets, and events with a high missing transverse energy [29].

The most important figure of merit of a calorimeter is its energy resolution which can be parametrized as:

$$\frac{\sigma(E)}{E} = \frac{a}{\sqrt{E}} \oplus \frac{b}{E} \oplus c \tag{1.4}$$

With a being the term related to the fluctuations of number of particles in a shower, b depending on the electronics noise and c a constant term that takes into account all the other effects usually determined from the experimental data. For energies of interest in high-energy physics the noise term is usually negligible.

Generally, calorimeters are divided in two types:

- Electromagnetic calorimeters, which detect particles that interact electromagnetically as electrons and photons.

- Hadronic calorimeters, which detect particles that interact via the strong force, as protons, neutrons, and neutral pions.

Figure 1.10 shows a cross section of the ATLAS Calorimeters and its constituents: the Liquid Argon (LAr) and the Tile Calorimeters. The Tile Calorimeter is purely hadronic, while the LAr Calorimeter is mainly electromagnetic, with hadronic components in the end-caps and in the forward regions.

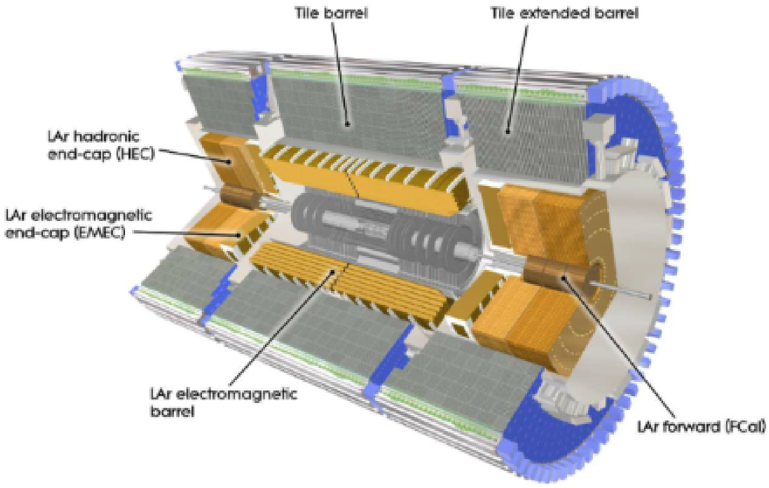

Figure 1.10: Cross-sectional view of the ATLAS Calorimeters and its components: the Liquid Argon (LAr) and the Tile Calorimeters [30].

The Liquid Argon Calorimeter (LAr) is located outside the solenoid surrounding the Inner Detector. The LAr Calorimeter is a sampling calorimeter, thus layers of an absorbing passive material are interleaved with Liquid Argon, the active material. The primary particles interact in the absorber and generate showers of secondary particles, which are detected in the active material, where their energy is measured. The absorber is made of lead in the electromagnetic part of LAr, copper in the hadronic part of the end-caps and copper-tungsten in the forward region. The choice of liquid Argon as an active material is motivated by its good linearity as an ionization medium, high radiation hardness, and stability over-time [5]. In order to maintain the Argon in the liquid state, the LAr Calorimeter has to be located in cryostates at 87 K [31].

Figure 1.11a shows the energy resolution as a function of the electron beam energy for a LAr electromagnetic module tested in a test beam. The term a of Equation 1.4 has a value of $10.1\,\%\sqrt{\text{GeV}}$ and dominates the energy resolution at low beam energies, while the constant term c is the most important term at very high beam energies and has a value of 0.17%. For beam energies > 10 GeV the relative energy resolution is < 4%.

The energy resolution is much degraded in the hadronic sections, mainly because of the much more complex showers generated by strong interactions. For hadrons interacting in the forward LAr Calorimeter the energy resolution parameters a and c from Equation 1.4 assume values of $95\,\%\sqrt{\text{GeV}}$ and 7.5%, respectively [32].

The Tile Calorimeter (TileCal) is a hadronic calorimeter that surrounds the LAr Calorimeter. It is a sampling calorimeter that implements iron plates as absorbing material and plastic scintillating tiles as active material. The parameters a and c from Equation 1.4 have values of $52\,\%\sqrt{\text{GeV}}$ and 5.7%, respectively, for stand-alone TileCal measurements of a pion beam [33]. The parameters are improved to values of 52 %$\sqrt{\text{GeV}}$ and 3.02% when the LAr information is also exploited (see Figure 1.11b). Similarly to the hadronic part of the LAr Calorimeter, the resolution is worse than in the electromagnetic part of the LAr Calorimeter mainly because of the more complex structure of hadronic showers.

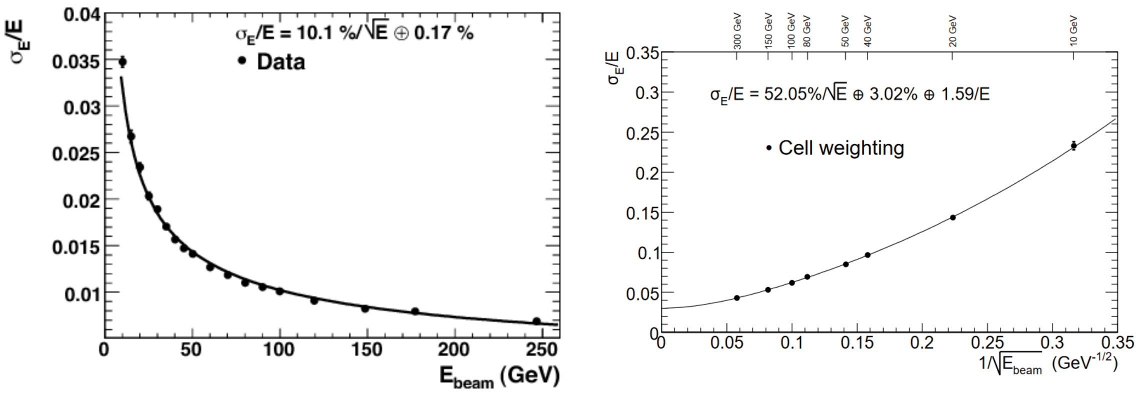

(a) Energy resolution as a function of the electron beam energy for a LAr electromagnetic module tested in a test beam [34]. Electronic noise was subtracted from the data.

(b) Energy resolution as a function of the inverse square root of the pion beam energy measured in a test beam for combined LAr electromagnetic and TileCal modules [33].

Figure 1.11: Energy resolution measured in test beams for a LAr electromagnetic module and a TileCal module with an electron and pion beam, respectively.

1.2.3 Muon Spectrometer

Although most of the particles are absorbed within the calorimeters, muons and neutrinos are able to escape detection. Neutrinos are neutral particles that interact only via the weak force, thus their interaction cross section is too small for them to be detected in ATLAS. Their energy is not measured directly, but it can be calculated using the energy missing to achieve full energy conservation in an event. Muons are charged particles that interact electromagnetically and leave a track in the Inner Detector. They do not generate showers in the electromagnetic calorimeter, since they do not emit a significant amount of Bremsstrahlung due to their large mass. They also do not generate showers in the hadronic calorimeters, since they do not interact via the strong force.

Although the muon momentum and identification can be performed with the Inner Detector, high-energy muons represent an important signature of several interesting phenomena, as Higgs boson physics or new physics processes. The Muon Spectrometer is the outermost detector of ATLAS and provides high-precision measurements of the muon energy and trajectory. The Muon Spectrometer also provides trigger functionalities to identify high-energy muons.

In order to provide the track curvature necessary for the momentum reconstruction, the Muon Spectrometer is located in a magnetic field generated by one toroid in the barrel and two toroids in the end-caps. The toroids generate a magnetic field with an average intensity of 0.5 T and 1 T in the barrel and end-caps, respectively.

Figure 1.12 shows a cross-sectional view of the ATLAS Muon Spectrometers and its main components. Both in the barrel and in the end-caps the tracking is performed mainly by exploiting hits from Monitored Drift Tubes, which provide a resolution of about 35 µm per chamber [5]. In the innermost end-cap layer Cathode-Strip Chambers are implemented due to their higher rate capability. They provide hits with a resolution of about 40 µm per chamber in the bending plane [5]. The trigger functionalities are provided by Resistive Plate Chambers and Thin Gas Chambers in the barrel and end-caps, respectively. They provide hits with a time resolution of 1.5 ns and 4 ns respectively [5], but their contribution to the tracking performance is rather limited because of their large spatial resolution (several mm). All these detectors are gas-based because of the large volume to be covered.

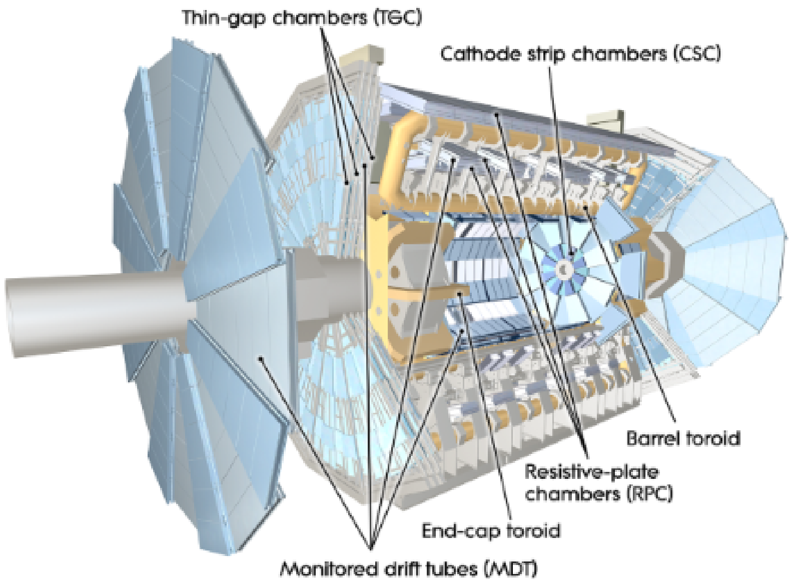

Figure 1.12: Cross-sectional view of the Muon Spectrometer and its main components [35].

Figure 1.13 shows the momentum resolution for muons in a cosmic-ray run obtained from the Inner Detector, the Muon Spectrometer and by combining the two. The Muon Spectrometer has the largest effect for muons with high momentum (> 100 GeV) due to its very large lever arm.

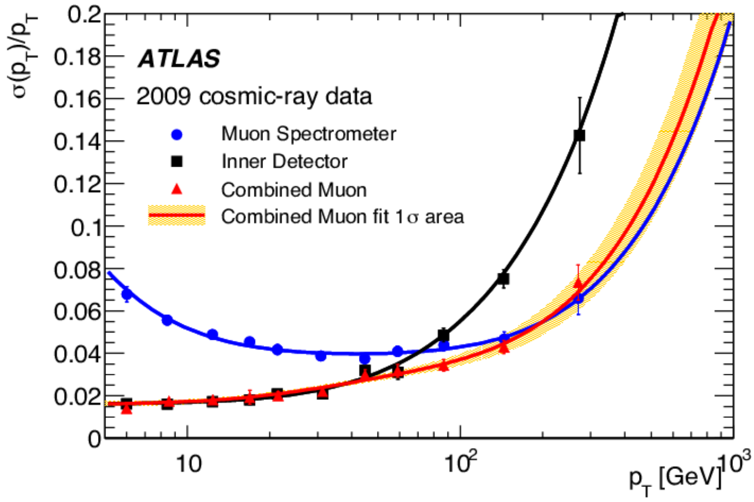

Figure 1.13: Transverse momentum resolution for muons in a cosmic-ray run from 2009 [36]. The resolution obtained by the Inner Detector, Muon Spectrometer, and by their combination are shown.

1.2.4 Selected Run 2 Results

One of the most important results in the recent history of physics is the discovery of the Higgs boson by the ATLAS [9] and CMS [10] collaborations in 2012. Such discovery would not have been possible without reliable operations and accurate measurements of all the sub-detectors of the two experiments. Figures 1.14a and 1.14b show recent Higgs physics results in two decay channels currently accessible: decay in two photons and in four leptons.

The diphoton analysis exploits events where a diphoton trigger had fired: two photons were promptly detected in the electromagnetic calorimeter with a transverse momentum of at least 35 GeV and 25 GeV for the leading and subleading photon candidates. The total diphoton invariant mass is obtained from the electromagnetic calorimeter and the energy resolution is crucial to discriminate the Higgs peak from the background. The hit information from the Inner Detector and hadronic calorimeters is used to discriminate photon candidates from electrons or jets.

The four lepton analysis exploits events where a single-lepton, dilepton or trilepton trigger has fired from the electromagnetic calorimeter or from the Muon Spectrometer. At least two pairs with the same-flavour and opposite charge are required in the final state, with the particle identification performed using information from all the sub-detectors. Several cuts on the transverse momenta of the particles are also applied, with the momenta being determined by the Inner Detector and Muon Spectrometer.

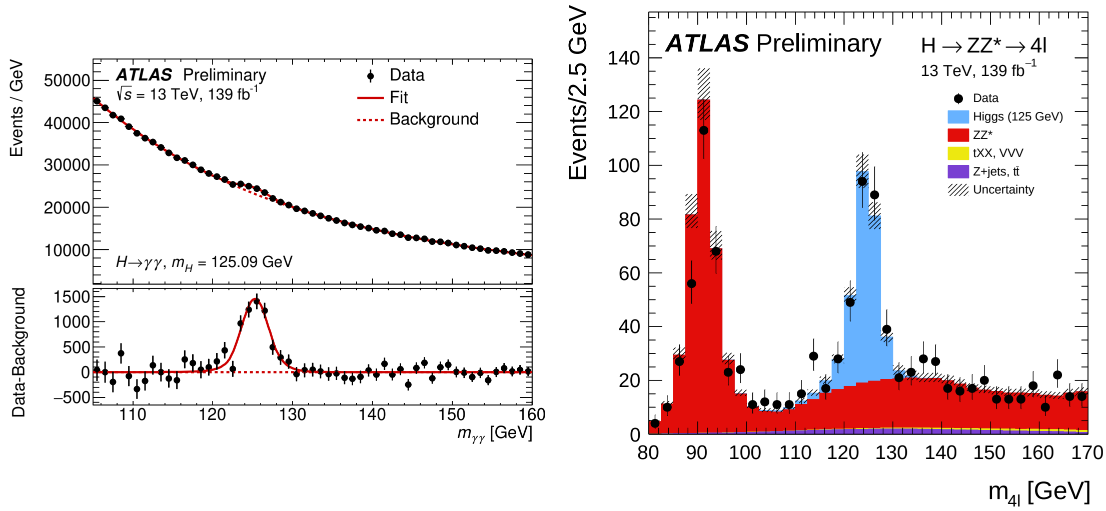

(a) Diphoton invariant mass distribution [37]. (b) Four-lepton invariant mass distribution [38].

Figure 1.14: Four-lepton and diphoton invariant mass distributions. The Higgs boson peak is visible at a mass of about 125 GeV.

The Higgs boson mass is measured by using its two-photons and four-leptons decay channels. With a preliminary dataset from the LHC Run 2, the ATLAS Collaboration measured a Higgs boson mass of [39]:

$$m_H\,(H \rightarrow \gamma\gamma) = 124.79 \pm 0.37\,\text{GeV} \quad m_H\,(H \rightarrow 4l) = 124.93 \pm 0.40\,\text{GeV} \tag{1.5}$$

The results are in good agreement with each other and with the average of the combined ATLAS and CMS Run 1 measurements [40]:

$$m_H = 125.09 \pm 0.24\,\text{GeV} \tag{1.6}$$

The combination of the ATLAS Run 1 and Run 2 measurements yields [39]:

$$m_H = 124.97 \pm 0.24\,\text{GeV} \tag{1.7}$$

One of the crucial aims of the ATLAS Experiment is to perform precision measurements of the Standard Model. Figure 1.15 shows the deviation of the current results from the theoretical expectations for several Standard Model total and fiducial production cross-section measurements. Most cross sections agree with the Standard Model predictions within uncertainties and no significant discrepancy from the Standard Model has been discovered until now.

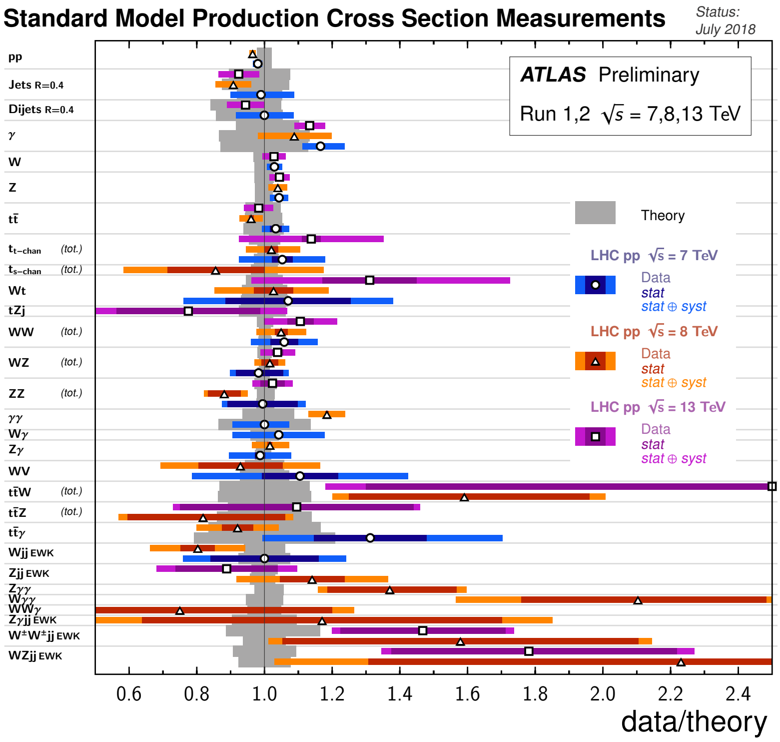

Figure 1.15: Data/theory ratio for several Standard Model total and fiducial production cross-section measurements [41].

1.3 High-Luminosity LHC

Increasing the luminosity of the LHC would greatly enhance the physics reach of ATLAS and of all the LHC experiments. In fact, a major purpose of the LHC experiments is the search for extremely rare phenomena, in particular new physics signatures. Moreover, all the Standard Model precision measurements would be greatly improved with additional statistics. For this reason, after Run 3 of the LHC will be completed and ATLAS will have collected more than 300 fb^{-1} [42], the LHC will be upgraded to the High-Luminosity LHC (HL-LHC), which is expected to start operations in 2027 [43].

The luminosity depends only on beam properties, such as the beam shape, number of particles per beam, and incidence angle between the two beams. In the case of two colliding Gaussian beams, the luminosity is given by [44]:

$$\mathscr{L} = \gamma \frac{N_{beam} f N_{bunches}}{4\pi\sigma_x\sigma_y} R \tag{1.8}$$

where γ is the relativistic Lorentz factor, N_{beam} the number of particles per bunch, f the bunch revolution frequency, $N_{bunches}$ the number of bunches, σ_x and σ_y the spatial dispersions of the bunches in the x and y directions, and R a geometric factor that decreases as the crossing angle between the two beams increases. The luminosity can be increased by increasing the number of colliding particles (either by increasing the number of bunches or the number of particles in a bunch), but also by reducing the size of the colliding beams.

The increase in luminosity for the HL-LHC is accomplished with an increase in the number of protons in the bunches (2.2×10^{11}, compared to 1.5×10^{11} in the LHC [45]) and with a reduced beam size. To reduce the size of the beams, new 11 T quadrupole magnets will be implemented in the final focus systems [46]. To achieve this effect a larger crossing angle is needed, reducing the geometrical factor R to about 0.31, down from 0.84 in the LHC [45]. This effect will be mitigated with the use of novel crab cavities, devices that can rotate longitudinally the bunches and therefore improve the overlap between them. The use of crab cavities will increase the geometric loss factor in the HL-LHC to a value of 0.83 [45].

The HL-LHC will run for about 10 years with an instantaneous luminosity of up to $7.5 \times 10^{34}\,\mathrm{cm}^{-2}\,\mathrm{s}^{-1}$ [45]. The total integrated luminosity recorded at the end of the HL-LHC operations will be up to $4000\,\mathrm{fb}^{-1}$, about ten times larger than that at the end of the LHC lifetime. The HL-LHC will greatly enhance the physics reach of the ATLAS Experiment. For example, at the end of lifetime of the HL-LHC the Higgs boson mass is expected to be measured with a precision of a few tens of MeV [47], one order of magnitude better than the currently achieved precision (Equation 1.7). Figure 1.16 shows two further examples of the enhanced physics reach offered by the HL-LHC.

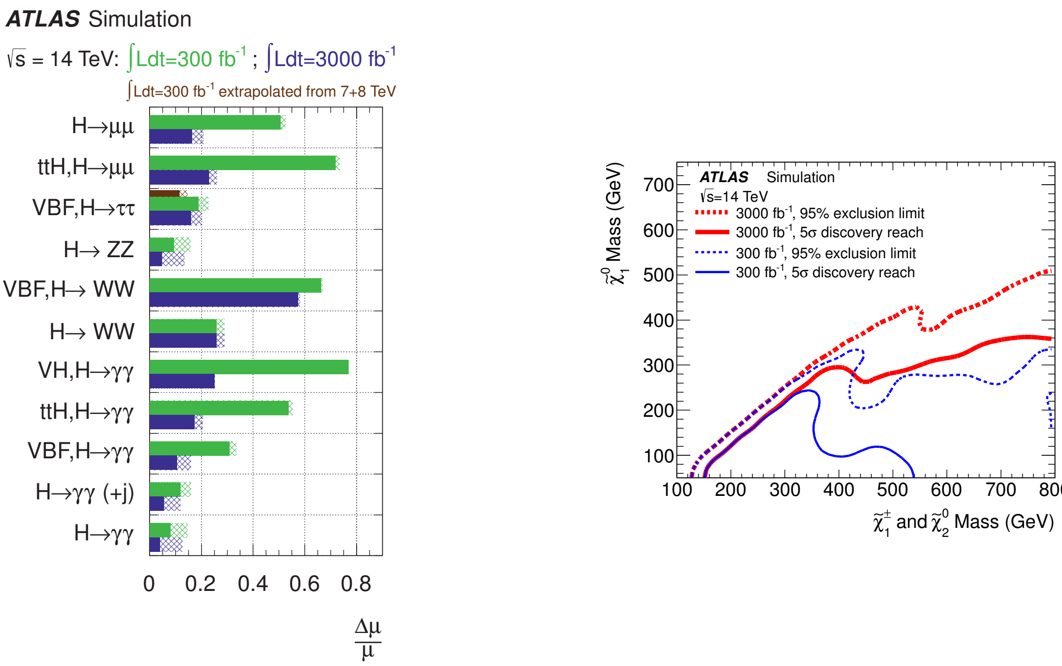

(a) Uncertainty on the Higgs boson signal strengths [48].

(b) Discovery reach (solid lines) and exclusion limits (dashed lines) for chargino and neutralinos in $\tilde{\chi}_1^{\pm}\tilde{\chi}_2^0 \rightarrow W^{(\star)}\tilde{\chi}_1^0 Z^{(\star)}\tilde{\chi}_1^0$ decays [48].

Figure 1.16: Comparison of physics reach expected at the end of lifetime of the LHC and at the end of lifetime of the HL-LHC.

The HL-LHC will create huge opportunities in terms of physics prospects but it will also generate a much harsher environment for the detectors. The biggest challenges are related to the much higher number of interactions per bunch crossing, which will increase from an average of 24 (in 2016) to an average of 200 inelastic proton-proton collisions, and much higher radiation levels. The trackers are particularly sensitive to these changes, since they are in the region where the tracks are the most dense and where radiation is the largest. For this reason, both the ATLAS and CMS experiments will fully replace their trackers as part of the so-called Phase-II upgrades.

1.4 ATLAS Inner Tracker

The current ATLAS Inner Detector will be replaced by a full-silicon tracker, called Inner Tracker (ITk), which is formed by inner pixel layers and outer strip layers. Figure 1.17 shows a cross-sectional view of the ITk, while Figure 1.18 shows its layout. Comparing the layout of the ITk to the one of the ID (Figure 1.4) a few differences can be noticed:

- The TRT region will be covered with silicon strip sensors. In fact, the TRT saturates in presence of a large number of interactions per bunch crossing (Section 1.2.1).
- The ITk Pixel Detector will cover a much larger area than the current Pixel Detector and it will extend to larger radii. In particular, the end-caps will extend the acceptance in the forward region to a pseudorapidity η of 4.0, up from 2.5 in the ID.
- The ITk Strip Detector will cover a much larger area than the SCT, since it will extend to the regions currently covered by the TRT.

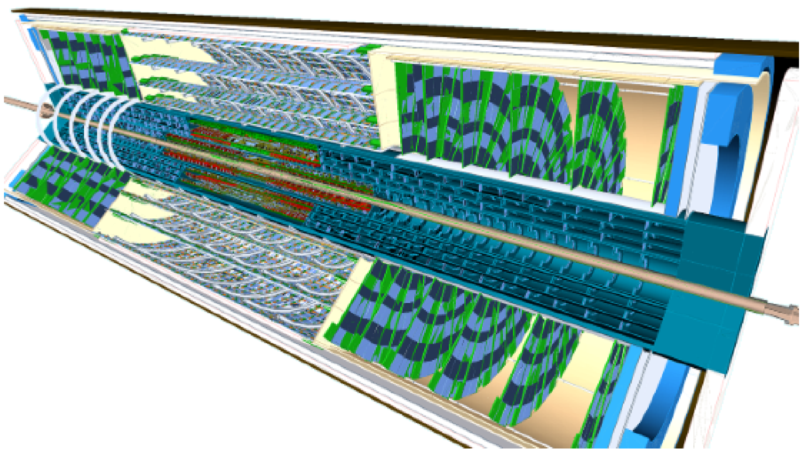

Figure 1.17: Cross-sectional view of the ATLAS Inner Tracker [49].

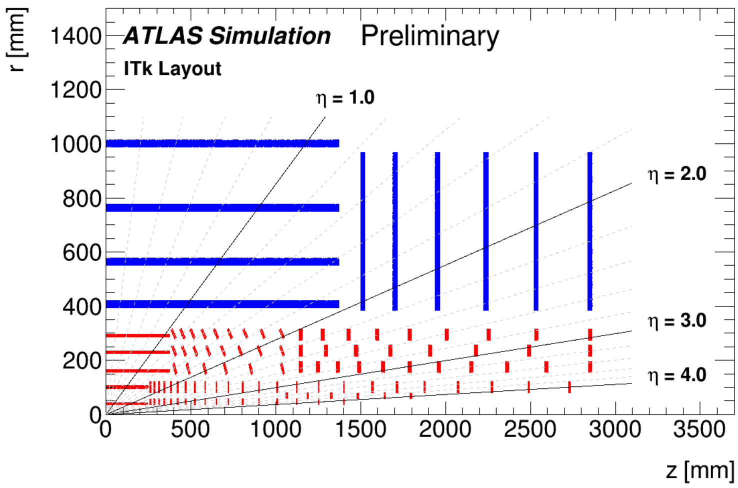

Figure 1.18: Layout of the ATLAS Inner Tracker with the Pixel Detector in red and the Strip Detector in blue [50].

A significant improvement in the ITk with respect to the ID is its material budget. The presence of excessive material in the tracker can seriously degrade the tracking performance, since it can induce particle interactions that can deflect a track, modify a particle momentum, or enhance pair production for a photon. A small material budget greatly increases the performance of a tracker. Figures 1.19a and 1.19b show the material budget in the ID and ITk, respectively. The material budget is expressed relative to the radiation length X_0, the average distance over which a high-energy electron loses all but 1/e of its energy by Bremsstrahlung. Because of the use of lightweight materials, the ITk will have a material budget much reduced with respect to the current ID.

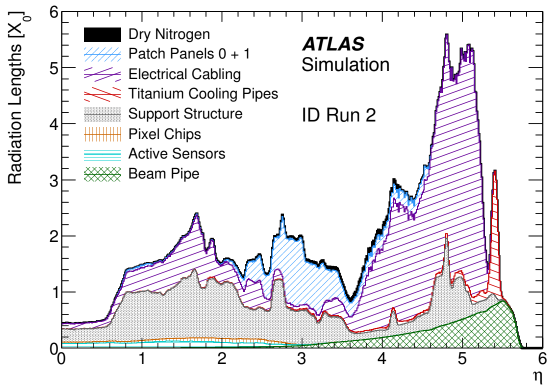

(a) Inner Detector [49].

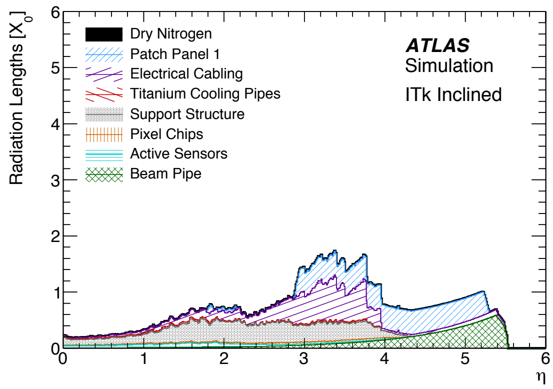

(b) Inner Tracker [49].

Figure 1.19: Radiation length as a function of the pseudorapidity in the Inner Detector and in the Inner Tracker.

1.4.1 ITk Strip Detector

The ITk Strip Detector will have a total active area of about 165 m^2, 2.5 times the area of the current SCT [49]. It will be divided in a central barrel with four barrel layers and two end-caps with six disks each (Figure 1.18).

Figure 1.20a shows the exploded view of an ITk Strip module, the basic building unit of the ITk Strip Detector. There will be a total of 17888 modules in the final detector, of which 10976 in the barrel and 6912 in the end-caps. Each module has a float-zone n-in-p sensor with an active area of about 10 cm × 10 cm, an active thickness of 300 µm, and an average strip pitch of 75.5 µm. Rectangular strips will be implemented in the barrel, with a length of 2.4 cm in the innermost two layers (Short Strip) and 4.8 cm in the outermost two layers (Long Strip). In the barrel the modules are mounted back-to-back with a total stereo angle of 52 mrad. In the end-caps the sensors will have radial strips, with different lengths at different radii, varying from 1.9 to 6 cm. In the end-caps the stereo angle is 40 mrad and is implemented in the sensor design. All the ITk Strip sensors will be produced by Hamamatsu Photonics K.K.

The readout ASICs (the ATLAS Binary Chips, ABC) and the Hybrid Controller Chips (HCC) are glued on the hybrid PCB (Printed Circuit Board), which is glued directly on the silicon sensor. Both the ABC and the HCC chips are fabricated in a CMOS 130 nm technology. Each readout chip is wire-bonded to 256 strips and provides preamplification, shaping and discrimination functionalities for every channel, in order to generate a binary output.
The last component of the module is the power board, which contains three components with different functionalities [51]:

- A DC-DC converter, which receives 11 V as an input and converts it to 1.5 V to supply the power to the front-end ASICs on the hybrids.
- A high-voltage switch that can disconnect the high-voltage from non-operating modules [52].
- The Autonomous Monitor and Control Chip (AMAC) which controls the high-voltage switch, monitors the current, voltage, and temperature and provides interlock functionalities.

The modules are mounted on the local supports: staves and petals (Figure 1.20b), for the barrel and end-caps, respectively. The local supports have a carbon fiber-based core with integrated titanium cooling pipes. On both sides of the local supports is glued a bus tape [53] which provides electrical connections and on which the modules are attached adhesively. The cooling will be provided by a CO_2 evaporative system, which will allow stable operations down to a temperature of −35 °C. The last component of the local supports is the End-Of-Substructure (EOS) card, which is the interface with the off-detector electronics [54].

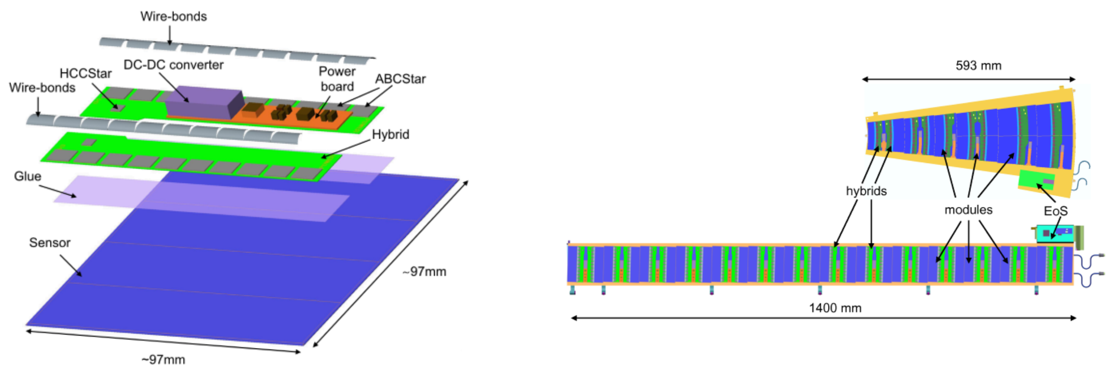

(a) Exploded view of a barrel module [49].

(b) A petal and a stave [49].

Figure 1.20: A module and local supports (petal and stave) for the ATLAS ITk Strip Detector.

Radiation damage is one of the most important challenges faced by the ITk Strip Detector. Figure 1.21a shows the simulated non-ionizing radiation dose in the ITk at the end-of-lifetime of the HL-LHC. The maximum non-ionizing dose of about $1.1 \times 10^{15}\ \mathrm{n_{eq}/cm^2}$ is expected in the innermost region of the last end-cap disks. As a comparison, the SCT sensors were designed to withstand a maximum non-ionizing dose of $2 \times 10^{14}\ \mathrm{n_{eq}/cm^2}$ [55]. Non-ionizing radiation damage has several consequences on the design choices of the sensors, as the use of the radiation-hard n-in-p technology.
Correspondingly, the ITk Strip Detector will be subject to an ionizing dose of up to about 50 MRad (500 kGy) (Figure 1.21b), while the SCT modules were designed to withstand 10 MRad (100 kGy) [56]. The large ionizing dose has significant effects on the ASIC design, such as the choice of the radiation-hard 130 nm technology [49].

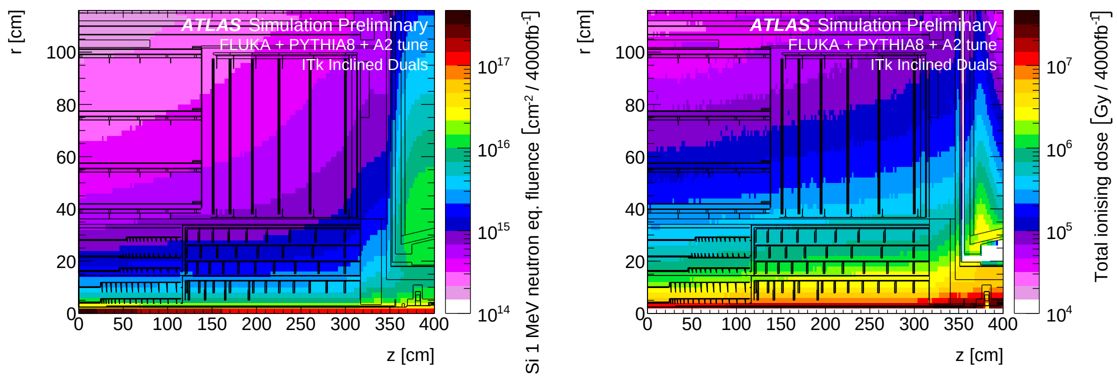

(a) Non-ionizing radiation dose [57].

(b) Total ionizing radiation dose [57].

Figure 1.21: Distributions of the expected non-ionizing and ionizing radiation doses in the ITk at the end-of-lifetime of the HL-LHC.

1.4.2 ITk Tracking and Physics Performance

In terms of tracking and physics performance, the aim for the ITk is to maintain or improve the performance of the ID despite the much larger pile-up. Figure 1.22a shows a comparison of the momentum resolution, arguably the most important figure of merit for a tracker, between the ITk and the ID [58]. The momentum is improved by a factor of about two in the ITk because of its smaller material budget and the better spatial resolution of the ITk Strip Detector with respect to the TRT.
Figure 1.22b shows the impact parameter resolution in z, $\sigma(z_0)$, as a function of the pseudorapidity for both the ITk and the ID. $\sigma(z_0)$ is improved significantly in the ITk at small pseudorapidities, mainly because of the smaller pixel pitch in the z direction in the ITk Pixel Detector with respect to the ID Pixel Detector.

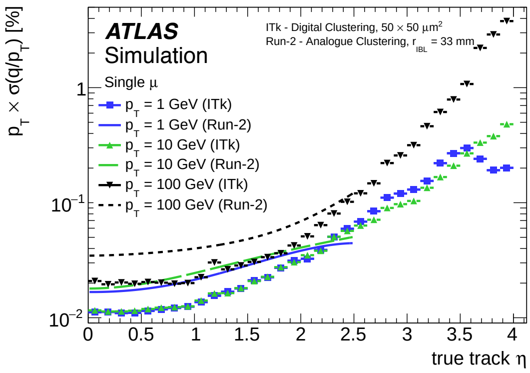

(a) Transverse momentum resolution [58].

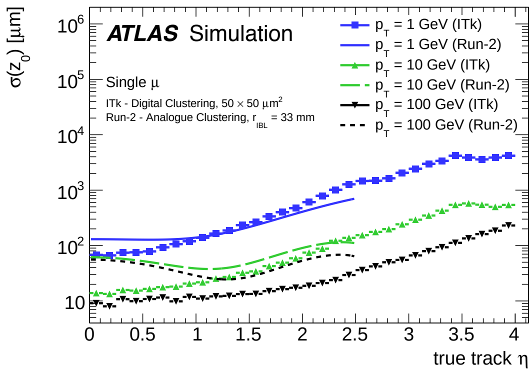

(b) Impact parameter resolution in z [58].

Figure 1.22: Transverse momentum resolution and impact parameter resolution in z as a function of the pseudorapidity for muons with three different energies, both in the ITk and in the ID.

Figure 1.23a shows the track reconstruction efficiency for a top-pair sample. Despite the much larger pile-up, the ITk exhibits a slightly larger efficiency than the ID.
Figure 1.23b shows the number of reconstructed vertices for top-pair events as a function of the number of interactions in a bunch crossing μ. A linear behavior is expected in absence of pile-up effects. The ID follows the expected linear for μ up to about 50, thus providing satisfactory performance in the LHC environment. At larger values of μ some vertices gets merged because of pile-up effects, and therefore the linear correspondence is lost. The ID can not provide satisfactory primary vertex reconstruction in the HL-LHC environment, where μ can reach 200. The ITk follows the linear behavior up to about 150 μ, the average number of interactions in a bunch crossing in the HL-LHC, and even at the maximum μ of 200 the number of merged vertices is only about 10%.

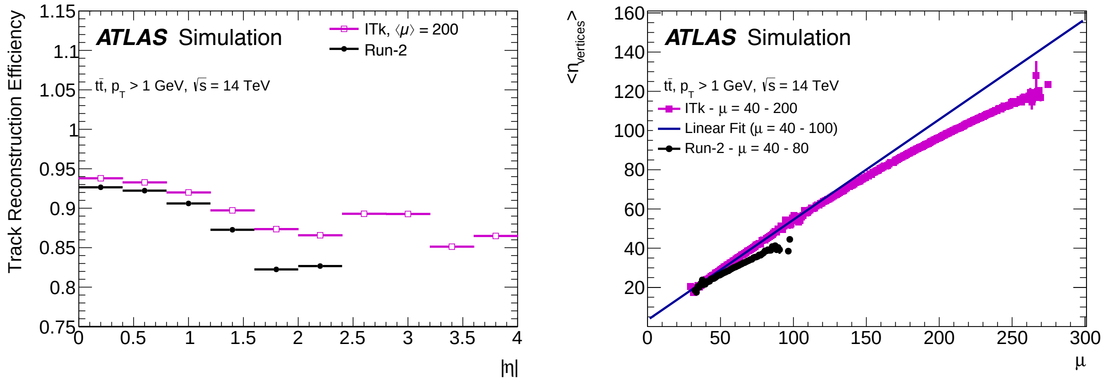

(a) Track reconstruction efficiency as a function of the pseudorapidity [58].

(b) Number of reconstructed primary vertices as a function of the number of interactions in a bunch crossing [58]. The ideal linear behavior is also shown.

Figure 1.23: Track reconstruction efficiency and number of reconstructed primary vertices for top-pair samples, both in the ITk and in the ID.

The ITk performance will also play a direct role in the reconstruction of physics objects. Figure 1.24a shows the electron charge mis-identification, the probability that an electron is reconstructed as a positron, in the ITk and in the ID. The mis-identification is decreased by at least a factor three in the ITk because of the lower Bremsstrahlung emission due to the smaller material budget with respect to the ID.
Figure 1.24b shows the probability that a photon from a diphoton Higgs decay is converted in an electron-positron pair in the tracker. Because of the very small material budget of the ITk, this probability is decreased by up to a factor 2.5 with respect to the ID.

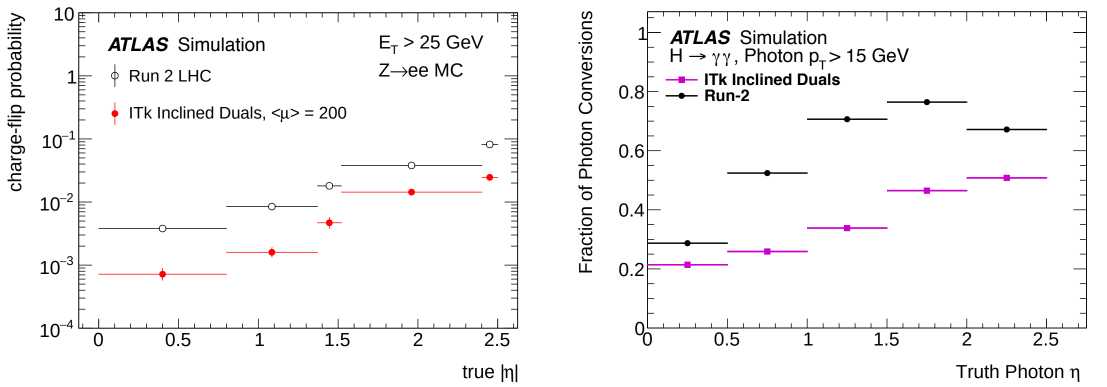

(a) Electron charge mis-identification probability [58].

(b) Probability that a photon from a diphoton Higgs decay is converted in an electron-positron pair in the tracker [58].

Figure 1.24: Electron charge mis-identification probability and photon conversion probability as a function of the pseudorapidity, both in the ITk and in the ID.

CHAPTER

2

SILICON SENSORS AND THEIR PROPERTIES

This Chapter introduces silicon sensors and their usage in high-energy physics. In Section 2.1 the characteristics of semiconductors are discussed and in Section 2.2 the semiconductor configuration used in radiation detectors, the pn junction, is explained. Section 2.3 discusses in detail the signal formation in silicon detectors: this is an important tool to fully understand the test beam results shown in Chapters 4 and 5. Section 2.4 introduces some crucial quantities used to characterize the electric performance of a silicon sensor. Several measurements of these quantities with ITk Strip sensors are discussed in Chapter 5. Section 2.5 explains the sources of noise in a silicon module. Noise plays a crucial role in the evaluation of the performance of strip modules discussed in Chapter 4. An important topic of this thesis is the evaluation of the performance of silicon modules after irradiation. Radiation damage in silicon sensors is discussed in Section 2.6. In Section 2.7 two sensor designs of interest for this thesis are discussed and compared: the SCT and the ITk Strip sensors.

2.1 Semiconductor Physics

A conductor is a material in which an electric current can flow, while in an insulator the current flow is suppressed. Semiconductors show both behaviors depending on the conditions in which they are operated. Some common semiconductors are silicon, germanium, and gallium arsenide.

A single atom (or molecule) has discrete energy levels, but when it is bonded to other atoms (or molecules) in a solid, the number of energy levels is so large that they be-

come very close to each other. These dense energy levels can be considered a continuum called energy band. The valence band contains electrons tightly bounded to their atoms, while the conduction band contains electrons free to move and to transport an electric current. The valence band and the conduction band are separated by the energy gap. At 0 K the valence band is totally filled, while the conduction band is empty. In normal conditions, however, at least a few electron move to the conduction band due to the non-zero thermal energy.
The electrical conduction of a material is determined by the energy gap. Conductors have almost or totally overlapping valence and conduction bands, hence their electrons can move freely and transport an electric current. Insulators have a very large energy gap (> 10 eV) and therefore their electrons are mostly in the valence band and no current can flow through them. Semiconductors have an intermediate energy gap (< 10 eV and > 0.2 eV[1]): if not stimulated they behave as insulators, but an external source can excite their electrons to the conduction band thus making them behave as conductors. Silicon has a band gap of 1.12 eV, an energy that can be provided, for example, by visible light.

Semiconductors can be used for radiation detection, since a particle crossing them produces a detectable electric signal. To generate a single charge carrier in a semiconductor an energy of about 1 eV is needed, much less than in gas detectors (about 10 eV) [59]. Many more charge carriers are then generated in a semiconductor detector, guaraneeing an excellent energy resolution.

Silicon, as most semiconductors, is a crystalline solid, therefore its constituents are arranged in an ordered and periodic structure. Silicon has four valence electrons (type IV material) which form the bonds with the neighboring atoms in the crystal lattice.

A common way to adjust the properties of a silicon crystal consists in replacing some silicon atoms with impurities. This procedure is called doping. When an atom with five valence electrons (type V material) is added to the crystal, an additional energy level is created close to the conduction band. The additional electron can easily be excited up to the conduction band and move freely. The so-called n-type silicon is obtained by inserting many impurities of this type, called donors. Phosphorus atoms are usually chosen for this purpose.
The opposite effect happens if an atom with three valence electron (type III material) is used. In this case, an energy level close to the valence is created. An electron from the valence band can be excited to this level, thus leaving a hole in the valence band. The hole can move freely and it essentially behaves as an electron in a conduction band but with positive charge. Silicon with many impurities of this type, called acceptors, is

[1] This energy range should be taken just as an example, since no well-defined limits on the energy gap of semiconductors exist.

called p-type and it is usually obtained using boron atoms.

2.2 pn Junctions

Apparently, pure silicon exhibits several interesting properties for radiation detection. However, a typical particle signal consists of ~10^4 charge carriers, but ~10^9 free charge carriers are always present in silicon at room temperature [60]. The signal would be indistinguishable from the background. To use silicon as a radiation detector it is necessary to reduce the number of free charge carriers. Ideally, this could be accomplished with operations at extremely low temperatures, but this is a very impractical solution. The most common solution consists in removing the free charge carriers by using an electric field.

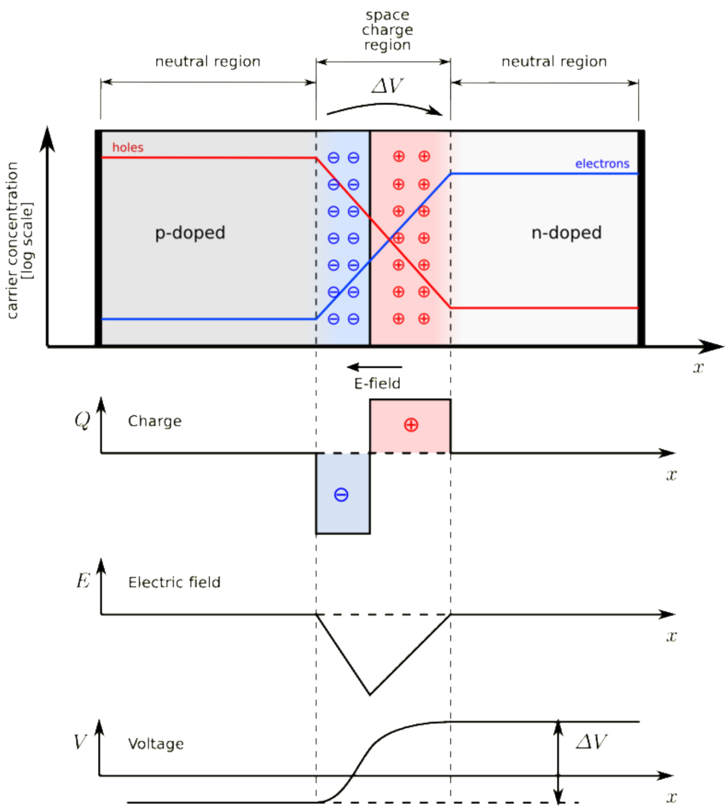

Figure 2.1: Charge, electric field, and electric potential profiles in a pn junction [61].

The electric field is obtained by juxtapositioning a p-type region to an n-type region. Such a device is called pn junction and it is explained in Figure 2.1. The electrons (holes) from the n-type (p-type) region naturally diffuse toward the p-type (n-type) region. Close to the junction interface electrons and holes can recombine, thus depleting this region of charge carriers. In the depleted region the ionized donors and acceptors create an electric field that counteract the diffusion process. This electric field can be exploited for particle detection: when an electron-hole pair is generated in the depleted region the electric field induces an electron (hole) drift toward the n-type (p-type) region. However, with no additional influences the depleted region extends only for ~10 μm.

In particle detectors the pn junctions are commonly operated in the so-called reverse-biased configuration. This is obtained by connecting the n-type region to a positive electrode and the p-type region to a negative one. When a bias voltage is applied with this polarity, more impurities are ionized hence widening the depleted region.

Assuming all the impurities in the depleted region to be ionized and the intrinsic charge carrier density to be negligible with respect to the impurity density, the charge density in the depleted region can be described by [62]:

$$\rho(x) = \begin{cases} -q_e N_A & \text{for } -w_A < x < 0 \\ q_e N_D & \text{for } 0 < x < w_D \\ 0 & \text{otherwise} \end{cases} \tag{2.1}$$

where $\rho(x)$ is the charge density, q_e the electron charge, N_A and N_D the acceptor and donor density, respectively, and w_A and w_D the width of the depletion region in the p- and n-type regions, respectively. The charge density is related to the electric potential by the Poisson equation:

$$\frac{\partial^2 V(x)}{\partial x^2} = -\frac{\rho(x)}{\epsilon_0 \epsilon_{Si}} \tag{2.2}$$

where $V(x)$ is the electric potential, ϵ_0 the vacuum permittivity, and ϵ_{Si} the silicon permittivity. The electric field in the depleted region is obtained by integrating Equation 2.2 after inserting the charge density from Equation 2.1:

$$E(x) = -\frac{\partial V(x)}{\partial x} = \begin{cases} -\frac{q_e N_A}{\epsilon_0 \epsilon_{Si}}(x+w_A) & \text{for } -w_A < x < 0 \\ \frac{q_e N_D}{\epsilon_0 \epsilon_{Si}}(x-w_D) & \text{for } 0 < x < w_D \end{cases} \tag{2.3}$$

A negative (positive) electric field is present in the p-type (n-type) region. The electric field depends linearly on the position and has a maximum value at the center of the junction (see Figure 2.1). By imposing continuity at the junction interface in Equation 2.3 the following relationship is obtained:

$$N_A w_A = N_D w_D \tag{2.4}$$

This equation ensures the charge neutrality in the pn junction and it shows that the depletion extends further in the less doped region.
The electric potential can be obtained by integrating Equation 2.3:

$$V(x) = \begin{cases} -\frac{q_e N_A}{2\epsilon_0 \epsilon_{Si}}(x+w_A)^2+V_{-\infty} & \text{for } -w_A < x < 0 \\ \frac{q_e N_D}{2\epsilon_0 \epsilon_{Si}}(x-w_D)^2+V_{\infty} & \text{for } 0 < x < w_D \end{cases} \tag{2.5}$$

where $V_{-\infty}$ and V_{∞} are integration constants. By imposing continuity at the junction interface in Equation 2.5 one obtains the total potential difference as a function of w_A and w_D:

$$\Delta V = V_{\infty} - V_{-\infty} = -\frac{q_e}{2\epsilon_0 \epsilon_{Si}}(N_A w_A^2 + N_D w_D^2) \tag{2.6}$$

Particle detectors usually implement a very highly-asymmetrical pn junction: one region has a much higher doping density than the other. In this case it follows from Equation 2.4 that the depletion extends almost only in the lightly-doped region. From Equation 2.6 one can obtain the depletion thickness:

$$w = \sqrt{\frac{2\epsilon_0 \epsilon_{Si}}{q_e N} \cdot (V_{bias})} \tag{2.7}$$

where N is the impurity density in the lightly-doped region and ΔV has been replaced by V_{bias}[2]. The depletion thickness increases as the bias voltage increases. The full depletion voltage is defined as the voltage at which all the silicon thickness is depleted and it can be obtained from Equation 2.7:

$$V_{fdv} = \frac{q_e N W^2}{2\epsilon_0 \epsilon_{Si}} \tag{2.8}$$

where W is the silicon active thickness. The larger the impurity density in the lightly-doped region, the higher voltage is needed to fully deplete the silicon bulk. The full depletion voltage is a crucial figure of merit of a silicon sensor, since a fully-depleted sensor collects a larger signal than an underdepleted one. Therefore, a low full depletion voltage is usually preferred for particle detectors.

Equations 2.3 and 2.5 are valid in the case of a diode, a single readout channel with a large surface area. The electric field and potential distributions inside most silicon sensors are more complex, since silicon sensors are usually segmented in readout channels with size $\ll$ 1 mm in order to improve their spatial resolution. Figure 2.2 shows a cross section of the electric potential distribution in a silicon sensor similar to the ones developed for the ITk Strip Detector (Section 1.4.1). In most of the bulk the potential follows the regular behavior described by Equation 2.5. Close to the surface, however, the readout strips distort the electric potential and the electric field lines are then directed toward the implanted strips.

[2] A built-in potential is always present in a pn junction. This potential should be added to the bias voltage, but it is neglected in Equation 2.7 since it is usually much smaller (< 1 V) than the bias voltage.

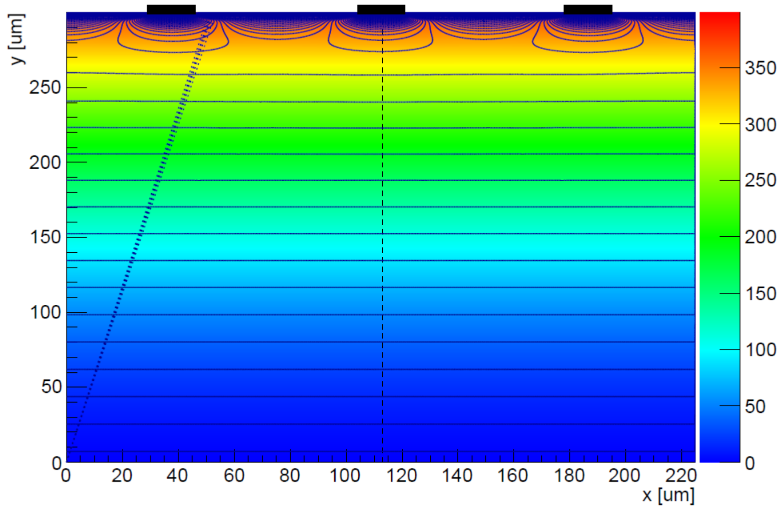

Figure 2.2: Cross section of the electric potential distribution in an n-in-p strip sensor with thickness 300 μm, pitch of 75 μm, readout strip width of 16 μm, full depletion voltage of 300 V, and an applied bias voltage of 400 V. Equipotential lines are also shown. The image has been generated with Weightfield2 [63].

The main properties of a silicon sensor can be described using the electrical resistivity, which, in case of a material with a dominant type of impurity, is given by [60]:

$$\rho = \frac{1}{q_e \mu N} \tag{2.9}$$

where μ is the majority carrier mobility, the proportionality factor between the drift velocity of a charge carrier and the electric field:

$$\vec{v} = \mu \vec{E} \tag{2.10}$$

where $\vec{v}$ is the drift velocity. Using these quantities Equation 2.8 can be rewritten as:

$$V_{fdv} = \frac{W^2}{2\epsilon_0 \epsilon_{Si} \mu \rho} \tag{2.11}$$

A high resistivity implies a low full depletion voltage and is then often preferred for particle detection purposes.

2.3 Signal Formation

2.3.1 Electric Charge Generation

A particle crossing the silicon bulk can excite a valence electron into the conduction band. The electron is then free to move in the crystal and can be collected in a read-out channel. The mean energy loss per unit path length, also called stopping power, is described by the Bethe formula [64]. Figure 2.3 shows the average collision stopping

power for electrons in silicon. The collision stopping power is related to the energy lost by collisions that result in the ionization or excitation of atoms, but the energy can be lost also by radiation, as in the case of Bremsstrahlung.
For low particle energies, the collision stopping power decreases as the electron energy increases. The collision stopping power has then a minimum at about 1 MeV and then it increases slowly as the energy increases. For most practical purposes the stopping power can be considered constant for energies > 1 MeV. This is a general property of the Bethe formula: at high energies the collision stopping power remain essentially constant at a value corresponding to its minimum value. A particle with this property is called Minimum Ionizing Particle (MIP). MIPs represent the majority of the collision fragments of interest in an LHC proton-proton collision. All particle types have a comparable collision stopping power when they are MIPs. These properties are particularly useful for testing purposes, since the sensor response does not depend on the energy or type of a MIP, as is the case for test beam particles.

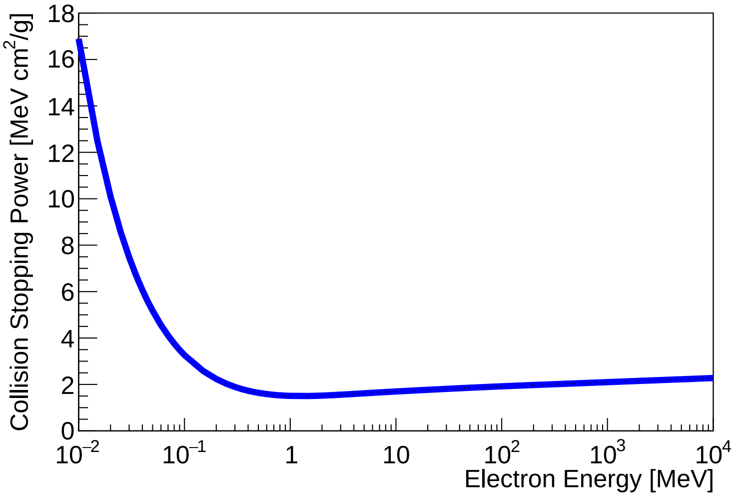

Figure 2.3: Average collision stopping power for electrons in silicon as a function of the electron energy [65].

To generate an electron-hole pair in silicon an average energy of 3.6 eV is used [66]. On average a MIP releases 390 eVμm^{-1}, thus creating 108 (electron – hole pairs)/μm [60].

The Bethe formula provides the average energy loss of a particle, but it does not provide any information on the energy loss distribution. The probability distribution of the energy loss is described by the Landau distribution, a highly-skewed distribution which resembles a Gaussian distribution with an additional long tail at large energy losses (see Figure 2.4). The tail is generated by delta rays [60], electrons with a relatively high energy which can traverse several hundreds of μm of silicon and hence release a large energy. The average energy loss is skewed toward large values by a few rare events with a very large energy loss [64]. The most probable energy loss is then a much better-defined quantity for experimental purposes.

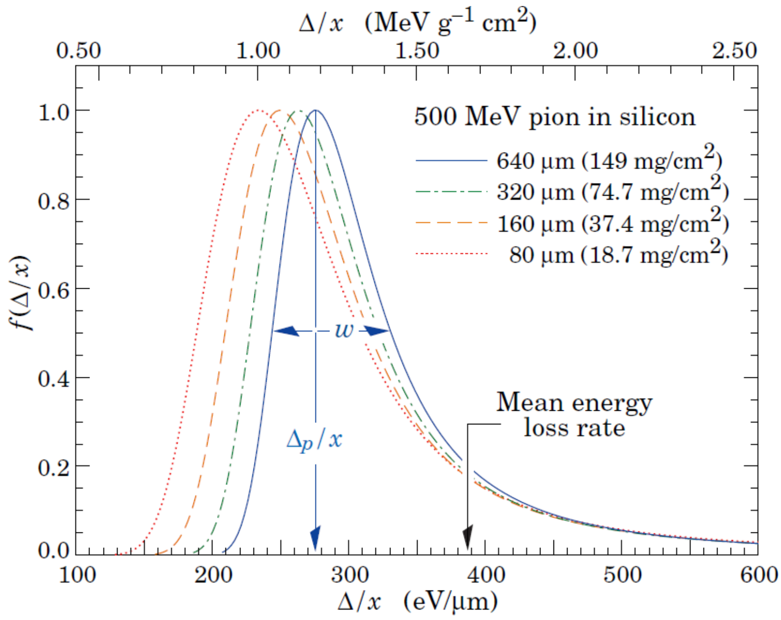

Figure 2.4: Energy loss (Landau) distributions in silicon for 500 MeV pions [64]. The average energy loss is also shown.

2.3.2 Electric Charge Drift

The interaction of a particle in the silicon bulk generates electrons and holes which drift toward opposite electrodes because of the electric field in the depleted region. While the electron velocity follows the direction of the electric field lines, the holes move in the opposite direction because of their positive charge. The drift velocity depends on the mobility and on the electric field (see Equation 2.10). A common parametrization for the mobility is [67]:

$$\mu = \frac{v_m}{E_c} \frac{1}{\left(1+(E/E_c)^\beta\right)^{1/\beta}} \tag{2.12}$$

where μ is the mobility and E is the electric field. v_m is the saturation velocity, E_c the critical electric field over which the velocity saturates, and β a parameter describing the transition to the saturation. These three parameters are determined experimentally and their values from the Jacoboni model [67] are summarized in Table 2.1. Several other models for the mobility can be found in literature, as the BFK [68] and the MINIMOS [69] models.

Charge Carrier	v_m [cm s^{-1}]	E_c [V cm^{-1}]	β
Electron	$1.53 \times 10^9\, T^{-0.87}$	$1.01\, T^{1.55}$	$2.57 \times 10^{-2}\, T^{0.66}$
Hole	$1.62 \times 10^8\, T^{-0.52}$	$1.24\, T^{1.68}$	$0.46\, T^{0.17}$

Table 2.1: Mobility parameters in the Jacoboni model [67]. T is the temperature in Kelvin.

Figure 2.5 shows the electron and hole drift velocities in silicon at 27 °C. It is visible that the drift velocity starts saturating at large electric fields. At velocity saturation the holes have a drift velocity about 20% smaller than the electrons. The difference is larger at smaller electric fields, for example at an electric field of $1 \times 10^3\,\mathrm{V\,cm^{-1}}$ the drift velocity of holes is 33% that of the electrons. The drift velocity increases with the electric field although the mobility decreases.

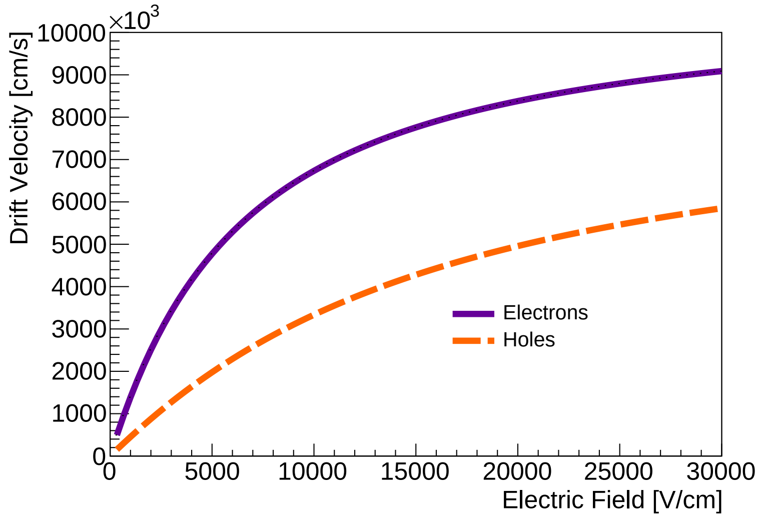

Figure 2.5: Drift velocity in silicon at 27 °C for electrons and holes. The horizontal axis range corresponds to electric field values of interest for this thesis. The values are obtained using Equation 2.10, the mobility parametrization described with Equation 2.12, and the parameters shown in Table 2.1.

The mobility and the drift velocity increase at low temperature. For example, at an electric field of $1 \times 10^4\,\mathrm{V\,cm^{-1}}$ the electron (hole) drift velocity is 27% (40%) larger at −35 °C compared to 27 °C.

The drift velocity does not comprehensively describe the motion of a charge carrier. A thermal motion is always present and it is superimposed to the drift. Unlike the drift velocity the thermal motion has no preferential direction, therefore on average it does not produce a net movement. Because of this effect, however, the position distribution probability of a charge carrier assumes a Gaussian distribution that widens over time, with a spatial dispersion given by:

$$\sigma_{\mathrm{diffusion}} = \sqrt{2 \cdot Dt} = \sqrt{2 \cdot \frac{\mu k_B T}{q_e} t} \tag{2.13}$$

where D is called diffusion constant, k_B is the Boltzmann constant, and t is the time elapsed from the start of the diffusion process. The longer the drift time of a charge carrier, the more diffusion can deviate its position from the electric field lines. The spatial dispersion can be considered independent from the mobility since a change in the mobility in Equation 2.13 is also accompanied by an opposite change of the drift time. Therefore, in case of operations in the same conditions, electrons and holes exhibit a similar diffusion dispersion. The diffusion dispersion increases with the temperature because of a faster thermal motion and it decreases as the electric field increases because of a reduced drift time.

Most silicon detectors used in high-energy physics are operated in a magnetic field in order to provide a particle momentum measurement (see Section 1.2.1). The Lorentz force affects the drift of the charge carriers making them propagate with an angle with respect to the electric field direction. This angle is called Lorentz angle and it is given by:

$$\tan(\theta_L) = \mu B_\perp \tag{2.14}$$

where θ_L is the Lorentz angle and $B_\perp$ is the component of the magnetic field orthogonal to the charge carrier motion. The higher the mobility, the larger the Lorentz angle. Therefore, electrons exhibit a Lorentz angle larger than holes. The Lorentz angle increases at low temperature and at low electric field (bias voltage) because of the higher mobility.
The presence of a magnetic field also influences the scattering mechanisms of the charge carriers inside the silicon, thus affecting their drift velocity. This can be taken into account as an additional factor, called Hall factor, multiplied to the mobility:

$$\mu_B = r_H \mu_N \quad \text{with } r_H = \begin{cases} 1.15 & \text{for electrons [70]} \\ 0.9 & \text{for holes [71]} \end{cases} \tag{2.15}$$

where μ_B is the mobility in presence of a magnetic field, μ_N the mobility without magnetic field (given by Equation 2.12 and Table 2.1), and r_H the Hall factor.

2.3.3 Shockley-Ramo Theorem

The charge carriers drift until they reach an electrode. The electric signal, however, is not generated by their collection at the electrode, but it is formed during their drift motion by means of electric induction. This mechanism is described by the Shockley-Ramo theorem [72,73]. The charge induced on an electrode by a charge motion is given by:

$$Q = -q\Delta V_w \tag{2.16}$$

where Q is the charge induced on the electrode, q is the charge of the drifting particle, and V_w is called weighting potential. The latter can be calculated by setting the potential of the electrode to 1 V and the potential of all the other conductors in the system to ground potential, while also removing all the free charge in the silicon bulk.

An equivalent formula for the induced current on the electrode can be obtained by differentiating Equation 2.16 with respect to time:

$$I = qvE_w \tag{2.17}$$

where I is the current induced on the electrode, v the velocity of the charge carrier and E_w the weighting field, which can be obtained in a similar way as the weighting potential V_w.
Although electrons and holes have charge with opposite sign, they generate a signal with the same polarity on the readout electrode since they move in opposite directions. For this reason, they have ΔV_w and v with opposite sign in Equation 2.16 and 2.17, respectively.

Figure 2.6 shows the weighting potential distribution in a silicon sensor similar to the ones developed for the ITk Strip Detector. The weighting potential sharply increases in proximity of the readout strip, thus most of the signal is induced when the charge carriers cross this region.

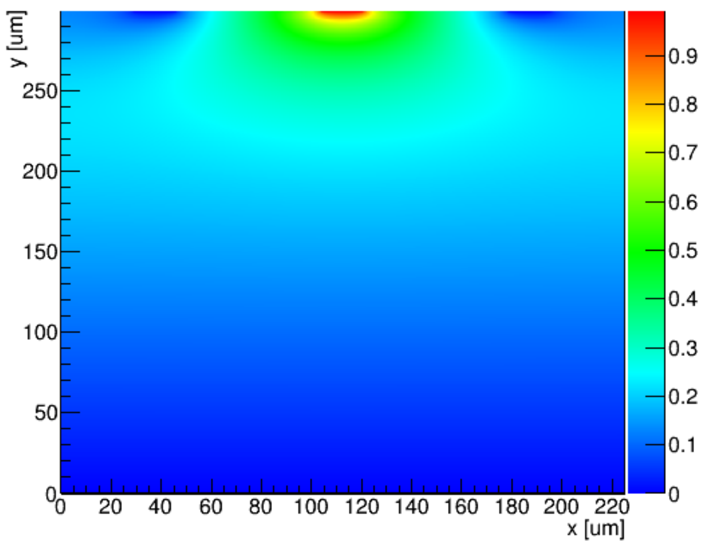

Figure 2.6: Cross section of the weighting potential distribution in a strip sensor with thickness of 300 µm, pitch of 75 µm, and a readout strip width of 16 µm. The x axis covers three strips, with the weighting potential calculated for the central one (while the other two strips are set to ground potential). The image has been generated with Weightfield2 [63].

Both electrons and holes contribute to the signal, but their contributions depends on the sensor configuration. The SCT implements p-in-n sensors where the holes drift toward the readout strips, while the electrons drift toward the sensor backplane. In case of a signal generated by a MIP the holes contribute to about 80% of the total signal, while electrons generate the remaining 20% (quantities obtained with Weightfield2 [63]). The situation is reversed in n-in-p sensor as the ones for the ITk Strip

Detector. In this case, the electrons generate about 80% of the total signal, while the holes contribute the remaining 20%.

2.4 Fundamental Quantities

Leakage Current

One of the crucial properties of a silicon sensor is the leakage current, the current that flows through the sensor. The leakage current is generated mainly by the creation of electron-hole pairs in energy levels close to the middle of the energy gap. The larger the volume of a sensor, the larger its leakage current. Only pairs generated in the depleted region are collected and contribute to the leakage current, thus in case of an under-depleted sensor the leakage current approximately increases with the bias voltage and saturates for bias voltages larger than the full depletion voltage [74]:

$$I_L \propto w \propto \sqrt{V_{bias}} \tag{2.18}$$

The leakage current increases as the temperature increases and its dependence on the temperature is described by [66]:

$$I_L(T) \propto T^2 e^{-E_g/2k_B T} \tag{2.19}$$

where E_g is 1.21 eV [75]. The leakage current contributes to heating the sensor by Joule heating. At high temperature the leakage current is large enough to increase the temperature of the sensor, which in turn increases the leakage current, which increases the temperature, and so on. This effect is called thermal runaway and it makes a sensor inoperable at high temperature. The leakage current is larger in irradiated sensors and so the thermal runaway becomes a very significant problem. For this reason, irradiated sensors can be operated only at low temperature (usually < 0 °C).

Bulk Capacitance

Another crucial quantity of a silicon sensor is the bulk capacitance. A silicon sensor can be approximated as a parallel-plate capacitor with width defined by the thickness of the depleted region. The bulk capacitance can then be described using Equation 2.7:

$$C_{bulk} = \begin{cases} A\frac{\epsilon_0\epsilon_{Si}}{W}\sqrt{\frac{V_{fdv}}{V_{bias}}} & \text{for } V < V_{fdv} \\ A\frac{\epsilon_0\epsilon_{Si}}{W} & \text{for } V > V_{fdv} \end{cases} \tag{2.20}$$

where A is the active area of the sensor surface, V_{fdv} the full depletion voltage, and W the active thickness. The bulk capacitance decreases as the bias voltage increases and it saturates when the full depletion voltage is reached.

Coupling Capacitance, Inter-Strip Capacitance, and Inter-Strip Resistance

In strip sensors the readout is segmented in several strips on the surface. Most strip sensors implement a capacitive coupling between the grounded strip, which collects the charge carriers, and an aluminum layer on top of it, which is connected to the front-end chips. The fast signal induced by a traversing particle is transmitted capacitively to the front-end chips, while the static leakage current is transferred to the bias line through a dedicated resistance called bias resistance. The coupling capacitance is the capacitance between a strip implant and the aluminum layer on top of it.

The electric relationship between adjacent strips have an important role in the performance of a silicon sensor. The inter-strip capacitance is the capacitance between two adjacent strips. The inter-strip capacitance is a major contributor to the load capacitance, therefore it plays a crucial role in the noise of a silicon module (see Section 2.5). Moreover, the charge collected in a strip can be induced to an adjacent strip through the inter-strip capacitance in a process defined as crosstalk in this thesis. The fraction of charge shared to each adjacent strip by crosstalk can be estimated as [76]:

$$P_{\text{crosstalk}} = \frac{C_{\text{inter-strip}}}{C_{\text{coupling}}+C_{\text{inter-strip}}+C_{\text{backplane}}} \tag{2.21}$$

where $P_{\text{crosstalk}}$ is the fraction of charge that is induced to an adjacent strip, and $C_{\text{backplane}}$ is the capacitance of a strip with respect to the backplane and it is related to the bulk capacitance. Similarly, the fraction of charge collected by an implant that gets induced in the same readout channel is:

$$P_{\text{transmission}} = \frac{C_{\text{coupling}}}{C_{\text{coupling}}+C_{\text{inter-strip}}+C_{\text{backplane}}} \tag{2.22}$$

A large crosstalk has a negative impact on a sensor performance, since it reduces the charge collected by the leading strip, and hence the hit detection efficiency, and it deteriorates the spatial resolution. In order to minimize the crosstalk a small inter-strip capacitance and a large coupling capacitance are needed.

The inter-strip resistance is the resistance between two adjacent strips. A large inter-strip resistance is needed to guarantee isolation of individual strips. A low inter-strip resistance can also lead to an increase of noise in a silicon module (see Section 2.5).

2.5 Noise in Silicon Sensors

Noise is a fundamental figure of merit of a silicon detector. A high noise can create fake hits which affect negatively the track reconstruction. Noise is usually expressed as Equivalent Noise Charge (ENC), the amount of charge at the input of the front-end chip which would generate the same output as the noise in the system. The noise of a silicon sensor module depends mostly on the sensor geometry and on the front-end chips. The noise can be divided in four main contributions [60]:

$$\mathrm{ENC} = \sqrt{\mathrm{ENC}_C^2 + \mathrm{ENC}_I^2 + \mathrm{ENC}_{R_P}^2 + \mathrm{ENC}_{R_S}^2} \tag{2.23}$$

The most important contribution in LHC (and HL-LHC) devices is the one given by the load capacitance [60]:

$$\mathrm{ENC}_C = a + b \cdot C_{load} \tag{2.24}$$

where a and b are parameters that depend on the preamplification stage and C_{load} is the load capacitance of a strip. Longer and wider strips exhibit a larger noise because of a larger load capacitance. The noise is lower in fully-depleted sensors than in under-depleted sensors because of a smaller bulk capacitance (see Equation 2.20). Figure 2.7 shows the noise as a function of the input capacitance in ITk Strip prototype structures. As described in Equation 2.24, an approximately linear dependence is observed.

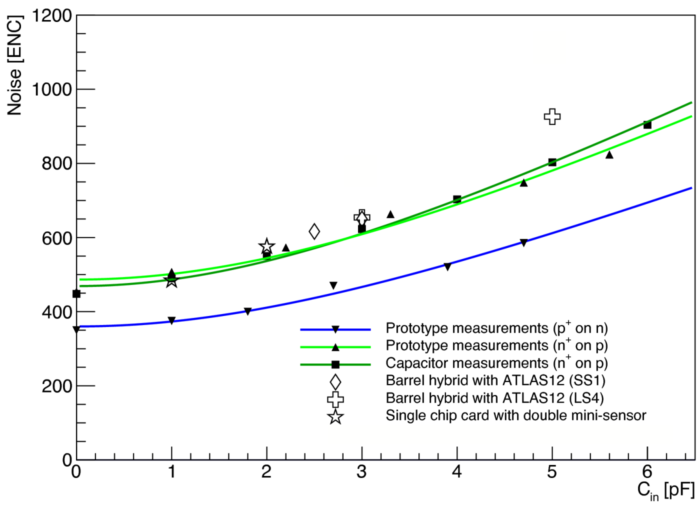

Figure 2.7: Noise as a function of the input capacitance in ITk Strip prototype structures with the prototype front-end chip ABC130 [49]. Different input capacitances correspond to different strip lengths. The blue and green lines indicate noise measurements with front-end chips bonded to capacitors and resistors to simulate a silicon sensor. The noise in prototype modules is labeled by open points.

The leakage current generates a contribution often called shot noise [60]:

$$\mathrm{ENC}_I = \frac{e}{2}\sqrt{\frac{I \cdot t_P}{q}} \tag{2.25}$$

where e is the Euler number, I the leakage current of a single strip, and t_P the peaking time of the shaping stage of the front-end chip (about 20 ns in the SCT and ITk Strip Detector). This contribution is generally small but after irradiation the leakage current can increase significantly and affect the noise. Since the leakage current decreases with the temperature, operating the sensors at low temperature contributes to limiting this noise contribution.

The last two contributions are related to thermal noise in the resistors present in the sensor geometry. The first is related to the parallel resistances [60]:

$$\mathrm{ENC}_{R_P} = \frac{e}{q_e}\sqrt{\frac{k_B T t_P}{2R_P}} \tag{2.26}$$

where R_P is the resistance in parallel to the preamplifier stage. The most significant parallel resistances are the inter-strip and bias resistances. The sensor design should ensure that these resistances have a large value in order to minimize this noise contribution.

The final contribution is the thermal noise from the series resistances [60]:

$$\mathrm{ENC}_{R_S} = C_{load}\frac{e}{q_e}\sqrt{\frac{k_B T R_S}{6t_P}} \tag{2.27}$$

where R_S is the resistance in series to the preamplifier stage. The most important series resistance is the aluminum layer resistance and the sensor design should ensure that its value is small enough to minimize this noise contribution.

2.6 Radiation Damage

Sensors for the LHC and for the future HL-LHC are designed to last for about ten years of operations in a harsh environment. A critical problem is represented by radiation, which modifies the silicon properties and severely degrades the performance over time. Radiation damage has many consequences on several design choices for sensors for high-energy physics.

2.6.1 Bulk Damage

A particle crossing a silicon sensor can dislocate an atom out of its lattice position. The displaced atom leaves a vacancy in the crystal lattice and gets dislocated to a position outside the crystal lattice becoming an interstitial atom. Vacancies and interstitial atoms are defects of the crystal lattice. They can recombine to recover the silicon lattice structure, but in general defects can also combine with each other to form more complex defects. Defects can also interact with impurities as the doping atoms.

Different type of particles at different energies produce a different amount of bulk damage. The Non-Ionizing Energy Loss (NIEL) hypotesis assumes that the number of defects created in the silicon crystal scales linearly with the amount of energy lost in atom-displacing collisions. Using the Lindhard partition function $P(E_R)$ the displacement damage cross section can be calculated as [77]:

$$D(E) = \sum_{\nu} \sigma_{\nu}(E) \int_0^{E_R^{max}} f_{\nu}(E, E_R) P(E_R) dE_R \tag{2.28}$$

where ν indicates all possible interactions between the particle and the silicon atoms, σ is the interaction cross section, E_R the recoil energy of the silicon atom, and f_{ν} the probaby for the displacement of a silicon atom.

With the displacement damage cross section it is possible to define a parameter to normalize the damage produced by different particles with different energies. This parameter is called hardness factor and it relates the displacement damage generated by a particle with energy spectrum $\phi(E)$ to the one produced by monochromatic neutrons with an energy of 1 MeV [77]:

$$\kappa \equiv \frac{\int D(E)\phi(E)dE}{D(E_{neutron} = 1\,\text{MeV}) \int \phi(E)dE} \tag{2.29}$$

Figure 2.8 shows the hardness factor for several particles and energies.

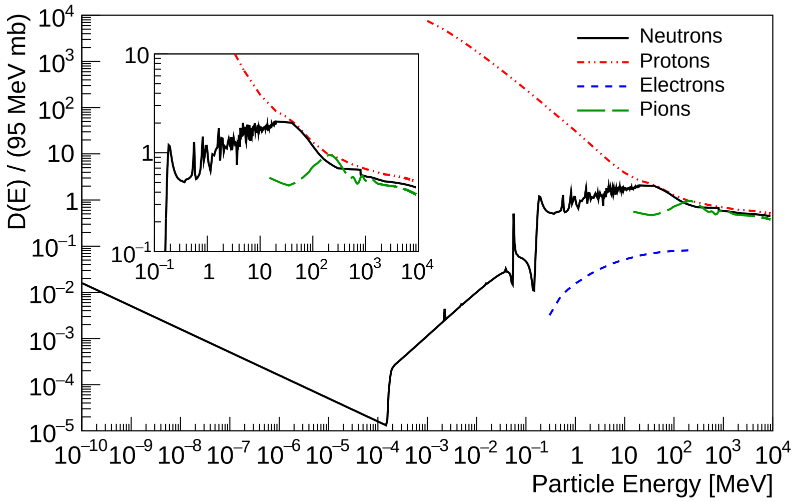

Figure 2.8: Hardness factor for several particles and energies (95 MeV mb is the displacement damage cross section D(E) for neutrons at 1 MeV) [77, 78].

Using the hardness factor defined in Equation 2.29 it is possible to normalize the flux of an arbitrary irradiation, to the flux of 1 MeV neutrons which would produce the same amount of displacement damage [77]:

$$\phi_{eq} = \kappa\phi = \kappa \int \phi(E)dE \tag{2.30}$$

This is called NIEL equivalent fluence and it has units of a 1 MeV neutron flux: 1MeV n/cm^2 or, in short, n_{eq}/cm^2.

Leakage Current

Bulk damage has several negative effects on the performance of a sensor. Both deep defects close to the middle of the energy gap and shallow defects close to the valence and conduction bands are created. The defects in the center of the energy gap can easily create electron-hole pairs thus increasing the leakage current of the sensors [79]. The increase in leakage current caused by bulk damage scales linearly with the NIEL equivalent fluence [77]:

$$\frac{\Delta I}{V_{ol}} = \alpha \cdot \phi_{eq} \tag{2.31}$$

where V_{ol} is the volume of the silicon bulk and α is called current-related damage rate.

Full Depletion Voltage

The full depletion voltage is affected mainly by defects close to the middle of the energy gap [79]. Figure 2.9 shows the full depletion voltage as a function of the NIEL equivalent fluence in an n-bulk sensor. The full depletion voltage first decreases as the NIEL fluence increases because the radiation-induced acceptor-like defects counteract the effect of the n-type doping. At NIEL fluences larger than $2 \times 10^{12}\ n_{eq}/cm^2$ the bulk becomes p-type and the full depletion voltage increases with the NIEL fluence. For p-bulk silicon sensors the type inversion does not happen and the full depletion voltage just increases with the NIEL fluence.

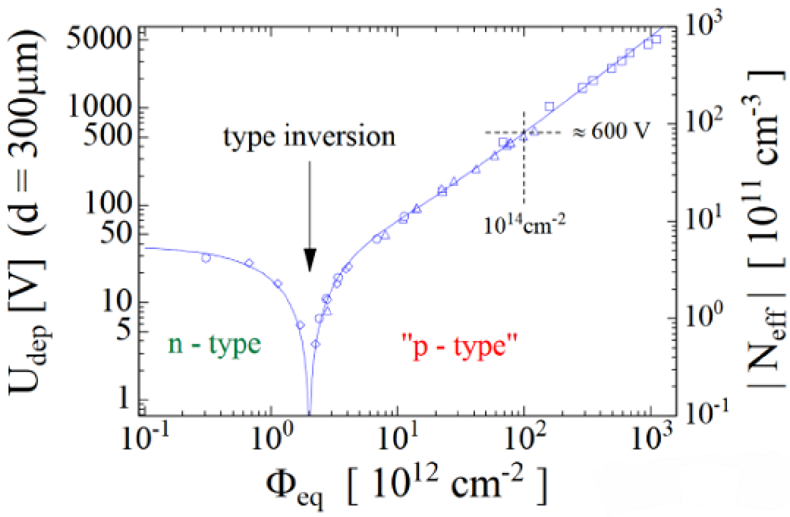

Figure 2.9: Full depletion voltage as a function of the NIEL fluence in an n-bulk sensor (on the right axis the effective doping concentration is shown) [77, 80].

A larger bias voltage is needed to fully deplete an irradiated silicon sensor. Since there are practical limits on the maximum bias voltage that can be provided to a sensor, it may be needed to operate highly-irradiated sensors with a bias voltage below the full depletion voltage. This reduces the amount of charge carriers that is collected in the depletion region. This has important consequences on sensor design and it is the reason for the shift from the p-in-n technology used in the SCT to the n-in-p technology chosen for the ITk Strip (see Section 2.7).

Trapping

The deep defects can capture the charge carriers during their drift in the silicon bulk hence decreasing the signal collected by a silicon sensor. The trapping probability for a charge carrier can be parametrized as [81]:

$$p(t) = \left(1\text{-}e^{-\frac{t}{\tau_{eff}}}\right) \tag{2.32}$$

where p(t) is the probability for a charge carrier to get trapped in the time t and τ_{eff} is called effective trapping time and it is defined by [81]:

$$\frac{1}{\tau_{eff}} = \sum_{TR} N_{TR}(1\text{-}P_{TR})\sigma_{TR}v_{th} \tag{2.33}$$

where TR are all the defects that can trap charge carriers, N_{TR} is the trap concentration, P_{TR} its occupancy probability, σ_{TR} the carrier cross section for trapping, and v_{th} the thermal velocity of the charge carrier.
The density of defects that can produce trapping N_{TR} increases with irradiation. After irradiation it is more probable for charge carriers to get trapped and hence the signal collected by the electrodes is reduced.

Annealing

The negative effects of bulk damage can be mitigated by exploiting the annealing, which consists in maintaining the sensor at a high temperature for a short amount of time in order to exploit the thermal processes in the silicon bulk. Figure 2.10a shows the current-related damage rate α, which is proportional to the leakage current (see Equation 2.31) as a function of the annealing time at 60 °C. The beneficial effect of annealing is clear, with the leakage current decreasing over time.

The effect of the annealing on the effective doping concentration, which is proportional to the full depletion voltage (see Equation 2.8), is more complex and it is shown in Figure 2.10b. The effective doping concentration, and thus the full depletion voltage, decreases over time until about 80 minutes at 60 °C. For longer times the annealing has a negative effect and it increases the effective doping concentration and full depletion voltage. The latter effect is known as reverse annealing.

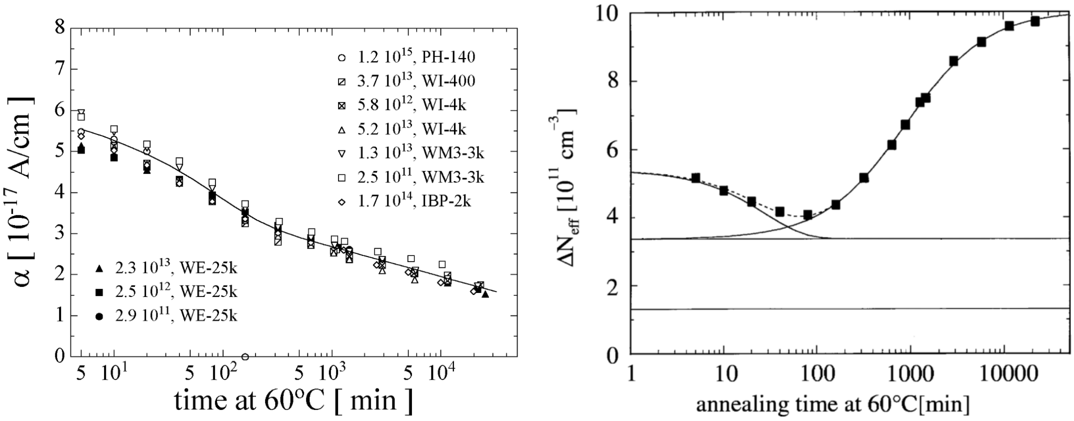

(a) Leakage Current [77].

(b) Full Depletion Voltage [77].

Figure 2.10: Effect of annealing at 60 °C on the current-related damage rate α (which is proportional to the leakage current) and effective doping concentration (which is proportional to the full depletion voltage), as a function of the duration of the annealing.

The time scale for the annealing effects increases exponentially as the temperature decreases. The ATLAS SCT is usually operated at about 0 °C in order to slow down the annealing effects [82]. During operational shutdowns, however, the SCT is maintained at room temperatures for short periods in order to maximize the beneficial effects of the annealing on the leakage current and full depletion voltage.

2.6.2 Surface Damage

Surface damage is mainly generated by ionization in the passivation silicon dioxide (SiO_2) layer on the surface by traversing particles [74]. Surface damage depends mainly on the Total Ionizing Dose (TID) released by a particle in the surface SiO_2 layer and it does not depend directly on the NIEL fluence.

SiO_2 is an insulator with energy gap of about 17 eV [83]. Most of the electron-hole pairs generated in SiO_2 promptly recombine, but in the presence of an electric field a few of them drift toward the electrode or toward the Si-SiO_2 interface. Electrons have a larger drift velocity and are quickly collected. Holes drift much slower and can be trapped in deep defects. Because of the large energy gap in SiO_2 the trapped holes can not escape the insulation layer, therefore they form a fixed positive oxide charge which is mainly located close to the Si-SiO_2 interface. This fixed positive charge induces a negative space charge on the bulk side of the interface [84] called electron accumulation layer [60, 66, 85]. This effect plays an important role in the design of radiation-hard silicon sensors (see Section 2.7).

Ionizing radiation also generates traps on the Si-SiO_2 interface which create energy levels close to the center of the energy gap. These energy levels can generate electron-hole pairs and thus increase the leakage current similarly to deep defects in the bulk.

2.7 SCT and ITk Strip Sensors

In a strip detector the readout is segmented in strips which collect the charge carriers and transfer the signal to the readout chips. Figure 2.11 shows the cross section of an n-in-p strip sensor similar to the ones for the ITk Strip Detector. P-in-n sensors, as the ones used in the SCT, are similar to the one shown in Figure 2.11 with the difference of having an n-type bulk, a p-type implant, an n^+-type backplane, and the absence of p-stops. The distance between the center of two strips is called pitch and it is 80 µm and 75.5 µm for the SCT and ITk Strip, respectively.

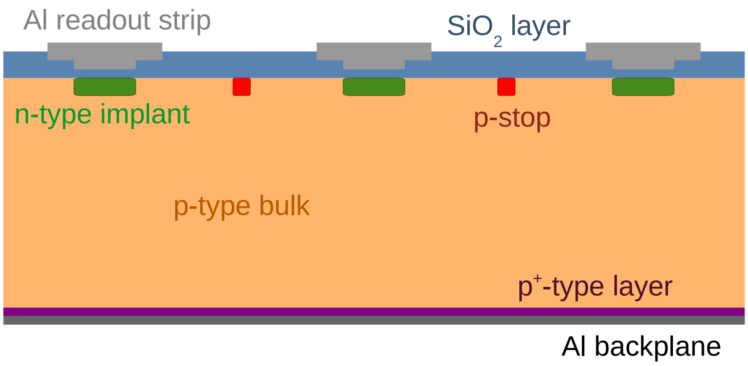

Figure 2.11: Cross section of an n-in-p silicon strip sensor. A similar layout is used in p-in-n sensors, but with a p-type implant, an n-type bulk, and an n^+-type backplane. Moreover, p-stops are not implemented in p-in-n sensors.

In the ITk Strip sensors, the bulk is p-type silicon with relatively small density of doping atoms (the doping density is less than $4.7 \times 10^{12}\,\mathrm{cm}^{-3}$ by design[3]), while every strip has an n-type implant with high doping density close to the surface. The ground potential is applied to the implant. To create the reverse-biased pn junction on the backplane a conductive aluminum layer on which the bias voltage is applied (negative for n-in-p and positive for p-in-n sensors). The backplane aluminum layer is in contact with a thin p^+-type layer to apply the voltage to the silicon bulk. In this way, electrons (holes) drift toward the grounded implant in n-in-p (p-in-n) sensors, while holes (electrons) drift toward the backplane.

An aluminum strip is implemented on top of the implants: the signal is first collected in the implants and then induced capacitively to the aluminum layer. The signal is then transferred to the front-end chips through aluminum wire-bonds. The implant has width of 16 µm and the aluminum layer has width of 22 µm in both the SCT and

[3]This follows from the specification on the silicon resistivity of $\rho > 3\,\mathrm{k}\Omega\,\mathrm{cm}$ [49] and Equation 2.9.

ITk Strip sensors [86]. P-stops are p-type implants with a very high doping density located in the inter-strip region between two strips [87, 88]. They improve the isolation of the strips by acting on the electron accumulation layer located close to the Si-SiO_2 interface. P-stops are used in n-in-p sensors which are prone to the accumulation of electrons on the surface [89] because of the electric field lines direction. No similar structure is needed in p-in-n sensors.
A SiO_2 layer on the surface helps protecting the silicon bulk from the environment. Often, additional passivation layers are added on top of the SiO_2 and aluminum layers.

After irradiation the bulk of p-in-n sensors becomes of p-type, an effect known as type inversion (see Section 2.6.1). After type inversion the depletion region extends from the backplane. In this case, when the sensor is operated underdepleted, a region with no electric field separates the implant and the depletion region with the effect of severaly reducing the collected signal. At NIEL fluences reached in the HL-LHC environment ($> 1 \times 10^{15}\ n_{eq}/cm^2$), it becomes impractical to provide bias voltages larger than the full depletion voltage. The consequent signal loss caused by underdepletion would be too large to guarantee a reliable tracking performance.
The drawbacks related to type inversion are avoided using the n-in-p technology as for the ITk Strip sensors. In n-in-p sensors the electric field always extends from the implant, therefore these sensors can be operated underdepleted with no exceptional loss of signal.

Table 2.2 compares the drift properties of the charge carriers in the SCT and in the ITk Strip sensors. The drift time is shorter in the ITk Strip sensors because of the collection of electrons instead of holes. Because of the shorter drift time, a smaller fraction of the charge carriers gets trapped (see Equation 2.32), thus increasing the signal after irradiation. The diffusion dispersion is larger in the SCT because of the smaller bias voltage and the higher temperature, with the effect that more charge is shared to adjacent strips.

Quantity	SCT	ITk Strip
Average Drift Time [ns]	5.7	1.7
$\sigma_{diffusion}$ [μm]	3.5	2.2
Lorentz Angle [°]	4.8	8.6

Table 2.2: Charge charriers drift properties in the SCT and ITk Strip. The quantities have been calculated using formulas from Section 2.3.2. Only hole (electron) drift is considered for the SCT (ITk Strip), since it gives the largest contribution to the total signal (see Section 2.3.3). All the quantities are calculated at the center of the bulk thickness. A bias voltage of 150 V and 400 V is used in the calculations for the SCT and ITk Strip, respectively. A temperature of 0 °C is assumed for the SCT sensors and of −20 °C for the ITk Strip sensors.

CHAPTER

3

TEST BEAM INFRASTRUCTURE AND SOFTWARE

This Chapter introduces the basic test beam concepts. Section 3.1 describes the test beam facilities where the measurements discussed in this thesis were performed, followed in Section 3.2 by the description of the main instrument used during the test beams, the EUDET-type beam telescope. The aim of test beams is often the characterization of irradiated devices. Section 3.3 describes the irradiation facilities where some of the modules and sensors discussed in this thesis were irradiated. Section 3.4 introduces the EUTelescope software used for track reconstruction of test beam data. The reconstruction steps performed in a typical analysis are described in detail following an example with ITk Strip test beam data implemented in EUTelescope v2.0.

3.1 Test Beam Facilities

3.1.1 DESY II Test Beam Facility

DESY II is a synchrotron in the DESY campus in Hamburg. It accelerates electrons from an energy of 0.45 GeV to up to 6.3 GeV [90]. Its main purpose is as injector for the PETRA III synchrotron, but a beam extraction for test beam purposes is also installed.

Figure 3.1 shows schematically the DESY II test beam facility and the beam generation steps. A carbon fiber target is located in the DESY II beam pipe in order to generate Bremsstrahlung photons, which are then converted in electron-positron pairs in a secondary metal target. A dipole magnet is used to select the type (electron or positron) and momentum of the beam. Finally, the beam is collimated and delivered to the test beam areas. An electron beam momentum in the range of 1-6 GeV can be selected by the test beam users.

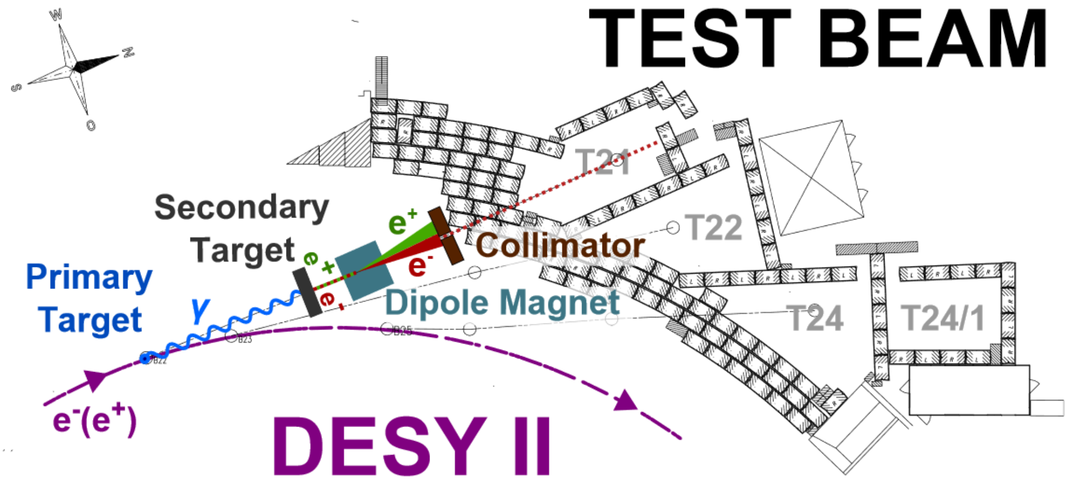

Figure 3.1: Schematic view of the DESY II test beam facililty [90].

The DESY II test beam facility comprises three beam lines and four test beam areas: T21, T22, T24, and T24/1. Two beam lines, T21 and T22, are typically equipped with an EUDET-type telescope. Figure 3.2 shows the beam rate in the beam line T22 as a function of the electron beam momentum. The maximum beam rate of about 4 kHz cm^{-2} is obtained with an electron momentum of about 2 GeV.

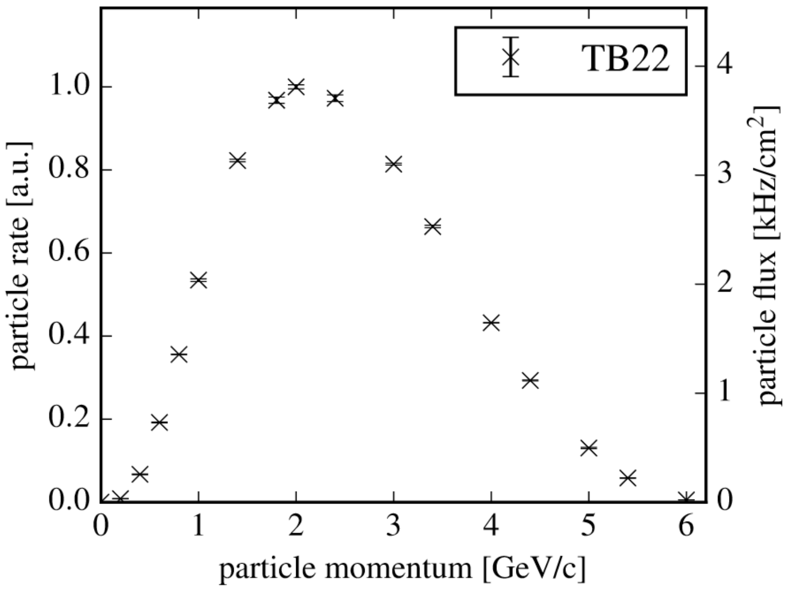

Figure 3.2: Particle rate as a function of the beam momentum for an electron beam in the DESY test beam area T22 [90].

3.1.2 CERN SPS Test Beam Facility

The CERN SPS test beam facility is located in the CERN North Area (Figure 3.3) close to Prévessin, France. The SPS synchrotron accelerates protons to an energy of 450 GeV and it is the final pre-acceleration stage before the injection of the proton bunches into the LHC.

Figure 3.3: The CERN North Area.

A fraction of the SPS beam is extracted and directed toward primary targets that convert the SPS protons in secondary particles, mainly pions. Six beam lines are obtained in this way, with more than ten test beam areas. The SPS beam is usually extracted every 16.8 s and the spill length is 4.8 s [91]. A maximum particle momentum of 200 GeV is achievable in the beam line H6, with up to 1×10^{18} particles per spill [92].

3.2 EUDET-Type Beam Telescopes

The high-energy test beam particles can cross a large amount of material without being significantly affected by scattering. By measuring their position in different locations along their path, particle tracks can be reconstructed and extrapolated on a Device Under Test (DUT) with a resolution of a few μm. This is the basic concept of beam telescopes, one of the most powerful instruments for detector characterization.

Currently, the most successful beam telescopes are the EUDET-type telescopes (Figure 3.4) [93]. There are seven EUDET-type telescopes worldwide: DATURA and DURANTA at DESY (in T21 and T22, respectively), AIDA, ACONITE, and AZALEA at CERN (in H6B, H6A at CERN SPS and in T10 at CERN PS, respectively), ANEMONE at Universität Bonn, and CALADIUM at SLAC [94].

Figure 3.4: The DURANTA EUDET-type telescope installed at the test beam area T22 of the DESY II test beam facility. The six telescope planes are visible, with the active Mimosa26 sensors being located at the center of the planes behind a black kapton tape. The pipes on the side transport water to cool the Mimosa sensors. The Mimosa sensors are read out by the boards on top of the telescope planes, which also provide the trigger interface. The black scintillator in front of the first plane provides the triggers for the whole set-up.

The EUDET-type telescopes consist of six planes with Mimosa26 silicon pixel sensors [95] each with a pitch of 18.4 µm in both directions, a total active area of about 1 x 2 cm^2, and a physical thickness of 50 µm. A single Mimosa sensor provides hits with a spatial resolution of 3.24 µm for DATURA and ACONITE [96] and about 4.1 µm for DURANTA [97]. By combining the hits on the six telescope planes, the telescope can provide track information with a resolution lower than 2 µm [96].
The DUT is usually placed at the center of the telescope. Any material added by the DUT deteriorates the tracking resolution. A tracking resolution of about 10 µm is obtained for a typical set-up for the ITk Strip test beams (see Section 3.4).

The trigger functionalities are provided by four scintillators placed before the first telescope plane and after the last one. When a beam particle crosses the telescope, a signal is generated in the scintillators. A coincidence of signals in several scintillators is a signature of a crossing particle and when this happens, a trigger signal is transmitted to all the devices in the set-up. When the devices receive a trigger, they transmit to the common Data Acquisition (DAQ) software the hit information of the readout frame corresponding to the trigger.

The Mimosa sensors have an integration time of 115 µs [96], much larger than the typical integration time of LHC devices (~25 ns). Due to the short integration time, an LHC device generally records only the hits of the particles generating a trigger. The Mimosa planes, however, can record additional particle tracks during their long inte-

gration time. In order to measure the hit detection efficiency of a DUT only the tracks crossing within a single DUT readout frame must be selected. This is accomplished by adding a reference plane: a pixel plane with an integration time comparable to the one of the DUT. An FE-I4 pixel plane (see Section 1.2.1) was used for the data discussed in this thesis. It has an integration time of ~25 ns, an active area of about 1.7 x 2 cm^2 and pixel size of 50 x 250 $\mu\mathrm{m}^2$. By selecting in the analysis only tracks with a hit on the FE-I4, it is possible to measure the hit detection efficiency of an ITk Strip module.
In a test beam in June 2019 an ALPIDE sensor [98] was used as a reference plane. ALPIDE has an active size of about 1.4 x 3 cm^2 and pixel size of 26.88 x 29.24 $\mu\mathrm{m}^2$. It has an integration time of several µs [99], much longer than the FE-I4 pixel plane. Therefore, the ALPIDE plane provides a worse discrimination of tracks out-of-time with respect to the DUT readout frame.

Every device in a test beam set-up has its own DAQ system. The telescope has a DAQ system based on National Instruments hardware and the software LabView, while the FE-I4 is read out by the USBpix board [100] and the STControl software. The DAQ systems have to be synchronized and controlled by a common system. These functionalities are provided by the Trigger Logic Unit (TLU, Figure 3.5) [101, 102] and by the software EUDAQ [103] (and the more recent EUDAQ2 [104, 105]). The TLU receives the scintillator signals and, in presence of coincident signals, it transmits a trigger to all the devices in the set-up. When a device is in a state in which it can not collect data, it issues a signal to the TLU which prevents further triggers to be generated (Busy signal). The TLU and the DAQ systems are controlled by EUDAQ, which also collects in a single binary file the data streams of all the devices. EUDAQ also provides online monitoring functionalities, with hit maps and correlation plots (see Section 3.4) created during data taking using a fraction of the recorded events.

Figure 3.5: A Trigger Logic Unit (TLU). The telescope planes are connected by the gray RJ45 cable on the left. The upper right LEMO interface receive the trigger signal from the scintillators. The lower four cables provide the power to the scintillators. The TLU is connected to the DAQ computer by the black cable in the bottom right corner.

3.3 Irradiation Facilities

In many test beams the main focus is on the characterization of irradiated devices. The radiation environment of the LHC (and HL-LHC) in the tracker region consists of several particles, e.g collision fragments, neutrons coming from the moderator surrounding the central ATLAS solenoid, and photons generated by interactions in the tracker material. Both ionizing and non-ionizing particles contribute to the high-radiation levels. It is impossible to replicate exactly this radiation environment in an irradiation facility. However, several irradiation facilities are present worldwide, each one with different characteristics that can provide different information on the radiation damage on silicon sensors and modules.

Some of the modules and sensors discussed in this thesis were irradiated at the following irradiation facilities:

- The IRRAD proton facility at the CERN PS East Hall, with a proton beam of energy 24 GeV [106, 107].
- The Ljubljana Neutron Irradiation Facility at the Jožef Stefan Institute (JSI), with neutrons from a TRIGA Mark-II nuclear reactor [108].
- The Karlsruher Institut für Technologie (KIT) proton irradiation facility, where a proton beam of energy 25 MeV is extracted from the Karlsruhe Kompakt Zyklotron (KAZ) [109].
- The TERABALT radiation set at UJP Prague, a ^{60}Co-based irradiator with gamma-rays of energy of ~1 MeV [110].

In Table 3.1 the hardness factor and TID per NIEL fluence are compared for the CERN PS, JSI and KIT facilities. The CERN PS proton irradiation facility provides a TID per NIEL fluence comparable to the radiation environment expected at the HL-LHC in the ITk Strip Detector. The KIT proton irradiation facility provides about three times more TID at the same NIEL fluence. At JSI a very small amount of TID is experienced by the samples, since neutrons do not interact electromagnetically and thus generate a minimal amount of ionization on the silicon surface. Therefore, the irradiation at JSI produces bulk damage in the silicon with only minimal surface damage. Finally, gamma-rays release a TID, but their energy release is too small to displace silicon atoms and create bulk damage. For this reason, the irradiation from UJP Prague essentially generates only surface damage and do not produce any significant bulk damage. The same happens for x-ray irradiations as the ones discussed in Chapter 4.

Facility	Hardness Factor	TID per 1 x 10^{14} n_{eq}/cm^2
CERN PS	0.62 [111]	4.8 MRad (48 kGy) [112]
JSI	0.90 [113]	~0.1 MRad (1 kGy) [114]
KIT	2.2 [111]	15 MRad (150 kGy) [115]

Table 3.1: Hardness factor (see Section 2.6.1) and TID per NIEL fluence in the irradiation facilities where modules and sensors discussed in this thesis were irradiated. UJP Prague is not shown since gamma-rays do not produce any significant bulk damage, therefore the hardness factor and the NIEL fluence can not be defined.

3.4 EUTelescope Reconstruction Framework

The EUTelescope framework [116,117] was created in the context of the EUDET project to reconstruct tracks obtained with a beam telescope. EUTelescope is a modular and general framework written mainly in C++. It is embedded in the ILCSoft framework [118] and it is a group of Marlin [119] (Modular Analysis & Reconstruction for the LINear collider) processors. The data is stored using the Linear Collider I/O (LCIO) [120] data format, an event-based storage format which can be read via C++, among others. The geometry is described using the Geometry API for Reconstruction (GEAR) [121] geometry description toolkit, which stores the geometry parameters, such as the strip pitch or the rotation angle of a sensor, using XML files.

Figure 3.6: EUTelescope logo.

Figure 3.7 shows the steps performed in a typical reconstruction. A single step comprises many processors. The starting LCIO file is created by converting with EUDAQ2[1] the binary file generated during a test beam. The track fitting is performed using the General Broken Lines algorithm (GBL) [122, 123] implemented in the GBL software [124]. The GBL algorithm is a tracking algorithm which allow scattering material to be included in the re-fit of a particle track [125]. To align the geometry, the tracks obtained by the GBL fit are processed by Millepede II [126], a package for least squares fits with a large number of parameters. Millepede-II returns the best alignment parameters to minimize the χ_2 of the tracks. The final EUTelescope step produces a ROOT file [127]

[1]With EUDAQ1 the conversion is performed during the first EUTelescope step.

with the track and hit information. This ROOT file can be analyzed directly by the user with a customized analysis code.

The example *GBL_DUT* is implemented in EUTelescope v2.0. It reconstructs data taken with the EUDET-type telescope DURANTA at the DESY T22 beam area with a beam momentum of 4 GeV. The DUT is an ITk Strip module and an FE-I4 pixel plane is used as reference plane. The following explanation of the typical EUTelescope steps is based on this example.

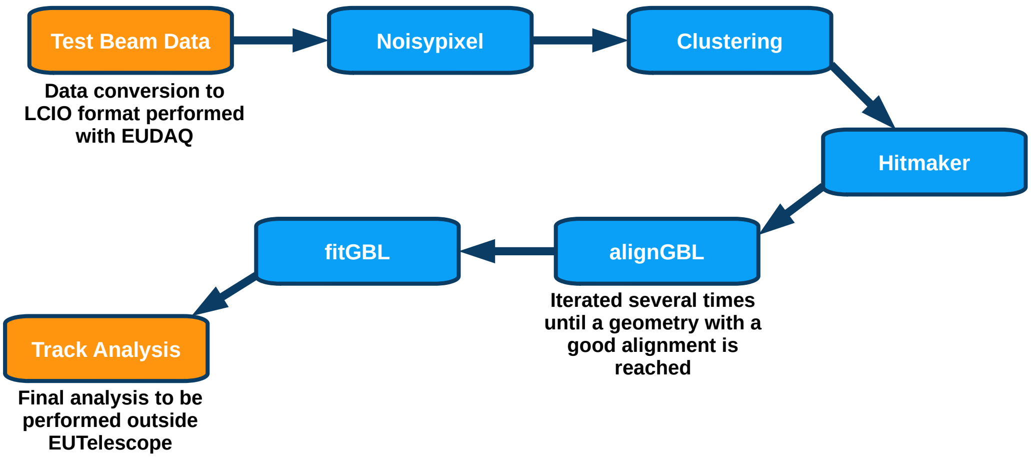

Figure 3.7: A typical EUTelescope workflow.

Noisypixel

The presence of channels with a high noise occupancy could significantly slow down the track reconstruction process. Noise hits can also generate fake tracks with severe consequences on the final test beam results. The identification and masking of noisy channels is of crucial importance. The first EUTelescope step, called *noisypixel*, identifies channels with a very large occupancy and flags them as noisy. The cut on the firing frequency is set by the user. For the Mimosa planes usually a channel is flagged as noisy if on average it registers an hit more than once every 1000 events (firing frequency of 0.001, 0.1%). No such cut is applied on the DUT, therefore eventual noisy channels can be analyzed and masked in the analysis performed with the final ROOT file.

Figure 3.8 shows the number of channels flagged as noisy in a Mimosa plane as a function of the selected firing frequency cut. Most pixels exhibit a very low firing frequency, generated mostly by the beam occupancy. About 100 pixels, however, have a relatively large firing frequency and hence are labeled as noisy.

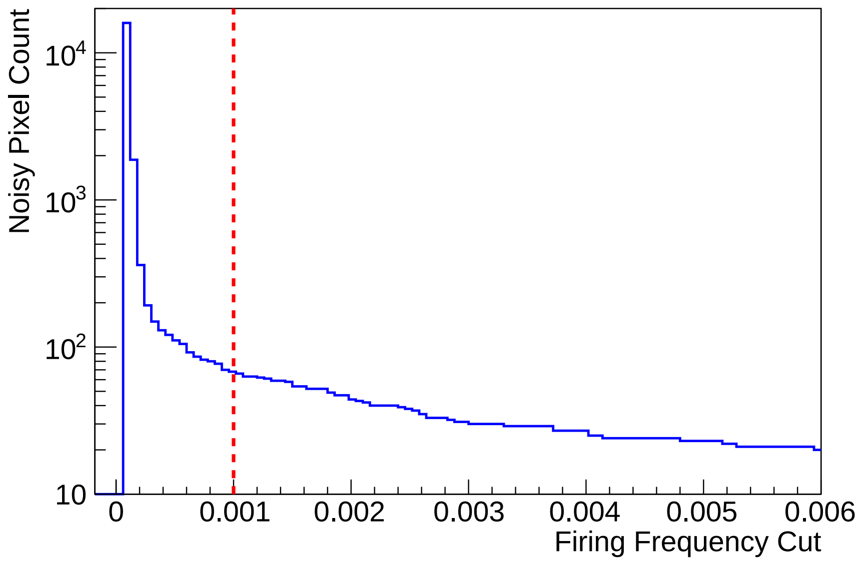

Figure 3.8: Number of channels flagged as noisy as a function of the firing frequency cut on Mimosa plane 0. The red dashed line indicates the cut implemented in the analysis.

Clustering

The second step, called *clustering*, groups together adjacent firing channels to form clusters. In this step, all the clusters that contain a channel flagged as noisy are removed from further processing.

Figure 3.9 shows the cluster positions on Mimosa plane 1. The beam shape can be noticed in the cluster distribution.

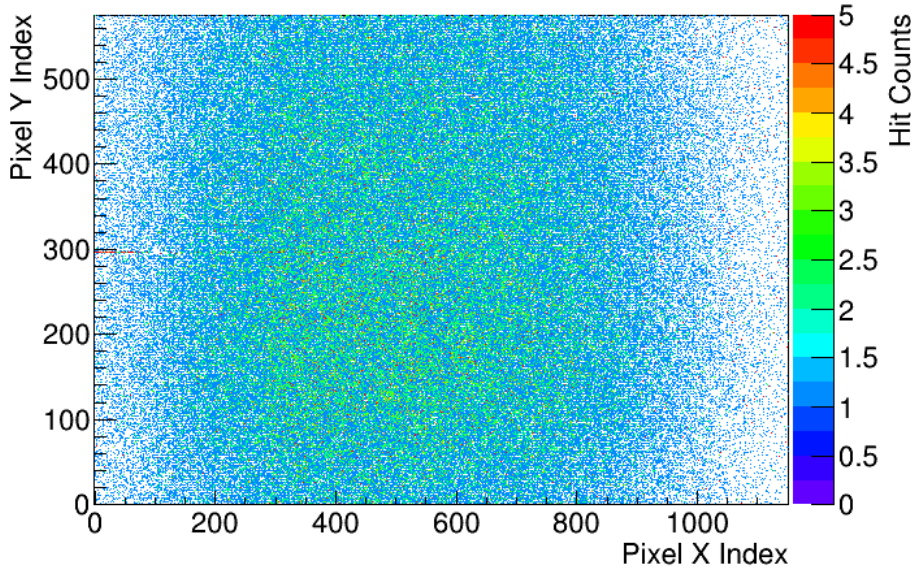

Figure 3.9: Cluster positions on Mimosa plane 1.

Hitmaker

The following step is called *hitmaker* and provides three important functionalities:

- Transformation of the coordinate system from pixel coordinate system to local and global coordinate systems.
- Creation of correlation plots with hits from different planes.
- Geometry pre-alignment with an accuracy of ~100 μm.

Figure 3.10 shows the coordinate systems used in EUTelescope. The pixel coordinate system is used in the clustering and is defined by the channel numbers in x and y. The local coordinate system has axes parallel to the plane axes and is centered at the center of that plane. Every device has its own local coordinate system. The global coordinate system is defined by the axes of the first Mimosa plane. The global coordinate system is common to all the planes in the set-up. The hitmaker step transforms the clusters coordinates from the pixel coordinate system to the local and global coordinate systems using the geometry parameters defined in the GEAR file.

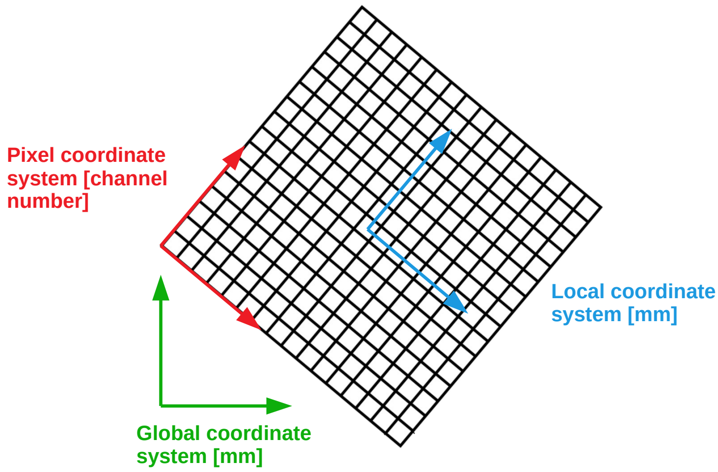

Figure 3.10: Coordinate systems used in EUTelescope.

Figure 3.11 shows a correlation plot between the hits on the DUT and the hits on the first Mimosa plane, both in the global coordinate sytem. Beam particles travel parallel to the telescope axis, thus they generate hits with correlated positions on all the planes. Therefore, in a correlation plot most hit pairs should lie on a line parallel to the bisector as in Figure 3.11. A different distribution would indicate the presence of a problem in the data or in the EUTelescope configuration, as the use of wrong geometry parameters in the GEAR file. The correct behavior of the correlation plots represents a very important sanity check for the reconstruction process.

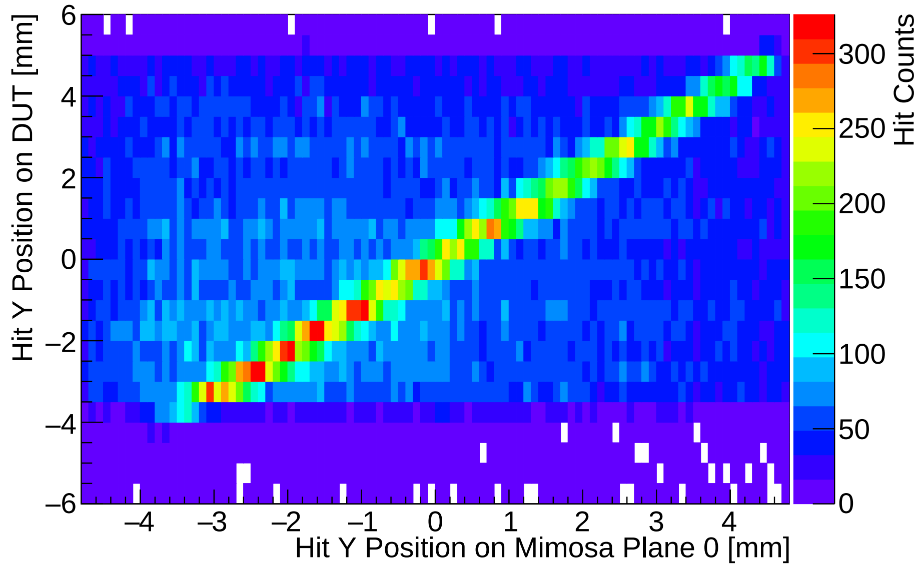

Figure 3.11: Correlation plot between the y position of the hits on the DUT, an ATLAS ITk Strip module, and the y position of the hits on the Mimosa plane 0. The y direction is parallel to the DUT strip pitch.

The track fitting and geometry alignment procedures can be performed only if a relatively well-aligned starting geometry is used. For this reason, a pre-alignment procedure based only on hit positions is needed. The pre-alignment procedure is performed in the global coordinate system. The average difference between the hit positions on a plane with respect to the hit positions on the first telescope plane is subtracted from the plane positions and a new updated GEAR file is created. In fact, this difference should be zero in a well-aligned geometry. This is done separately for every plane in both x and y directions and the plane positions can be aligned with an accuracy of ~100 μm. Figure 3.12 shows the pre-alignment procedure and its effect.

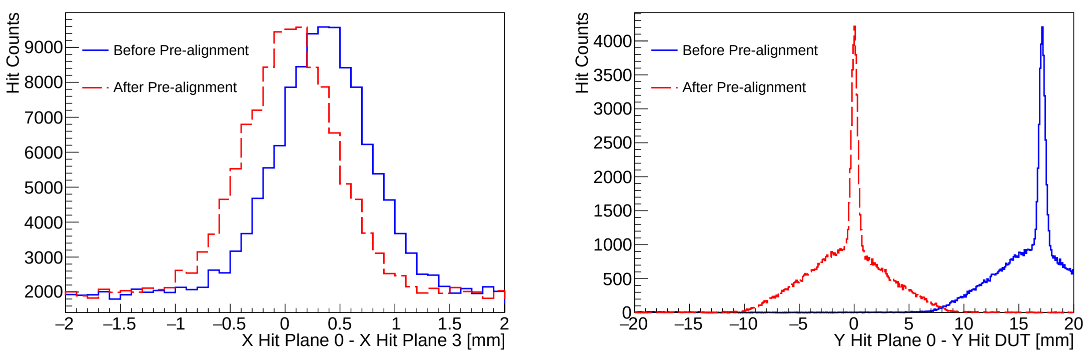

(a) Telescope plane 3 in the x direction.

(b) DUT plane in the y direction.

Figure 3.12: Distance between hit positions on a plane and on telescope plane 0, which defines the global coordinate system. The distance is shown both before and after the pre-alignment procedure.

AlignGBL

The *alignGBL* step can be divided in three processes:

- Track finding (identification of hits that belong to a track).
- Track fitting.
- Geometry alignment using the fitted tracks.

The track finding is performed using the triplet method. The six telescope planes are divided in two arms of three planes each, one upstream and one downstream with respect to the beam.
For each arm, the hits on the first and last planes are used to calculate the slope of a candidate track. The hit pairs with a slope within an user-selected cut are considered as candidate tracks and are called doublets. Figure 3.13 explains how the slope cuts are applied. Different slope cuts are defined in x and y for each arm. Figure 3.15a shows an example of a slope distribution. The slope cuts are set at 6 mrad, which corresponds to about 6σ of the peak of the distribution.
The positions of the hits in the doublets are fitted linearly and extrapolated on the central plane. A triplet track candidate is formed if a hit is located within an user-selected distance from the doublet extrapolation. Figure 3.14 explains how this residual cut is set. Separate residual cuts are set in x and y for each arm. Figure 3.15b shows an example of a triplet residual distribution. The residual cuts are set at about 0.04 mm, which corresponds to about 4σ of the peak of the distribution.

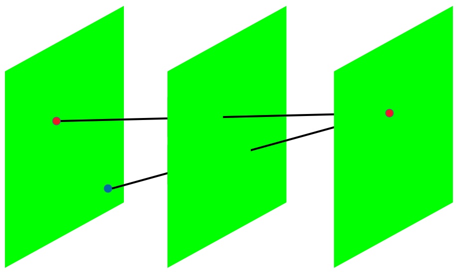

Figure 3.13: The two red points form a track with a small slope, thus they are considered as a candidate track and they form a doublet. The blue point and the red point on the third plane, however, form a track with a large slope, so this pair is rejected.

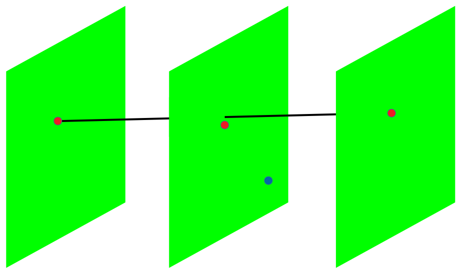

Figure 3.14: The red point on the central plane is close to the linear extrapolation formed by the doublet on the first and third plane. The three hits form a triplet used as a track candidate. This is not the case for the blue point which is located very far from the linear extrapolation.

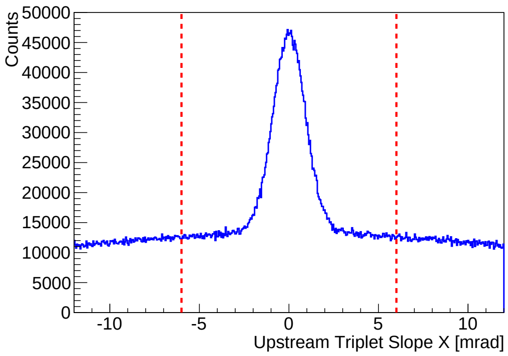

(a) Slope distribution in x for the upstream triplet.

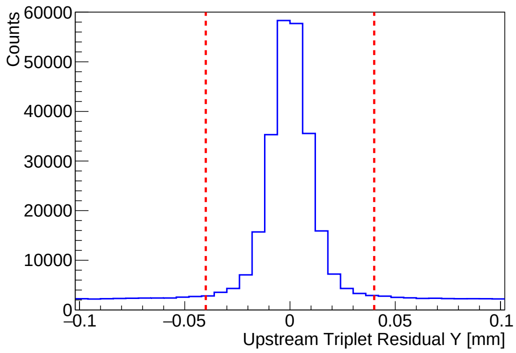

(b) Residual distribution in y for the upstream triplet.

Figure 3.15: Slope and triplet residual distributions from the track finding procedure. The red dashed lines indicate the selected cuts.

The triplets of each arm are extrapolated to the center of the telescope. If the extrapolation of two triplets is within an user-selected cut, the two triplets form a track that can be fitted. Figure 3.16 explains this cut. Separate cuts are set in x and y. Figure 3.17a shows an example of a triplet matching residual distribution. The triplet matching residual cuts are set at about 0.09 mm, which corresponds to about 4σ of the peak of the distribution. Moreover, in order to achieve the best track purity, if two triplets on one arm are matched to the same triplet on the other arm with a cut twice as large as the selected cut, both triplets are discarded.

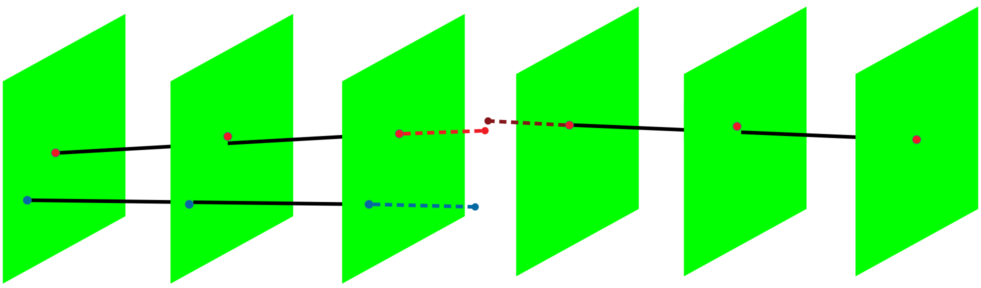

Figure 3.16: The extrapolation of the triplet formed by the red points in the first arm is close to the extrapolation of the triplet in the second arm. The two triplets are then grouped into a track that can be fitted. The extrapolation of the triplet formed by the blue points, however, is not close to any other triplet extrapolation. This triplet do not form a track candidate.

A set of six hits that passed all the track finding cuts can be fitted using the GBL software. If one or more DUTs[2] are present their hits can be added to the track to be fitted. The track obtained with the telescope planes is linearly extrapolated on the DUT plane.

[2]In the EUTelescope framework every device that is not part of the six telescope planes is considered a DUT, including the reference plane.

A DUT hit is added to the track if it is located within an user-selected cut from the track extrapolation. This method is similar to the one used to form triplets explained in Figure 3.15b. Separate cuts in x and y are set collectively for all the DUTs. Figure 3.17b shows an example of residual distribution for the DUT hit matching. Two separate structures are visible: one produced by the hits on the FE-I4 reference plane (between −0.12 mm and 0.12 mm) and the other produced by the hits on the strip DUT (between −0.04 mm and 0.04 mm). A cut of 0.2 mm is selected. In presence of a strip DUT a tight cut can be set on the direction of the strip pitch, but a very large cut (> 1 cm) must be set in the direction along the strips.

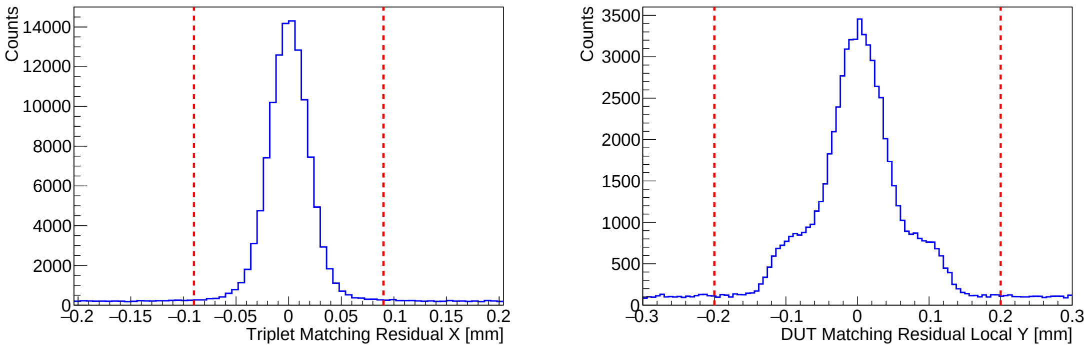

(a) Residual distribution in x for the triplet matching.

(b) Residual distribution in y for the DUT hit matching.

Figure 3.17: Triplet matching and DUT residual distributions from track finding procedure. The red dashed lines indicate the selected cuts.

The tracks obtained with the fit are used to improved the alignment of the geometry. The alignment is usually performed in an iterative procedure. A first alignment iteration is performed starting with the pre-aligned GEAR file and a new updated GEAR file is created. The second iteration uses the GEAR file produced by the first alignment iteration and so on. Because of geometry misalignments, it is useful to use large track finding cuts in the first alignment iteration. Three alignment iterations are usually sufficient to align the plane positions with an accuracy < 3 μm.

FitGBL

The final step, called *fitGBL* performs the track finding and the track fitting similarly to the GBLAlign step. It does not, however, perform the geometry alignment, but it stores the track and hit information in a ROOT file that can be analyzed by the user. The hits on selected planes can be excluded from the track fitting in order to obtain an unbiased extrapolation of the tracks on those planes. This operation is usually performed for DUT planes. The user can also customize the information to be stored in the final file, for example the user can select to store the information of just a few planes or to store only the tracks with a hit on a given plane (usually the reference plane).

A residual is the distance between a hit and the fitted track extrapolation. If the hit is used in the track fitting procedure, the track position is biased by the hit position. No bias is present if the hit information is not used in the track fitting. In the latter case the residual distribution can be used to obtain information on the tracking resolution if the spatial resolution of the plane is known. In fact, if the unbiased residual distribution of a plane exhibits a Gaussian shape[3], its width is related to the tracking resolution and to the intrinsic spatial resolution of the plane [96]:

$$\sigma_{\text{residual}} = \sqrt{\sigma^2_{\text{intrinsic}} + \sigma^2_{\text{tracking}}} \tag{3.1}$$

Figures 3.18a and 3.18b show respectively the unbiased and biased residual distributions of the Mimosa plane closest to the ITk Strip module. The tracking resolution can be estimated using the width of the unbiased residual distribution (Figure 3.18a) and the intrinsic resolution of 4.1 µm of the Mimosa plane hits. Using this procedure a tracking resolution of 9.9 µm is calculated. This procedure provides the tracking resolution on a Mimosa plane, with the tracking being performed by only five Mimosa planes. A small improvement in resolution can be assumed on the ITk Strip module when the hit information of all six Mimosa planes is used for tracking.

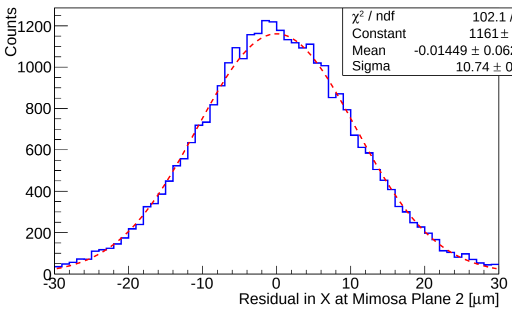

(a) Unbiased residual distribution.

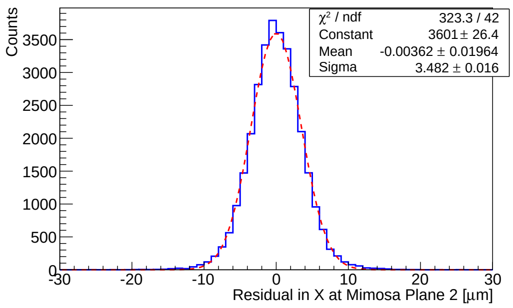

(b) Biased residual distribution.

Figure 3.18: Unbiased and biased residual distributions of Mimosa plane 2. The distributions are fitted with a Gaussian distribution (red dashed line).

Figure 3.19 shows the reduced χ^2 distribution of the tracks fitted using hits from the six telescope planes and the FE-I4 plane. The most probable value of the reduced χ^2 distribution depends on the number of degrees of freedom in the fit:

$$\text{mode} = 1 - \frac{2}{\text{ndf}} \quad \text{with ndf} = 2 \cdot N_{\text{planes}} - 4 \tag{3.2}$$

where ndf is the number of degree of freedoms and N_{hits} is the number of planes used

[3] The residual distribution does not exhibit a Gaussian shape for sensors with a small amount of charge sharing between channels, as non-irradiated ITk Strip sensors, for which the residual distribution is approximately rectangular (see Section 4.3.2).

in the fit. The distribution of Figure 3.19 exhibits a most probable value compatible with the expected value of 0.8 within the binning error of the histogram.

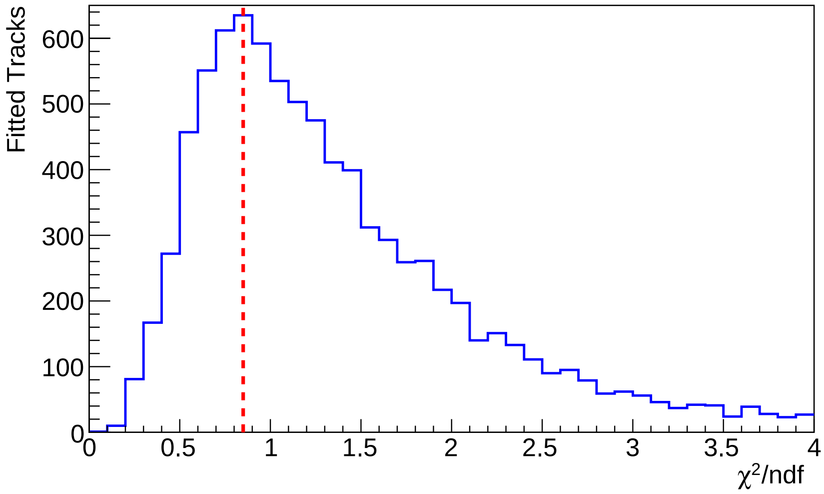

Figure 3.19: Reduced χ^2 distribution of the fitted tracks. The red dashed line indicates the position of the most probable value.

CHAPTER

4

TEST BEAM STUDIES OF ITK STRIP PROTOTYPE MODULES

This Chapter discusses the test beam characterization of prototype ITk Strip modules. Section 4.1 introduces the modules tested and Section 4.2 describes the set-up used during the test beams. Section 4.3 introduces the main quantities under study and the data analysis procedure is described in Section 4.4. In Section 4.5 the threshold calibration procedure is studied and it is shown that this procedure provides reliable and accurate results. Section 4.6 describes the study of the module response to a beam particle crossing its boundary regions. Section 4.7 describes the evaluation of the performance of the current ITk Strip prototype modules, showing that they will provide excellent performance for the entire lifetime of the HL-LHC. Section 4.8 discusses the charge sharing and shows that irradiated sensors exhibit an enhanced charge sharing in the inter-strip region. The results discussed in this Section laid the basis of the studies described in Chapter 5.
Additional material to this Chapter is provided in Appendix A.

4.1 Measurements Performed

Table 4.1 contains the list of the test beams and ITk Strip modules (see Section 1.4.1) discussed in this thesis. Three different sensor iterations have been tested, in chronological order: ATLAS12, ATLAS12EC, and ATLAS17LS. Their properties are summarized in Table 4.2. Figure 4.0 shows a module with each sensor type. ATLAS12 and ATLAS17LS are barrel sensors with rectangular strips, while ATLAS12EC are end-cap sensors with radial strips and their geometry is explained in Figure 4.1.

Test Beam	Beam Line	Module Name	Sensor	Chipset	Irradiation [n_{eq}/cm^2]
May 2016	DESY T22	RAL LS4	ATLAS12	ABC130	None
July 2016	CERN H6A	RAL LS3 Irrad	ATLAS12	ABC130	8×10^{14} at CERN PS
May 2017	DESY T22	RAL SS	ATLAS12	ABC130	None
		FR R0	ATLAS12EC	ABC130	None
June 2018	DESY T22	RAL 17LS	ATLAS17LS	ABC130	None
		LIV 17LS	ATLAS17LS	ABC130	None
April 2019	DESY T21	FR R0Star	ATLAS12EC	ABCStar	None
		RAL LSStar	ATLAS17LS	ABCStar	None
June 2019	DESY T22	FR R0Star Irrad	ATLAS12EC	ABCStar	1.5×10^{15} at CERN PS
Sep. 2019	DESY T22	RAL LSStar Irrad	ATLAS17LS	ABCStar	5.1×10^{14} at JSI

Table 4.1: List of test beams and DUTs discussed in this thesis. The module names contain the assembly location: RAL for Rutherford Appleton Laboratory, FR for University of Freiburg, and LIV for University of Liverpool. The module names also contain the module type: SS for Short Strip barrel, LS for Long Strip barrel, and R0 for the end-cap inner ring. The sensor iteration, chipset, and irradiation level are also listed.

Sensor Iteration	Type	Pitch	Length [cm]	V_{fdv} [V]
ATLAS12	Barrel Short Strip	74.5 µm	2.4	365 [128]
ATLAS12EC	End-cap R0	1.93×10^{-4} rad	1.9	303 [129]
		1.93×10^{-4} rad	2.4	
		1.72×10^{-4} rad	2.9	
		1.72×10^{-4} rad	3.2	
ATLAS17LS	Barrel Long Strip	75.5 µm	4.8	297 (Appendix B.1)

Table 4.2: List of sensor iterations discussed in this thesis, with their type, strip pitch, strip length, and full depletion voltage. For ATLAS12EC, the strip pitch and length of each segment starting from the innermost one (see Figure 4.1b) are listed.

(a) Barrel Short Strip module.

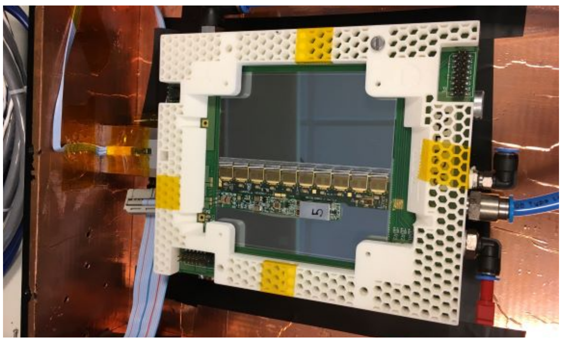

(b) Barrel Long Strip module.

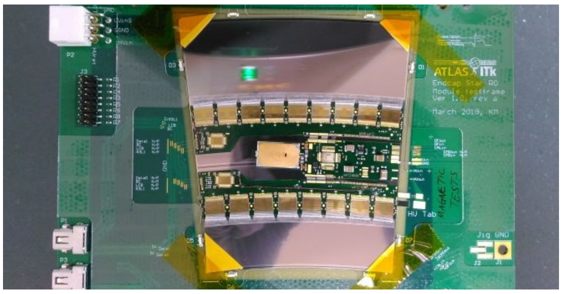

(c) End-cap R0 module.

Figure 4.0: ITk Strip barrel and end-cap modules.

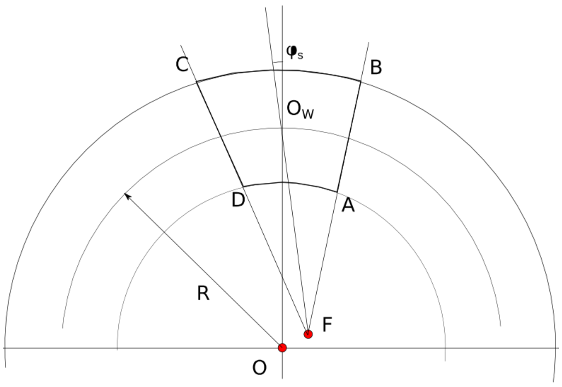

(a) The sensor geometry is formed connecting ABCD, where CB and DA are centered at the center of the beam pipe. The strips are pointing to F, which is displaced from the center of the beam pipe in order to implement the stereo angle [49].

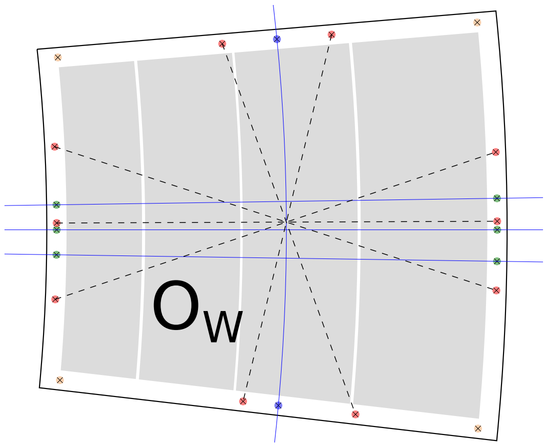

(b) The sensor is divided in four strip segments of different length. The two innermost segments are connected to a hybrid called H0, while the two outermost segments are connected to a hybrid called H1 [49].

Figure 4.1: Schematic explanation of the geometry of ATLAS12EC sensors used in R0 modules, the modules for the inner ring of the ITk Strip end-caps.

In terms of sensor performance, the main difference between sensor iterations is related to the full depletion voltage. The full depletion voltage is lower for ATLAS12EC and ATLAS17LS than for ATLAS12. The full depletion voltage increases linearly with the NIEL fluence (see Figure 2.9), therefore for irradiated sensors operated at the same bias voltage, ATLAS12EC and ATLAS17LS sensors have a wider depletion region than ATLAS12 sensors. Therefore, ATLAS12EC and ATLAS17LS sensors collect a larger signal after irradiation and are more radiation-hard than ATLAS12 sensors.
Before 2019, the modules were built with the prototype front-end chipset comprising HCC130 and ABC130. The modules tested in 2019, however, were built with the production-grade HCCStar and ABCStar, which implement a different chip architecture, have an optimized front-end stage [130] and do not exhibit an increase of noise after TID irradiation (see Section 4.7.2), in contrast to the 130 chipset [131].

The earliest modules (RAL LS4, RAL LS3 Irrad, and FR R0) did not comprise a power board (see Section 1.4.1). The power board was added in later modules and different power board versions were implemented in the devices tested. The power board, however, does not play a significant role in the test beam results discussed in this thesis.

RAL LS3 Irrad was fully irradiated at CERN PS. The CERN PS IRRAD facility was chosen because it produces a TID per NIEL fluence comparable to the HL-LHC radiation environment (see Section 3.3). This property is crucial for the ABC130 front-end chip, which exhibits an increased noise depending on the TID absorbed. RAL LS3 Irrad was not subject to any annealing, since the high temperature required for this procedure could damage the glue, hybrid, front-end chips, and test frame. In fact, modules are usually tested only up to 40 °C, and only for limited periods of time [49].

The Star chipset does not exhibit any dependence of the noise on the TID. For this reason, a different approach has been chosen for the latest irradiated modules. FR R0Star Irrad and RAL LSStar Irrad were built with irradiated components: the sensor and the hybrids were irradiated separately and then assembled together. This approach guarantees more flexibility in the test beam organization and better component management with respect to a full-module irradiation. The sensors were irradiated at CERN PS and JSI and then annealed for 80 minutes at 60 °C in order to exploit the beneficial annealing (see Section 2.6.1) as it will happen in the ITk. Only the TID plays a role in the ASIC behavior, thus hybrids and front-end chips were irradiated at Rutherford Appleton Laboratory (RAL) using x-rays.

4.2 Experimental Set-up

Figures 4.2 and 4.3 show examples of set-ups used during the ITk Strip test beams. The module is mounted perpendicular to the beam in a cooling box at the center of a EUDET-type telescope. A pixel reference plane is mounted before the last telescope plane. An FE-I4 reference plane was used in all the test beams with the exception of the June 2019 test beam, when an ALPIDE reference plane was used[1].
The modules have size of ~10 x 10 cm^2 while the beam is collimated to a size of 1 x 1 cm^2. A beam energy in the range 4-5 GeV was used at DESY T22, 5.8 GeV at DESY T21, and 120 GeV at CERN SPS. The typical track pointing resolution is 10 μm at DESY and 4 μm at CERN (obtained with the method described in Section 3.4). The tracking resolution is larger than the nominal EUDET-type telescope resolution of about 2 μm [96]. This is explained by multiple scattering induced by the material budget of the cooling box and by the large distance of about 10 cm between the Mimosa planes and

[1] In September 2019 both the ALPIDE and FE-I4 reference planes were installed (see Figure 4.3), but only the hit information of the latter is used in the track reconstruction and analysis because of its better discrimination of out-of-time tracks.

the ITk Strip module. This distance is necessary to fit the cooling box in the set-up. The cooling box is mounted on a translational stage that allows the beam to be pointed at different locations of the module. In a typical measurement, the beam is pointed to a region consisting of strips bonded to a single front-end chip [132].

Figure 4.2: Test beam set-up in June 2018. The cooling box is open to show the ITk Strip module under test.

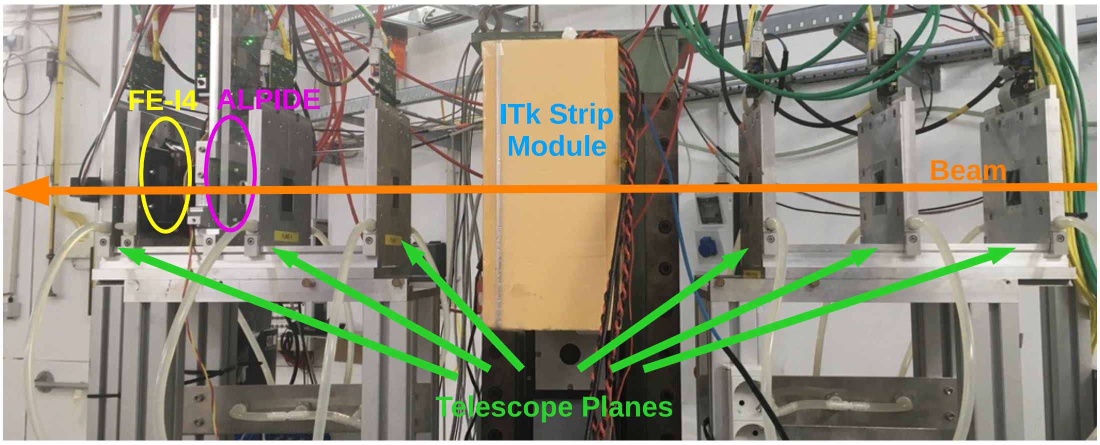

Figure 4.3: Test beam set-up used in September 2019. The ITk Strip module is placed at the center of the telescope in a cooling box. The cables on the side of the cooling box provide communication with the module, low-voltage power to the power board, and bias voltage to the sensor. The reference plane is mounted before the last telescope plane (in the picture both the FE-I4 and ALPIDE reference planes are installed). During data taking the telescope arms are moved as close as possible to the cooling box to optimize the tracking resolution.

A TTi QL355TP power supplier provides the low voltage power to the module (11 V if a power board is present, 1.5 V otherwise). The bias voltage is provided by a Keithley 2410 SourceMeter. All the measurements are performed using the baseline bias voltages for the ITk Strip Detector: 400 V for non-irradiated modules and 500 V for irradiated modules. The module DAQ comprises a Digilent Nexys Video FPGA board (Digilent Atlys FPGA board in the earliest test beams) and the software ITSDAQ (Inner Tracker Strip

DAQ) [133]. Nitrogen is flushed inside the cooling box in order to maintain the relative humidity below 5% and hence prevent condensation.

In order to prevent thermal runaway in the sensor (see Section 2.4) and to reduce the temperature in the power board and hybrids, it is necessary to provide cooling to the modules. Non-irradiated modules were cooled with 15 °C water, except in the test beam in April 2019, when the modules were cooled by circulating air with a fan inside the cooling box.
Irradiated modules can be operated only at low temperature (see Section 2.4). Figure 4.4a shows the cooling box used at CERN H6A. A chiller flushes cool air in coils inside the inner volume of the cooling box (Figure 4.4a). With this set-up a temperature of about −35 °C on the sensor is reached.
The material budget of the cooling box used at CERN is too large for it to be used with the low-energy electron beam provided at DESY. The scattering of beam particles in the box walls would significantly deteriorate the telescope tracking performance, thus worsening the test beam results. At DESY, irradiated modules were tested with a dry ice-based cooling box developed at the University of Freiburg (Figure 4.4b). An aluminum container is placed inside a styrofoam box with an opening on the top side of the box. The aluminum container is filled with dry ice, which cools the container wall and the inner volume of the box. A fan circulates the air inside the box in order to guarantee uniform cooling in the whole volume. The dry ice slowly evaporates and the aluminum container needs to be refilled about every two hours. This is done without unmounting the box by using the opening of the aluminum container on the top side of the box. With this set-up a temperature of about −50 °C is reached on the sensor.

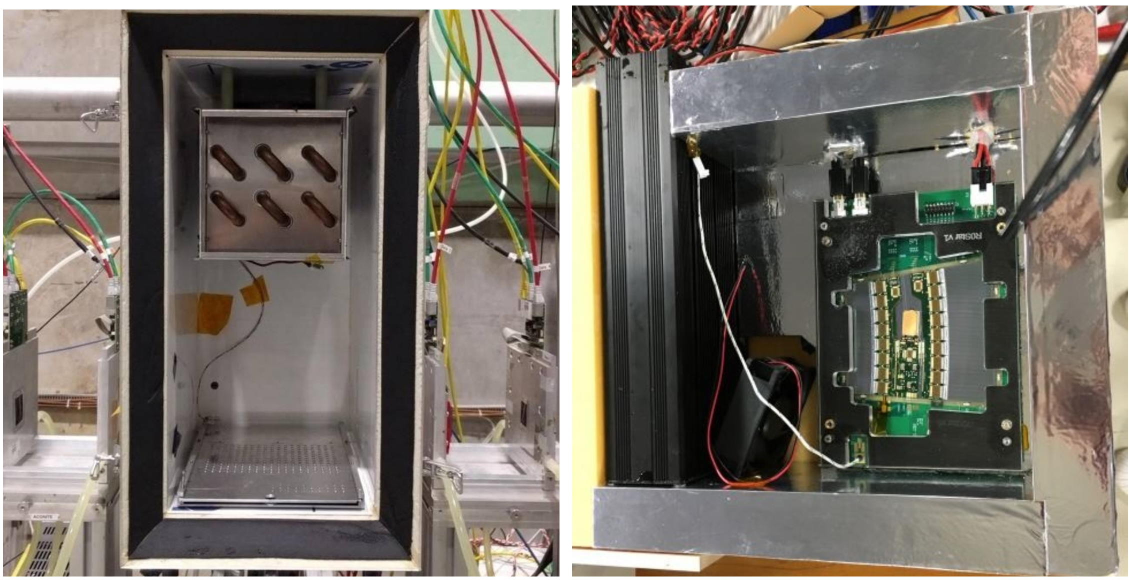

(a) Cooling box used at CERN. (b) Cooling box used at DESY.

Figure 4.4: Cooling boxes used to test irradiated modules during ITk Strip test beams.

4.3 Observables of Interest

The ITk Strip test beams have the aim to characterize prototype modules. The tracks detected by the telescope are reconstructed using the EUTelescope reconstruction framework as described in Section 3.4. The EUTelescope output is analyzed with a customized ROOT code. The focus on the analysis lies in the evaluation of the performance of the prototype ITk Strip modules, with a focus on hit detection efficiency, cluster size, and charge sharing.

4.3.1 Hit Detection Efficiency and S-Curve

The most important parameter for most radiation detectors is the hit detection efficiency: the probability of detecting a particle crossing the active area. In test beams it is possible to measure the hit detection efficiency using the track and hit information:

$$\epsilon = \frac{N_{\text{DUT and reference}}}{N_{\text{reference}}} \tag{4.1}$$

where ϵ is the hit detection efficiency, $N_{\text{reference}}$ is the number of tracks matched to a hit in the reference plane, and $N_{\text{DUT and reference}}$ is the number of tracks matched to both a hit on the DUT and a hit on the reference plane.
In order to guarantee a high-quality track selection, tracks with a reduced χ^2 larger than 5-8 are discarded. The exact value is chosen based on the beam conditions and material budget of the set-up.

Because of the large integration time of the ALPIDE reference plane (see Section 3.2), an additional event selection is applied in the data from the June 2019 test beam when it was used. In order to minimize the number of out-of-time tracks considered in the efficiency calculation, all the events with more than one hit recorded on the ALPIDE reference plane are discarded. Without this event selection, the efficiency calculated with Equation 4.1 would be reduced by about 20%.

In order to match a hit to a track, only hits within a given distance from the track extrapolation are considered. The distance cut should be large enough to include all the hits generated by a beam particle, but also tight enough to avoid the inclusion of uncorrelated hits in the efficiency calculation. Since strips are essentially one-dimensional devices, a single cut along the strip pitch direction is set. For barrel modules the distance cut is set to 200 μm, which corresponds to about three strips in each direction with respect to the track. For end-cap modules the distance cut is set on the angular residual and it has a value of 6×10^{-4} rad. Figure 4.5 shows the residual distributions and the distance cuts for a barrel and an end-cap module.

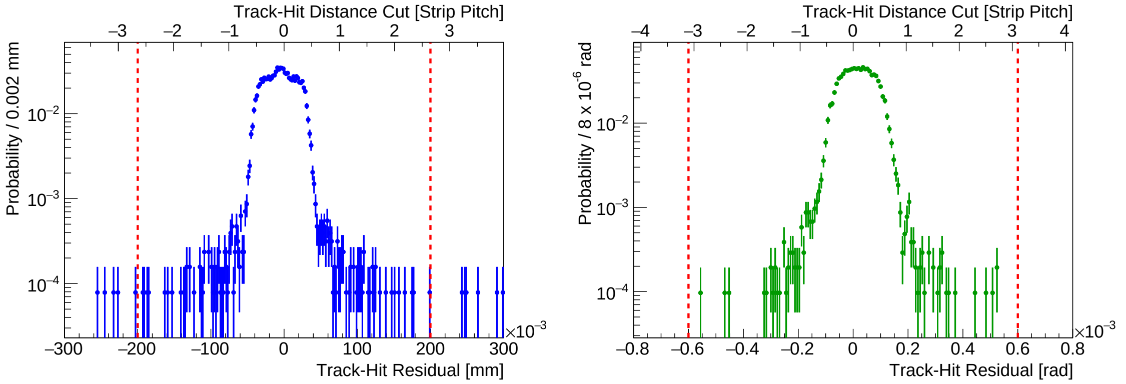

(a) LIV 17LS with a threshold of 0.78 fC (4875 e) .

(b) FR R0Star with a threshold of 0.98 fC (6125 e).

Figure 4.5: Residual distributions and distance cuts used for the track-hit matching (red dotted lines) for a non-irradiated barrel module and a non-irradiated end-cap module.

Some hits are at large distance from the track extrapolation and therefore are discarded from the efficiency calculation. This is generally caused by charge sharing or by a misreconstructed track position. This loss of hits can create an underestimation of the efficiency which would limit the accuracy of the test beam results. Figure 4.6 shows the efficiency calculated for a non-irradiated barrel module as a function of the distance cut. The efficiency saturates for cuts > 150 µm. For the chosen cut of 200 µm the efficiency lost because of the cut is < 0.3%, significantly less than the maximum inefficiency of 1% set by the ITk Strip requirements. Using a larger distance cut would have only a small effect on the calculated efficiency value, but it would also include uncorrelated hits which may significantly bias the results.

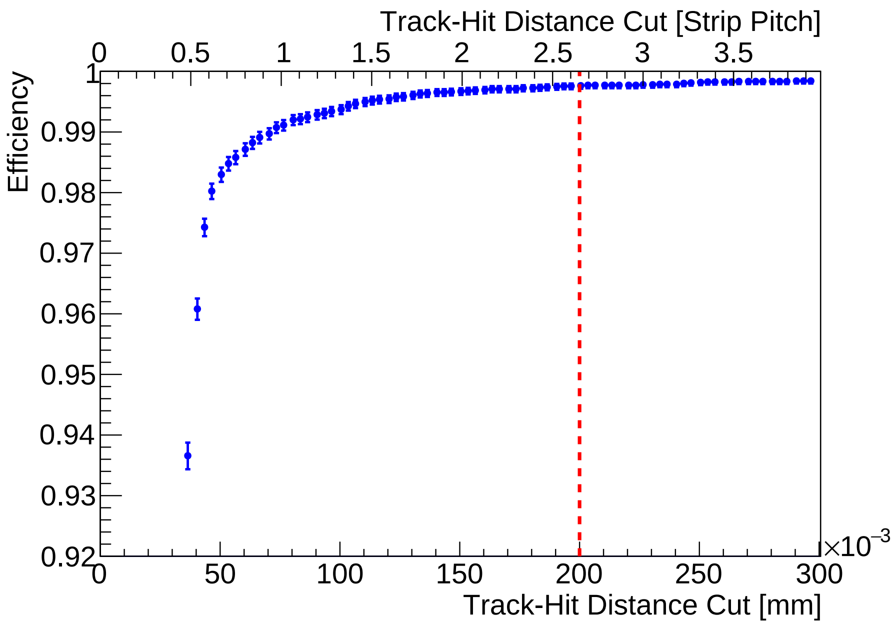

Figure 4.6: Efficiency as a function of the distance cut for the non-irradiated module LIV 17LS at a threshold of 0.78 fC (4875 e). The red dashed line indicates the distance cut implemented in the analysis.

The ITk Strip modules implement a binary readout. With a binary readout it is impossible to obtain the information on the charge collection using a single measurement. This can be done, however, by combining the information of several measurements performed with different thresholds. Figure 4.7 shows an s-curve, the curve given by the efficiency as a function of the threshold set in the front-end chips. The s-curves are fitted with an empirical skewed error function [134, 135]:

$$\epsilon = \epsilon_{max} \cdot \mathrm{erfc}\left(x \cdot \left[1{+}0.6\frac{e^{-\zeta x}{-}e^{\zeta x}}{e^{-\zeta x}{+}e^{\zeta x}}\right]\right) \qquad \text{with } x = \frac{q_{thr}{-}\mu}{\sqrt{2}\sigma} \tag{4.2}$$

where erfc denotes the complementary error function and q_{thr} is the threshold. The fit parameters are:

- the maximum efficiency ϵ_{max}.
- the median charge μ, which corresponds to the charge value at which the efficiency is 50%.
- the width of the error function distribution σ, which is related to the noise and to the width of the Landau distribution.
- the skew ζ, which takes into account the tail of the Landau distribution.

The median charge μ is the parameter of interest, while the maximum efficiency[2], the width σ, and the skew ζ can be considered nuisance parameters of the fit.

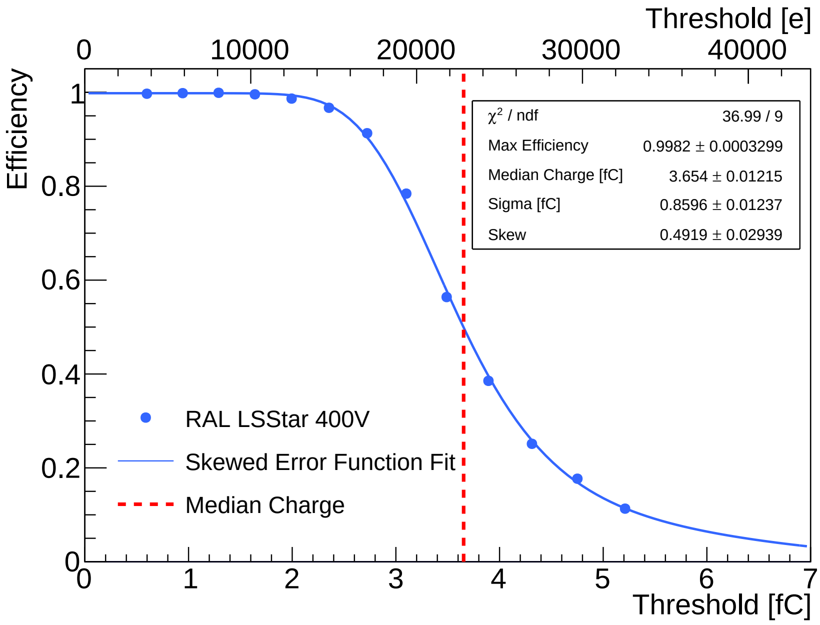

Figure 4.7: S-curve and skewed error function fit for the non-irradiated module RAL LSStar. The red dashed line indicates the median threshold. The uncertainties of the efficiency are smaller than the markers.

[2]The maximum efficiency can be determined directly from the efficiency calculated in measurements with low thresholds. The fit parameter ϵ_{max} can then be considered a nuisance parameter of the fit.

The skewed error function is an empirical distribution to describe the test beam results, but it is not directly related to any physics process in the sensor. This fit is used to measure a well-defined point of the s-curve, the median threshold. For a Landau-Gauss distribution the Most Probable Value is at about 90% of the median charge. The skewed error function is used in place of the physically-motivated Landau-Gauss distribution because the leading strip charge distribution does not exhibit a Landau-Gauss shape in irradiated devices (see Appendix A.5). In fact, the leading strip charge distribution collects only a fraction of the total signal generated by a beam particle.

A hit is detected if a strip collects a charge higher than the threshold set in the front-end chips. In other words, a hit is detected if the leading strip, the strip that has collected the most charge, has collected a charge higher than the threshold. The efficiency is then directly related to the integral of the charge distribution of the leading strip:

$$\epsilon(q_{thr}) \equiv \int_{q_{thr}}^{\infty} S_{LS}(q)dq \tag{4.3}$$

where $S_{LS}(q)$ is the (normalized) leading strip charge distribution. The relationship between the s-curve and the leading strip charge distribution is explained in Figure 4.8. The efficiency at a given threshold decreases based on the amount of entries in the leading strip charge distribution at that charge value. The efficiency drops significantly at thresholds corresponding to the peak of the leading strip charge distribution.

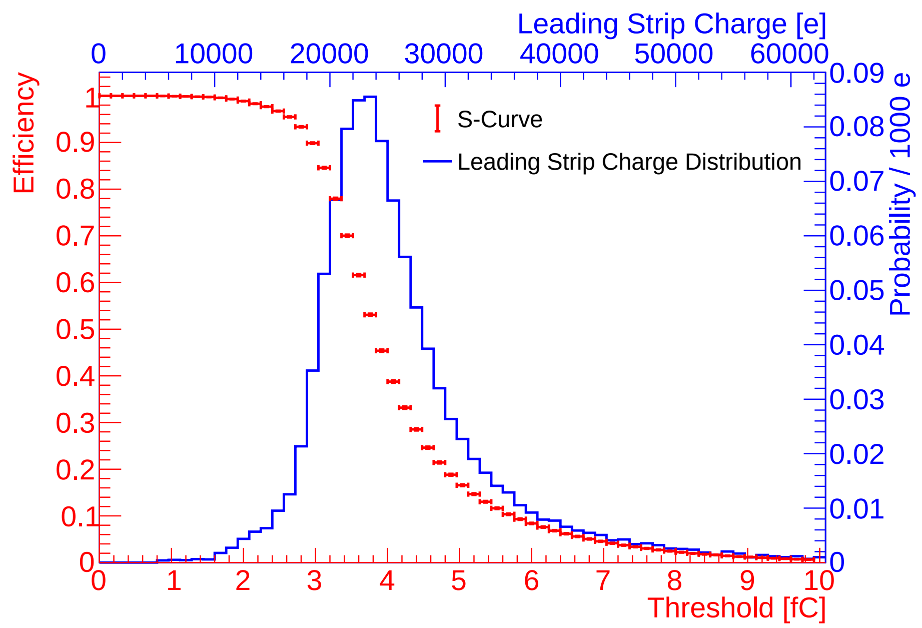

Figure 4.8: S-curve (red) and leading strip charge distribution (blue) obtained in a test beam with the Alibava system [136]. The Alibava system is an analog readout system for the characterization of silicon strip sensors. It allows the leading strip charge distribution to be measured directly. The measurement is performed with a non-irradiated ATLAS12 mini-sensor and bias voltage of 500 V.

4.3.2 Cluster Size

Another quantity that can be measured with a binary readout is the cluster size, the number of adjacent strips that record a hit when a particle crosses the active area. Figure 4.9a shows the cluster size distribution for three different thresholds for a non-irradiated module. Most of the clusters are formed by a single strip, but because of charge sharing a few clusters can be formed by more than one strip. Clusters with more than a single strip are present mainly in measurements where a low threshold is used. Figure 4.9b shows the average cluster size as a function of the threshold in a non-irradiated module. For thresholds < 2 fC (12 500 e) the average cluster size decreases as the threshold increases. For higher thresholds the cluster size is approximately constant.

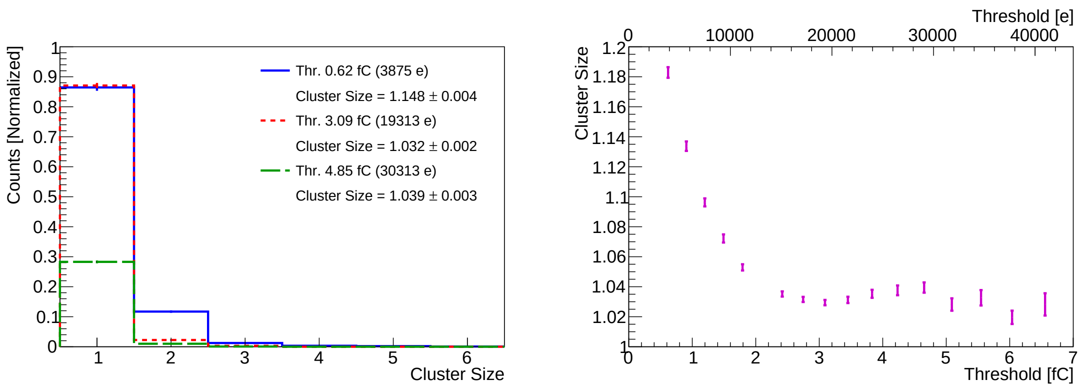

(a) Cluster size distribution.

(b) Average cluster size.

Figure 4.9: Cluster size distribution at three different thresholds and average cluster size as a function of the threshold for the non-irradiated module RAL 17LS.

In general, the more significant the charge sharing, the larger the average cluster size. The most important charge sharing mechanisms for non-irradiated modules are:

- charge carrier diffusion during their drift in the silicon bulk (see Section 2.3.2).
- crosstalk in the front-end chips or in the strip implants (see Section 2.4).
- delta rays, relatively high-energy electrons generated by a hard-interaction of a beam particle with an electron of a silicon atom (see Section 2.3.1).

Figure 4.10 shows the average cluster size as a function of the threshold for a non-irradiated module. This is compared to the average cluster size obtained with a simulations performed with Allpix^2, a generic and modular framework based on Geant4 for the simulation of silicon detectors [137]. Qualitatively, the simulation replicates the shape of the measurement. For thresholds > 2 fC (12 500 e) the simulation agrees quantitatively with the data, but for lower thresholds a disagreement is present. The disagreement can be explained by an imperfect charge carrier propagation model (in the simulation a simple ballistic model without the Shockley-Ramo theorem is used), an underestimation of the crosstalk, or the presence of an additional charge sharing mechanism as the one discussed in Section 4.8.

Figure 4.10 contains the average cluster size obtained with Allpix^2 simulations without the diffusion and delta ray contributions. The diffusion contribution is removed by setting a null diffusion constant in the charge propagation module of Allpix^2. The delta ray contribution is removed by setting the Geant4 production cut to 3 mm, therefore only particles with a range in silicon > 3 mm are propagated, preventing most of the delta ray propagation[3].
Diffusion plays a significant role only for thresholds < 2 fC (12 500 e), which correspond to about half the average total signal. In fact, if the total charge is shared between two strips, the second leading strip can not collect more than half the average total signal. A similar behavior is expected for charge sharing mechanisms that affect the charge carrier propagation, such as crosstalk and the charge division mechanism explained in Section 4.8. Delta ray electrons, however, often generate large clusters with a large amount of energy released in each strip of the cluster. The delta ray contribution to the cluster size is approximately uniform for all thresholds and is the dominant contribution to the cluster size for thresholds higher than half the average total signal.

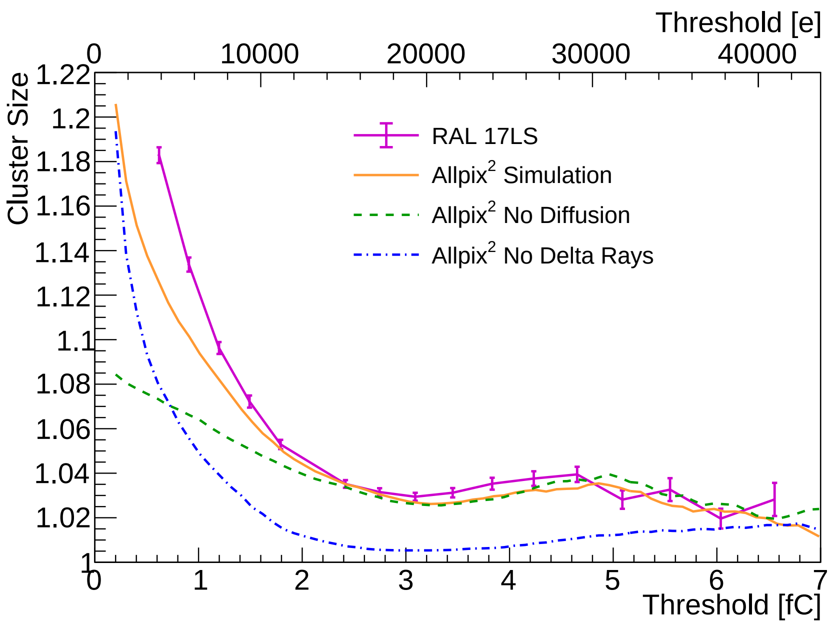

Figure 4.10: Average cluster size as a function of the threshold for the non-irradiated module RAL 17LS, compared to an Allpix^2 simulation. The average cluster size obtained with Allpix^2 without the diffusion and delta ray contributions are also shown.

[3]The energy release corresponding to a delta ray electron is actually simulated, but the delta ray electron is not propagated [138]. The result is that the delta ray energy is released in a single point and it is not shared to the neighboring strips.

Charge sharing also has important effects on the spatial resolution provided by a sensor. Figure 4.11 shows the residual distributions of a non-irradiated module for hits with different cluster size. For hits with unitary cluster size the distribution is approximately rectangular with a width given by the strip pitch. Hits with cluster size equal to two are generated mainly by the diffusion of charge carriers generated by a beam particle crossing a region between two strips. The centroid of the hits is between the two strips, close to the particle track position. Therefore, the residual distribution for hits with cluster size equal to two exhibits then a sharp peak around zero. The few hits with a cluster size larger than two are generated mainly by a delta ray electron that traverses many strips. In this case, the centroid of the hit is displaced from the track position by more than half strip pitch.

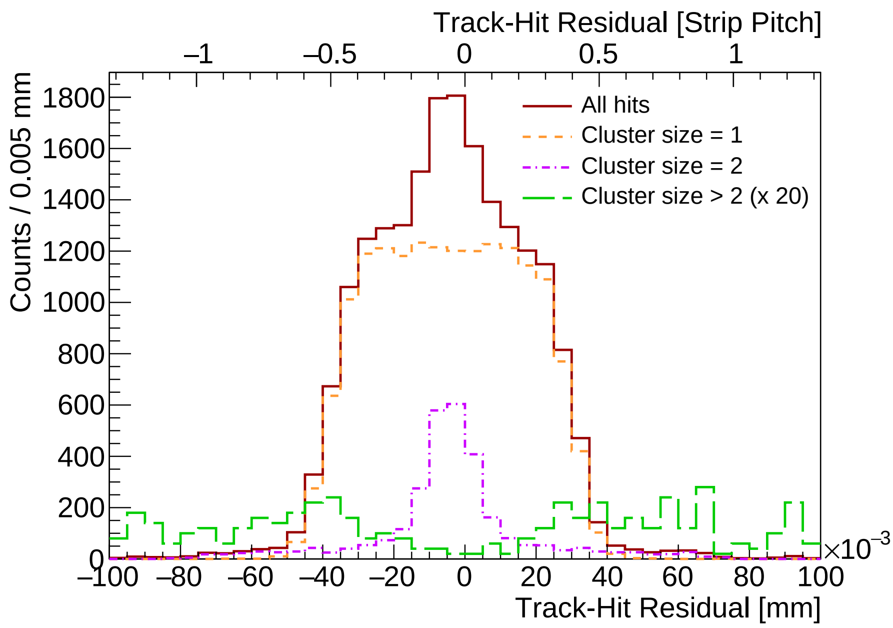

Figure 4.11: Track-hit residual distribution for all hits, and for hits with cluster size equal to one, two, and more than two. The counts obtained for the latter are multiplied by 20 for visibility. The measurement is performed with the non-irradiated module LIV 17LS with a threshold of 0.49 fC (3063 e). The distributions are shifted from the origin by a few μm because of a small misalignment in the geometry used for the track reconstruction.

4.3.3 Signal Estimation

The signal of a silicon sensor is a common parameter to estimate its performance and the Signal-to-Noise is arguably the most important figure of merit for the performance of a silicon module. The Signal is usually defined as the Most Probable Value (MPV) of the cluster charge distribution measured with an analog readout [139, 140]. The cluster charge is obtained by summing the charge collected by the strips in a cluster and it is commonly measured in dedicated set-ups with radioactive sources. The cluster charge, however, can only be measured directly with an analog readout since it requires the knowledge of the charge collected by each channel in a cluster. An alternative approach is needed to estimate the signal with a binary readout.

The cluster charge distribution differs from the leading strip charge distribution because of charge sharing. Before irradiation, diffusion is often the most dominant charge sharing effect and it plays a role only if the charge carriers are generated in the proximity ($\lesssim 10\,\mu m$, see Section 2.7) of the inter-strip region. By selecting only tracks crossing the center of a strip, it is possible to minimize the diffusion charge sharing and the leading strip charge distribution becomes a good approximation of the cluster charge distribution. Using this track selection it is possible to estimate the Signal measured with an analog readout. This is performed by selecting only tracks crossing the central 40% of a strip, which for a barrel sensor corresponds to a distance of less than $14.9\,\mu m$ from a strip center [49]. Although this track selection minimizes the charge sharing, the contributions to the charge sharing from crosstalk and delta rays are still present. The former can be estimated to decrease the signal by just a few percent of the total charge (see Equation 4.6), while the latter affects only a small fraction of the events.

Figure 4.12 shows a comparison between the efficiency obtained selecting particles crossing a strip in proximity of its center and the cluster charge distributions obtained with an Alibava readout system and a radioactive source. A qualitative and partially quantitative agreement is observed, which proves the validity of the track selection used in the test beam analysis.

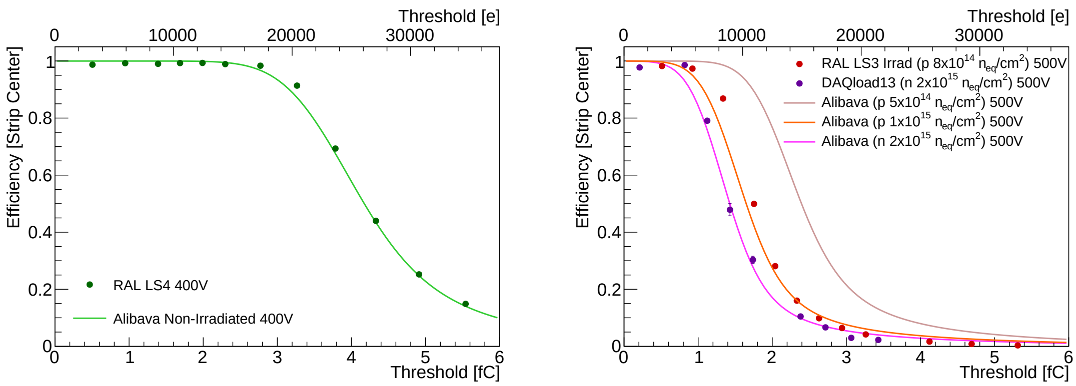

(a) The non-irradiated module RAL LS4 compared to a non-irradiated ATLAS12 mini-sensor.

(b) RAL LS3 Irrad and DAQload13, a mini-module with a fully-equipped hybrid and a miniature sensor irradiated with neutrons at JSI tested in the May 2016 test beam. The curves are compared to mini-sensors irradiated at JSI and KIT to similar NIEL fluences.

Figure 4.12: Comparison of the s-curve obtained selecting tracks crossing a strip in proximity of to its center and the integrated cluster charge distribution measured at JSI with the Alibava system using mini-sensors and a radioactive source [49, 141].

The cluster charge distribution is given by the convolution of a Landau distribution, related to the energy release in silicon by a traversing particle (see Section 2.3), with a Gaussian distribution, related to the noise in the system. The s-curve obtained with tracks crossing the center of a strip are fitted with an integrated Landau-Gauss distribution as shown in Figure 4.13. The Landau MPV obtained from the fit is the Signal of the module. Although the Gaussian width of the distribution is theoretically related to the noise in the system, the value obtained from the fit is usually much larger than the noise obtained with other procedures. There is some trade-off between the Landau width and the Gaussian width parameters, which are similar quantities difficult to separate with a numerical fit. The Landau and Gaussian widths are then considered nuisance parameters of the fit.

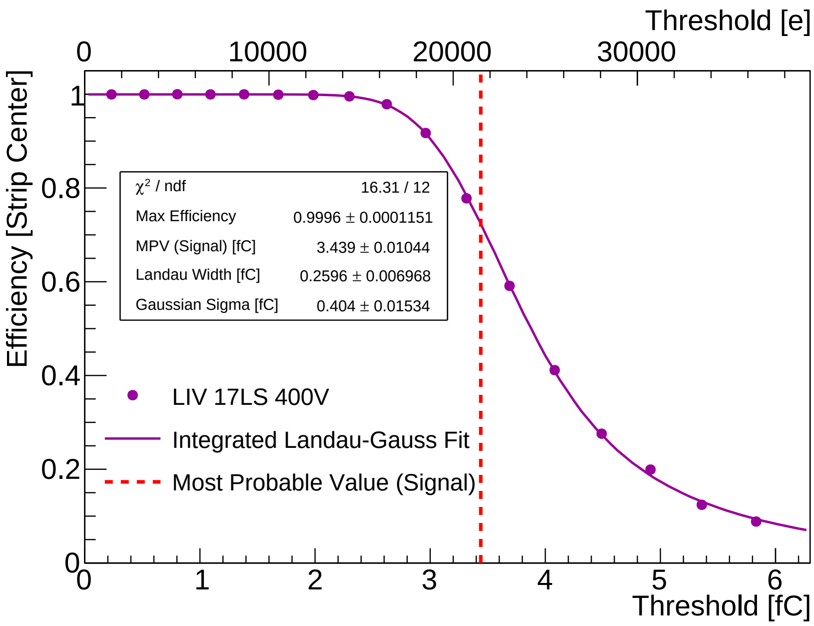

Figure 4.13: S-curve obtained considering only tracks crossing the central 40% of a strip for the non-irradiated module LIV 17LS. The data is fitted with an Integrated Landau-Gauss distribution. The red dashed line indicates the MPV (Signal).

4.4 Data Analysis

4.4.1 Threshold Calibration

An s-curve is obtained by sequential measurements with different thresholds. The threshold is set in the comparators of the front-end chips through a Digital-to-Analog Converter (DAC) in units called DAC. However, to fully understand the test beam results, the knowledge of the value of each threshold in units of charge is needed.
The calibration of the threshold values to units of charge is performed in two steps:

- Conversion from DAC units to mV, the unit for the signal in the front-end chips.

- Conversion from mV to fC (or, equivalently, number of electrons).

Figure 4.14 shows the conversion curve from DAC units to mV for ABCStar obtained by front-end simulations. A similar curve is obtained for the ABC130 front-end chips with the same method [131].

A calibration circuit is implemented in the chip architecture in order to convert the threshold values in units of charge: voltage pulses with settable amplitude and length are injected in a capacitor with known capacitance (60.0 ± 0.6 fF [131]), thus generating a signal with a well-defined charge. The pulses are generated with the same frequency of the readout cycle (40 MHz).

Figure 4.15 shows a threshold scan used to calibrate a threshold to units of charge. A threshold scan is performed by injecting a signal of known charge several times while reading each channel. The procedure is repeated for several thresholds. The response is expected to be a step function: for thresholds lower than the injected charge a hit is recorded at every readout cycle, while for thresholds higher than the injected charge no hit is recorded. However, because of the presence of noise with a Gaussian distribution in the system, the response has the shape of a complementary error function distribution. The mean value of the distribution corresponds to the amplitude of the signal. This is the threshold where 50% of the hits are recorded and it is called Vt_{50}. The standard deviation of the error function is the noise in the channel in mV and it can be eventually be converted in units of charge.

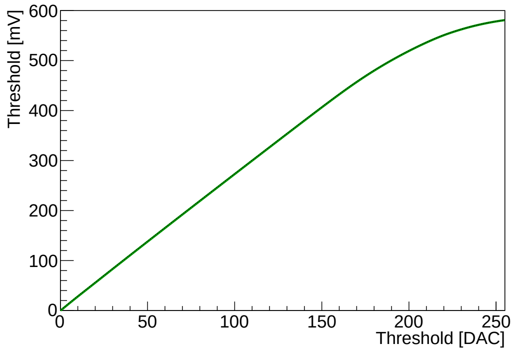

Figure 4.14: Conversion curve from DAC units to mV obtained by ABCStar front-end simulations [142].

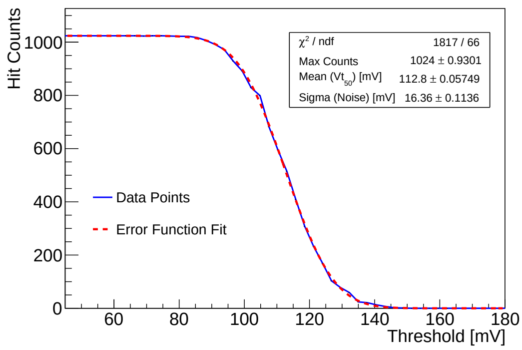

Figure 4.15: Threshold scan performed with the non-irradiated module FR R0Star and a charge injection of 1.0 fC (6250 e). The complementary error function fit used to obtain the Vt_{50} is also shown.

With a threshold scan a single threshold is calibrated. To obtain the calibration for every threshold, the threshold scan procedure is repeated for several different charge injections. Figure 4.16 shows a response curve, the curve given by the Vt_{50} as a function of the charge injected in the front-end channels. This curve is fitted with an empirical function [143]:

$$Vt_{50}(q_{inj}) = p_0 + \frac{p_1}{1+\exp\left(-\frac{q_{inj}}{p_2}\right)} \tag{4.4}$$

where q_{inj} is the injected charge and p_0, p_1, and p_2 are fit parameters. The calibration procedure with the response curve is performed separately for every chip.

Using the conversion curve shown in Figure 4.14 it is possible to convert the thresholds from the DAC units to mV units. Then, by using the fit parameters obtained with a response curve and inverting Equation 4.4, it is possible to calculate the value of the threshold in units of charge for any threshold value in mV.
The calibration procedure is performed for each module during the test beam or in a laboratory at a temperature comparable to the one in the test beam set-up.

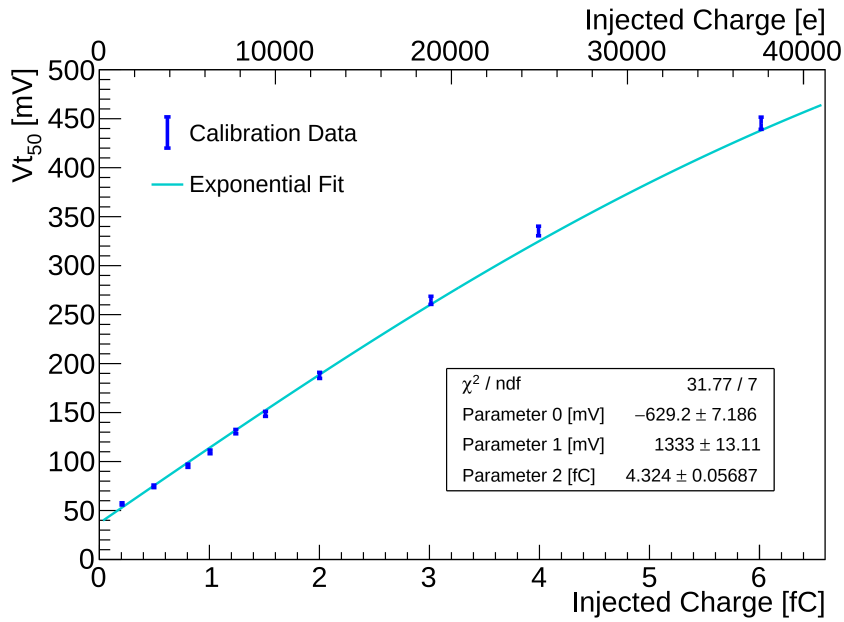

Figure 4.16: Vt_{50} as a function of the charge injected in the front-end channels (response curve) for the non-irradiated module FR R0Star. The fit used to parametrize the calibration is also shown.

4.4.2 Timing Cut

The readout frequency of the ITk Strip front-end chips is the same as the LHC (and HL-LHC) bunch crossing rate (40 MHz). In the ATLAS Detector, the timing of the readout can be synchronized to the peak of the signals generated by the collision fragments in order to maximize the hit detection efficiency. In the SCT the synchronization is performed every year in special runs and the readout timing is optimized with a precision of 2 ns [144]. A similar operation will be performed in the ITk Strip Detector.

In test beams, particle do not arrive with a defined frequency but they arrive at random times, therefore it is not possible to synchronize the readout cycle with the particle signals. To read out the channels only at the peak of the signals a different approach is used. The relative position of the readout with respect to the signal shape depends only on the time difference between the arrival of the beam particle and the readout. The DAQ FPGA measures the time difference between the arrival of a trigger (which depends on the time of arrival of the particle) and the readout of the channels. This time difference is measured using a clock with rate of 640 MHz (clock cycle of 1.56 ns).

Figure 4.17 shows the hit detection efficiency for a threshold close to the median charge as a function of the trigger-readout time delay measured by the DAQ FPGA. In the analyses discussed in this thesis, only the six bins with the highest efficiency are considered. This corresponds to a time window of width of 9.36 ns.
One can select events with a defined trigger-readout time delay, create an s-curve and fit it with a skewed error function. With this procedure one can obtain the median charge as a function of the trigger-readout time delay, which is a measurement of the pulse shape at the discriminator stage of the front-end chips [145]. The pulse shape obtained in this way is shown in Figure 4.17. The time bins with the highest efficiency correspond to the peak of the pulse shape generated by the incoming particles.

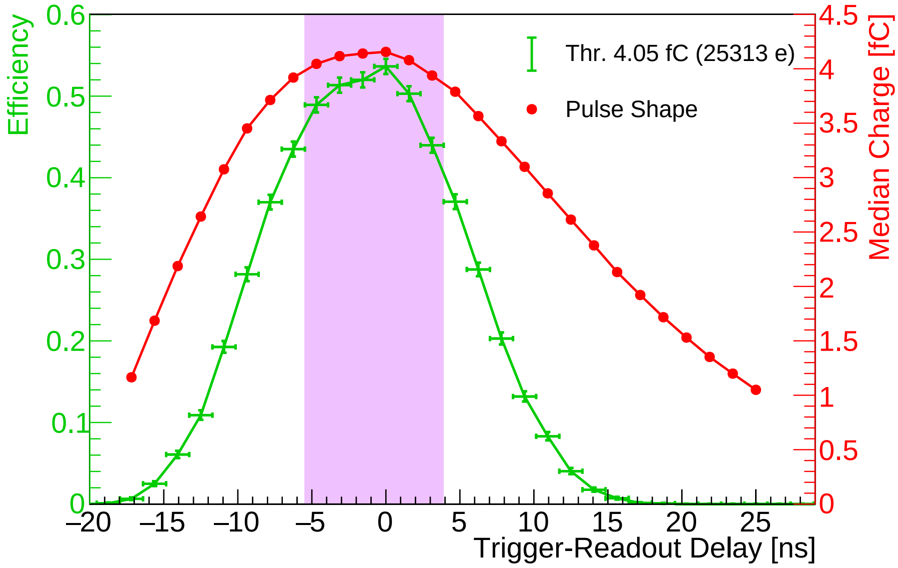

Figure 4.17: Hit detection efficiency for a threshold close to the median charge (green) and median charge (red) as a function of the trigger-readout time delay for the non-irradiated module RAL SS. The zero of the x axis is set to the peak of the pulse shape. The purple area highlights the time window selected in the analysis.

Figure 4.18a shows the efficiency as a function of the trigger-readout delay for several thresholds. For thresholds much lower than the median charge, the efficiency saturates for several time bins. In this case, an accurate selection of the optimal time window is impossible. To select the time window it is chosen to use measurements with a threshold close to the median charge, where the peak efficiency is about 50%.

Figure 4.18b shows the average cluster size as a function of the trigger-readout delay. The time window chosen to maximize the efficiency also corresponds to the peak of the average cluster size.

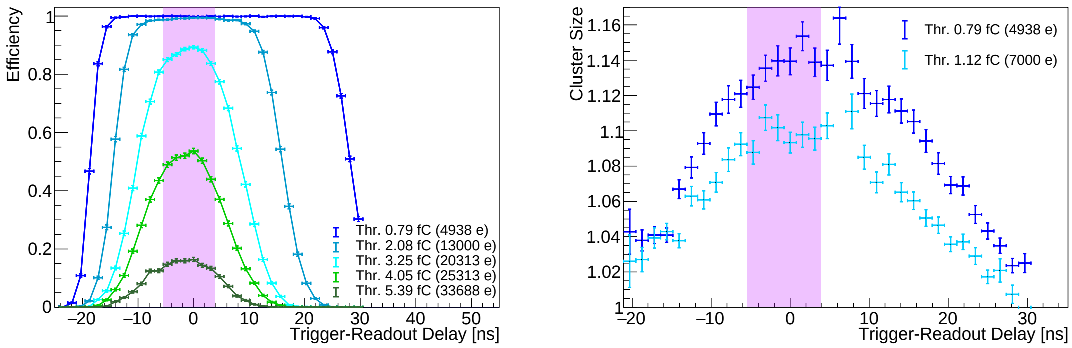

(a) Efficiency. (b) Cluster Size.

Figure 4.18: Efficiency and average cluster size as a function of the trigger-readout delay for several thresholds for the non-irradiated module RAL SS. The pink areas highlight the time window implemented in the analyses discussed in this thesis.

4.4.3 De-synchronization Masking

In a test beam the devices are operated by independent DAQ systems that are synchronized by the TLU and EUDAQ. The de-synchronization of a device with respect to the others is a common problem and can happen if a trigger is not correctly transmitted by the communication lines, or if a spurious trigger is recorded by a device.

The ITk Strip DAQ (ITSDAQ) independently sends two data streams to EUDAQ: one containing the hit information and timestamps from the front-end ASICs, and another containing the Timing, Trigger and Control (TTC) information from the DAQ FPGA. The data stream containing the hit information exhibited de-synchronization issues in multiple test beams. The DAQ FPGA, however, does not exhibit any synchronization problem because of the robustness of its incoming trigger lines.
An automatic check was implemented and deployed in ITSDAQ which identifies de-synchronized events and re-synchronize the data online. However, this procedure can be applied only after a few thousand events affected by de-synchronization have been recorded. These de-synchronized events lower the average efficiency of a test beam run typically by 3-10%.

Figure 4.19a shows the efficiency as a function of the event number in a run with LIV 17LS. Although the efficiency is generally 100%, very low efficiency is visible in two regions because of de-synchronization. The de-synchronization is corrected in the analysis by comparing timestamps in the two ITSDAQ data streams on an event-by-event basis [146]. The TTC data stream is always synchronized to the other devices in the test beam set-up, therefore it can be used as a reference for the synchronization of the hit information data stream.

Figure 4.19b shows the timestamp difference between TTC and hit information data streams, as a function of the event number. For synchronized events the timestamps exhibit a constant difference, while for de-synchronized events the timestamp difference exhibits random values. Only events for which the timestamp difference is the same as the one recorded in the previous three events are considered in the analysis, while the other events are discarded.

Figure 4.19c shows the efficiency calculated after the application of the de-synchronization masking procedure. The events with low efficiency are discarded and the average efficiency becomes about 100%. The procedure is applied similarly for the front-end chips ABC130 and ABCStar, with the only difference that the timestamp is stored in an 8 bit variable for ABC130 and in a 3 bit variable for ABCStar.

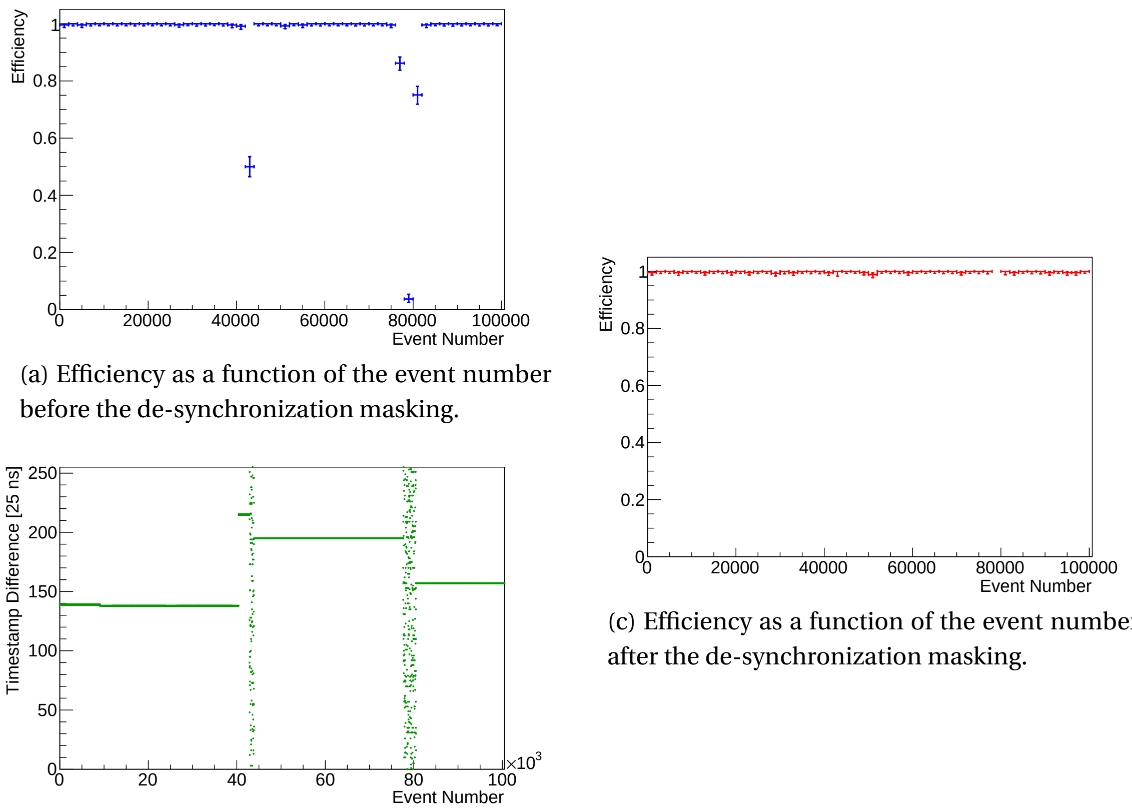

(a) Efficiency as a function of the event number before the de-synchronization masking.

(b) Timestamp difference between hit information and DAQ FPGA data streams, as a function of the event number.

(c) Efficiency as a function of the event number after the de-synchronization masking.

Figure 4.19: Explanation of the procedure used to mask events with de-synchronization between the ITk Strip module and the telescope. The measurement is performed with the non-irradiated module LIV 17LS with a threshold of 0.78 fC (4875 e).

4.5 Calibration Validation

In the ITk Strip test beams an s-curve is measured with the beam pointing to several positions corresponding to different front-end chips. It is possible to quantify the precision and accuracy of the calibration procedure explained in Section 4.4.1 by comparing the s-curves measured in different ASICs with the theoretical expectations. This procedure is performed using the MPV (Signal) obtained with non-irradiated devices, for which a well-defined theoretical expected value can be calculated.

The MPV (Signal) for a minimum ionizing particle in 300 μm of silicon is 22 400 e (3.58 fC) [60]. ATLAS12 and ATLAS17LS sensors have an active thickness of $302.0 \pm 0.8\,\mu\mathrm{m}$ and $303.4 \pm 0.9\,\mu\mathrm{m}$, respectively [147]. Using the average thickness of 302.7 μm the MPV (Signal) can be calculated as:

$$\mathrm{MPV}(302.7\,\mu\mathrm{m}) = \frac{302.7\,\mu\mathrm{m}}{300\,\mu\mathrm{m}} \cdot \mathrm{MPV}(300\,\mu\mathrm{m}) = 22\,602\,\mathrm{e}\ (3.62\,\mathrm{fC}) \tag{4.5}$$

Because of crosstalk, part of the charge collected in each strip is shared with the neighbors. The fraction of charge shared from the leading strip to the neighbors and to the backplane can be estimated with Equation 2.21 and by using coupling, inter-strip, and backplane capacitances from electrical measurements (see Appendices B.3 and B.1):

$$P_{\mathrm{transmission}} = \frac{24.28\,\mathrm{pF\,cm^{-1}}}{24.28\,\mathrm{pF\,cm^{-1}}+0.75\,\mathrm{pF\,cm^{-1}}+0.29\,\mathrm{pF\,cm^{-1}}} = 0.959\ (95.9\%) \tag{4.6}$$

The MPV (Signal) in the leading strip can be calculated using Equations 4.5 and 4.6:

$$\mathrm{MPV}_{\mathrm{leading}} = \mathrm{MPV}(303\,\mu\mathrm{m}) \cdot P_{\mathrm{transmission}} = 22\,602\,\mathrm{e} \cdot 0.959 = 21\,679\,\mathrm{e}\ (3.47\,\mathrm{fC}) \tag{4.7}$$

The $\mathrm{MPV}_{\mathrm{leading}}$ uncertainty is dominated by the crosstalk model used in Equation 4.6. In fact, the formula is only an approximation of the crosstalk mechanisms in a module. An additional source of uncertainty is the starting value of the MPV (Signal) in 300 μm of silicon. For example, an alternative value of 22 000 e can be found in literature [66].

Figure 4.20 shows the MPV (Signal) measured in test beams with the beam pointing at different front-end chips of non-irradiated devices, compared to the theoretical MPV calculated in Equation 4.7. The distribution of the measured MPV (Signal) exhibits a peak in the proximity of the expected MPV.
A few outliers with an MPV (Signal) of about 3.7 fC are present. These outliers could be explained by an imperfect calibration procedure. The outliers deviate from the theoretical MPV by about 6% and such a deviation does not pose a problem for the future ITk Strip operations. All the outliers are obtained with the prototype front-end chip ABC130 and no such outliers have been observed with the production-grade front-end chip ABCStar, although the statistics for the latter is limited.

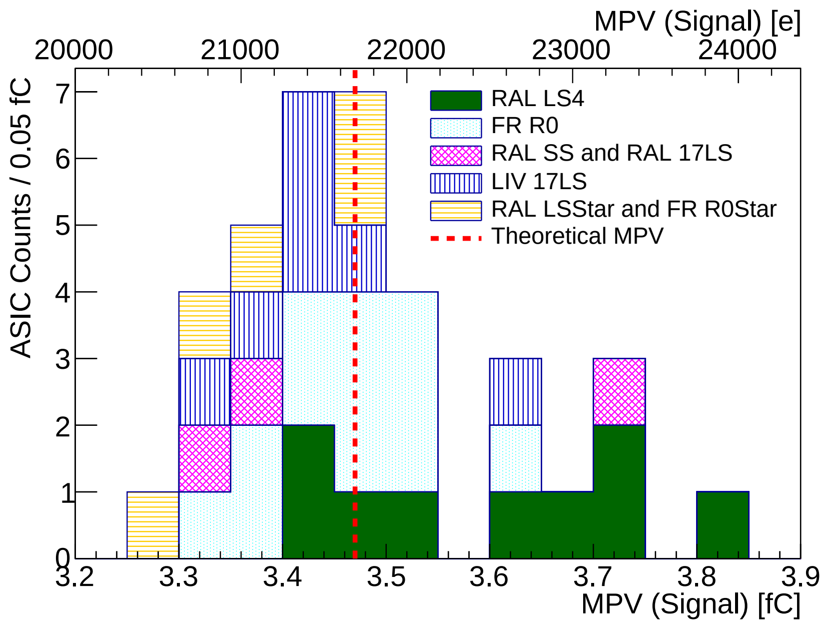

Figure 4.20: MPV (Signal) measured for several ASICs in non-irradiated modules tested in ITk Strip test beams. The red dotted line shows the theoretical MPV (Signal) calculated in Equation 4.7.

Table 4.3 contains a quantitative comparison of the average MPV (Signal) obtained from different non-irradiated devices and the theoretical expectation. The combined average MPV (Signal) of all modules is compatible with the expected value within uncertainties and deviates from it by less than 1%. These results demonstrate the good accuracy of the threshold calibration procedure. The standard deviation of the MPV (Signal) is 0.13 fC (829 e), or 3.8% of the average value, a small dispersion that does not pose any problem for the module operations. The results therefore prove that the threshold calibration procedure in the current ITk Strip prototype modules will provide an accurate and precise calibration during the future data-taking operations.

Module	MPV (Signal) [fC] (e)	σ_{MPV} [fC] (e)	σ_{MPV}/MPV [%]
Expected Value	3.47 (21679)		
All Modules Combined	3.48 ± 0.02 ($21\,774 \pm 125$)	0.13 (829)	3.8
RAL LS4	3.60 ± 0.05 ($22\,500 \pm 313$)	0.14 (875)	3.9
FR R0	3.46 ± 0.02 ($21\,625 \pm 125$)	0.08 (500)	2.4
LIV 17LS	3.44 ± 0.04 ($21\,500 \pm 250$)	0.10 (625)	2.9
RAL LSStar and FR R0Star	3.39 ± 0.04 ($21\,188 \pm 250$)	0.10 (625)	2.8

Table 4.3: List of non-irradiated modules tested in test beams, the average MPV (Signal) from measurements performed with the beam pointing at different front-end chips, the standard deviation, and the standard deviation divided by the average MPV (Signal). Only devices with measurements with the beam pointing on at least three different ASIC are shown. The data for RAL LSStar and FR R0Star is grouped for increased statistics.

4.6 Characterization of Boundary Regions

The average response of a sensor to a particle is determined mostly by the central region of a sensor. However, to fully understand the behavior of a sensor, the knowledge of the response to a particle crossing its boundary regions is needed. This response determines the active area of the sensor and it provides important information for simulation and tracking algorithms.
Figure 4.21 shows the three boundary regions characterized during the ITk Strip test beams:

- The field shaping strip region. The field shaping strips are the first and last strips and they are not connected to a readout channel, although they are connected to the grounded bias line. Their purpose is to reduce possible detrimental effects of the sensor edges on the active channels.
- The end-of-strip region along the strip axis.
- The inter-segment region: the interface region between two strip segments, which are divided by a grounded bias rail that crosses the sensor width.

These boundary regions were studied in the June 2018 test beams with non-irradiated barrel modules with ATLAS17LS sensors.

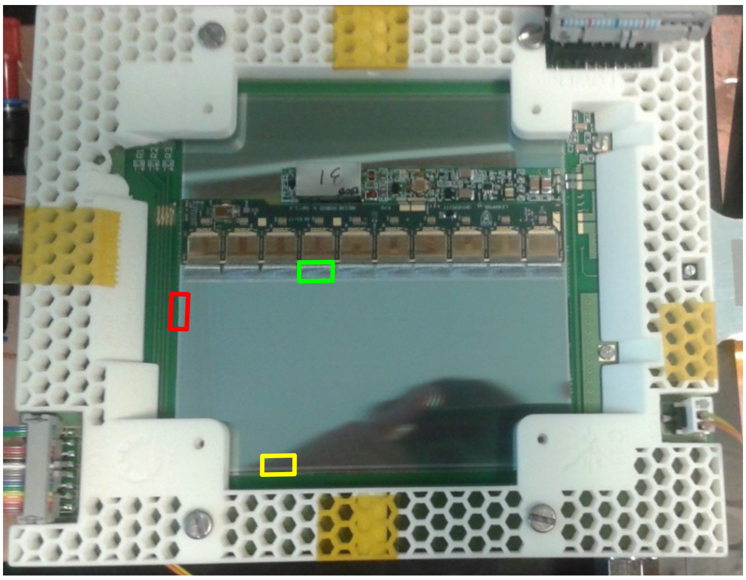

Figure 4.21: Boundary regions characterized during the ITk Strip test beams: the region including the field shaping strip and the first active strip (red), the end-of-strip region (yellow), and the inter-segment region (green). In the picture the interface between the upper and lower strip segments is covered by the readout wire-bonds.

4.6.1 Field Shaping Strips

Although the field shaping strips are not connected to a readout channel, a particle crossing them can still generate a detectable signal in the adjacent active strip because of charge sharing. Figure 4.22a shows the efficiency as a function of the track position in the field shaping strip region. As expected, the higher the threshold, the lower the efficiency in the field shaping strip region. High efficiency in the field shaping strip region is a desirable effect for the ITk Strip Detector since it implies a larger active area for a module. The active area would be increased by about 0.16% if all the hits on the field shaping strip were detected.
With a threshold of 0.64 fC (4000 e) almost all the particles crossing the field shaping strip are detected. With a threshold of 1.09 fC (6813 e), close to the baseline threshold of 1 fC (6250 e), only about 50% of the particles crossing the field shaping strip are detected. Finally, with a threshold of 1.55 fC (9688 e) the efficiency for particles crossing the field shaping strip is about 20%.

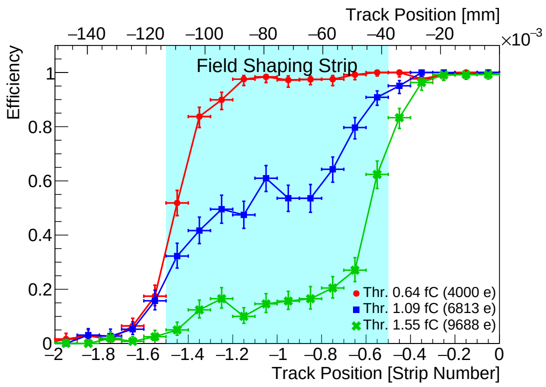

(a) Efficiency as a function of the track position in the field shaping strip region. Measurements with three different thresholds are shown. The cyan area highlights the field shaping strip position.

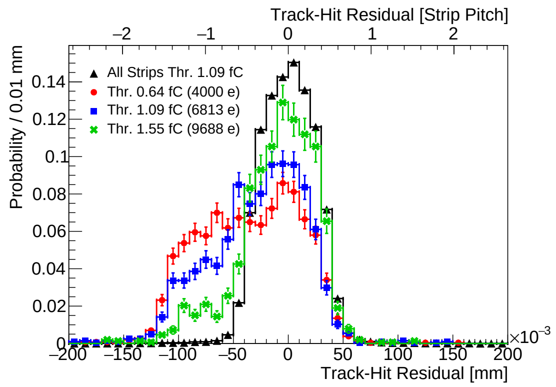

(b) Residual distribution for all the hits (black), compared to the residual distribution obtained for three thresholds with hits including the first active strip (red, blue, and green).

Figure 4.22: Hit detection efficiency and residual distribution for particles crossing the field shaping strip region for the non-irradiated module RAL 17LS.

A high efficiency in the field shaping strip has the advantage of increasing the active area of the sensor. However, the increase of the active area is rather modest and the additional hits introduce undesirable effects for the spatial resolution. Particles crossing the field shaping strip generate a signal in the adjacent strip, thus producing a hit with a large track-hit residual. A wide residual distribution could have detrimental effects on the ITk reconstruction algorithms. Therefore, a good knowledge of the spatial resolution of the hits generated by particles crossing the field shaping strip region is crucial.

Figure 4.22b shows the residual distribution for hits that include the first active strip, compared to the residual distribution for all other hits. The spatial resolution of the hits can be estimated with the standard deviation of their residual distribution. The standard deviation of hits that include the first active strip is 0.045 mm, 0.043 mm and 0.035 mm for a threshold of 0.64 fC, 1.09 fC, and 1.55 fC, respectively. At these three thresholds the standard deviation of the other hits is 0.024 mm and does not depend on the threshold. Hits including the first (or the last) active strip have a spatial resolution almost twice as large as the nominal one and this effect is only partially mitigated if a high threshold is used.

4.6.2 End-of-Strip Region

Figure 4.23 shows the efficiency as a function of the track position along the strip axis in the end-of-strip region. The lower the threshold, the further the region with high efficiency extends, thus increasing the active area. For a threshold of 0.49 fC (3063 e) the 50% efficiency point extends about 0.02 mm further with respect to a threshold of 1.38 fC (8625 e). This effect corresponds to an increase of the active area of 0.04%. The difference is very small and it is not significant for the choice of the operational threshold to be used in the ITk Strip Detector.

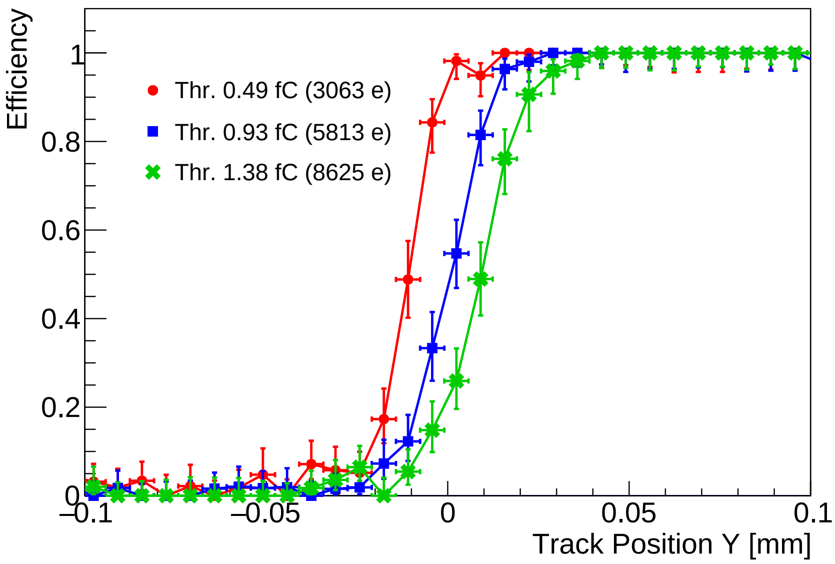

Figure 4.23: Efficiency as a function of the track position along the strip axis for three thresholds for the non-irradiated module LIV 17LS. The origin has been defined as the 50% efficiency point of the curve with threshold of 0.93 fC.

4.6.3 Inter-Segment Region

The strip segments in a sensor are separated by a grounded bias rail. A loss of efficiency in the interface region would be detrimental to a sensor performance because it would imply a loss of hits in the central region of a sensor. Figure 4.24 shows the efficiency with a threshold of 1.38 fC (8625 e) as a function of the track position along the strip axis in the inter-segment region. No significant loss of efficiency is measured, proving that the whole inner region of a sensor contributes to the efficiency. This result is confirmed by measurements with lower thresholds (see Appendix A.2).

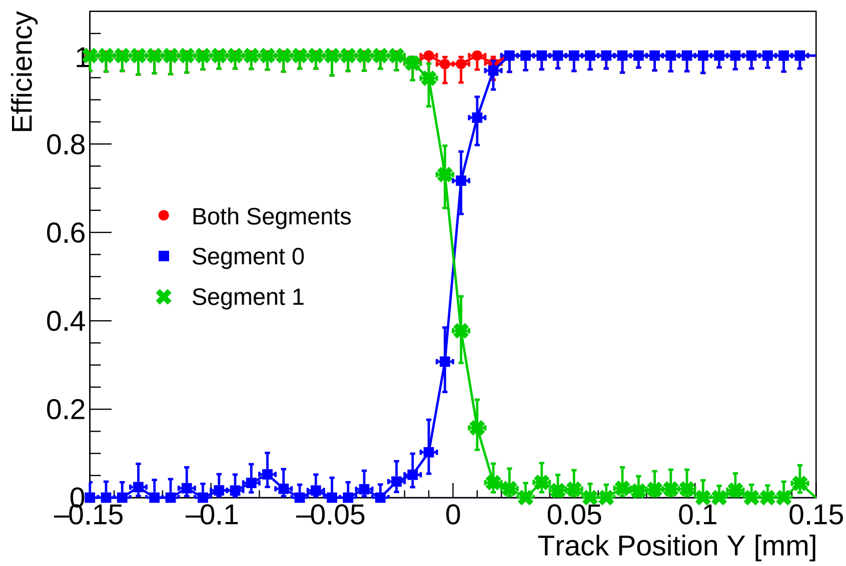

Figure 4.24: The red points show the efficiency in the inter-segment region as a function of the track position along the strip axis for the non-irradiated module LIV 17LS with a threshold of 1.38 fC (8625 e). The blue and green points show the efficiency obtained if only one segment is considered. The origin is defined as the point where the efficiency in the two segments is equal.

4.7 Module Performance Before and After Irradiation

The main figure of merit of a silicon module for a tracking detector is its hit detection efficiency, since the loss of any hit along a particle track has significant consequences on the information available to the tracking algorithms. Another important parameter of a module is the probability of recording a fake hit. Fake hits affect the quality of the data recorded by the detector and can potentially create issues for the tracking algorithm, such as the mis-reconstruction of fake tracks or the distortion of real tracks. Fake hits also contribute to the bandwidth necessary to transmit the hit information to the off-detector electronics. The only source of fake hits in a silicon module is noise hits, which are generated when the noise fluctuation in a channel is larger than the threshold at a given readout cycle. The probability that a noise hit is generated in a strip at a given readout cycle is called noise occupancy.

Both the hit detection efficiency and the noise occupancy decrease as the threshold is increased. The use of a low threshold would provide high efficiency, but the noise occupancy could reach levels problematic for tracking and bandwidth purposes. The use of a high threshold would guarantee operations with a very low noise occupancy, but the reduced efficiency could imply a loss of hits too large for efficient tracking. The operational threshold must be carefully chosen to balance these two competing behaviors. The operational threshold for the ITk Strip Detector is required to provide a hit detection efficiency > 99% and a noise occupancy < 10^{-3} (0.1%). It is crucial to prove that a range of thresholds satistying both these requirements exists for all the ITk Strip modules for the entire HL-LHC lifetime.

4.7.1 Non-Irradiated Modules

Figure 4.25 shows the efficiency and noise occupancy as a function of the threshold for a non-irradiated barrel module with the prototype front-end ABC130. The noise occupancy is measured by taking data without the beam and dividing the total number of hits by the number of readout cycles recorded and by the number of strips examined. The efficiency is > 99% for thresholds < 2 fC (12 500 e) while the noise occupancy is < 10^{-3} for thresholds > 0.5 fC (3125 e). Any threshold between these two values satisfies both the efficiency and noise occupancy requirements for the ITk Strip Detector. This wide range of operational thresholds will guarantee flexibility in the choice of the operational conditions. For example, the efficiency is > 99.9% for thresholds < 1.4 fC (8750 e) where the noise occupancy is $\ll 10^{-7}$.

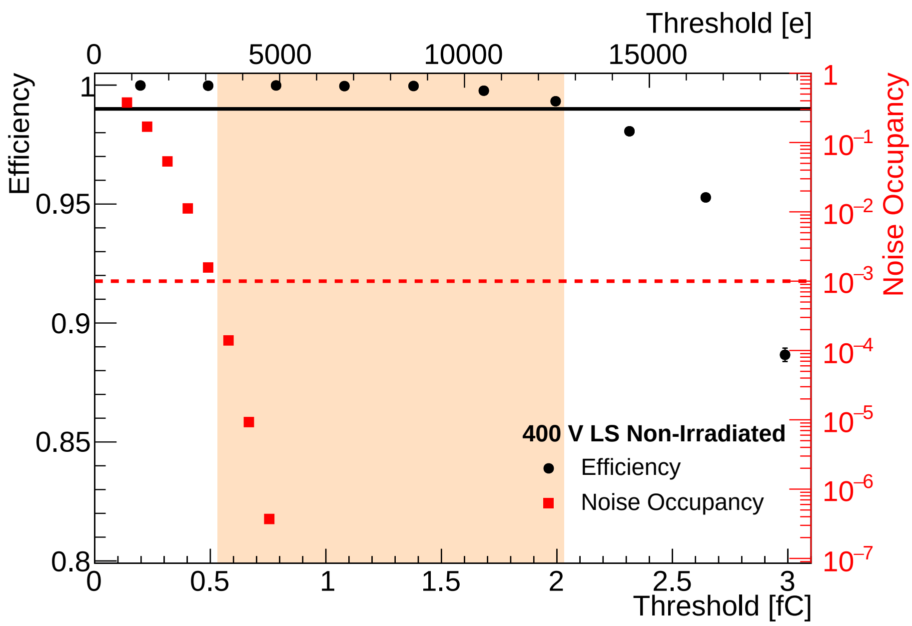

Figure 4.25: Efficiency and noise occupancy as a function of the threshold for the non-irradiated module LIV 17LS. The black and red lines indicate the requirements on the efficiency and noise occupancy, respectively. The orange area highlights the range of thresholds where the ITk Strip requirements are satisfied.

Similar results are obtained for several non-irradiated modules, as end-cap modules (Figure 4.26a) and modules with the production-grade front-end ABCStar (Figure 4.26b). In all cases a range of operational thresholds exists with a width of about 1.4 fC (8750 e) between ~0.5 fC (3125 e) and ~1.9 fC (11 875 e). Small variations in the position and width of the operational window are related to different sensor iterations, imprecision of the calibration, or small shifts of the signal baseline.

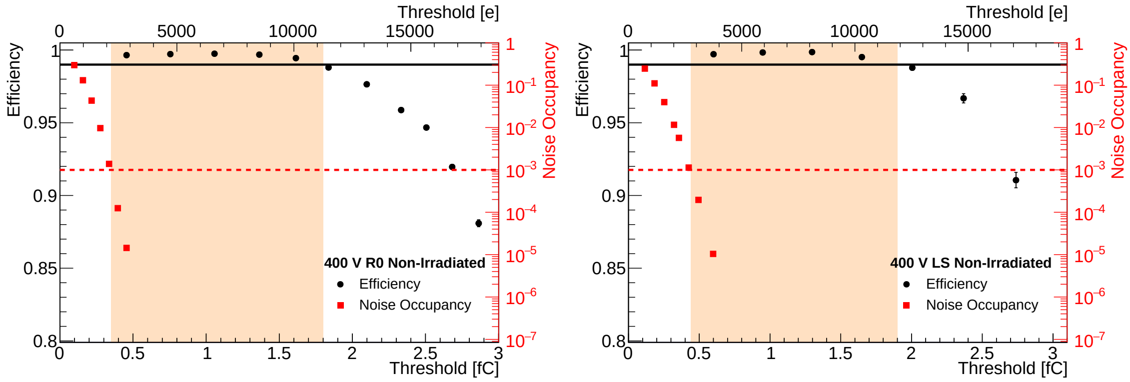

(a) FR R0.

(b) RAL LSStar.

Figure 4.26: Efficiency and noise occupancy as a function of the threshold for the non-irradiated modules FR R0 and RAL LSStar. The black and red lines indicate the requirements on the efficiency and noise occupancy, respectively. The orange areas highlight the range of thresholds where the ITk Strip requirements are satisfied.

4.7.2 Irradiated Modules

The presence of an operational window must be guaranteed for the entire lifetime of the HL-LHC. Although a wide range of operational thresholds is present for non-irradiated modules, the width (and potentially the existence) of the operational window is affected by radiation damage.

Figure 4.27 shows the efficiency as a function of the threshold for non-irradiated and irradiated modules tested in ITk Strip test beams. The efficiency is drastically reduced after irradiation as a consequence of radiation damage.
Figure 4.28 shows the noise measured in structures and modules with the prototype front-end chip ABC130. The noise is increased by about 20% after irradiation as a consequence of the TID released in the front-end chips.
Radiation damage significantly deteriorates the performance of a module by reducing the hit detection efficiency and increasing the noise occupancy. It is crucial to prove that a range of operational thresholds exists in modules irradiated to radiation levels comparable to the one they will have experienced at the end of lifetime of the HL-LHC.

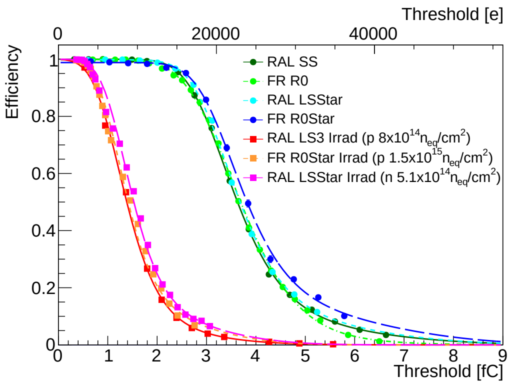

Figure 4.27: S-curves for non-irradiated and irradiated modules tested in the ITk Strip test beams.

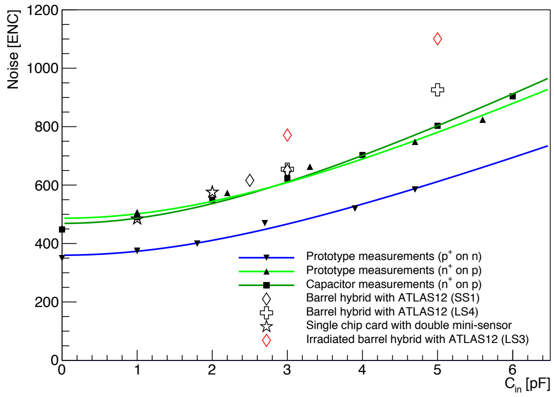

Figure 4.28: Noise as a function of the input capacitance in ITk Strip structures with the prototype front-end chip ABC130 [49]. Prototype modules are labeled by open points and RAL LS3 Irrad is labeled by red points.

RAL LS3 Irrad was irradiated with protons at CERN PS to a fluence of 8×10^{14} n_{eq}/cm^2, which corresponds to the maximum NIEL fluence expected at the end of lifetime of the HL-LHC in the Short Strip region of the ITk Strip barrel, including a safety factor of 1.2. The TID provided by the irradiation was 37.2 MRad (372 kGy).

Figure 4.29 shows the efficiency and noise occupancy as a function of the threshold for RAL LS3 Irrad [49]. The noise occupancy was measured in a laboratory after the test beam. The efficiency measured in the data point with the lowest threshold is about 97.5%, lower than the requirement of 99%. Therefore, it can not be proved that a range of thresholds satisfying the ITk Strip requirements exists, although a narrow window of operational thresholds may exist at about 0.4 fC (2500 e).

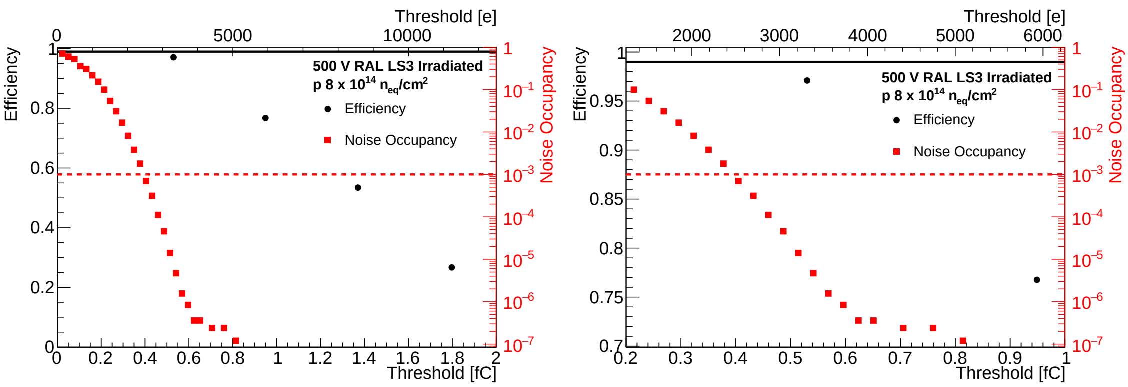

(a) All thresholds.

(b) Zoom on thresholds < 1 fC.

Figure 4.29: Efficiency and noise occupancy as a function of the threshold for RAL LS3 Irrad [49]. The black and red lines indicate the requirements on the efficiency and noise occupancy, respectively.

Although the performance of RAL LS3 Irrad is very marginal, the final modules for the ITk Strip Detector are expected to perform significantly better for three reasons:

- The prototype front-end ABC130 exhibits an increased noise after irradiation [131], while this is not the case for the front-end ABCStar (see Figure 4.30b).
- The production-grade sensors are more radiation-hard than the ATLAS12 sensor of RAL LS3 Irrad because of an increased silicon resistivity (2.5 kΩcm for ATLAS12 [128], compared to 3.2 and 3.0 kΩcm for ATLAS12EC [129] and ATLAS17LS [147], respectively).
- RAL LS3 Irrad was not subject to short term annealing, thus reducing its charge collection.

With these three improvements it is expected that later modules will satisfy the ITk Strip requirements up to the end of lifetime of the HL-LHC.

Since the measurements with RAL LS3 Irrad were inconclusive, new measurement were crucial when the production-grade front-end ABCStar front-end became available. RAL LSStar Irrad was built for this purpose with:

- ATLAS17LS sensor irradiated to a NIEL fluence of $5.1 \times 10^{14}\,\mathrm{n_{eq}/cm^2}$ with neutrons at JSI. The NIEL fluence corresponds to the maximum fluence expected in the Long Strip region of the ITk Strip barrel at the end of lifetime of the HL-LHC, including a safety factor of 1.4. The sensor was subject to short term annealing.
- Hybrid, front-end chips, and power board irradiated with x-rays at RAL with a TID of up to 20 MRad (200 kGy) (see Figure 4.30a), which corresponds to the maximum TID expected in the Long Strip region of the ITk Strip barrel at the end of lifetime of the HL-LHC, including a safety factor of 2.2.

Figure 4.30b shows the noise as a function of the TID measured in the hybrid during the x-ray irradiation. The noise does not increase with the TID, in contrast to the prototype front-end ABC130.

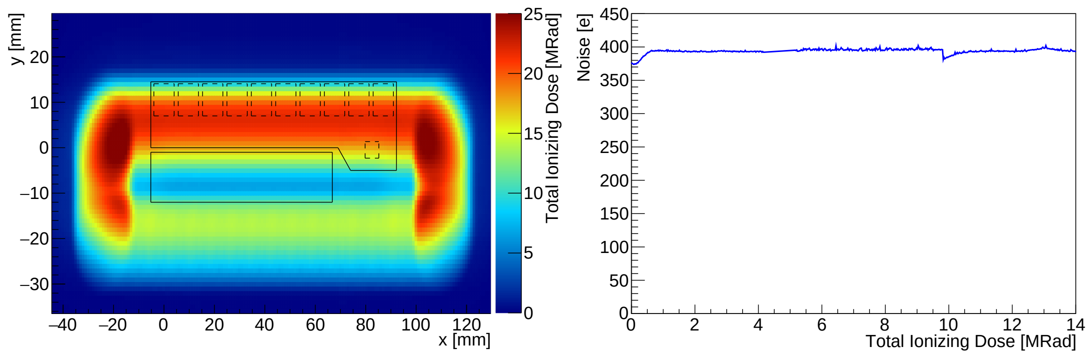

(a) TID distribution in the hybrid and power board [148].

(b) Noise as a function of the TID [148]. The changes in noise at 0 MRad and 10 MRad are caused by a temperature change in the set-up.

Figure 4.30: TID distribution and noise as a function of the TID for the x-ray irradiation of RAL LSStar Irrad. The hybrid was not wire-bonded to a sensor during irradiation.

Figure 4.31 shows the efficiency and noise occupancy as a function of the threshold for RAL LSStar Irrad. The noise occupancy is measured during the test beam and a small improvement is expected in a more controlled set-up, such as the ITk or a laboratory, because of better electrical connections and grounding. The ITk Strip requirements are satisfied for thresholds between about 0.4 fC (2500 e) and 0.55 fC (3438 e), thus proving that the current prototype Long Strip modules will provide good performance for the entire lifetime of the HL-LHC, including a safety factor 1.4.

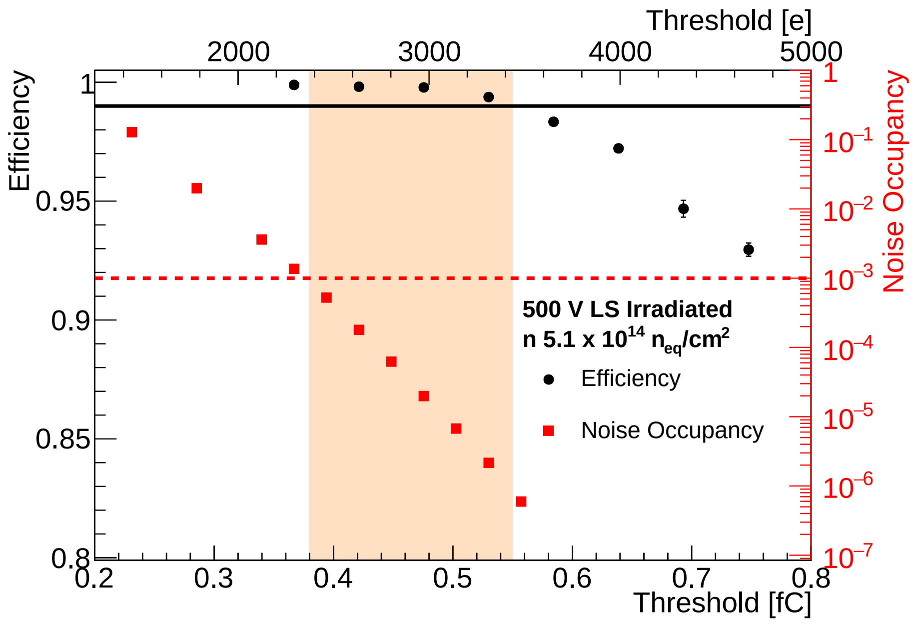

Figure 4.31: Efficiency and noise occupancy as a function of the threshold for RAL LSStar Irrad. The black and red lines indicate the requirements on the efficiency and noise occupancy, respectively. The orange area highlights the range of thresholds where the ITk Strip requirements are satisfied.

The measured MPV (Signal) is 1.63 ± 0.05 fC ($10\,183 \pm 298$ e), the noise is 0.100 ± 0.002 fC (625 ± 11 e), and the Signal-to-Noise is 16.3 ± 0.3. The MPV (Signal) is 20% smaller than the value measured in source measurements with an Alibava readout with sensors irradiated at JSI at the same NIEL fluence [149]. The noise is also 24% smaller than the one measured with the non-irradiated RAL LSStar at room temperature, which is 0.131 ± 0.001 fC (818 ± 7 e). The underestimation of both signal and noise is explained by a dependence of the front-end gain on the temperature [150] that has been confirmed in independent measurements with other modules in several laboratories. For this reason, the measured position and width of the operational window slightly differ from the real values, although the proof of existence of a range of operational thresholds does not depend on the absolute scale of the thresholds.

An end-cap module, FR R0Star Irrad, was built from irradiated components with:

- ATLAS12EC sensor irradiated to 1.5×10^{15} n_{eq}/cm^2 with protons at CERN PS. The NIEL fluence corresponds to the maximum NIEL fluence expected in the ITk Strip Detector at the end of lifetime of the HL-LHC, including a safety factor of 1.4. The sensor was subject to short term annealing.

- Hybrid, front-end chips, and power board irradiated with x-rays at RAL with a TID of up to 35 MRad (350 kRad), lower than the maximum TID expected at the end of lifetime of the HL-LHC in the inner section of the end-caps, 46 MRad (460 kRad). However, the module performance does not depend on the TID, since the noise in the front-end ABCStar does not depend on it (see Figure 4.30b).

Figures 4.32a and 4.32b show the efficiency and noise occupancy as a function of the threshold for the innermost and outermost segments of FR R0Star Irrad, respectively. The performance in the two central segments is discussed in Appendix A.4. As for RAL LSStar Irrad, the noise occupancy is measured during the test beam and an a small improvement is expected in the ITk. The efficiency saturates at around 99.5% as a consequence of residual out-of-time tracks recorded by the ALPIDE reference plane used in the June 2019 test beam when FR R0Star Irrad was tested.
The ITk Strip requirements are satisfied for thresholds between about 0.37 fC (2313 e) and 0.54 fC (3375 e) for the innermost segment, and between about 0.44 fC (2750 e) and 0.52 fC (3250 e) for the outermost segment. This proves that the current prototype R0 modules will provide good performance for the entire lifetime of the HL-LHC, including a safety factor 1.4.

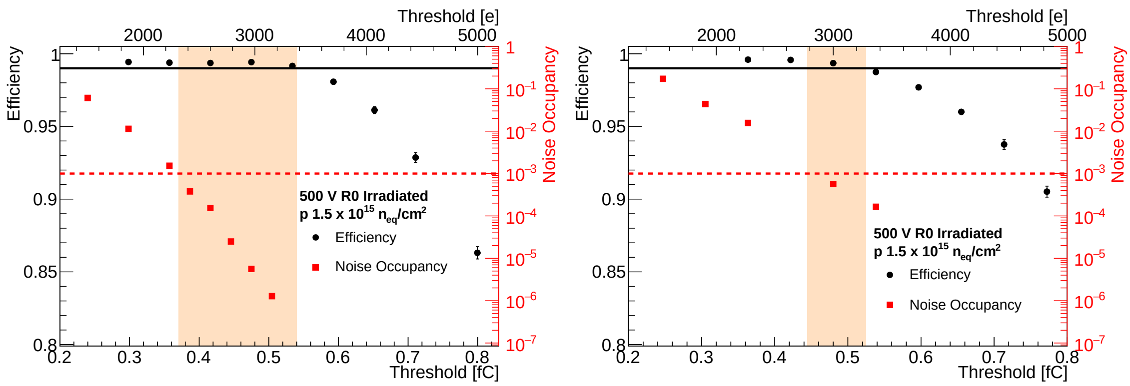

(a) Innermost segment.

(b) Outermost segment.

Figure 4.32: Efficiency and noise occupancy as a function of the threshold for the innermost and outermost segments of FR R0Star Irrad (see Figure 4.1b). The black and red lines indicate the requirements on the efficiency and noise occupancy, respectively. The orange areas highlight the range of thresholds where the ITk Strip requirements are satisfied.

For the innermost segment the measured MPV (Signal) is 1.49 ± 0.04 fC (9313 ± 250 e), the noise is 0.100 ± 0.013 fC (626 ± 81 e), and Signal-to-Noise is 14.9 ± 1.9. For the outermost segment the measured MPV (Signal) is 1.65 ± 0.05 fC (10313 ± 309 e), the noise is 0.138 ± 0.019 fC (864 ± 121 e), and the Signal-to-Noise is 11.9 ± 1.7, very close to the expected value of 12.2 for the same region at the end of lifetime of the HL-LHC with a safety factor 1.5 [151]. The latter is the minimum Signal-to-Noise expected in the ITk Strip Detector. The results in Figure 4.32b show that a range of thresholds satisfying the efficiency and noise occupancy requirements exists in these conditions, one can then safely assume that the efficiency and noise occupancy requirements will be satisfied in the whole ITk Strip Detector for the entire lifetime of the HL-LHC.

4.8 Effects of Radiation Damage on Charge Sharing

The studies in the previous Section provide the crucial demonstration that the current ITk Strip prototype modules will guarantee excellent performance for the entire lifetime of the HL-LHC. In order to further understand the response of the modules to a particle, it is useful to study the effects of radiation damage on the charge sharing. This is very important because the hit detection efficiency depends on the leading strip spectrum, therefore an increased charge sharing would reduce the efficiency at a given threshold. Moreover, charge sharing has important effects on the hit spatial resolution and on the bandwidth needed to transmit the data to the off-detector electronics.

Naively, one could expect the charge sharing to decrease after high-fluence hadron irradiation. In fact, in highly irradiated sensors part of the bulk thickness is not depleted, hence for a given bias voltage the average electric field is larger than in non-irradiated ones. Since the charge carriers diffusion decreases as the electric field in the sensor increases (see Section 2.3.2), one would expect the charge sharing to be reduced in highly-irradiated sensors. However, an increase of charge sharing has been observed in n-in-p strip sensors after low dose electron irradiation [152]. This is caused by surface damage, which has two main effects:

- Deflection of the electric field line toward the Si-SiO_2 interface on the sensor surface. The electric field distribution becomes similar to the field in a pad diode.
- Approximately ideal charge division between the strips adjacent to a charge deposition.

The last point implies that the charge sharing depends linearly on the inter-strip position of the charge deposition [85]. In particular, for a charge deposition exactly between two strips, the charge is divided evenly between the two strips.

Figure 4.33a shows the average cluster size as a function of the threshold for several non-irradiated and irradiated modules tested during the ITk Strip test beams. At thresholds > 2 fC (12 500 e) the dominant contribution to cluster size is given by delta ray electrons (see Section 4.3.2) and all modules exhibit a compatible cluster size. For thresholds between 0.6 fC (3750 e) and about 2 fC (12 500 e) the cluster size is larger in non-irradiated modules compared to the irradiated ones. In irradiated modules the cluster size increases steeply at low thresholds and for thresholds lower than about 0.6 fC (3750 e) it is larger than in non-irradiated modules. This is an evidence of a larger fraction of charge shared in the irradiated modules.

Figure 4.33a provides information on the absolute amount of charge shared, but a more meaningful information is given by the fraction of charge shared. Figure 4.33b shows the average cluster size as a function of the threshold divided by the MPV (Signal) of each module. For thresholds lower than 0.5, irradiated modules exhibit a cluster size significantly larger than non-irradiated ones. This is an evidence that in irradiated modules a significantly larger fraction of charge is shared to the neighboring strips.

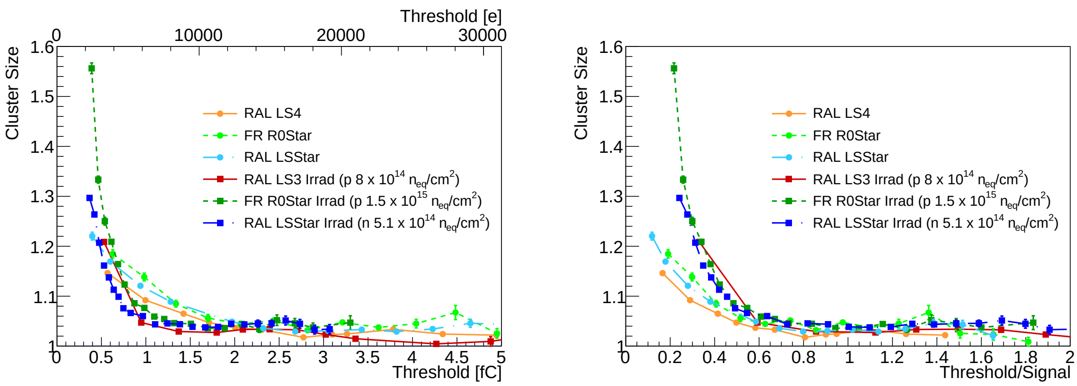

(a) Average cluster size as a function of the threshold.

(b) Average cluster size as a function of the threshold divided by the MPV (Signal).

Figure 4.33: Average cluster size as a function of the threshold and of the threshold divided by the MPV (Signal), for non-irradiated and irradiated ITk Strip prototype modules.

4.8.1 Efficiency and Charge Collection Profile

Figure 4.34 shows the efficiency as a function of the threshold for non-irradiated and irradiated modules, compared with the efficiency obtained by selecting only tracks crossing in the proximity of the center of a strip (see Section 4.3.3). The strip centers correspond to the regions where the charge sharing is minimal. The median charges obtained by fitting the curves with a skewed error function fit are summarized in Table 4.4. In non-irradiated modules the difference between the curves is minimal, and the median charge differs by only about 2%. In irradiated modules the efficiency is significantly lower than the one obtained considering only tracks crossing the strip centers. The median charge obtained with the standard s-curve is about 22% lower than that obtained by selecting tracks crossing the strip centers. This is a direct consequence of the increased charge sharing related to radiation damage.

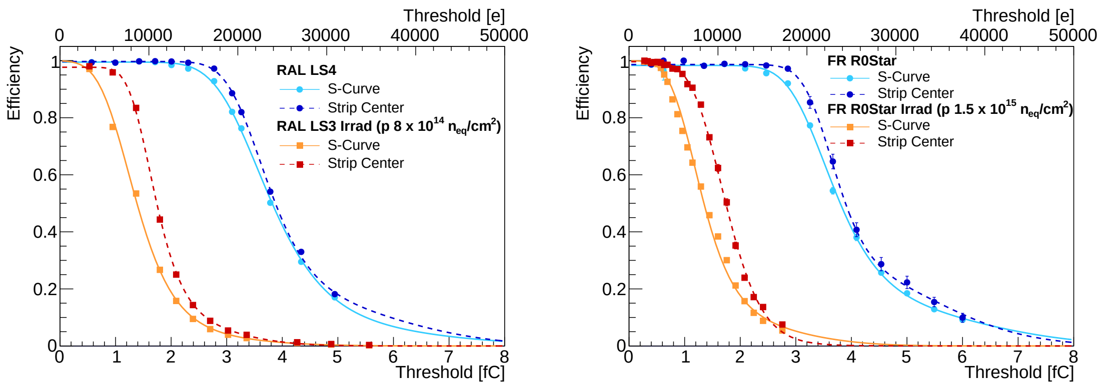

(a) Barrel modules RAL LS4 and RAL LS3 Irrad.

(b) End-cap modules FR R0Star and FR R0Star Irrad.

Figure 4.34: Efficiency as a function of the threshold for non-irradiated and irradiated barrel and end-cap modules, compared to the efficiency obtained by selecting only tracks crossing in the proximity of the center of a strip. The skewed error functions obtained from fitting are also shown.

Module	μ [fC] ([e])	μ_{center} [fC] ([e])	Ratio μ/μ_{center}
RAL LS4	3.82 ± 0.01 (23875 ± 63)	3.88 ± 0.02 (24250 ± 125)	0.985 ± 0.006
FR R0Star	3.82 ± 0.02 (23875 ± 125)	3.91 ± 0.04 (24438 ± 250)	0.977 ± 0.011
RAL LS3 Irrad	1.385 ± 0.002 (8656 ± 13)	1.755 ± 0.004 (10969 ± 25)	0.789 ± 0.002
FR R0Star Irrad	1.347 ± 0.003 (8419 ± 19)	1.743 ± 0.008 (10894 ± 50)	0.773 ± 0.004

Table 4.4: Median charge values obtained by fitting the curves in Figure 4.34 with a skewed error function. Their ratio is also shown. The uncertainties are taken from the fit.

To analyze this effect in more detail it is useful to study the sensor response for beam crossing different relative positions across a strip. Figure 4.35 shows the median charge collected on the leading strip as a function of the inter-strip position of the beam particle track. The median charge values are normalized to the maximum in each curve. The curve predicted by a simple charge division model is also shown. In this model, it is assumed that no charge carriers are shared if the signal is generated below the strip implant, while in the inter-strip region the charge carriers are shared following ideal charge division.

Non-irradiated modules exhibit a relatively flat distribution, with a small decrease close to the strip boundaries related to charge carriers diffusion. Irradiated modules exhibit a significant loss of charge on the leading strip in all the inter-strip region and their distribution is in qualitative agreement with the one predicted by the charge division model. This result proves that charge division between strips is present in proton-irradiated sensors.

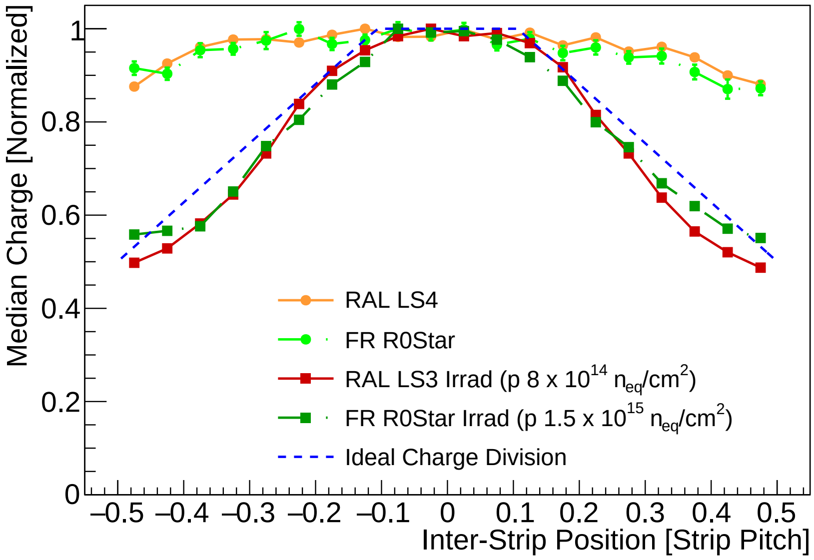

Figure 4.35: Normalized median charge as a function of the inter-strip position in non-irradiated and irradiated modules. The x axis is normalized by the strip pitch: the origin correspond to the strip center, and -0.5 and 0.5 correspond to the strip boundaries. The curve predicted by a simple charge division model is also shown.

4.8.2 Bond Pad Region

Figure 4.36 shows the efficiency as a function of the track position along the strip in RAL LS3 Irrad. Two regions with increased efficiency and width of about 200 µm are visible. These regions correspond to the positions where the bond pads are located[4]. Bond pads are opening in the passivation on top of the aluminum strip and are used to wire bond the strips to the ASIC readout channels. In order to accomodate the wire bond feet, bond pads have width of about 56 µm and length of about 200 µm [153]. The bond pads are arranged in two separate rows, altenately on odd and even strips (see Figure 4.37). Below the bond pads the strip implant has an increased width in order to cover the full bond pad area [154].

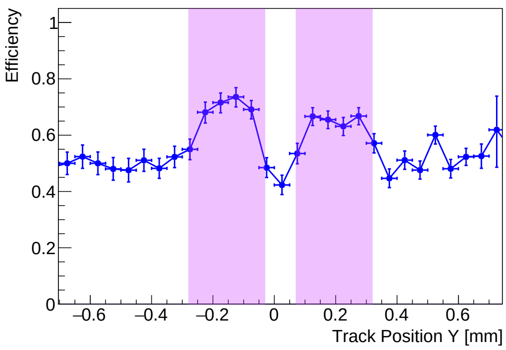

Figure 4.36: Efficiency as a function of the track position along the strip axis for RAL LS3 Irrad with a threshold of 1.37 fC (8563 e). The purple areas highlight the bond pads.

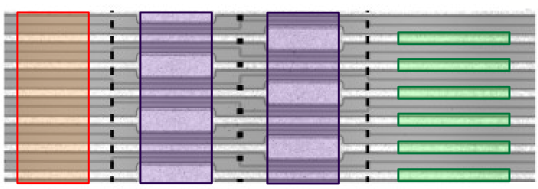

Figure 4.37: Microscope image of several strips in the region around the bond pads [155]: in orange the standard region, in purple the bond pad region, and in green the strip centers.

[4]The identification of the bond pad positions is explained in Appendix A.7.

Figures 4.38a and Figure 4.38b show the efficiency as a function of the threshold in the standard region, in the bond pad region, and at strip centers (see Section 4.3.3), for a non-irradiated and an irradiated module. For the non-irradiated module the efficiency measured in the bond pad area is compatible to the one measured in the rest of the sensor. For the irradiated module the efficiency in the bond pad region is significantly higher than in the standard region. This effect is explained by a mitigation of the charge division mechanism by the wider implant coverage of the bond pads, and it is further discussed in Chapter 5.

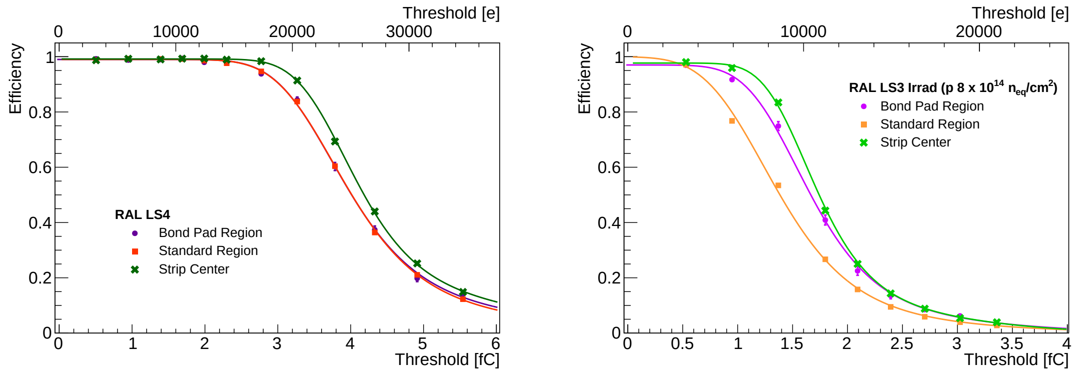

(a) RAL LS4. (b) RAL LS3 Irrad.

Figure 4.38: Efficiency as a function of the threshold in the standard region, in the bond pad region, and at the strip centers, for the non-irradiated module RAL LS4 and for RAL LS3 Irrad. The curves are fitted with a skewed error function distribution.

Table 4.5 summarizes the median charge values obtained in the different regions for RAL LS4 and RAL LS3 Irrad. In the non-irradiated module, the median charges obtained in the bond pad region and in the rest of the sensor are compatible within uncertainties and they are 4% lower than the median charge obtained by selecting tracks crossing at the center of a strip. In the irradiated module, the median charge in the bond pad region is much larger than that in the standard region by 20% and it is only about 4% lower than that obtained by selecting tracks crossing at the center of a strip.

Module	Region	μ [fC] ([e])	Ratio μ/μ_{center}
	Standard	4.026 ± 0.006 ($25\,163 \pm 38$)	0.961 ± 0.003
RAL LS4	Bond Pad	4.02 ± 0.02 ($25\,125 \pm 125$)	0.959 ± 0.005
	Strip Center	4.19 ± 0.01 ($26\,188 \pm 63$)	1
	Standard	1.385 ± 0.002 (8656 ± 13)	0.773 ± 0.004
RAL LS3 Irrad	Bond Pad	1.69 ± 0.02 ($10\,563 \pm 125$)	0.963 ± 0.011
	Strip Center	1.755 ± 0.004 ($10\,969 \pm 25$)	1

Table 4.5: Median charge values obtained from a skewed error function fit from the curves shown in Figure A.9. The ratio between each median charge and the one obtained for the same module by selecting tracks crossing at the center of a strip is also shown.

CHAPTER

5

SENSORS WITH ENLARGED ALUMINUM LAYER AND STRIP IMPLANT

In order to investigate the results discussed in Section 4.8.2, special mini-sensors were produced in the latest iteration of ATLAS ITk Strip sensors. These sensors comprise five zones with different layouts, including the default layout for the ATLAS ITk Strip Detector. The layouts differ in the width of the aluminum layer and strip implant. Several sensors were irradiated with protons, neutrons, and gamma-rays, in order to study independently the effects of surface and bulk damage.
The sensors are introduced in Section 5.1. Section 5.2 discusses the electrical characterization of non-irradiated and irradiated sensors. Section 5.2.1 discusses the results obtained with the default ATLAS layout. This Section introduces the experimental procedures used. In this Section it is also shown that the current sensors satisfy the ATLAS ITk Strip specifications for all the radiation types tested and for a wide range of radiation levels. Section 5.2.2 compares the electrical results obtained with the alternative layouts are to the ones obtained with the default ATLAS layout. The focus is on the study of the relationship between the sensor layout and the radiation damage mechanisms. Section 5.3 discusses test beam measurements performed with non-irradiated and proton-irradiated sensors. The results prove that the layout significantly affects the amount of charge sharing in irradiated sensors and hence their hit detection efficiency. An alternative layout which provides improved efficiency and satisfies the ATLAS ITk Strip specifications is identified.
Additional material to this Chapter is provided in Appendix B.

5.1 Introduction

Test beam measurements show that the efficiency in irradiated sensors is degraded by an enhanced charge sharing in the inter-strip region (see Section 4.8). This effect is mitigated by the wide implant coverage of the bond pads (see Section 4.8.2). In order to study this phenomenon in more detail, sensors with different layouts were implemented and produced in the first batch of ATLAS17LS sensor wafers. These sensors, called R&D sensors [153], comprise five different zones with different aluminum layer and strip implant widths (see Figure 5.1 and Table 5.1). Only configurations with an aluminum layer wider than the strip implant are chosen since the presence of a metal overhang mitigates electrical breakdown phenomena [156, 157].

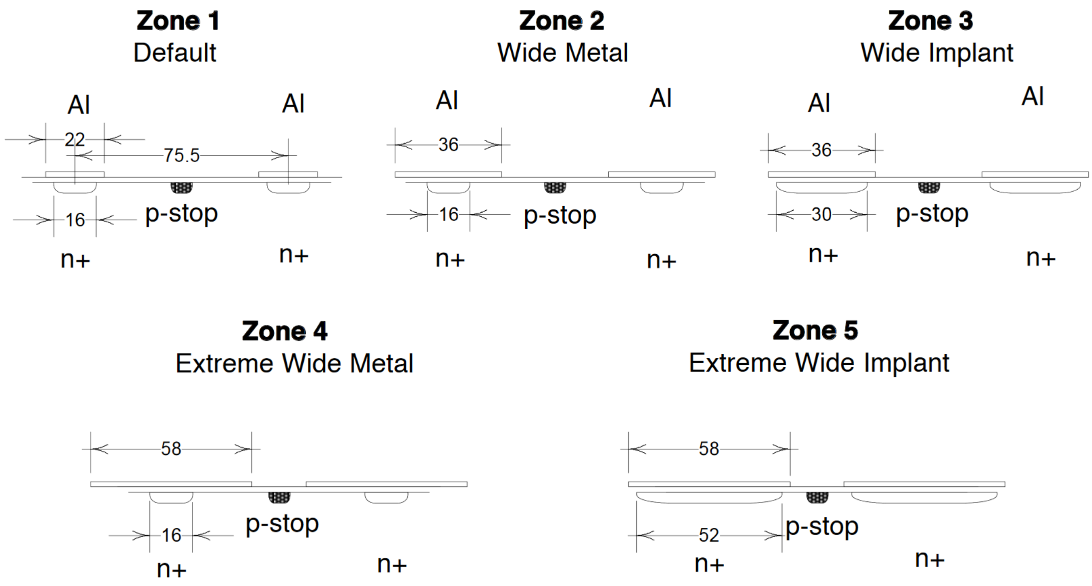

Figure 5.1: The five sensor layouts implemented in the R&D sensors (dimensions in µm).

Zone	Aluminum Width [µm]	Implant Width [µm]
Default ATLAS	22	16
Wide Metal	36	16
Wide Implant	36	30
Extreme Wide Metal	58	16
Extreme Wide Implant	58	52

Table 5.1: Aluminum and implant widths in the five zones of the R&D sensors.

Figure 5.2 shows a microscope picture of an R&D sensor. The zones comprise twenty strips each and they are separated by a grounded bias rail that crosses the sensor length. Except for the aluminum layer and strip implant widths, all the strips have the same characteristics, in particular:

- Strip pitch of 75.5 µm.
- Active thickness of about 300 µm.
- Full Depletion Voltage of about 300 V.

Sensors with three different strip lengths have been produced: 0.8 cm (mini-sensors), ~2.4 cm (Short Strip mini-sensors), and ~4.8 cm (Long Strip mini-sensors). A few sensors were produced with a reduced active thickness of ~260 µm (Thin sensors) [147].

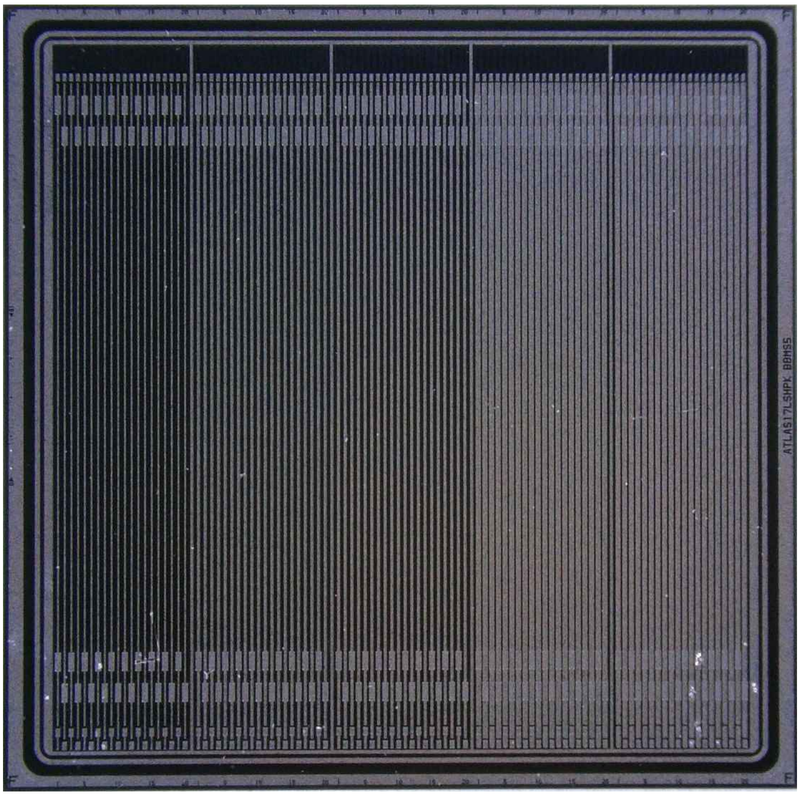

Figure 5.2: Microscope image of an R&D mini-sensor.

5.2 Electrical Characterization

Several sensors were irradiated with gamma-rays at UJP, with protons at KIT, and with neutrons at JSI (see Section 3.3). Several mini-sensors are characterized electrically with probe station measurements at the DESY campus in Zeuthen.

Figure 5.3 shows the probe station set-up used for the measurements. In a typical measurement, a mini-sensor placed on a cooling chuck is connected to a voltage source to provide the bias voltage to the sensor backplane. All the measurements discussed in this thesis are performed with a chuck temperature of −20 °C, the reference temperature for the ITk Strip specification on the inter-strip resistance of irradiated sensors [49]. The chamber containing the chuck is flushed with dry air in order to maintain a relative humidity of less than 5% and hence prevent condensation.

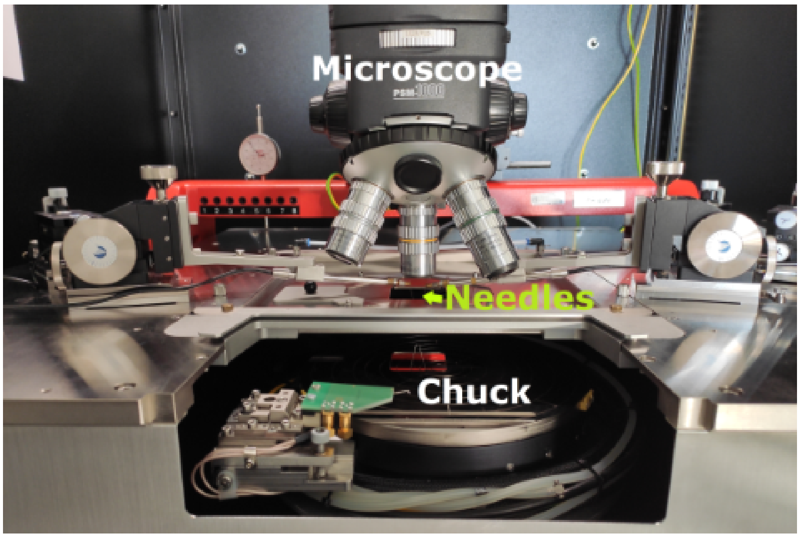

Figure 5.3: Probe station set-up at the DESY campus in Zeuthen. During the measurements, a mini-sensor is placed on the cooling chuck which also provides the bias voltage to the sensor backplane. A vacuum is applied through the cooling chuck in order to hold the mini-sensor in place. The probe needles are controlled manually with micromanipulators (on the right and on the left in the picture) and provide electrical contact between the pads on the surface of the mini-sensor and the devices used during the measurements (voltage sources, amperometer and LCR meter).

Figure 5.4 shows an image of a corner of an R&D mini-sensor. The passivation on the sensor surface has openings (pads) that can be used to access various sensor structures. The following pads have been exploited for the measurements discussed in this thesis:

- The bias ring pad, which is connected to the bias line that provides the ground potential to all the strip implants.
- The AC pads, which are connected to the aluminum layers.
- The DC pads, which are connected to the strip implants.

During the measurements, the pads are electrically connected by probe needles to a Source/Measure Unit (SMU) or to an LCR meter. A voltage difference is applied between the backplane, which is maintained at a negative voltage by the chuck, and the strip implants, which are maintained at ground potential by a probe needle in contact with the bias ring pad. Depending on the quantity that is being measured, additional pads are connected to an SMU or to the LCR meter.

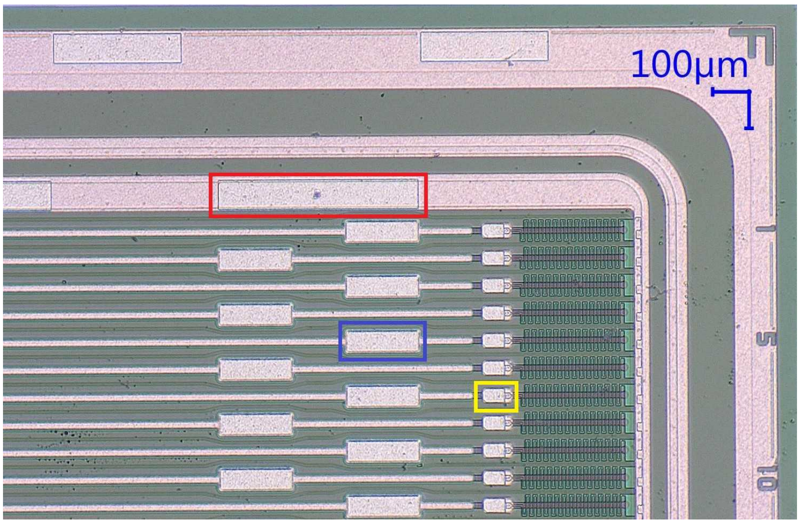

Figure 5.4: Microscope image of the corner of an R&D mini-sensor. The boxes highlight the pads used for electrical connection during the probe station measurements: the bias ring pad (red), an AC pad (also called bond pad, blue), and a DC pad (yellow).

The following SMUs and LCR meter are used to perform the measurements:

- Keithley 2410 SourceMeter to apply the bias voltage.
- Keithley 6485 Picoammeter to measure currents.
- Keithley 6487 Picoammeter/Voltage Source to apply the slave voltage in the interstrip resistance measurements (see Section 5.2.1).
- Agilent E4981A LCR meter to measure capacitances.

The SMUs and the LCR meter are controlled and read out by the LabView-based software MeasureSoft [158].

5.2.1 ATLAS ITk Strip Layout

Current-Voltage Characteristics

The leakage current is measured by applying a bias voltage to the sensor and measuring the current with an amperometer in series with the bias voltage source.
Figure 5.5 shows the current-voltage characteristics for several R&D mini-sensors. The mini-sensors irradiated with gamma-rays exhibit a leakage current larger than non-irradiated mini-sensors due to surface damage (see Section 2.6.2 and [159]). The leakage current increase caused by bulk damage is even larger (see Section 2.6.1). As expected from Equation 2.31, R&D mini-sensors irradiated with hadrons (protons and neutrons) to a comparable NIEL fluence exhibit a similar leakage current.

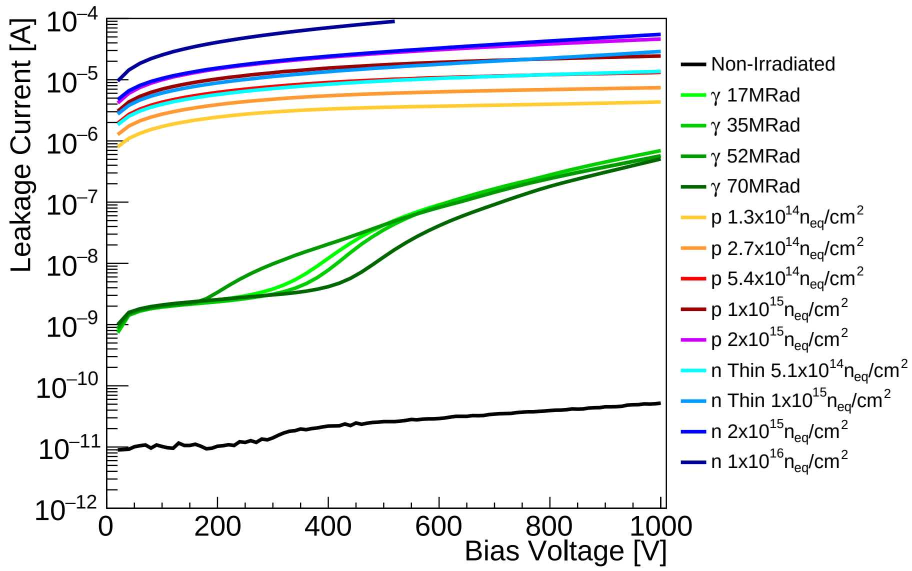

Figure 5.5: Current-voltage characteristics for several R&D mini-sensors. Results for sensors non-irradiated (black) and irradiated with gamma-rays (UJP, green), protons (KIT, red), and neutrons (JSI, blue) are shown. The measurement step size is 20 V.

Inter-Strip and Coupling Capacitance

The inter-strip capacitance is an important parameter since it is the dominant term to the load capacitance, which determines the noise of a silicon module (see Section 2.5). A low inter-strip capacitance is commonly preferred. The sensors for the ATLAS ITk Strip Detector are required to have an inter-strip capacitance lower than 1 pF cm^{-1} at a bias voltage of 300 V [49].
In this thesis, the inter-strip capacitance is defined as the capacitance between the aluminum layers of adjacent strips. The inter-strip capacitance is measured by contacting the AC pads of three adjacent strips with three probe needles. The probe needle in contact with the central strip is connected to one electrode of the LCR meter, while the other electrode is connected to the other two probe needles. In this way, the capacitance between the central strip and both neighboring strips is measured. At low frequencies the test signal would be shunted to ground through the bias resistor [160], the inter-strip capacitance measurements are then performed with the highest available LCR meter test frequency of 1 MHz. To maximize the signal recorded by the LCR meter, the highest LCR meter test amplitude of 1 V is chosen. The capacitance measured by the LCR meter is normalized by the strip length.

The coupling capacitance determines the coupling between the strip implants, where the signal generated by a particle is collected, and the front-end channels (see Section 2.4). A large coupling capacitance is commonly preferred. The sensors for the ATLAS ITk Strip Detector are required to have a coupling capacitance larger than 20 pF cm^{-1} [49].

The coupling capacitance is measured by contacting the AC and DC pads of the same strip with two probe needles connected to the two electrodes of the LCR meter. The measurements are performed with a test frequency of 1 kHz and a test amplitude of 1 V. A lower test frequency is chosen with respect to inter-strip capacitance measurements because at high frequencies only a small fraction of the strip implant would contribute to the coupling capacitance [160]. The capacitance measured by the LCR meter is normalized by the strip length.

Figure 5.6 shows the inter-strip and coupling capacitances measured in the default ATLAS zone for several non-irradiated and irradiated R&D mini-sensors. All the mini-sensors tested satisfy the ATLAS ITk Strip specifications[1]. The average inter-strip and coupling capacitances are $0.747 \pm 0.004\,\mathrm{pF\,cm^{-1}}$ and $24.28 \pm 0.14\,\mathrm{pF\,cm^{-1}}$, respectively (see Appendix B.3). For bias voltages of interest for the ITk Strip Detector (> 300 V) both quantities do not depend on the bias voltage. However, for lower bias voltages the inter-strip capacitance of non- and gamma-irradiated sensors exhibit large variations. A similar behavior has been observed in other studies [83, 161] and it is related to the depletion conditions in the inter-strip region [162]. No significant dependence on the radiation dose or type is visible for bias voltages of interest for the ITk Strip Detector. The deviation between measurements is comparable with strip-by-strip variations.

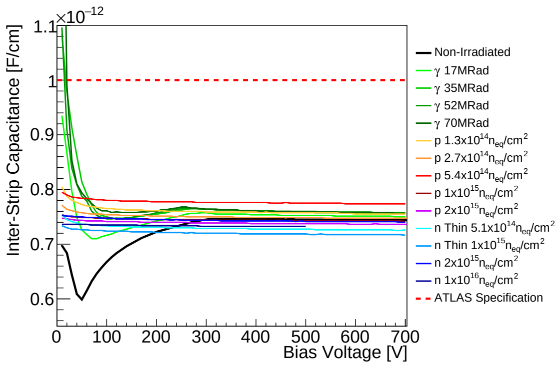

(a) Inter-strip capacitance as a function of the bias voltage. The red dashed line indicates the upper limit specified for the ATLAS ITk Strip Detector.

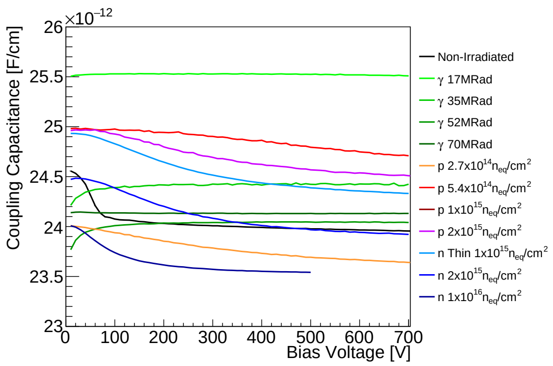

(b) Coupling capacitance as a function of the bias voltage.

Figure 5.6: Inter-strip and coupling capacitance measured in the default ATLAS zone as a function of the bias voltage for several R&D mini-sensors non-irradiated (black) and irradiated with gamma-rays (UJP, green), protons (KIT, red), and neutrons (JSI, blue). The measurement step size is 10 V.

[1]The ATLAS ITk Strip specification for the inter-strip capacitance is defined for a test frequency of 100 kHz while the measurements described in this Chapter are performed with a test frequency of 1 MHz. However, previous studies show that the inter-strip capacitance is constant for test frequencies larger than 50 kHz [128].

Inter-Strip Resistance

The inter-strip resistance is related to the strip isolation and it is strongly affected by surface damage, since it is very sensitive to the characteristics of oxide charge and electron accumulation layer [60]. A large inter-strip resistance is commonly preferred. The sensors for the ATLAS ITk Strip Detector are required to have an inter-strip resistance larger than 20 $M\Omega$ cm at a bias voltage of 400 V [49]. The inter-strip resistance is measured by contacting the DC pads of two adjacent strips with two probe needles. One probe needle is connected to an additional voltage source and the other is maintained at ground potential and is connected to an amperometer. A small voltage, called slave voltage, is applied on the first probe needle, while the current flowing between the two strips is measured using the second probe needle. This procedure is repeated for several slave voltage values between −2.5 V and 2.5 V. A linear fit is performed on the curve obtained in this way in order to retrieve the inter-strip resistance (see Figure 5.7a):

$$I_{\text{inter-strip}}(V_{\text{slave}}) = a + bV_{\text{slave}} = I_{\text{leakage}} + \frac{1}{R_{\text{inter-strip}}} V_{\text{slave}} \tag{5.1}$$

where a and b are the fit parameters, I_{leakage} the leakage current of the strip connected to the amperometer, and $R_{\text{inter-strip}}$ the inter-strip resistance. The inter-strip resistance obtained with the fit is normalized by the strip length.

Figure 5.7b shows the inter-strip resistance measured in the default ATLAS zone as a function of the bias voltage for several non-irradiated and irradiated R&D mini-sensors. All the mini-sensors satisfy the ATLAS ITk Strip specification at 400 V. Before irradiation, the inter-strip resistance is larger than 10 $G\Omega$ cm and does not depend on the bias voltage applied. Radiation damage decreases significantly the inter-strip resistance. The gamma-irradiated mini-sensors (10-100 $M\Omega$ cm at 400 V) exhibit an inter-strip resistance lower than the hadron-irradiated ones (1 $G\Omega$ cm). A similar effect has been observed by other studies [115] and it is explained by the mitigation of the detrimental effects of surface damage by bulk damage[2]. A possible explanation for this effect is that the negative space charge in the silicon bulk compensates the positive oxide charge generated by surface damage (see Section 2.6.2) and thus it suppresses the accumulation of electrons at the Si-SiO_2 interface [163].
The neutron- and proton-irradiated sensors exhibit a comparable inter-strip resistance. For gamma-irradiated sensors the inter-strip resistance increases exponentially with the bias voltage, while for proton- and neutron-irradiated sensors it saturates at high bias voltages. It can then be speculated that in presence of both surface and bulk damage, the inter-strip resistance depends primarily on the latter (see Appendix B.5 for more information).

[2]As explained in Section 3.3, gamma-rays mainly generate surface damage, neutrons mainly generate bulk damage, and protons generate both bulk and surface damage.

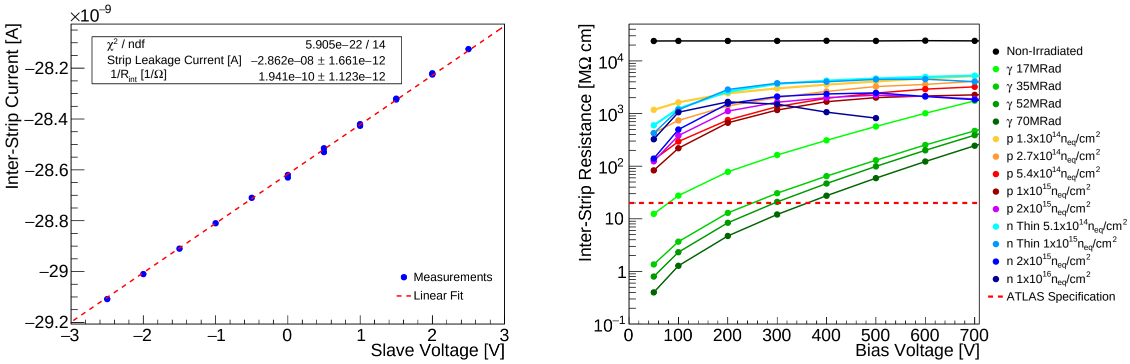

(a) Example of inter-strip measurement procedure.

(b) Inter-strip resistance as a function of the bias voltage. The red dashed line indicates the lower limit specified for the ATLAS ITk Strip Detector.

Figure 5.7: Example inter-strip resistance measurement procedure and inter-strip measurements in the default ATLAS zone for several R&D mini-sensors non-irradiated (black) and irradiated with gamma-rays (UJP, green), protons (KIT, red), and neutrons (JSI, blue).

5.2.2 Alternative Layouts

Leakage Current

With the inter-strip resistance measurement procedure it is possible to obtain the leakage current of a single strip. In this way, the leakage current of strips in each zone of the R&D sensors can be investigated. Figures 5.8a and 5.8b show the current-voltage characteristics for single strips in the five zones of hadron-irradiated R&D mini-sensors. No difference is visible between the results from different zones. For each mini-sensor the leakage current measured in each zone differs by less than 6% to the one measured in the default ATLAS zone. This is explained by the fact that the leakage current depends mainly on bulk effects and the bulk is the same in all the R&D sensor zones. The leakage current does not depend on the aluminum layer or strip implant widths.

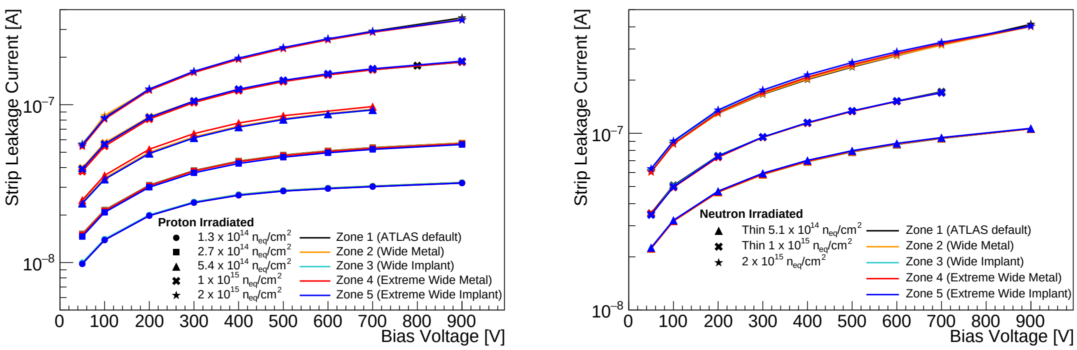

(a) Proton (KIT) irradiated R&D mini-sensors.

(b) Neutron (JSI) irradiated R&D mini-sensors.

Figure 5.8: Current-voltage characteristics measured for single strips in the five zones of hadron-irradiated R&D mini-sensors. Different colors refer to different zones and different markers refer to different radiation levels.

Inter-Strip and Coupling Capacitance

Figure 5.9a shows the inter-strip capacitance as a function of the bias voltage in the five zones of a non-irradiated R&D mini-sensor. For bias voltages > 300 V the inter-strip capacitance is constant.

Figure 5.9b shows the coupling capacitance measured at 500 V in the five zones of a non-irradiated mini-sensor, normalized to the value measured in the default ATLAS zone. The zones with only a wide aluminum layer, Zone 2 (Wide Metal) and Zone 4 (Extreme Wide Metal), exhibit an inter-strip capacitance larger than in the default ATLAS zone by 25% and 100%, respectively. In the corresponding zones with an enlarged strip implant, Zone 3 (Wide Implant) and Zone 5 (Extreme Wide Implant), the inter-strip capacitance is further increased by about 10%. The inter-strip capacitance depends primarily on the aluminum layer width.

Additionally to the default ATLAS zone, also Zone 2 (Wide Metal) satisfies the ATLAS ITk Strip specification, which makes it a potential alternative to the default ATLAS layout. The specification is not satisfied by the other zones. Measurements with irradiated R&D mini-sensors are in agreement with these results and are shown in Appendix B.8.

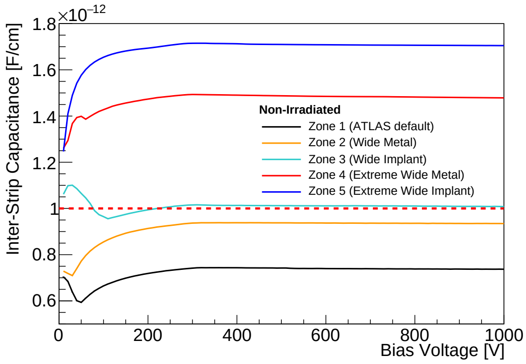

(a) Inter-strip capacitance as a function of the bias voltage. The measurement step size is 10 V. The red dashed line indicates the upper limit specified for the ATLAS ITk Strip Detector

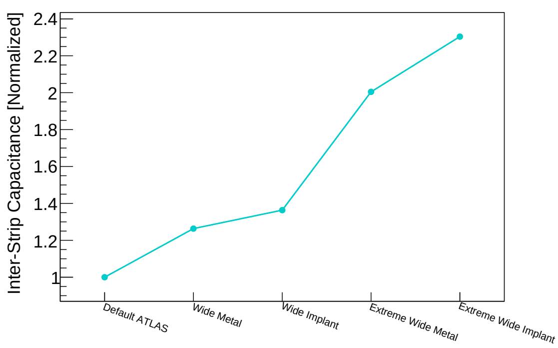

(b) Inter-strip capacitance with a bias voltage of 500 V, normalized to the value obtained in the default ATLAS zone. The lines connecting the data points are added for visibility.

Figure 5.9: Inter-strip capacitance in the five zones of a non-irradiated R&D mini-sensor.

Figure 5.10a shows the coupling capacitance as a function of the bias voltage in the five zones of a non-irradiated R&D mini-sensor. For bias voltages > 300 V the coupling capacitance is constant.

Figure 5.10b shows the inter-strip capacitance measured at 500 V in the five zones of a non-irradiated mini-sensor, normalized to the value measured in the default ATLAS zone. The zones where both the aluminum layer and strip implant widths are increased, Zone 3 (Wide Implant) and Zone 5 (Extreme Wide Implant), exhibit a coupling capacitance larger than in the default ATLAS zone by 60% and 160%, respectively. The zones where only the aluminum layer is enlarged, Zone 2 and Zone 4, exhibit only

a marginal (< 5%) increase with respect to the default ATLAS zone. The coupling capacitance is defined by the overlap width between the aluminum layer and the strip implant and it is not significantly affected by a wider aluminum overhang.
All five zones satisfy the ATLAS ITk Strip specification. Measurements with irradiated R&D mini-sensors are in agreement with these results and are shown in Appendix B.9.

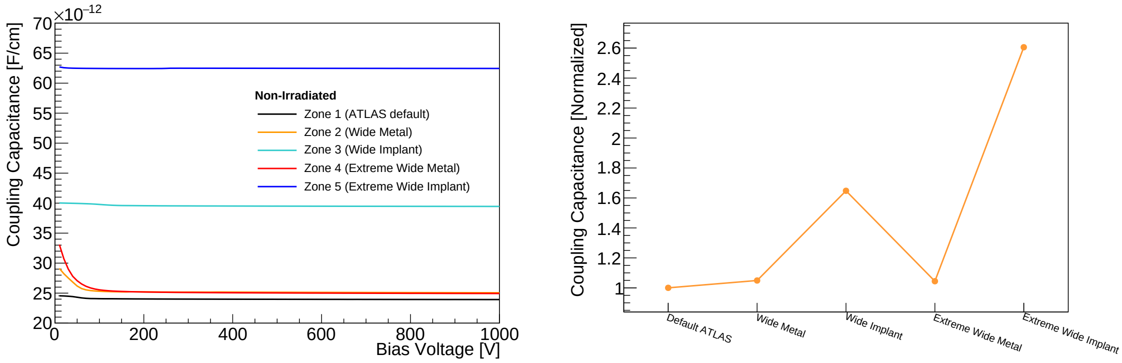

(a) Coupling capacitance as a function of the bias voltage. The measurement step size is 10 V.

(b) Coupling capacitance with a bias voltage of 500 V, normalized to the value obtained in the default ATLAS zone. The lines connecting the data points are added for visibility.

Figure 5.10: Coupling capacitance in the five zones of a non-irradiated R&D mini-sensor.

Inter-Strip Resistance

Figure 5.11a shows the inter-strip resistance as a function of the bias voltage in the five zones of an R&D mini-sensor irradiated with gamma-rays to a TID of 52 MRad (520 kGy). All five zones satisfy the ATLAS ITk Strip specification at 400 V.
The zones with an enlarged aluminum layer and narrow strip implant (Zone 2 and Zone 4) exhibit an inter-strip resistance more than 50% larger than in the default ATLAS zone. This is explained by the fact that the metal overhang modifies the electric field lines close to the silicon surface. In this way, the metal overhang suppresses the electron accumulation layer and depletes its underlying region [164], thus improving the isolation between adjacent strips. A wide aluminum layer therefore mitigates some of the detrimental effects of surface damage.
In the zones with both aluminum layer and implant enlarged (Zone 3 and Zone 5), the inter-strip resistance is comparable or lower than in the default ATLAS zone. Apparently, this can look as a wide strip implant enhances the surface damage effects. However, in these zones a decrease of inter-strip resistance is expected because of geometrical reasons. The strip implants are closer to each other with respect to the strip implants in the default ATLAS region. The measured inter-strip resistance is determined by two competing factors: for wider strip implants it should increase due to mitigation of the surface damage effects and it should decreases due to the implant

geometry. The results for these zones then can not be interpreted in a conclusive way. Figure 5.11b shows the inter-strip resistance normalized to the values obtained in the default ATLAS zone, as a function of the bias voltage. The lower the bias voltage, the more significant the effect of an enlarged aluminum layer or strip implant is. This effect is particularly visible for Zone 4 (Extreme Wide Metal), in which for every bias voltage the inter-strip resistance is larger than in the default ATLAS zone by at least a factor 2. This effect is less pronounced for gamma-irradiated sensors subject to a lower TID (see Appendix B.10).

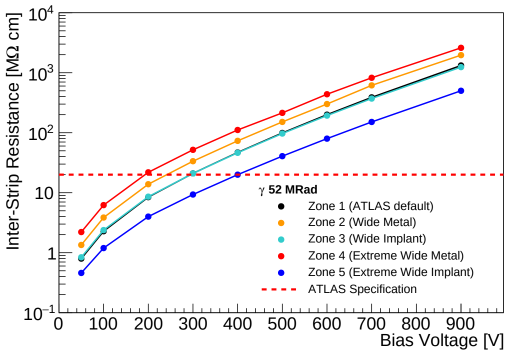

(a) Inter-strip resistance as a function of the bias voltage.

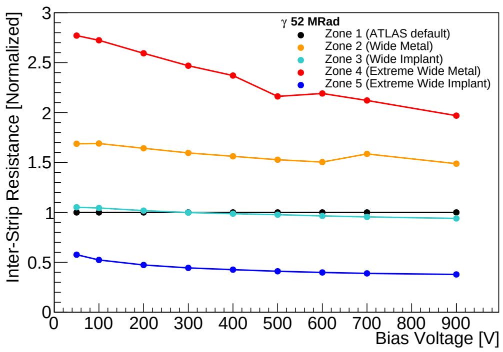

(b) Inter-strip resistance, normalized to the values obtained in the default ATLAS zone, as a function of the bias voltage.

Figure 5.11: Inter-strip resistance in the five zones of an R&D mini-sensor irradiated with gamma-rays (UJP) at a TID of 52 MRad (520 kGy).

Figures 5.12 and 5.13 show the inter-strip resistance as a function of the bias voltage in the five zones of R&D mini-sensors irradiated with protons (KIT) and neutrons (JSI) at a NIEL fluence of $2 \times 10^{15}\ \mathrm{n_{eq}/cm^2}$. All five zones satisfy the ATLAS ITk Strip specification at 400 V.

For proton and neutron irradiated sensors the relationship between the inter-strip resistance measured in different zones is in qualitative agreement (Figure 5.12b and 5.13b), but it differs significantly from the one measured for gamma-irradiated sensors (Figure 5.11b). This is a further evidence that in presence of both surface and bulk damage, the latter is the dominant factor that determines the inter-strip resistance behavior.

For bias voltages > 300 V the inter-strip resistance in all the zones with an alternative layout is generally smaller than in the default ATLAS zone by up to a factor 2. Since in hadron-irradiated sensors the inter-strip resistance is defined primarily by bulk properties, a reduction is expected in the zones with alternative layouts because of geometrical considerations. However, this does not necessarily prove that surface damage effects are not present, since this information may be concealed in the inter-strip resistance measurements by the dominant contribution of the bulk damage.

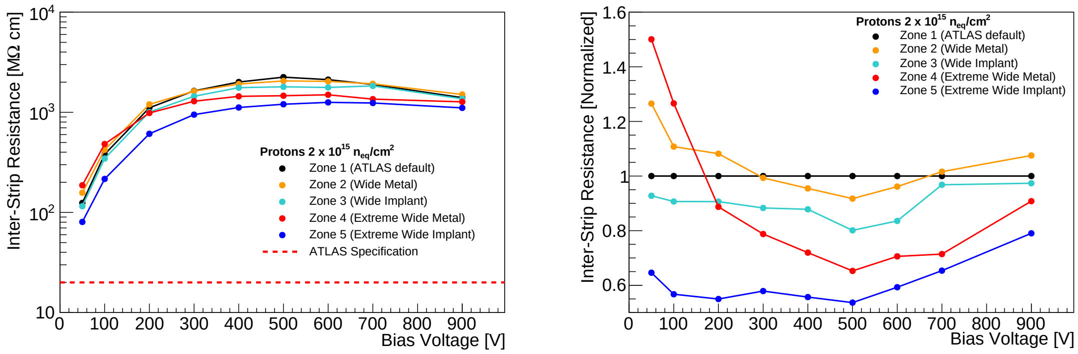

(a) Inter-strip resistance as a function of the bias voltage.

(b) Inter-strip resistance, normalized to the values obtained in the default ATLAS zone, as a function of the bias voltage.

Figure 5.12: Inter-strip resistance in the five zones of an R&D mini-sensor irradiated with protons (KIT) at a NIEL fluence of $2 \times 10^{15}\ \mathrm{n_{eq}/cm^2}$.

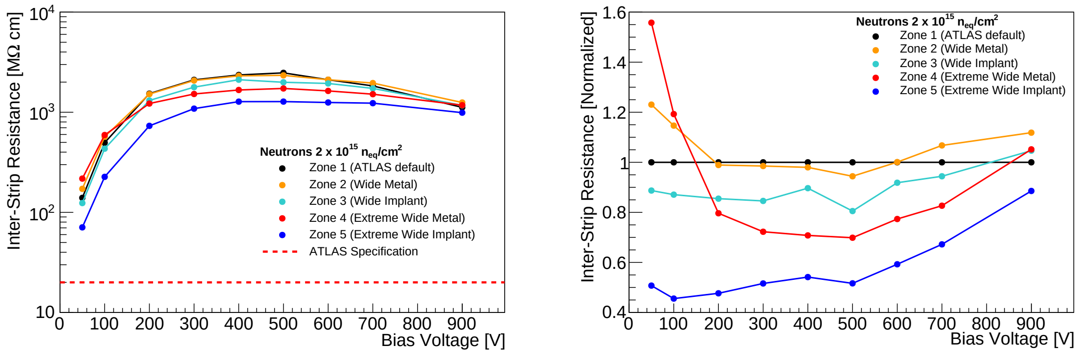

(a) Inter-strip resistance as a function of the bias voltage.

(b) Inter-strip resistance, normalized to the values obtained in the default ATLAS zone, as a function of the bias voltage.

Figure 5.13: Inter-strip resistance in the five zones of an R&D Thin mini-sensor irradiated with neutrons (JSI) at a NIEL fluence of $2 \times 10^{15}\ \mathrm{n_{eq}/cm^2}$.

5.3 Test Beam Measurements

Test beam measurements are necessary to understand the effect of the aluminum layer and strip implant widths on the charge collection and charge sharing. A mini-module (also called DAQload) was built at the DESY campus in Zeuthen using an end-cap R0 H1 hybrid and five R&D Short Strip mini-sensors wire-bonded to five ABC130 front-end chips. Figure 5.14 shows a picture of the mini-module. Four of the five sensors were irradiated with protons at KIT (NIEL fluences of 2.7×10^{14}, 5.4×10^{14}, and $1 \times 10^{15}\ \mathrm{n_{eq}/cm^2}$), while the last sensor was non-irradiated. Sensors subject to proton irradiation were used, since it is the most similar to the radiation environment in the

ATLAS ITk Strip Detector. The irradiated sensors had been annealed at 60 °C for 80 minutes in order to exploit the effects of beneficial annealing (see Section 2.6.1).

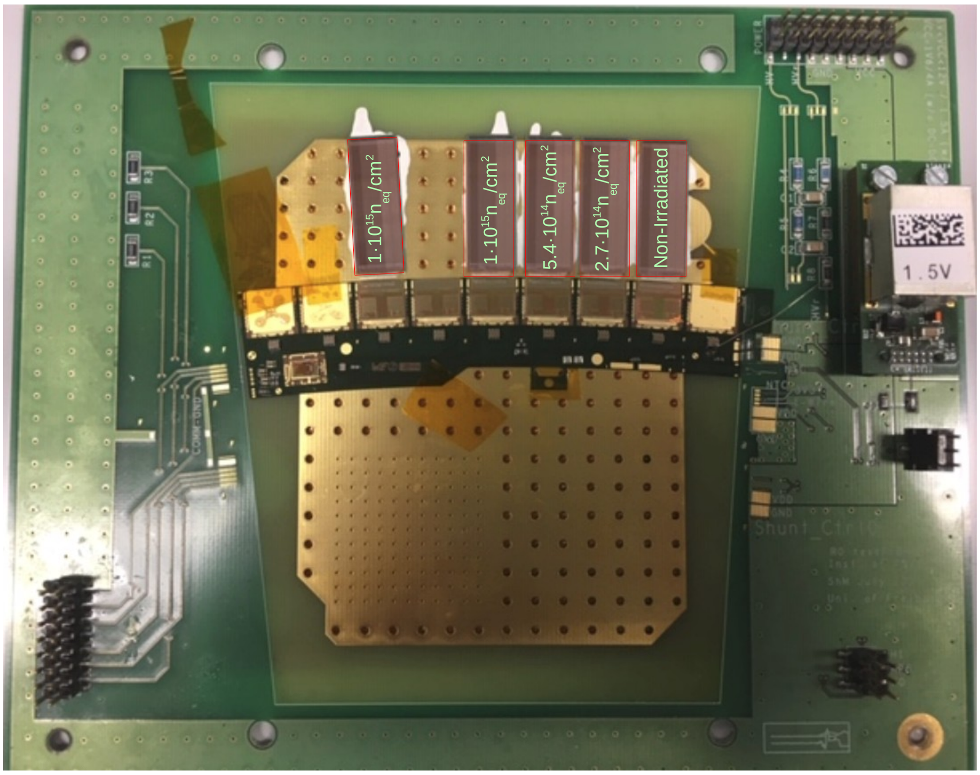

Figure 5.14: Mini-module (DAQload) with R&D Short Strip mini-sensors tested in the June 2019 test beam. The hybrid hosts six ABC130 chips, which are wire-bonded to five R&D Short Strip mini-sensors. One mini-sensor was non-irradiated and the other four were irradiated with protons (KIT) to NIEL fluences in the range 2.7-10 × 10^{14} n_{eq}/cm^2.

The mini-module was tested at DESY during the June 2019 ITk Strip test beam (see Section 4.1). The measurements are performed with a bias voltage of 500 V (the baseline to be used in the ITk Strip Detector at the end of lifetime of the HL-LHC) and using the cooling set-up for irradiated modules discussed in Section 4.2. A beam energy of 5 GeV is selected and a collimation size of 2x1 cm^2 is used, in order to maximize the beam spot coverage on the mini-sensors.

The analysis procedure is described in Sections 4.3 and 4.4. The front-end channels wire-bonded to the sensors exhibit common-mode noise with magnitude of about 1500 e (0.24 fC). The common mode noise is generated in the large unshielded area used to apply the bias voltage to the sensor backplanes (gold area in Figure 5.14). The common mode noise generates some events with a very large channel occupancy. In order to mitigate this effect on the results, an additional event selection is applied in the analysis procedure: events with more than five hits in the sensor under test are discarded.

5.3.1 Results

Figure 5.15 shows the efficiency and cluster size as a function of the threshold in the five zones of the non-irradiated R&D Short Strip mini-sensor. The results in the five zones are compatible within uncertainties with some larger discrepancies that can be attributed to imprecisions of the threshold calibration procedure (see Section 4.4.1).

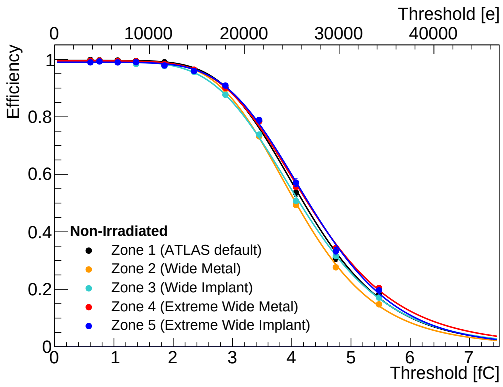

(a) Efficiency as a function of the threshold.

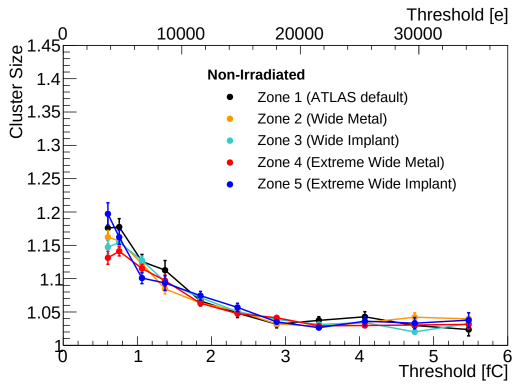

(b) Cluster size as a function of the threshold.

Figure 5.15: Efficiency and cluster size as a function of the threshold in the five zones of the non-irradiated R&D Short Strip mini-sensor.

Figures 5.16a, 5.17a, and 5.18a show the efficiency as a function of the threshold in the five zones of the proton (KIT) irradiated R&D Short Strip mini-sensor. In this case, efficiency and cluster size exhibit significant differences between the different zones. The efficiency is mostly determined by the aluminum layer width: the wider the aluminum layer, the larger the efficiency. For a given aluminum layer width, an enlarged strip implant further increases the efficiency although only by a small amount.

The larger efficiency in the zones with wide aluminum layer and strip implant is explained by a reduced charge sharing. This effect is visible only in irradiated sensors, it can be then attributed to a mitigation of the charge division mechanism discussed in Section 4.8 which is also observed only in irradiated devices.

Figures 5.16b, 5.17b, and 5.18b show the cluster size as a function of the threshold in the five zones of the proton (KIT) irradiated R&D Short Strip mini-sensors. At low thresholds[3] the cluster size in the zones with an alternative layout is smaller than in the default ATLAS zone. In particular, the cluster size at low threshods depends mostly on the aluminum layer width: the wider the aluminum layer, the smaller the cluster size at low thresholds. For a given aluminum layer width, an enlarged strip implant decreases the cluster size at low thresholds only by a marginal amount, similarly to the efficiency.

[3] Charge sharing mechanisms that affect the charge carrier propagation only influence the cluster size at low thresholds (see Section 4.3.2).

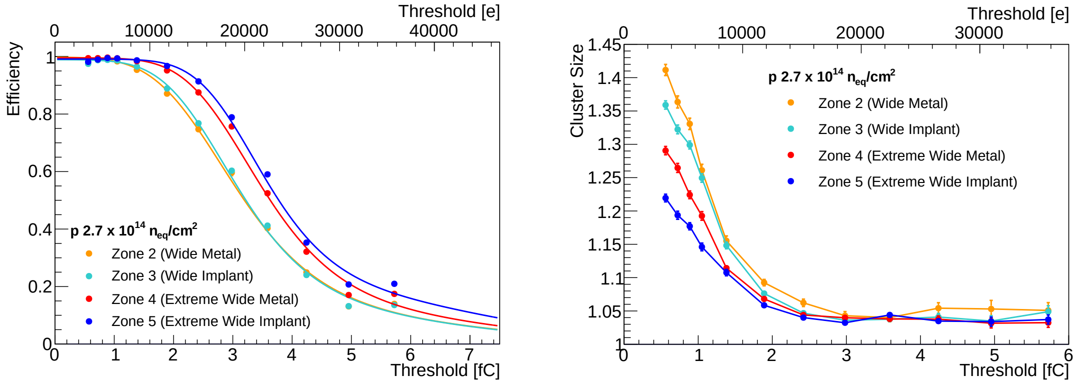

(a) Efficiency as a function of the threshold. (b) Cluster size as a function of the threshold.

Figure 5.16: Efficiency and cluster size as a function of the threshold in four zones of the R&D Short Strip mini-sensor irradiated with protons (KIT) at a NIEL fluence of $2.7 \times 10^{14}\ \mathrm{n_{eq}/cm^2}$. No measurements are shown for the default ATLAS zone because of a misalignment of the mini-sensor with respect to the beam spot during the data-taking.

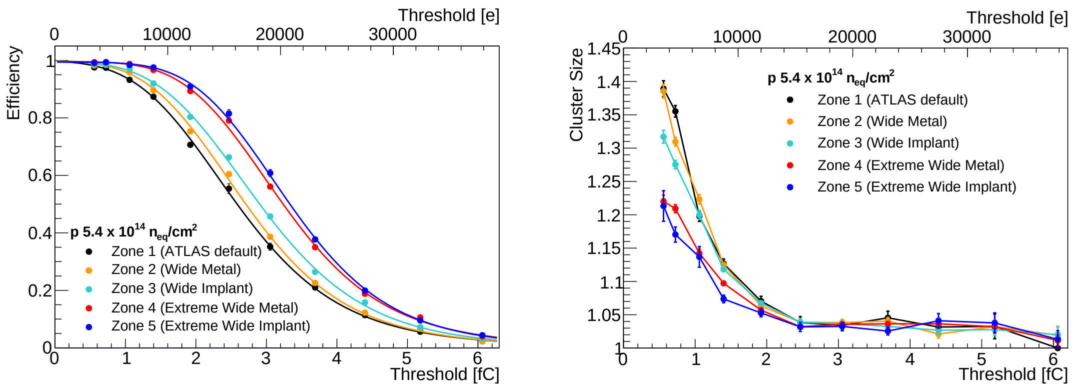

(a) Efficiency as a function of the threshold. (b) Cluster size as a function of the threshold.

Figure 5.17: Efficiency and cluster size as a function of the threshold in the five zones of the R&D Short Strip mini-sensor irradiated with protons (KIT) at a NIEL fluence of $5.4 \times 10^{14}\ \mathrm{n_{eq}/cm^2}$.

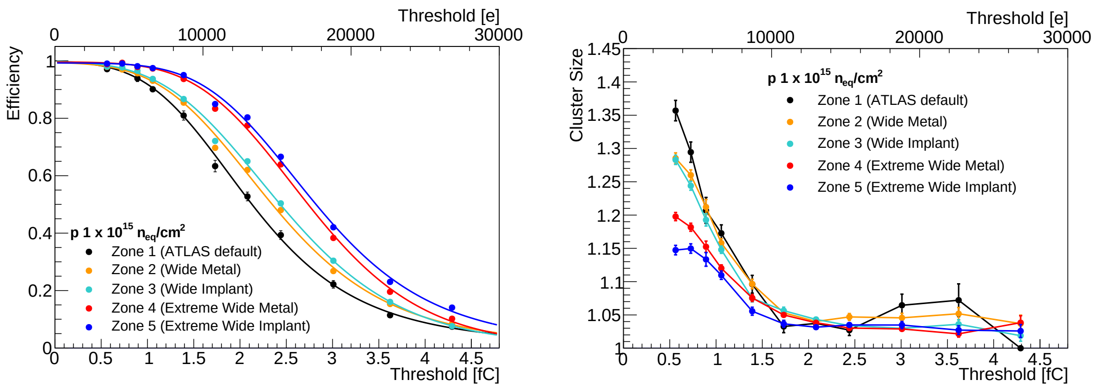

(a) Efficiency as a function of the threshold. (b) Cluster size as a function of the threshold.

Figure 5.18: Efficiency and cluster size as a function of the threshold in the five zones of an R&D Short Strip mini-sensor irradiated with protons (KIT) at a NIEL fluence of $1 \times 10^{15}\ \mathrm{n_{eq}/cm^2}$ (the second sensor from the left in Figure 5.14).

Table 5.2 summarizes the median charge for non-irradiated and irradiated R&D mini-sensors obtained by fitting with a skewed error function (see Section 4.3.1) the s-curves shown in Figures 5.15a, 5.16a, 5.17a, and 5.18a. The median charge in the zones with a wide aluminum layer (Zone 2 and Zone 3) is 11% larger than in the default ATLAS zone (Zone 1), while in the zones with an extreme wide aluminum layer (Zone 4 and Zone 5) it is 29% larger than in the default ATLAS zone (Zone 1). For a given aluminum layer width, the presence of a wide strip implant increases the median charge by 4%.

NIEL Fluence	Zone 1 [fC] ([e])	Zone 2 [fC] ([e])	Zone 3 [fC] ([e])	Zone 4 [fC] ([e])	Zone 5 [fC] ([e])
Non-Irradiated	4.21 ± 0.03 (26319 ± 169)	4.08 ± 0.02 (25506 ± 106)	4.15 ± 0.02 (25931 ± 113)	4.28 ± 0.02 (26769 ± 119)	4.30 ± 0.03 (26900 ± 175)
$2.7 \times 10^{14}\ n_{eq}/cm^2$		3.20 ± 0.02 (19994 ± 119)	3.24 ± 0.01 (20238 ± 88)	3.64 ± 0.02 (22744 ± 94)	3.79 ± 0.02 (23681 ± 100)
$5.4 \times 10^{14}\ n_{eq}/cm^2$	2.58 ± 0.02 (16150 ± 131)	2.71 ± 0.01 (16925 ± 81)	2.91 ± 0.01 (18163 ± 81)	3.24 ± 0.01 (20263 ± 88)	3.34 ± 0.02 (20881 ± 131)
$1 \times 10^{15}\ n_{eq}/cm^2$	2.13 ± 0.02 (13325 ± 150)	2.36 ± 0.01 (14719 ± 81)	2.44 ± 0.01 (15225 ± 69)	2.73 ± 0.01 (17131 ± 69)	2.83 ± 0.02 (17694 ± 94)

Table 5.2: Median charge in the five zones of non-irradiated and irradiated R&D Short Strip mini-sensors obtained by fitting with a skewed error function the curves in Figures 5.15a, 5.16a, 5.17a, and 5.18a. The uncertainties are taken from the fit.

The implementation of a wide aluminum layer or strip implant significantly improves the efficiency of irradiated devices by reducing the charge sharing mechanisms caused by surface damage. This is explained by the fact that the aluminum overhang depletes its underlying region from the electron accumulation layer thus decoupling the strip implants [164,165]. This effect is confirmed by the inter-strip resistance measurements performed with gamma-irradiated sensors (Section 5.2.2).

The results discussed in this Section prove that by implementing a wide aluminum layer and strip implant, the leading strip charge collection can be substantially increased, thus improving the radiation-hardness of a sensor. The aluminum layer has an effect on the leading strip charge collection comparable to the strip implant. The aluminum layer width, however, has a smaller effect on the electrical characteristics of a sensor than the strip implant width. By using a slightly increased metal overhang width it is possible to enhance the leading strip charge collection, and hence the hit detection efficiency, while not significantly deteriorating the electrical properties of a sensor. In particular, Zone 2 (Wide Metal) of the R&D mini-sensors satisfies all the ATLAS ITk Strip specifications, but it additionally provides a median charge about 10% larger than the default ATLAS layout. This result can be exploited for the design of future radiation-hard strip sensors.

The results also show that it is possible to manipulate directly the charge sharing of irradiated sensors by modifying the width of the sensor structures. A possible application is the implementation of a very narrow aluminum layer and strip implant, in order to maximize the charge sharing and thus the spatial resolution provided by the sensor.

CHAPTER

6 BEAM-INDUCED BACKGROUND IN THE SEMICONDUCTOR TRACKER

Chapters 4 and 5 focus on the performance of single modules for the future Inner Tracker. However, several other elements affect the performance of a tracker, both related to the detector itself or to external factors. This Chapter discusses a background directly generated by the beam: the Beam-Induced Background. An online monitoring system is developed to monitor in real time the effects of this background in the Semiconductor Tracker (SCT), the current strip detector described in Section 1.2.1. The online monitoring system is implemented in the ATLAS software Athena and was operational during part of the Run 2 data-taking of the ATLAS Experiment.
Section 6.1 introduces the Beam-Induced Background and its effects observed on the hit multiplicity of the SCT are described in Section 6.2, with a focus on the properties needed to understand the online monitoring system. Section 6.3 introduces the timing property of the Beam-Induced Background, one of its main signature which is exploited in the online monitoring system. In Section 6.4 the event selection of the online monitoring system is explained. The online histograms and their purposes are described in detail in Section 6.4.1.

6.1 Beam-Induced Background

The Non-Collision Background (NCB) is formed by hits that are not created by particle tracks generated by proton-proton collisions. Its most important sources are the electronic noise, cosmic rays and the interaction of the beam with the environment. The latter is usually called Beam-Induced Background (BIB) and has two main origins [166]:

- Deflection of beam protons due to scattering with gas molecules in the beam pipe (beam gas events).

- Secondary particles generated by the interaction of beam halo protons with the beam collimators (beam halo events).

Beam halo events have origin in the tertiary collimators that are located at a distance of 145-148 m from the interaction point [167]. Figure 6.1 shows an event of this type. Beam halo events are generated at fixed locations, while the beam gas events can occur anywhere in the beam pipe and their rate is proportional to the local pressure of the gas [167].

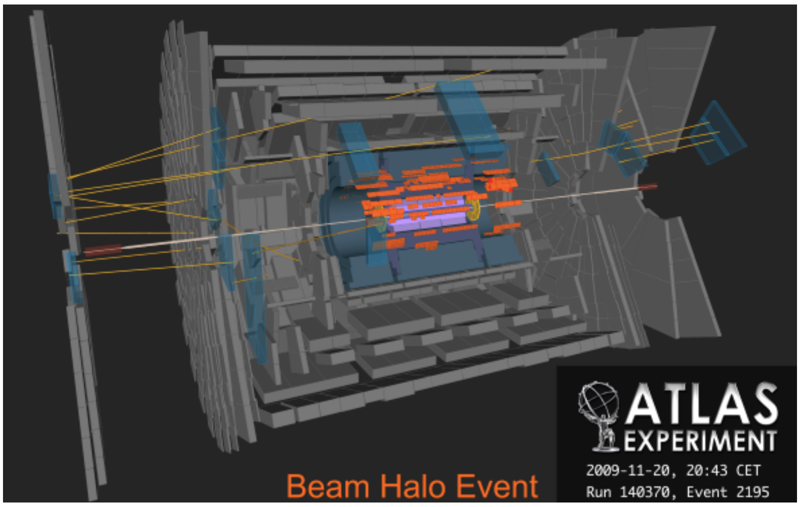

Figure 6.1: Event display of a beam halo event in 2009 [168].

The BIB can significantly affect the data from the ATLAS Detector. Events with a large BIB component can produce a large hit occupancy in the sub-detectors that can affect the track reconstruction in the Inner Detector [169]. Moreover, BIB particles can create fake high-energy jets in the calorimeters which can be mis-identified as signatures of new physics processes [169]. This affects in particular analyses that exploit monojet signatures [170–172].

To analyze the BIB it is crucial to distinguish it from collision events which generate a larger number of hits. Unpaired isolated bunches are usually exploited for this purpose. An unpaired isolated bunch does not have a corresponding bunch in the other beam within three Bunch Crossing Identification numbers (BCID), which correspond to 75 ns. No collisions should take place when these bunches cross the interaction point. However, because of the so-called ghost charge, protons outside the nominally filled bunches, a small number of collisions can happen. The ghost charge can be formed in the beam injectors or because of debunching in the LHC [166]. The isolation criterion ensures that the event is unlikely to contain a collision generated by ghost charge. Such collisions generate at least a primary vertex detectable by the track reconstruction, and this can be used to further discard events with ghost charge collisions.

The LHC filling scheme used to contain two unpaired bunches preceding the colliding bunches train [173]. Some of these bunches were isolated as well. Starting from 2017 the number of colliding bunches was increased and the two unpaired bunches in front of the trains are now closer to each other, reducing the number of isolated bunches. To increase the statistics available for the analysis of the BIB, it is now advantageous to consider non-isolated bunches.

6.2 Hit Multiplicity

Most of the BIB particles are generated far from the interaction point, either in the collimators or in the beam pipe. The BIB particles that reach the Inner Detector must have trajectories with very small angles with respect to the beam. For this reason, these particles will usually cross both end-caps, while the probability of crossing the barrel layers is much lower. The end-caps are then the best choice for the BIB analysis in the SCT.

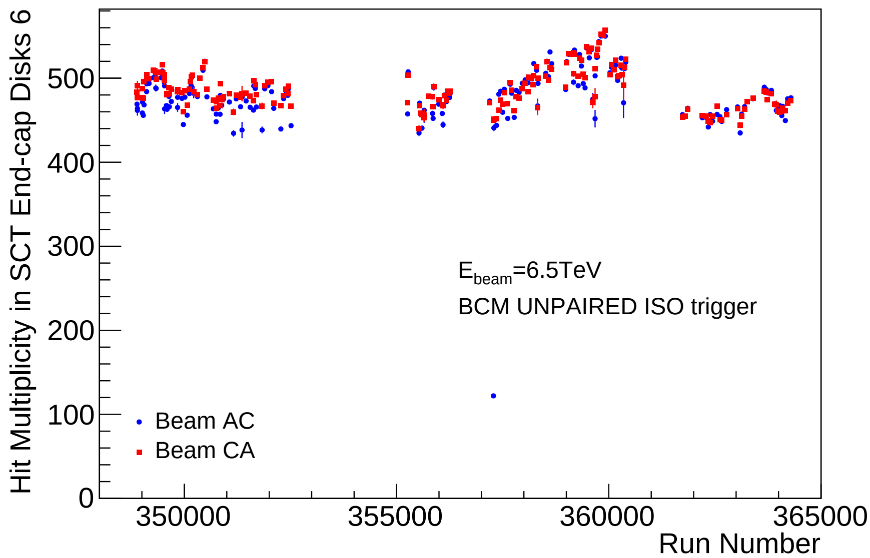

Figure 6.2: Average hit multiplicity on disk 6 of the SCT end-caps in events with a BCM unpaired isolated trigger (see Section 6.4), for every run in 2018. Only events in the Good Run List [174] and with no primary vertices are considered. The last requirement is set to discard events with ghost charge collisions.

The BIB can affect the performance of the SCT by increasing its hit occupancy. It is important to monitor the BIB in the SCT. Figure 6.2 shows the hit multiplicity on disk 6 of the end-caps for unpaired bunches, for all the runs in 2018. Small variations are observed between different runs which are explained by different beam conditions. The beam that travels from end-cap C to end-cap A (beam CA) exhibits a hit multiplicity 0.7% larger than the beam in the other direction (beam AC) a very marginal difference that is not significant for monitoring purposes.

Figure 6.3 shows the average hit multiplicity on disk 6 of the SCT end-caps in run 336506 as a function of time, expressed in the form of luminosity block number (LumiBlock). A LumiBlock lasts about 60 s [175]. In this run the gas pressure inside the beam pipe is temporarily increased in localized regions, in order to increase the number of beam gas events. The average hit multiplicity is increased when the gas pressure is increased because of a larger number of BIB particles. The effect is particularly visible for beam AC when the gas pressure is increased at 148 m from the interaction point (between LumiBlock 300 and 380). In this case, the average hit multiplicity is increased by about 30% with respect to the one with standard gas pressure.

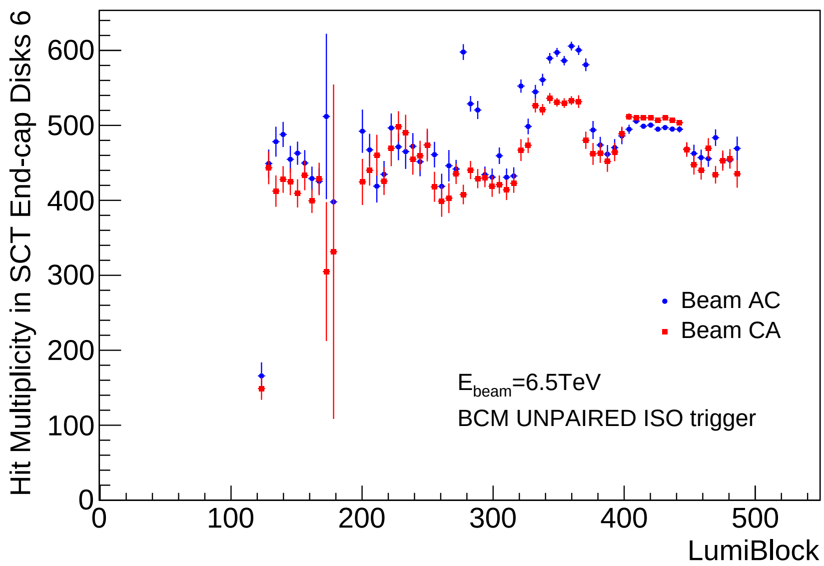

Figure 6.3: Average hit multiplicity on disk 6 of the SCT end-caps a function of the LumiBlock number in events with a BCM unpaired isolated trigger for run 336506. Every data point corresponds to the average value of five LumiBlocks. Only events with no primary vertices are considered. The gas pressure was temporarily increased in localized regions inside the beam pipe, at 148 m from the interaction point between LumiBlock 300 and 380, and at 58 m between LumiBlock 400 and 460.

During run 336506 the gas pressure is increased on purpose as an operational test, but a similar effect could happen because of an accident or because of operational choices. Several other effects can increase the BIB temporarily, as an accidental loss of a proton bunch or an erroneous configuration of the beam collimators. It is important to monitor the impact of the BIB in the SCT to be able to promptly detect an unexpected increase in occupancy which can affect the quality of the data.

During Run-2 of the LHC several runs contained a limited number of isolated bunches. In order to guarantee enough statistics in the monitoring system for every run, it isnecessary to consider also non-isolated bunches. Figure 6.4 compares the hit multiplicity on disk 6 of the SCT end-caps for unpaired isolated and non-isolated bunches. On average, non-isolated bunches produce a hit multiplicity 2.8% smaller than than that of isolated bunches (for beam AC the difference is 2.4%). This is explained by different beam conditions for the non-isolated bunches. Such a small difference is not significant for monitoring purposes, for which it is needed to identify much more significant variations as the one shown in Figure 6.3. In the online monitoring system non-isolated bunches are analyzed equivalently to the isolated ones, in order to increase the available statistics.

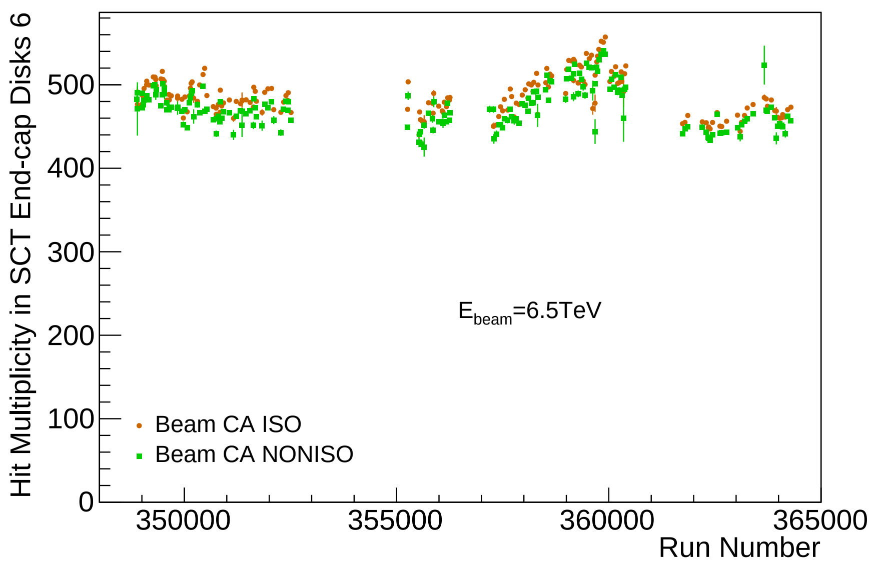

Figure 6.4: Average hit multiplicity on disk 6 of the SCT end-caps in events with beam CA for BCM unpaired isolated and non-isolated triggers (see Section 6.4), for every run in 2018. The same event selection as the one described in Figure 6.2 is applied.

Figure 6.5 shows the hit multiplicity in unpaired bunches for events in 2018 runs in the end-caps of the Pixel Detector (Figures 6.5a and 6.5c) and TRT (Figures 6.5b and 6.5d), as a function of the hit multiplicity in the disks 6 of the SCT end-caps in the same event. A correlation between the SCT hit multiplicity, and the one in the TRT, and Pixel detector is observed. Although the online monitoring code only uses SCT hits, it effectively provides information on the BIB hit multiplicity in all the ID region.

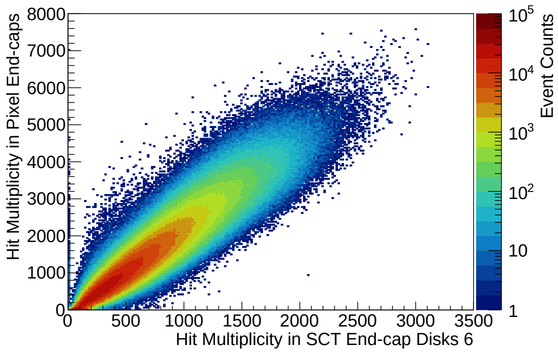

(a) SCT and Pixel with beam AC.

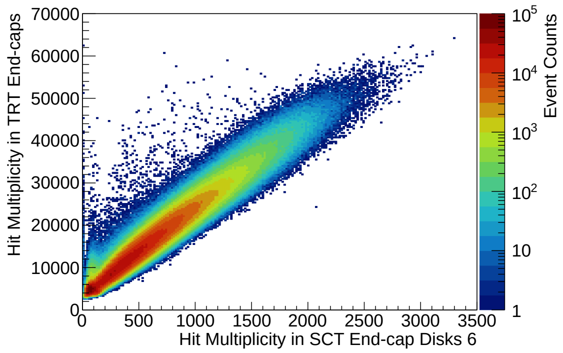

(b) SCT and TRT with beam AC.

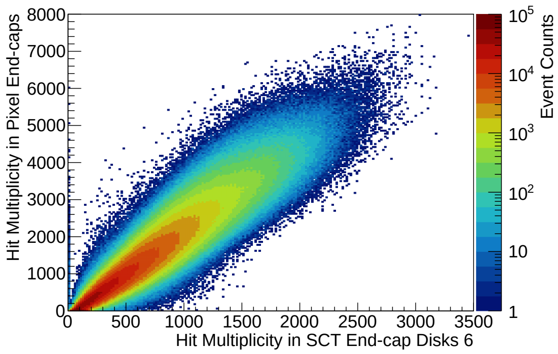

(c) SCT and Pixel with beam CA.

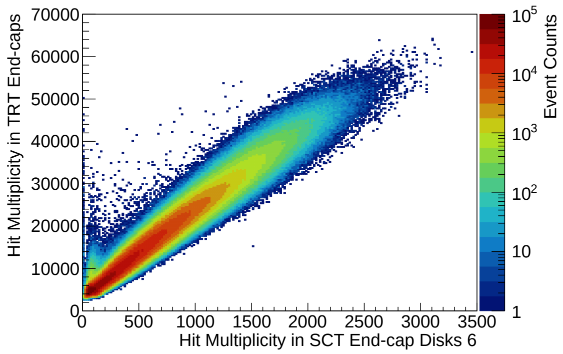

(d) SCT and TRT with beam CA.

Figure 6.5: Hit multiplicity for events in 2018 runs in the end-caps of the Pixel Detector and TRT, as a function of the hit multiplicity in the disk 6 of the SCT end-caps in the same event. Only events with a BCM isolated and non-isolated trigger (see Section 6.4), in the Good Run List, and with no primary vertices are considered.

6.3 Timing Properties

One important signature of the BIB particles arises from the timing of their hits. In collision events the two proton beams collide in the interaction point and generate collision fragments, that in turn reach the end-caps generating a signal in the SCT. The central time bin of every bunch crossing is synchronized with these signals, with the synchronization being performed during special collision runs every year.

BIB particles reach the ATLAS Detector from the end-cap sides, thus generating hits in the end-cap disks without passing by the interaction point. In the upstream end-cap (the first encountered by the beam), their signals are generated earlier than the signals generated by the collisions of particles from the same bunch. A simplified explanation of the timing of BIB and collision fragment hits is shown in Figure 6.6. For every end-cap disk the time difference can be estimated as:

$$\Delta t = \frac{2z}{c} \tag{6.1}$$

where z is the absolute distance of the disk from the interaction point and c is the speed of light, assumed to be the speed of the BIB particles. The larger z is, the larger the time difference is. The hits in the outermost disks will have a larger time difference than the ones in the innermost disks.

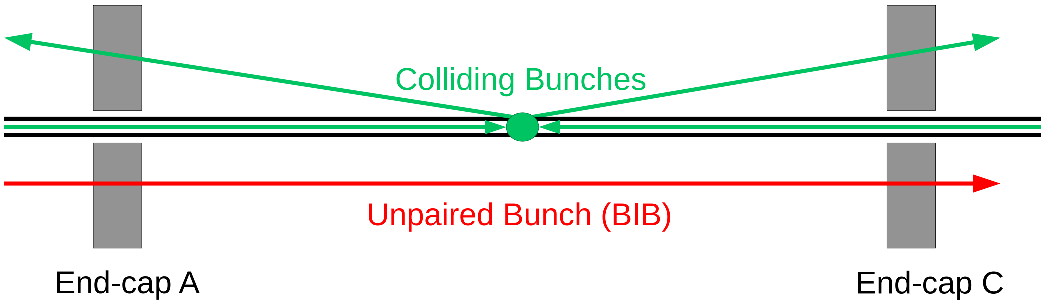

Figure 6.6: Schematic explanation for the timing of BIB hits with respect to hits generated by collision fragments. The paired bunches travel to the interaction and generate the collision fragments, that travel from the interaction point to the end-caps. BIB particles in an unpaired bunch, however, interact directly in the first end-cap they encounter, then they travel to the other end-cap where they generate another hit.

In the SCT a signal of a MIP (see Section 2.3.1) is larger than the 1 fC threshold for about 40 ns [134]. This means that if a particle arrives up to 20 ns before or after the collision fragments from a BCID, it will still generate a hit in the readout frame corresponding to that BCID. The time difference of the BIB hits can generate hits one readout earlier with respect to collision fragments generated by protons in the same bunch. A hit with these characteristics is usually called an early hit or, in the notation introduced in Section 1.2.1, 1XX hit.
Using Equation 6.1 for the three outermost disks of the SCT, number 7, 8, and 9, Δt can be calculated as 14.1, 16.7 and 18 ns, respectively. For the innermost disks Δt is much lower and it is 5.69 ns for disk 1. The probability of having an early hit in the inner disks is then much lower than in the outermost disks.
While BIB particles reach the upstream end-cap several nanoseconds before the collision fragments, this is not the case for the downstream end-cap. In this case, BIB hits are mostly in-time (X1X) because the particles must travel a distance comparable to the distance traveled by the beam and the collision fragments combined.

The time difference creates an excess of early hits on the upstream end-cap with respect to the downstream one. This asymmetry used to be exploited for the analysis of the BIB in the SCT [176]. Starting in 2016, only 01X hits are recorded (see Section 1.2.1) in the SCT and early hits are not stored anymore. A significant fraction of the hits on the upstream end-cap are early hits with 1XX pattern and they are now lost because of the 01X requirement. On the downstream end-cap the BIB produces mostly 01X which are regularly recorded. The BIB particles then produce an excess of 01X hits in

the downstream end-cap with respect to the upstream one.
The z asymmetry of an event is defined as [177]:

$$A_z = \frac{N_{hit}(EC\ A)\text{-}N_{hit}(EC\ C)}{N_{hit}(EC\ A)+N_{hit}(EC\ C)} \tag{6.2}$$

where $N_{hit}(EC\ A)$ and $N_{hit}(EC\ C)$ are the number of hits in the end-cap A and C, respectively (see Section 1.2.1 for the definition of A and C sides). Figure 6.7 shows an example of a z asymmetry plot for a run in 2017 for events with a single unpaired bunch, in which case the BIB is the dominating effect. The z asymmetry exhibits a peak at negative values in events with beam with direction AC, while the peak is at positive values for beam with direction CA, as expected in the case of an excess of hits in the downstream end-cap.

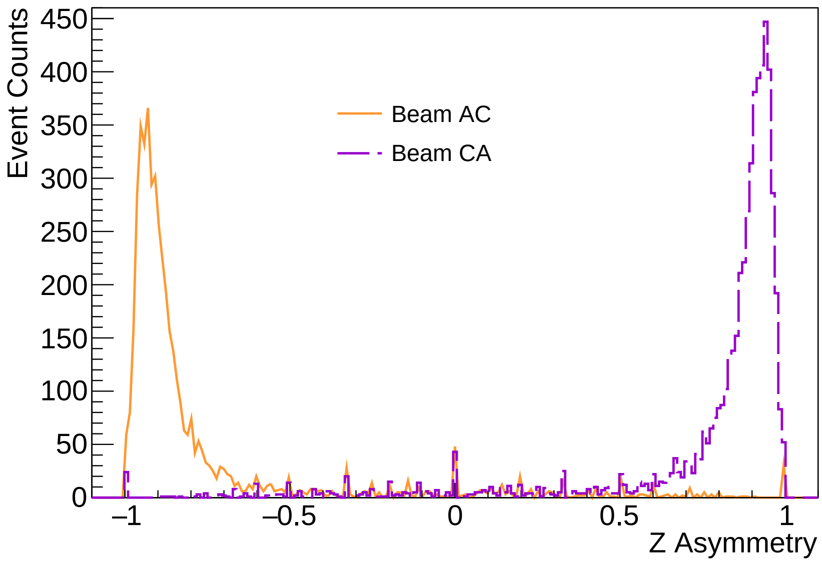

Figure 6.7: Z asymmetry obtained with space points in disks 7 and 8 in events with a BCM unpaired isolated trigger (see Section 6.4). The events are divided by the beam direction identified by the BCM trigger. The data is from run 331905 and LumiBlocks from 98 to 127.

6.4 Online Monitoring System

In order to create histograms less dependent on the electronic noise, space points (see Section 1.2.1) are used instead of RDOs (Raw Data Object), single strips with a signal over threshold. The probability of having two noise hits on back-to-back strips is very low, therefore space points generated by noise are extremely rare. Additionally, space points are two-dimensional entities and they allow for the creation of maps of the BIB hits with a granularity of the order of hundreds of μm. Every particle should generate a single space point in a disk, therefore the number of space point is directly related to the number of incident particles, thus giving an estimation of the flux of BIB particles.

The online monitoring code is implemented in the ATLAS software Athena [178] and it analyzes only events from the physics_Background stream, in which all the events containing unpaired bunches are stored. Only events where at least one of the following triggers has fired are analyzed by the code:

- L1_BCM_AC_UNPAIRED_ISO
- L1_BCM_CA_UNPAIRED_ISO
- L1_BCM_AC_UNPAIRED_NONISO
- L1_BCM_CA_UNPAIRED_NONISO
- HLT_mb_sp_ncb_L1RD0_UNPAIRED_ISO
- HLT_mb_sp_blayer_L1RD0_UNPAIRED_ISO

The first four triggers are fired when the BCM detector (see Section 1.2.1) has an early hit on one side of the ID and an in-time hit on the other side [179, 180]. These triggers select only unpaired bunches and identify the beam direction as well. The first two triggers are fired in case the bunch is also isolated, while the second two if the bunch is not isolated. The last two triggers are fired based on the number of space points recorded in the SCT and IBL (see Section 1.2.1). These triggers select only unpaired isolated bunches, but do not identify the beam direction.

Since some of the triggers do not identify the direction of the beam, the online monitoring system should identify it with other means. This is done by using the z asymmetry defined in Equation 6.2. As observed in Figure 6.7, the z asymmetry for disks 7 and 8 exhibits sharp peaks around -1 and 1 for beam AC and CA, respectively. In the online monitoring system, events with A_z(disks 7 and 8) < -0.5 are considered to arise from an event with an unpaired bunch with direction AC, while events with A_z(disks 7 and 8) > 0.5 with direction CA. Events with -0.5 < A_z(disks 7 and 8) < 0.5 are discarded (with the exception of the z asymmetry histograms). This criterion discards events where collisions due to ghost charge are predominant.

6.4.1 Monitoring Histograms

Z Asymmetry

Figure 6.8 shows a comparison of the z asymmetry calculated in different disks using RDOs and space points. The z asymmetry for both the RDOs and the space points exhibit the two peaks corresponding to the two beam directions. In the online monitoring system only the histograms obtained with space points are shown. The outermost disks exhibit peaks closer to the limits of -1 and 1 as a consequence of the larger time difference of their BIB hits.

In Figures 6.8c and 6.8d it is observed that the z asymmetry peaks obtained with space points are more separated than the ones obtained with RDOs. This is a further advantage of using space points instead of RDOs. On the upstream end-cap there is a significant probability that one (or both) the layers have an early hit that is not stored, and thus the corresponding space point can not be formed. In other words, the space point can be formed only if the hits on both sides of a disk are in-time hits, thus the probability of losing a space point because of early hits increases as the square of the probability of having an early hit on one side. The difference between space points and RDOs is more visible in the outermost disks where the probability of having early hits in the upstream disk is the largest.

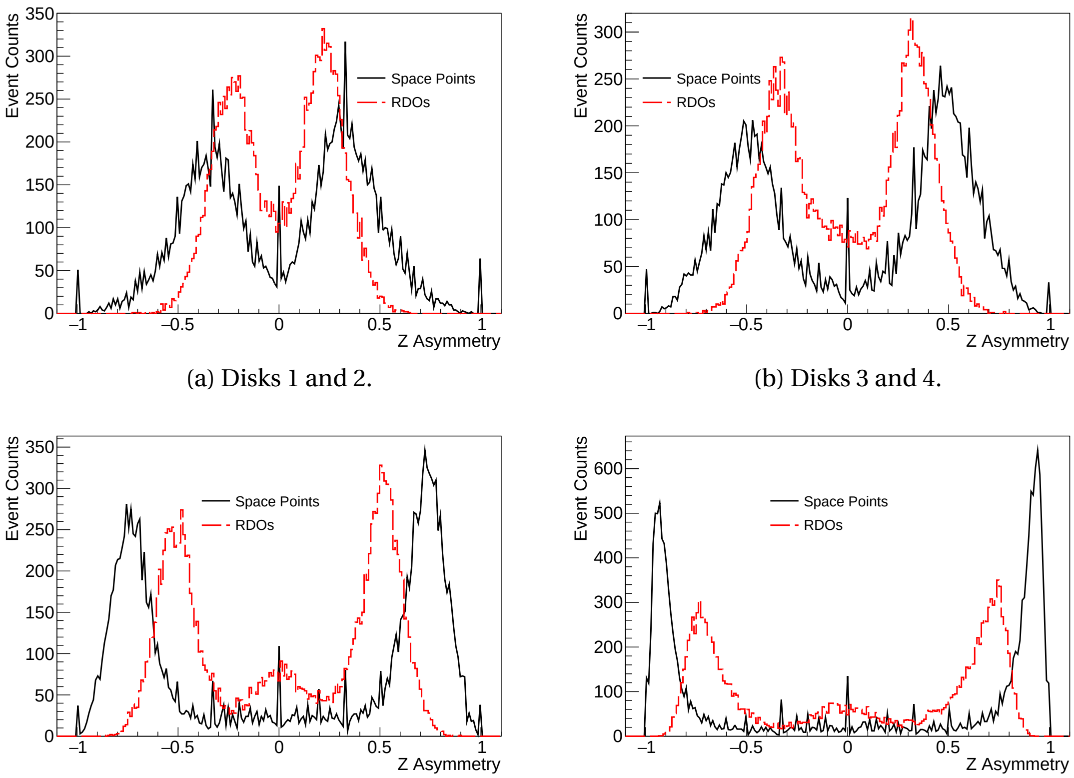

(a) Disks 1 and 2.

(b) Disks 3 and 4.

(c) Disks 5 and 6.

(d) Disks 7 and 8.

Figure 6.8: Comparison of z asymmetry obtained with RDOs and space points for different disks. The data is from run 301918 and LumiBlocks from 98 to 128.

One quadrant of disk 9 of the end-cap A has been permanently deactived because of problems with its cooling system. The z asymmetry would be distorted if a disk on one end-cap has a significant inactive area, and this effect would create misleading results. The disks 9 on both end-caps then are not implemented in any z asymmetry histogram.

Density per Disk

Another useful quantity to characterize the BIB is its area density. Although on the upstream end-cap the efficiency is strongly suppressed for timing reasons, on the downstream end-cap most of the particles generate a recorded hit. A measurement of the space point density on the downstream end-cap represents then a reliable estimation of the BIB density.

In the online monitoring system, histograms that show the average density of space points per event in all end-cap disks are implemented. Figure 6.9 shows an example of such histograms. It is observed that the downstream end-cap shows a larger space point area density than the upstream one, since most of the hits in the latter are not recorded. In the disks 2, 3, 4, 5 and 6 of the downstream end-cap it is observed that the density of space points increases for the outermost disks. This is explained by differences in the efficiencies due to timing of the BIB. The disks 1, 7, 8 and 9 do not follow this trend. The reason lies in the geometry of the SCT and in the distribution of the BIB. Figures 6.10 and 6.11 show that the BIB density decreases linearly with the radius. The above-mentioned disks lack modules at low radii (see Figure 1.4) where the BIB density is largest. The average BIB density on their area is therefore smaller with respect to the disks 2, 3, 4, 5 and 6.

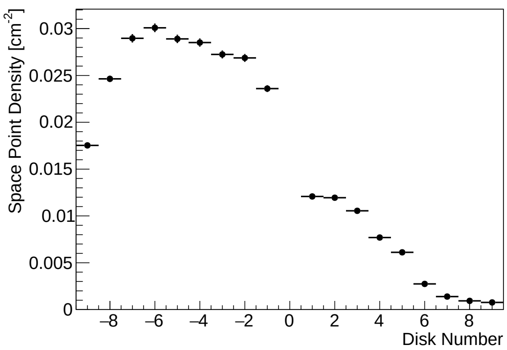

(a) Beam AC.

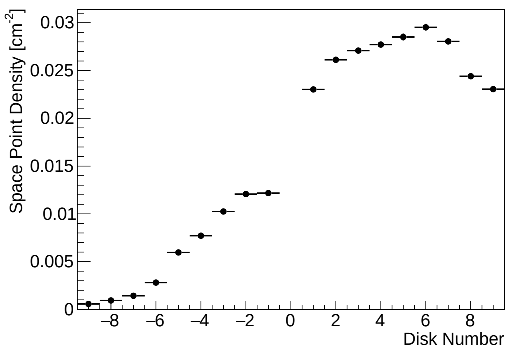

(b) Beam CA.

Figure 6.9: Average space point area density per event per disk in run 331905 and LumiBlocks from 106 to 128. Disks on end-cap C are assigned to negative numbers, while disks of end-cap A are assigned to positive numbers.

Two-Dimensional Maps

By using space points it is possible to obtain the position of a particle hit with a precision of the order of hundreds of µm. This feature is used to create maps of the BIB. Figure 6.10 shows some examples of such maps. In the online monitoring system the maps for all the disks in both end-caps are shown, with different plots for beam AC and beam CA.

The distribution of the BIB is consistent in all the disks. The presence of disabled modules generates some regions with no space points in the disks. One behavior of the BIB observed in these plots is that its density decreases with the radius. The same behavior is observed in simulations of the BIB density for radii where the SCT is located [181, 182]. Another behavior that is observed in the maps of Figures 6.10a, 6.10b and 6.10c is a small excess of space points at negative x values. Figure 6.10d shows a map from a different run in which a small excess is visible toward negative y values. With these maps it is then possible to monitor the distribution of the BIB.

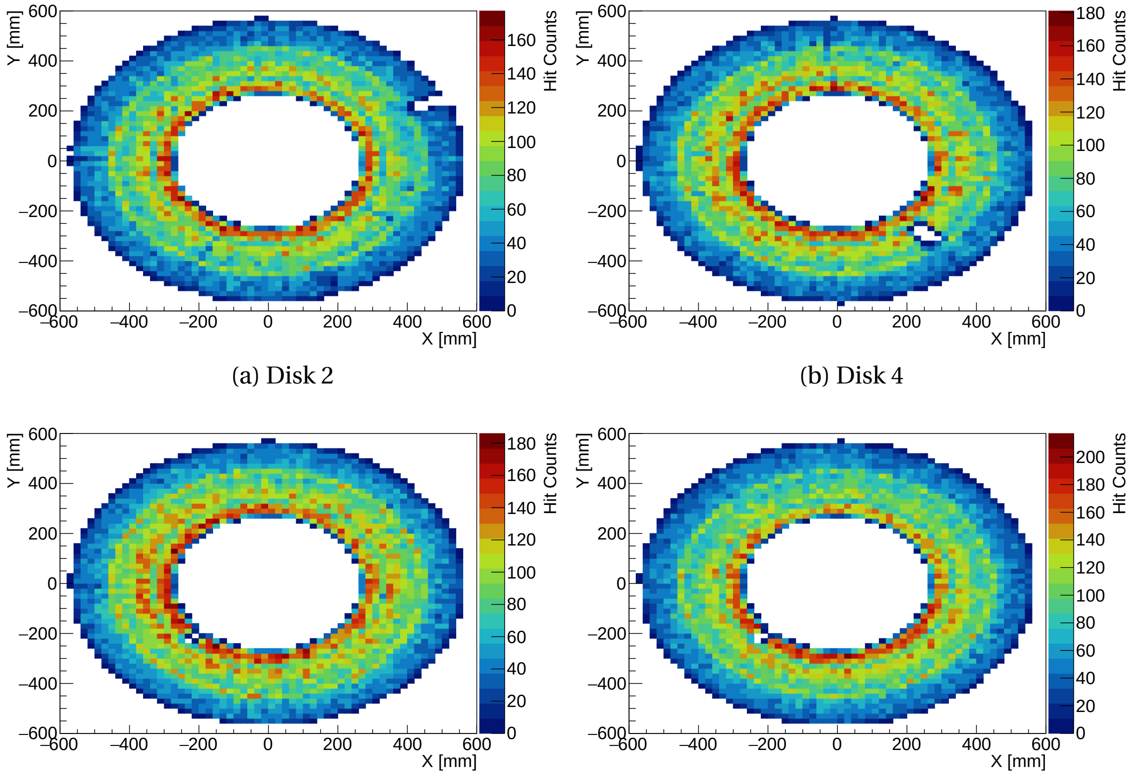

(a) Disk 2 (b) Disk 4

(c) Disk 6 (d) Disk 6

Figure 6.10: Space point two-dimentional maps in the end-cap A in different disks for events with beam CA in run 298771 and LumiBlock 248 (Figures (a),(b) and (c)) and run 301918 and LumiBlock 152 (Figure (d)).

Radial Maps

The two-dimensional maps provide very useful information regarding the distribution of the BIB, but their granularity can limit the conclusions that can be drawn from them. Histograms showing the density of the BIB as the function of the radius are also implemented. In these histograms the counts are integrated on the full polar angle, thus they provide a better radial granularity and their entries have higher statistics. Examples of such histograms are shown in Figure 6.11. In the online monitoring systems the radial maps of all the disks of end-caps are created for both beam direction.

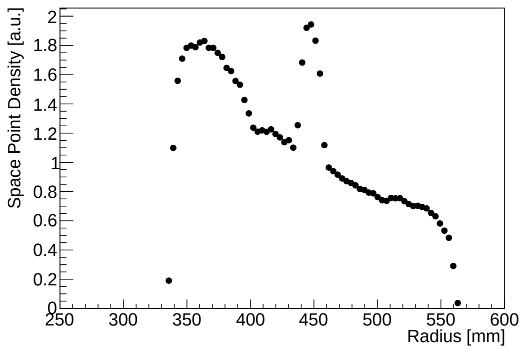

(a) Disk 1

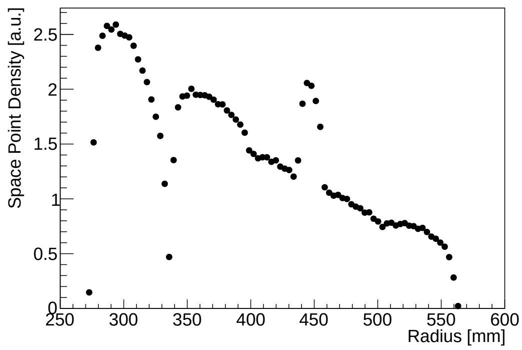

(b) Disk 4

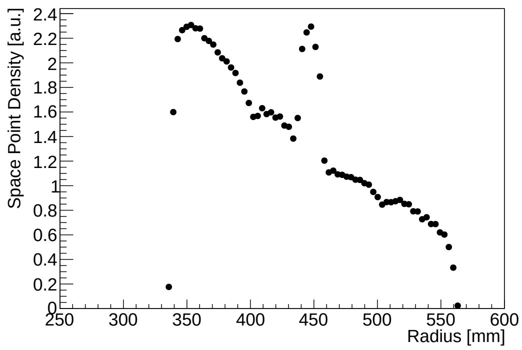

(c) Disk 7

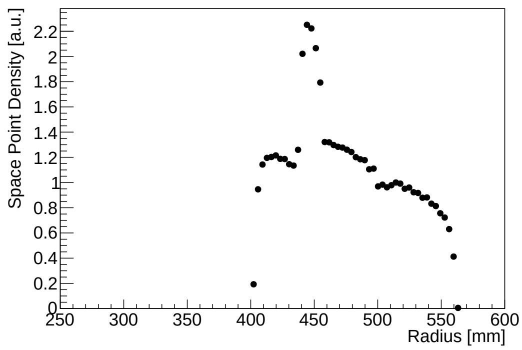

(d) Disk 8

Figure 6.11: Space point radial distribution in the end-cap A in different disks for events with beam CA in run 331905 and LumiBlocks from 106 to 128.

Generally, the BIB area density decreases with the radius, as visible also in Figure 6.10, with an approximately linear dependence. However, the BIB area density differs significantly from this linear behavior at some localized radii, exhibiting a much lower or much higher value. Such regions can also be noticed in the maps of Figure 6.10 in the form of rings with a very high or very low number of hits. This effect is caused by the SCT geometry and by the coverage of its modules. Every disk is composed by several concentric rings of modules with different geometries.
Table 6.1 summarizes the inner radius and the outer radius of every module type, and in which disk it is mounted. At some radii there is a small separation between two rings. In these region no active area is present and therefore no space points can be generated. At other radii two different rings overlap and then two space points can be produced by a single particle.

Module type	R_{in} (mm)	R_{out} (mm)	Disks
Inner	275.00	334.10	2 , 3 , 4 , 5 , 6
Middle	337.60	400.73	1 , 2 , 3 , 4 , 5 , 6 , 7
Middle	402.83	455.30	1 , 2 , 3 , 4 , 5 , 6 , 7
Middle Short	408.00	455.30	8
Outer	438.77	502.35	1 , 2 , 3 , 4 , 5 , 6 , 7 , 8 , 9
Outer	504.45	560.00	1 , 2 , 3 , 4 , 5 , 6 , 7 , 8 , 9

Table 6.1: List of module types in the SCT end-caps, with their inner and outer radii and the disks on which they are mounted [183].

Bunch Crossing Number (BCID)

The LHC filling scheme usually comprises two trains of unpaired bunches, one for each beam direction, in front of the colliding bunches trains. These initial bunches are crucial for the evaluation of the BIB. In the online monitoring system two histograms are implemented to monitor the average z asymmetry on the disks 7 and 8, and the average number of space points on disks 7 and 8 as a function of the bunch number (BCID). Figure 6.12 shows an example of these histograms. With these histograms it is possible to monitor if a bunch behaves unexpectedly.

In Figure 6.12a the two unpaired bunch trains are observed, with the first 12 BCIDs being occupied by bunches with direction CA and thus exhibiting a positive z asymmetry, and the following 12 BCIDs being occupied by bunches with direction AC and hence exhibiting negative z asymmetry.

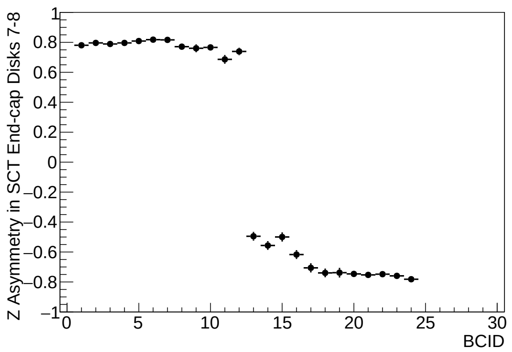

(a) Z asymmetry in disks 7 and 8

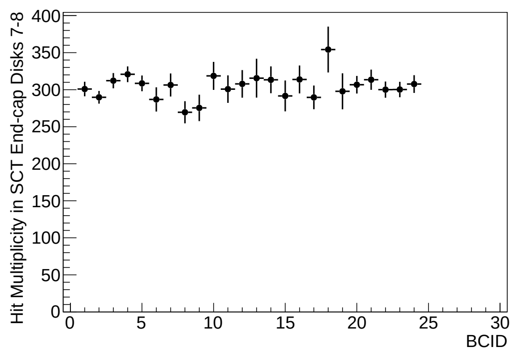

(b) Average space point multiplicity per event in disks 7 and 8 of both end-caps

Figure 6.12: Histograms as a function of the BCID for run 331905 and LumiBlocks between 106 and 128.

Luminosity Block

It is important to monitor the behavior and stability of the BIB within one run. An anomaly can be present only for a short time which would not produce a visible effect in histograms averaged over the whole run. In the online monitoring system, histograms as a function of time (expressed in LumiBlock number) are implemented. Figure 6.13 shows as an example the number of space points per event as a function of the LumiBlock number. Histograms of this type are created for disks 1 and 2, 3 and 4, 5 and 6, and 7 and 8.

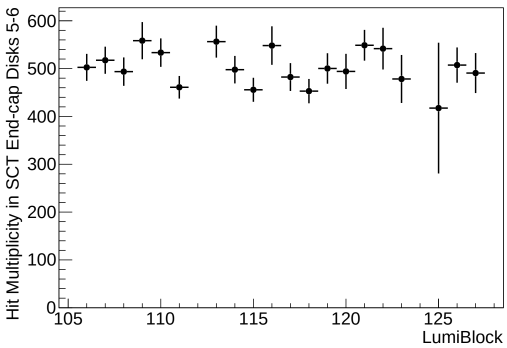

(a) Disks 5 and 6 and beam AC

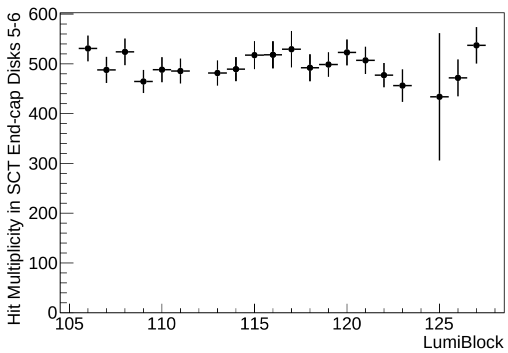

(b) Disks 5 and 6 and beam CA

Figure 6.13: Average space point multiplicity as a function of the LumiBlock number for part of run 331905.

Figure 6.14 shows the fraction of events with beam CA with respect to all the events analyzed, as a function of the LumiBlock number. If the number of bunches in the two directions is equal, this quantity should assume a value of 0.5. In Figure 6.14 the ratio has generally a value slightly larger than 0.5 as a consequence of the beam conditions in the run analyzed.

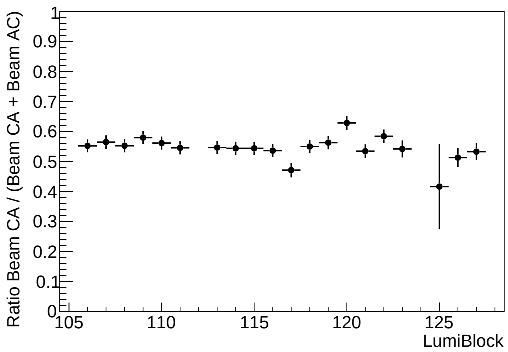

Figure 6.14: Fraction of unpaired bunches with beam CA for part of run 331905.

CONCLUSION

Starting from 2022, the Large Hadron Collider (LHC) will be upgraded to the High-Luminosity LHC which will greatly enhance the physics reach of the LHC experiments. The High-Luminosity LHC, however, will also generate unprecedented radiation levels and high pile-up, thus posing a serious challenge for the LHC experiments. The ATLAS Experiment will replace its current tracking system with an all-silicon detector, the Inner Tracker (ITk), comprising inner pixel layers and outer strip layers. The ITk Strip Detector will operate in a much harsher environment than the current strip detector, the Semiconductor Tracker (SCT). For this reason, an intense R&D program was completed to develop new radiation-hard sensors and front-end chips.

Test beams were a crucial tool for the characterization of ITk Strip prototype modules and provided important information for the development of the final production-grade ITk Strip modules.
The threshold calibration accuracy and precision are quantified with test beam measurements for several non-irradiated modules. The results prove that the current calibration procedure provides accurate and precise results, with an average deviation for the Most Probable Value from expectations of less than 1% and a relative dispersion of 3.8% for the Most Probable Value measured in different front-end chips.
The response of a non-irradiated silicon module to a beam particle crossing its boundary regions (field shaping strips, end-of-strip region, inter-segment region) is evaluated. Although it is observed that the choice of the operational threshold can modify the active area by a small amount (about 0.1%), no worrisome loss of hit detection efficiency is observed in the module boundary regions for thresholds close to 1 fC (6250 e), the baseline value for the ITk Strip Detector during the first years of operations.
The study of the performance of irradiated modules is crucial to prove the radiation-hardness of the current prototype modules. Several ITk Strip prototype modules were irradiated to radiation levels comparable to what they will have experienced at the end of lifetime of the High-Luminosity LHC (NIEL fluence of 5.1-15 $\times 10^{14}$ n_{eq}/cm^2 and TID of 20-37.2 MRad, 200-372 kGy). The operational threshold for the ITk Strip Detector is required to provide a hit detection efficiency > 99% and a noise occupancy < 10^3 (0.1%). Test beam measurements show that in non-irradiated modules the requirements are

satisfied for thresholds between ~0.5 fC (3125 e) and ~1.9 fC (11 875 e). Although radiation damage significantly deteriorates the module performance, a range of operational thresholds is present in irradiated modules implementing the latest front-end chips (ABCStar). In particular, for the region where the highest radiation level (15×10^{14} n_{eq}/cm^2 including a safety factor 1.4) and the lowest Signal-to-Noise ratio are expected, the requirements are satisfied for thresholds between about 0.44 fC (2750 e) and 0.52 fC (3250 e). These results proves that the current ITk Strip prototype modules will provide excellent performance for the entire duration of the High-Luminosity LHC lifetime, including a safety factor 1.4.
It is observed that irradiated modules exhibit a more pronounced charge sharing than non-irradiated modules. The enhanced charge sharing increases the cluster size of the hits and decreases the hit detection efficiency and it is explained by charge division in the inter-strip region caused by surface damage. It is also observed that in irradiated modules the hit detection efficiency is increased significantly in the region where the bond pads are located, as a consequence of a mitigated charge sharing. This is caused by the larger coverage provided by the wide aluminum layer and implant strip in that region.

Based on the above-mentioned observation, sensors with a special layout were produced. These sensors include five zones with different aluminum layer and strip implant widths, including a zone with the default ATLAS ITk Strip layout. Several sensors were irradiated with protons, neutrons, and gamma-rays.
Non-irradiated and irradiated sensors are characterized electrically with probe station measurements, with a focus on leakage current, inter-strip capacitance, coupling capacitance, and inter-strip resistance. The default ATLAS ITk Strip layout satisfies all the ATLAS ITk Strip specifications for all the radiation types tested and for a wide range of radiation levels. The alternative layouts satisfy the specifications on the coupling capacitance and inter-strip resistance, but they (except for one) do not satisfy the inter-strip capacitance specification. It is also observed that in gamma-irradiated sensors the presence of a wide aluminum layer increases the inter-strip resistance thus improving the strip isolation. This is interpreted as a consequence of the mitigation of surface damage effects by the aluminum layer and strip implant.
A few non- and proton-irradiated sensors are characterized in a test beam, in order to study the effect of the different sensor layouts on the hit detection efficiency. The test beam results show that in irradiated sensors the presence of a wide aluminum layer or strip implant enhances the hit detection efficiency by reducing the charge sharing. After irradiation the presence of an enlarged aluminum layer and strip implant increases the median charge of the leading strip charge distribution by up to 29%. As for the above-mentioned inter-strip resistance results, this is interpreted as a consequence of the mitigation of surface damage effects by the aluminum layer and strip implant.
The results prove that both the aluminum layer and strip implant widths play an im-

portant role on the hit detection efficiency of a sensor. The aluminum layer has an effect on the leading strip charge collection comparable to the strip implant, but additionally the aluminum layer width has a smaller effect on the electrical characteristics of a sensor. By using a slightly increased metal overhang width it is possible to enhance the leading strip charge collection, and therefore the hit detection efficiency, while not significantly deteriorating the electrical properties of a sensor. In particular, an alternative sensor layout with an aluminum layer width of 36 μm (up from 22 μm in the default ATLAS layout) is observed to meet all the ATLAS ITk Strip specifications, but to also additionally provide a leading strip median charge about 10% larger than the default ATLAS layout. This observation is an important information for the understanding of radiation damage in silicon sensors and can be exploited for the design of future strip detectors.

The Beam-Induced Background (BIB) is composed of particles generated by the interaction of the LHC beams with the surrounding environment. An online monitoring system based on space points is developed to study the BIB in the current strip detector, the Semiconductor Tracker (SCT). The online monitoring system was operative during part of the ATLAS data-taking in the LHC Run 2. The online monitoring system provides important information on the characteristics of the BIB in the SCT, for example, it is observed that the BIB mostly generates hits on the upstream end-cap and that its density decreases linearly with the radius.

APPENDIX

A

SUPPLEMENTAL MATERIAL TO CHAPTER 4

A.1 S-Curves of Non-Irradiated Modules

Figure A.1 shows the s-curves measured in ITk Strip test beams with the beam pointing at different ASICs of non-irradiated modules. The differences between curves measured for different ASICs are related to the precision and accuracy of the threshold calibration procedure discussed in Section 4.4.1.

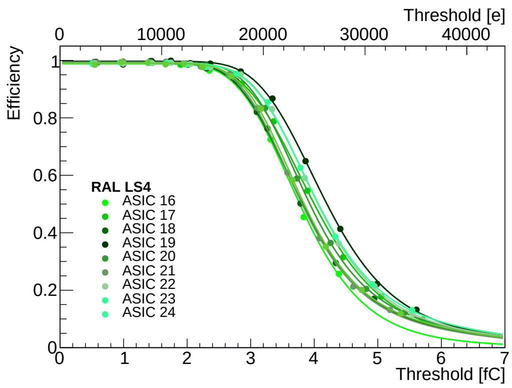

(a) RAL LS4.

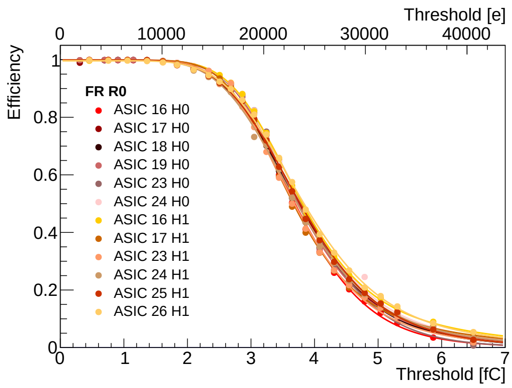

(b) FR R0.

Figure A.1: S-curves obtained with the beam pointed at several front-end chips for the non-irradiated modules tested in ITk Strip test beams.

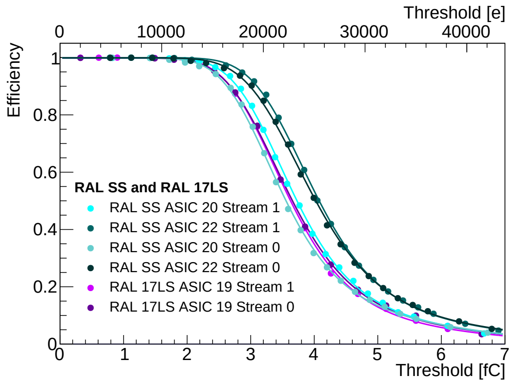

(c) RAL SS and RAL 17LS.

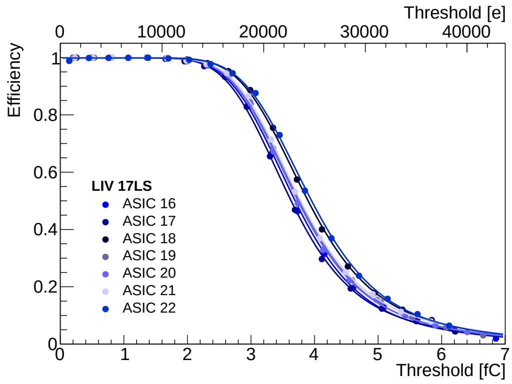

(d) LIV 17LS.

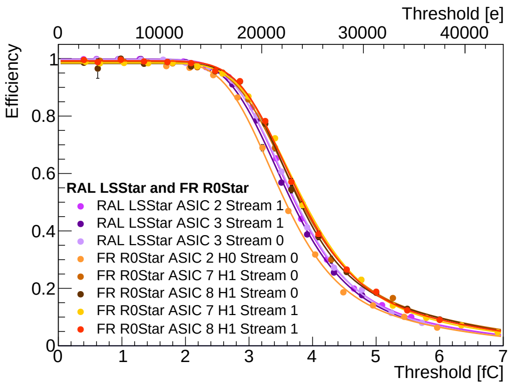

(e) RAL LSStar and FR R0Star.

Figure A.1: S-curves obtained with the beam pointed at several front-end chips for the non-irradiated modules tested in ITk Strip test beams.

A.2 Efficiency in the Inter-Segment Region

Figures A.2a and A.2b show the efficiency in the inter-segment region as a function of the track position along the strip axis for two thresholds. No significant loss of efficiency is observed, proving that the whole inner region of a sensor contributes to the efficiency.

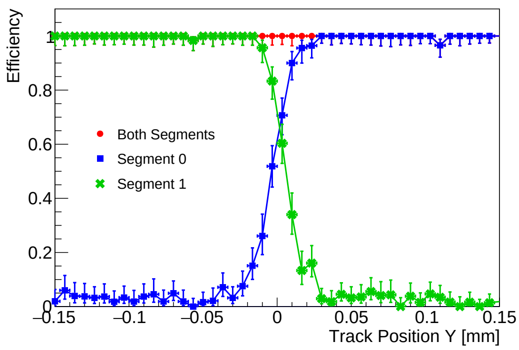

(a) Threshold 0.49 fC (3063 e).

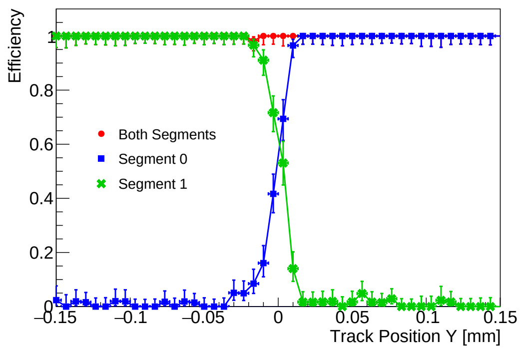

(b) Threshold 0.93 fC (5813 e).

Figure A.2: The red points show the efficiency in the inter-segment region as a function of the track position along the strip axis for the non-irradiated module LIV 17LS. The blue and green points show the efficiency obtained if only one segment is considered. The origin is defined as the point where the efficiency measured in the two segments is equal.

A.3 Performance for Long Strips in RAL LS3 Irrad

RAL LS3 Irrad was built with a sensor with Short Strips (2.4 cm length) and it comprised a single hybrid, although Short Strip modules comprise two hybrids (see Figure 4.1a). The hybrid was wire-bonded to two sensor segments and one of them was wire-bonded to the adjacent strip segment. In this way, these two segments are combined in single strips with length of 4.8 cm, as in the Long Strip region of the ITk Strip barrel.

Figure A.3 shows the efficiency and noise occupancy as a function of the threshold for the Long Strip segment in RAL LS3 Irrad. The noise is increased with respect to the one obtained in the Short Strip segment (see Section 4.7.2) because of a larger input capacitance to the front-end channels. No thresholds satisfying the ITk Strip requirements (see Section 4.7.2) are observed. However, RAL LS3 Irrad was irradiated to a fluence comparable to the maximum NIEL fluence expected at the end of lifetime of the HL-LHC in the Short Strip region of the ITk Strip barrel, including a safety factor of about 1.2. Sensors implementing Long Strips will not be subject to such a high radiation level in the ITk Strip Detector.

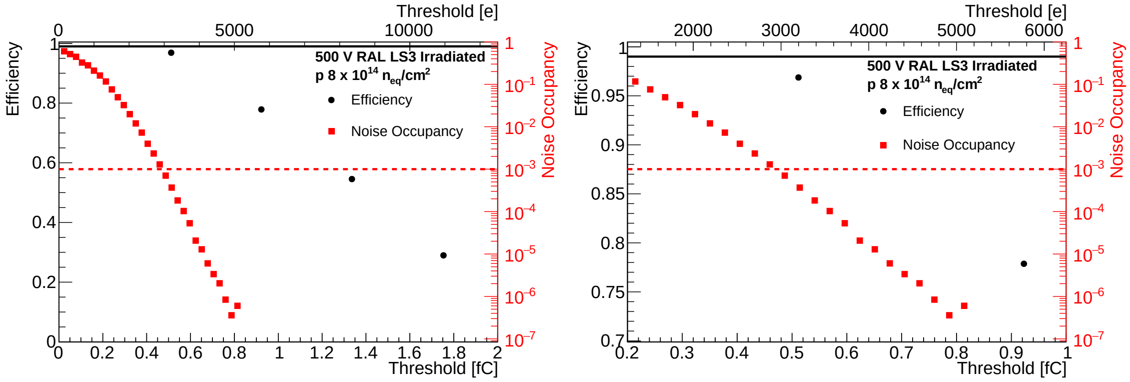

(a) All thresholds. (b) Zoom on thresholds < 1 fC.

Figure A.3: Efficiency and noise occupancy as a function of the threshold in the Long Strip segments of RAL LS3 Irrad [49]. The black and red lines indicate the requirements on the efficiency and noise occupancy, respectively.

A.4 Performance in the FR R0Star Irrad Central Segments

Figures A.4a and A.4b show the efficiency and noise occupancy as a function of the threshold for the second innermost and second outermost segments of FR R0Star Irrad, respectively. The ITk Strip requirements are satisfied for thresholds between about 0.38 fC (2438 e) and 0.52 fC (3250 e) for the second innermost segment, and between about 0.43 fC (2688 e) and 0.53 fC (3313 e) for the second outermost segment.
In the second innermost segment the measured MPV (Signal) is 1.38 ± 0.02 fC (8625 ± 125 e),

the noise is 0.100 ± 0.013 fC (684 ± 65 e), and the Signal-to-Noise is 12.6 ± 1.2. In the second outermost segment the measured MPV (Signal) is 1.61 ± 0.01 fC (10063 ± 63 e), the noise is 0.130 ± 0.012 fC (810 ± 78 e), and the Signal-to-Noise is 12.4 ± 1.2.

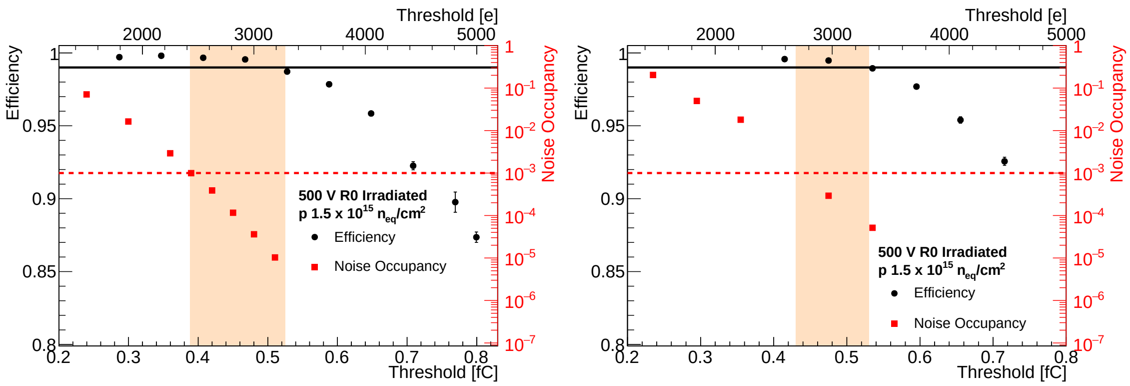

(a) Second innermost segment. (b) Second outermost segment.

Figure A.4: Efficiency and noise occupancy as a function of the threshold for the second innermost and second outermost segments of FR R0Star Irrad (see Figure 4.1b). The black and red lines indicate the requirements on the efficiency and noise occupancy, respectively. The orange areas highlight the range of thresholds where the ITk Strip requirements are satisfied.

A.5 Leading Strip Charge Distribution

It is useful to study the charge distribution in the leading strip, since it is directly related to the shape of the s-curves (see Section 4.3.1). With a binary readout it is not possible to measure directly the leading strip charge distribution, but it can be obtained indirectly by differentiating an s-curve. The difference in efficiency between two thresholds is related to the probability that a given amount of charge is collected by the leading strip:

$$Q((th_1+th_2)/2) = \frac{\epsilon(th_2)-\epsilon(th_1)}{th_1-th_2} \tag{A.1}$$

where th_1 and th_2 are the two thresholds, Q is the probability that a given amount of charge is collected by the leading strip, and ϵ is the measured efficiency.

Figure A.5 shows the charge distributions of two non-irradiated modules obtained using Equation A.1. Both the distribution obtained using the standard s-curve and the one obtained selecting only tracks crossing at the center of a strip are shown. All the distributions exhibit an approximately Landau-Gauss shape, with a well-defined peak and a long tail at large thresholds.

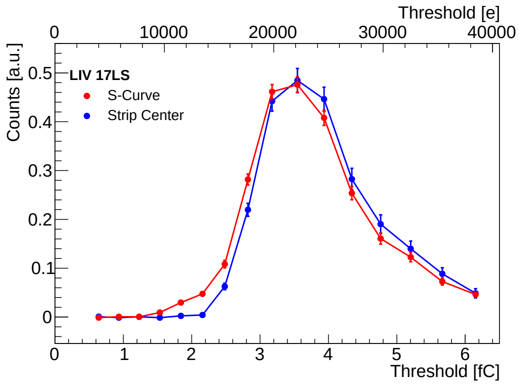

(a) LIV 17LS.

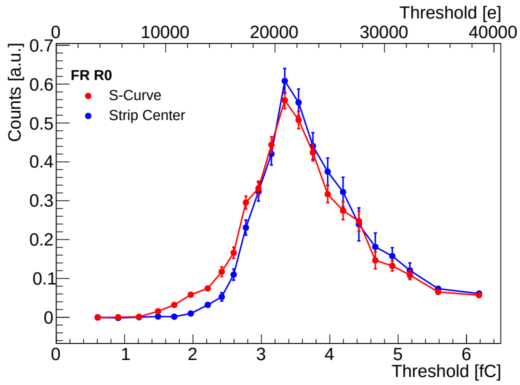

(b) FR R0.

Figure A.5: Charge distributions for non-irradiated modules tested in ITk Strip test beams. Both the distribution obtained using the standard s-curve, and the one obtained selecting only tracks crossing at the center of a strip are shown.

Figure A.6 shows the charge distributions of two irradiated modules obtained with the same procedure. Both the distribution obtained using the standard s-curve and the one obtained selecting only tracks crossing at the center of a strip are shown. The distributions obtained by selecting tracks crossing at the center of a strip exhibit a well-defined peak and a long tail at large thresholds, similarly to the Landau-Gauss distribution. The distributions obtained from the standard s-curve exhibit an approximately rectangular shape. A similar distribution has been observed in other studies [152] and it is attributed to the increased charge sharing caused by surface damage discussed in Section 4.8.

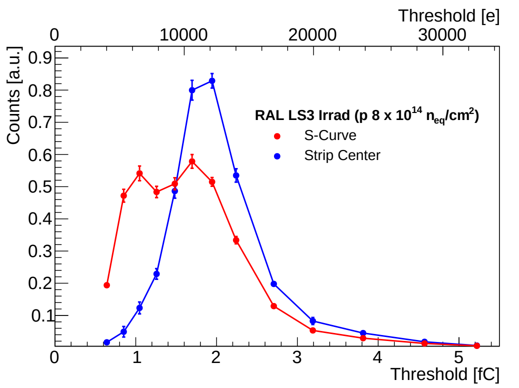

(a) RAL LS3 Irrad.

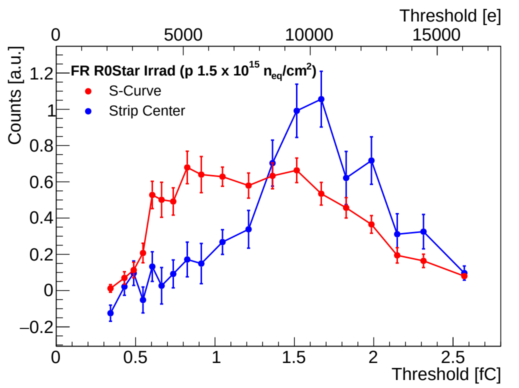

(b) FR R0Star Irrad.

Figure A.6: Charge distributions for irradiated modules tested in ITk Strip test beams. Both the distribution obtained using the standard s-curve, and the one obtained selecting only tracks crossing at the center of a strip are shown. For RAL LS3 Irrad an s-curve measured with a bias voltage of 600 V is used for the calculation.

The distortion of the leading strip charge distribution is confirmed qualitatively with the analysis of data taken with ATLAS12 mini-sensors in a test beam performed at DESY with the Alibava analog readout. The measurements are described in detail in [184] and additional details on the analysis of test beam data with an Alibava readout can be found in [74, 184]. The Alibava readout is used because it allows the charge distribution to be measured directly without the use of Equation A.1.

Figure A.7 shows the cluster charge distribution and the leading strip charge distribution obtained with non-irradiated mini-sensors. Both the cluster and leading strip charge distributions exhibit a shape similar to a Landau-Gauss distribution.

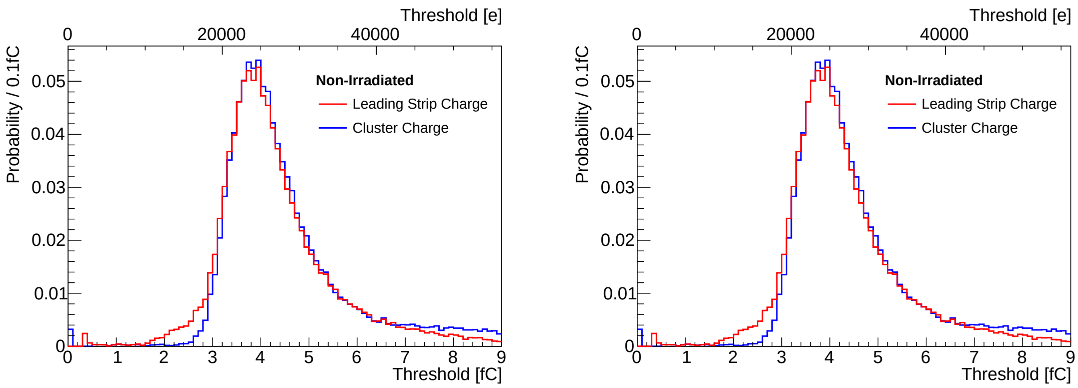

(a) Sensor 1.

(b) Sensor 2.

Figure A.7: Cluster and leading strip charge distributions measured in a test beam with the Alibava readout with non-irradiated sensors with a bias voltage of 500 V [184].

Figure A.8 shows the cluster charge distribution and the leading strip charge distribution obtained with mini-sensors irradiated with neutrons at JSI at a NIEL fluence of $1.2 \times 10^{14}\,\mathrm{n_{eq}/cm^2}$ and and $5 \times 10^{14}\,\mathrm{n_{eq}/cm^2}$. The sensors were annealed at 60 °C for 80 minutes. Although the cluster charge distribution has a shape similar to a Landau-Gauss distribution, the leading strip charge distribution differs significantly from it. The leading strip charge distribution exhibits a flat shoulder that extends to lower threshold values.

This result is in partial qualitative agreement with the distributions shown in Figure A.6, with the difference that the leading strip charge distribution of Figure A.8 shows a well-defined peak not present in Figure A.6. This difference can be explained by the different radiation type experienced by the sensors or by the different procedure used to obtain the charge distributions. Dedicated studies are necessary to fully understand the leading strip charge distributions for different radiation levels and types.

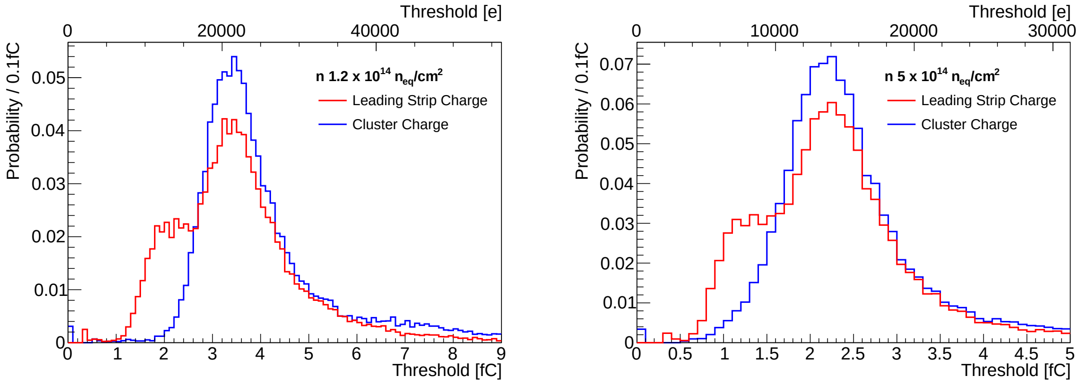

(a) NIEL fluence of $1.2 \times 10^{14}\ \mathrm{n_{eq}/cm^2}$.

(b) NIEL fluence of $5 \times 10^{14}\ \mathrm{n_{eq}/cm^2}$

Figure A.8: Cluster and leading strip charge distributions measured in a test beam with the Alibava readout with sensors irradiated with neutrons at JSI and with a bias voltage of 500 V [184].

A.6 Spatial Resolution Before and After Irradiation

The increased charge sharing in irradiated modules has the undesired consequence of reducing the efficiency and the charge collection on the leading strip. However, charge sharing also has the beneficial effect of improving the hit spatial resolution (see Section 4.3.2). Figure A.9 shows the residual distributions of non-irradiated and irradiated modules for thresholds close to the operational threshold expected to be used at the end of lifetime of the HL-LHC. The non-irradiated modules exhibit a residual distribution similar to the one explained in Figure 4.11. The irradiated modules exhibit an approximately Gaussian shape. Irradiated modules exhibit a narrower residual distributions than non-irradiated ones.

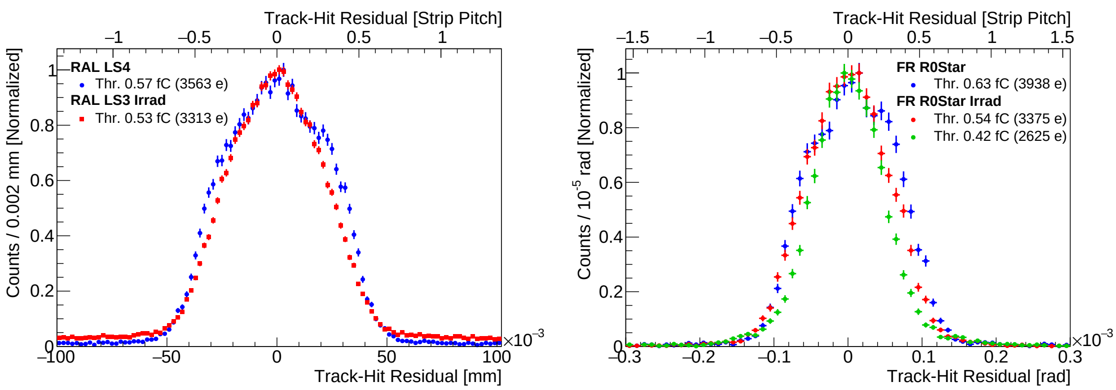

(a) Barrel modules.

(b) End-cap modules.

Figure A.9: Comparison of the residual distributions in non-irradiated and irradiated devices, for barrel and end-cap modules.

The spatial resolution can be estimated by measuring the Full Width at Half Maximum (FWHM) of the residual distributions. Table A.1 summarizes the FWHM of the residual distributions of Figure A.9. The FWHM of the residual distributions of irradiated modules is 20% smaller than in non-irradiated ones. Dedicated measurements are needed to verify these results and to quantify precisely the spatial resolution, since the FWHM values of Table A.1 are affected by the residual shape and by the test beam set-up used during the measurements.

Module	Threshold [fC] ([e])	FWHM
RAL LS4	0.57 (3563)	66 µm
RAL LS3 Irrad	0.53 (3313)	53 µm
FR R0Star	0.63 (3938)	1.58×10^{-4} rad
FR R0Star Irrad	0.54 (3375)	1.30×10^{-4} rad
FR R0Star Irrad	0.42 (2625)	1.14×10^{-4} rad

Table A.1: FWHM of the residual distributions shown in Figure A.9.

A.7 Identification of the Bond Pad Locations

The bond pad locations can be identified by exploiting the alternate layout of the bond pad rows shown in Figure A.10a. In the bond pad row on the left the even-numbered strips cover a wider area than the odd-numbered ones, and vice versa in the other bond pad row. Figure A.10b shows the number of tracks matched to a hit on an even-numbered or odd-numbered strip as a function of the track position along the strip axis. In two regions of width of about 200 µm an excess of counts is visible for even-numbered (odd-numbered) strips, with a low number of counts in odd-numbered (even-numbered) strips. This is a signature of the bond pad geometry and it is used in the measurements of Section 4.8.2 to identify the bond pad row locations.

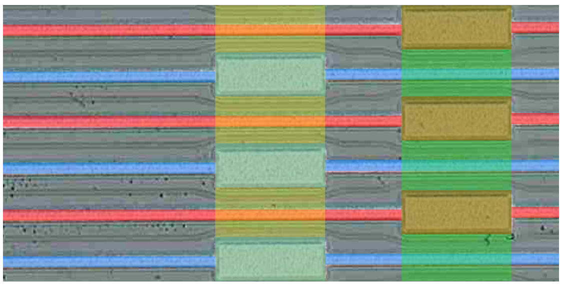

(a) Microscope image of several strips around the bond pad locations. Blue and red areas highlight the even-numbered and odd-numbered strips, respectively.

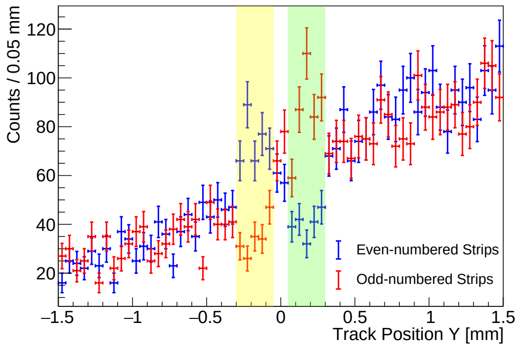

(b) Number of tracks matched to a hit on an even-numbered (blue) and odd-numbered (red) strip as a function of the track position along the strip axis. Only hits formed by a single strip are considered in the calculation.

Figure A.10: Explanation of the procedure to identify the bond pad locations. The measurement is performed with the non-irradiated module RAL LS4. The yellow and green areas highlight the locations of the two adjacent bond pad rows.

APPENDIX

B

SUPPLEMENTAL MATERIAL TO CHAPTER 5

B.1 Pre-Irradiation Electrical Characterization

Figures B.1a and B.1b show the current- and capacitance-voltage characteristics measured for several non-irradiated ATLAS 17LS R&D sensors. The capacitance measurements have been performed with an LCR meter test frequency of 1 kHz and amplitude of 1 V. Most of the sensors were eventually irradiated with protons at KIT. Some of the measurements are performed at the DESY campus in Hamburg. The measurements are performed at room temperature (~25 °C) and with a relative humidity of ~25%. The high relative humidity causes the electrical breakdown at low bias voltage observed for several mini-sensors [185].

Using the bulk capacitance measurements performed with Short Strip mini-sensors it is possible to estimate the capacitance of a strip with respect to the backplane:

$$C_{\text{backplane}} = \frac{C_{\text{bulk}}}{L \cdot N_{\text{strips}}} = \frac{72.7 \pm 0.2\,\text{pF}}{2.42\,\text{cm} \cdot 104} = 0.2877 \pm 0.0008\,\text{pF}\,\text{cm}^{-1} \tag{B.1}$$

where C_{bulk} is the bulk capacitance measured (see Figure B.1b), L the strip length, and N_{strips} the total number of strips[1].

[1] The total number of strips is actually 100, but four grounded bias rails cross the strip length to divide the zones. Each bias rail has a width equal to a strip pitch and it is electrically connected to all the strips. Therefore, for bulk capacitance measurement purposes, each bias rail crossing the sensor length gives a contribution comparable to a single strip.

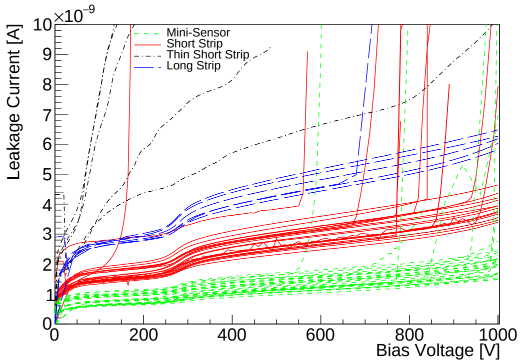

(a) Current-voltage characteristics.

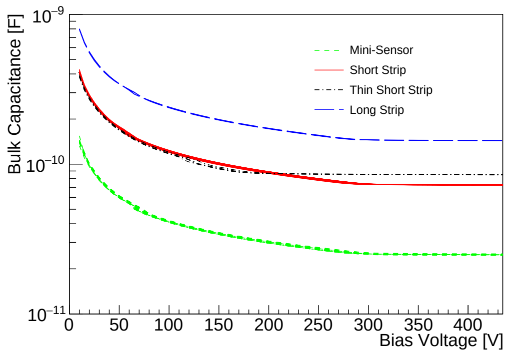

(b) Capacitance-voltage characteristics.

Figure B.1: Current- and capacitance-voltage characteristics of non-irradiated R&D sensors with three different strip lengths: 0.8 cm (mini-sensors), ~2.4 cm (Short Strip mini-sensors), and ~4.8 cm (Long Strip mini-sensors). Measurements performed with a few Short Strip mini-sensors from thin wafers are also shown.

With the capacitance-voltage characteristics measurements it is possible to retrieve the full depletion voltage of the sensor. The inverse squared of the bulk capacitance exhibits a kink at the full depletion voltage (see Equation 2.20). Figure B.2a shows the inverse squared of the bulk capacitance as a function of the bias voltage and shows how the full depletion voltage is obtained. The slope region ($150\,\mathrm{V} < V_{\mathrm{bias}} < 250\,\mathrm{V}$) and the constant region ($V_{\mathrm{bias}} > 350\,\mathrm{V}$) are fitted separately with two linear functions. The full depletion voltage is given by the intersection of the extrapolations of the fit functions. Figure B.2b shows the full depletion voltage obtained for non-irradiated R&D sensors. The average full depletion voltage is then quantified:

$$V_{\mathrm{fdv}} = 297 \pm 7\,\mathrm{V} \tag{B.2}$$

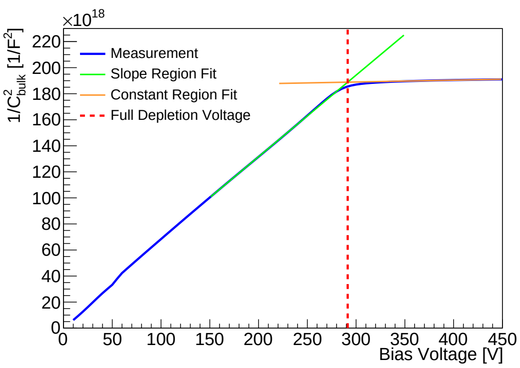

(a) Explanation of full depletion voltage measurements.

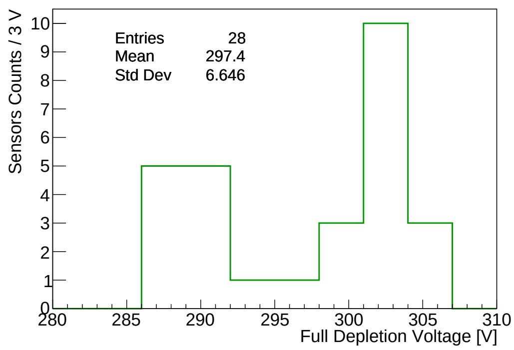

(b) Full Depletion Voltage.

Figure B.2: Explanation of the procedure to retrieve the full depletion voltage from capacitance-voltage characteristics, and full depletion voltage measured for several non-irradiated R&D sensors.

B.2 Capacitance-Voltage Characteristics

Figure B.3 shows the inverse squared of the bulk capacitance as a function of the bias voltage for several non-irradiated and irradiated R&D mini-sensors. This quantity exhibits a kink when the full depletion voltage is reached (see Equation 2.20).
The full depletion voltage is about 300 V in the non-irradiated sensor (see Equation B.2). The full depletion voltage is increased in hadron-irradiated sensors by bulk damage (see Section 2.6) and it is outside the range of the measurements performed. The full depletion voltage measured in gamma-irradiated sensors is about 30 V smaller than in the non-irradiated sensor. A similar effect has been observed in other studies [186].

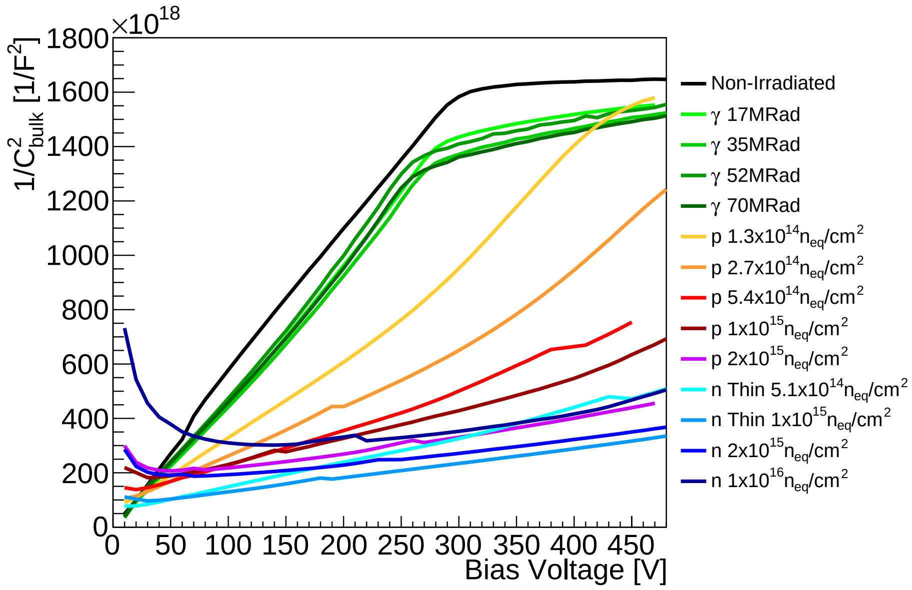

Figure B.3: Inverse squared of the bulk capacitance as a function of the bias voltage for R&D mini-sensors non-irradiated (black) and irradiated with gamma-rays (UJP, green), protons (KIT, red), and neutrons (JSI, blue). The measurement step size is 10 V.

B.3 Average Inter-Strip and Coupling Capacitance

Figure B.4 shows the inter-strip and coupling capacitance measured with a bias voltage of 500 V in the default ATLAS zone for non-irradiated and irradiated R&D mini-sensors (see Figure 5.6). The average inter-strip and coupling capacitances in the default ATLAS zone are then quantified:

$$C_{\text{inter-strip}} = 0.747 \pm 0.004\,\text{pF}\,\text{cm}^{-1} \qquad C_{\text{coupling}} = 24.28 \pm 0.14\,\text{pF}\,\text{cm}^{-1} \tag{B.3}$$

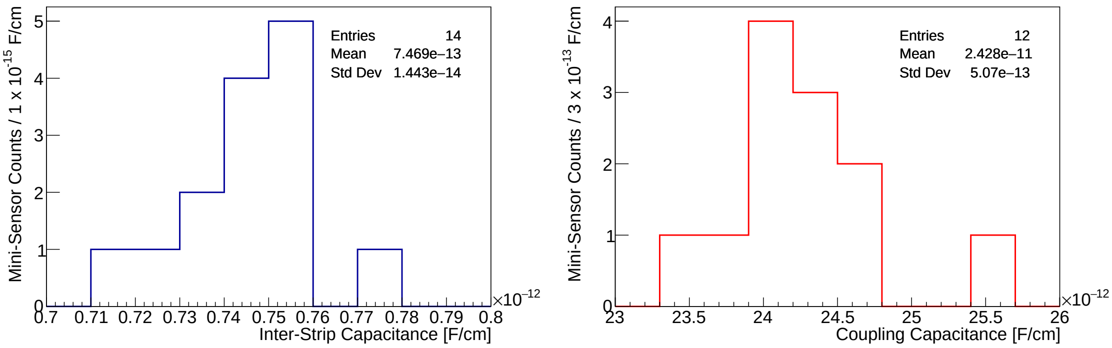

(a) Inter-strip capacitance.

(b) Coupling capacitance.

Figure B.4: Inter-strip and coupling capacitance measured with a bias voltage of 500 V in the default ATLAS zone for non-irradiated and irradiated R&D mini-sensors.

B.4 Temperature Dependence of $I_{leakage}$ and $R_{inter\text{-}strip}$

Figure B.5 shows the leakage current and the inter-strip resistance as a function of the cooling chuck temperature. The measurements are performed with an R&D Thin mini-sensor irradiated with neutrons (JSI) to a NIEL fluence of $1 \times 10^{15}\ n_{eq}/cm^2$ and a bias voltage of 400 V.
The leakage current increases as the temperature increases with an exponential dependence (see Equation 2.19). Similarly, the inter-strip resistance decreases as the temperature increases, following an exponential dependence.

Highly hadron-irradiated sensors exhibit a decreasing inter-strip resistance at high bias voltages (see Figure 5.7b). This can be explained by a rise of the temperature of the silicon bulk caused by self-heating, which in turn is caused by the high leakage current. For example, a rise of temperature from −20 °C to −18 °C decreases the inter-strip resistance from 4444 MΩ cm to 3230 MΩ cm.

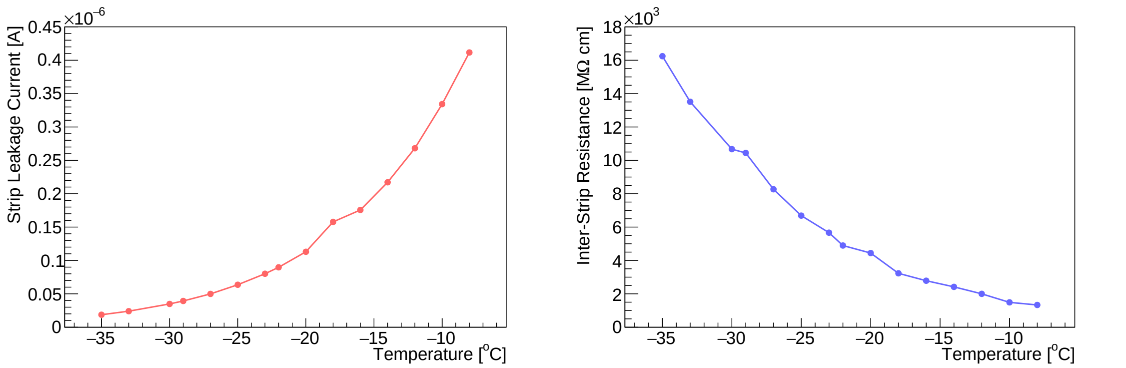

(a) Strip leakage current.

(b) Inter-strip resistance.

Figure B.5: Strip leakage current and inter-strip resistance in the default ATLAS zone as a function of the temperature for an R&D Thin mini-sensor irradiated with neutrons (JSI) to a NIEL fluence of $1 \times 10^{15}\ n_{eq}/cm^2$ and a bias voltage of 400 V.

B.5 TID and NIEL Fluence Dependence of $R_{\text{inter-strip}}$

Figure B.6a shows the inter-strip resistance measured in the default ATLAS zone as a function of the TID in irradiated R&D mini-sensors. The inter-strip resistance in proton-irradiated sensors is one order of magnitude or more larger than the one in sensors irradiated with gamma-rays at a similar TID.
Figure B.6b shows the inter-strip resistance measured in the default ATLAS zone as a function of the NIEL fluence in hadron-irradiated R&D mini-sensors. At a given NIEL fluence, the inter-strip resistance of proton- and neutron-irradiated sensors differs by less than a factor three. Moreover, the inter-strip resistance measured for Thin sensors is generally larger than the one measured in sensors with a standard thickness (see Figure 5.7b). The measurements for the R&D mini-sensors irradiated at a NIEL fluence of $2 \times 10^{15}\,n_{eq}/cm^2$, for which both the proton- and the neutron-irradiated sensors have standard thickness, differ by only about 10%.
Based on these results, it can be hypothesized that in hadron-irradiated sensors the inter-strip resistance depends mostly on the NIEL fluence and marginally on the TID.

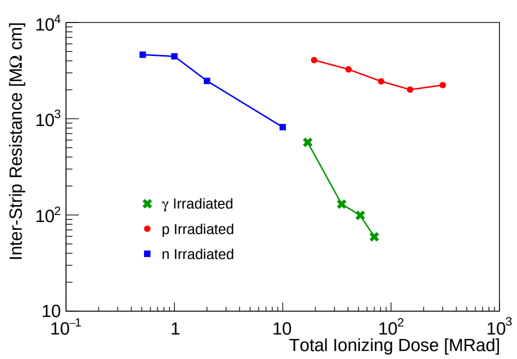

(a) As a function of the TID.

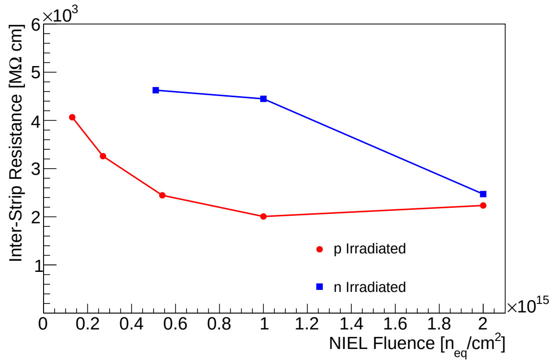

(b) As a function of the NIEL fluence.

Figure B.6: Inter-strip resistance measured with a bias voltage of 500 V in the default ATLAS zone as a function of the TID and of the NIEL fluence in irradiated R&D mini-sensors.

B.6 Implant and Bias Resistance

The implant resistance is measured by contacting the DC pads at the two extremes of strip with two probe needle and then measuring the resistance with the same procedure followed for the inter-strip resistance (see Section 5.2.1). A high implant resistance would increase the resistance in series to the front-end channels, therefore increasing the noise of a silicon module (see Section 2.5). A low implant resistance is commonly preferred. The sensors for the ATLAS ITk Strip Detector are required to have an implant resistance lower than $20\,\mathrm{k\Omega\,cm^{-1}}$ [49].
Figure B.7a shows the implant resistance in the five zones of a non-irradiated R&D

mini-sensor. All five zones satisfy the ATLAS ITk Strip specification. For geometrical reasons, the zones with an enlarged strip implant exhibit a lower implant resistance.

The bias resistance is the resistance between a strip implant and the bias line. It is measured by contacting the DC pad of a strip with a probe needle and applying a small slave voltage to it. The measurements then proceed as the inter-strip resistance measurements (see Section 5.2.1). The sensors for the ATLAS ITk Strip Detector are required to have an implant resistance between 1 and 2 MΩ [49].
Figure B.7b shows the bias resistance in the five zones of non-irradiated and irradiated R&D mini-sensors. The results obtained in different zones agree within 0.03 MΩ, with the exception of Zone 5 (Extreme Wide Implant) in gamma-irradiated sensors. In this case, because of the very low inter-strip resistance (see Appendix B.10), the bias resistors of the neighboring strips also contribute to the measured value. A few sensors exhibit a bias resistance larger than the ATLAS ITk Strip specification. However, the measurements are performed with a temperature of −20 °C and the bias resistance decreases as the temperature increases [112, 187]. It can be assumed that at room temperature all the sensors would satisfy the requirement for the ATLAS ITk Strip Detector.

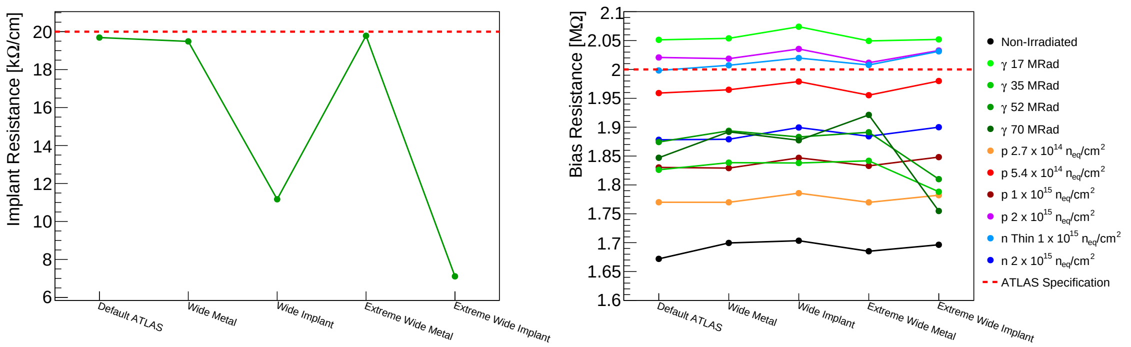

(a) Implant resistance for a non-irradiated sensor.

(b) Bias resistance for several non-irradiated and irradiated sensors.

Figure B.7: Implant and bias resistance in the five zones of R&D mini-sensors with a bias voltage of 500 V. The lines connecting the data point are added for visibility. The red dashed line indicates the upper limits specified for the ATLAS ITk Strip Detector.

B.7 Noise Measurements

Noise is one of the most important parameters of a silicon module. The noise generated by strips in the different zones is estimated by wire-bonding a non-irradiated R&D mini-sensor to an Alibava readout board. Figure B.8a shows the noise measured for all the strips. A few strips with very high noise are observed close to the zone boundaries. This is related to an increased input capacitance caused by the presence of the bias rail crossing the strip length.

Figure B.8b shows the average noise measured in each zone, normalized to the noise the default ATLAS zone. The presence of an enlarged strip implant significantly increases the noise due to the increased inter-strip capacitance.
The inter-strip capacitance exhibits large values in the zones with a large strip implant, with an increase with respect to the default ATLAS zone by 7% and 22% for Zone 3 and Zone 5, respectively. In the zones with only a wide aluminum layer (Zone 2 and Zone 4) only a marginal increase in noise is observed (< 2%). To understand this phenomenon, all the components of the inter-strip capacitance must be discussed. In this thesis, the inter-strip capacitance is defined as the capacitance between the aluminum layers of adjacent strips (see Section 5.2.1). However, the total inter-strip capacitance depends also on the capacitance between two adjacent strip implants. The aluminum overhang depletes its underlying electron accumulation layer and decouples the implants, thus decreasing the implant-implant capacitance. As the aluminum overhang width increases, the increase of the aluminum-aluminum inter-strip capacitance is partially compensated by a decrease of the implant-implant capacitance [164, 165]. The result is that the total inter-strip capacitance, and hence the noise, exhibits only a marginal dependence on the aluminum overhang width.

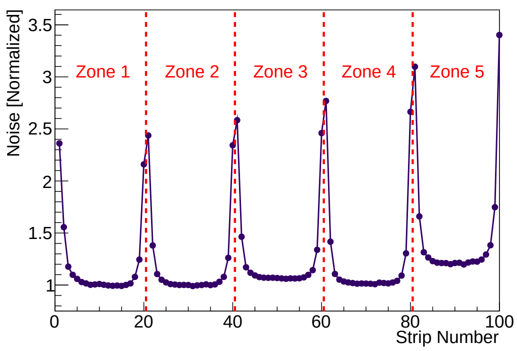

(a) Noise as a function of the strip number. The noise values are normalized to the average noise of the ten innermost strips of the default ATLAS zone (Zone 1).

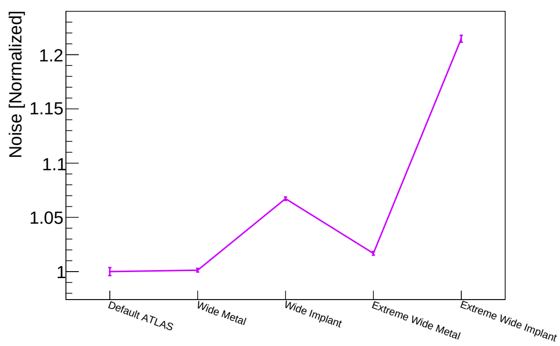

(b) Average noise measured in the five zones, normalized to the noise in the default ATLAS zone. Only the ten innermost strips of each zone are used to compute the average. The lines connecting the data points are added for visibility.

Figure B.8: Noise measurements performed with a non-irradiated R&D mini-sensor wire-bonded to an Alibava readout board with a bias voltage of 400 V.

B.8 Additional Inter-Strip Capacitance Results

Figure B.9 shows the inter-strip capacitance as a function of the bias voltage in the five zones of irradiated R&D mini-sensors. As in the results discussed in Section 5.2.2, the inter-strip capacitance increases as the aluminum layer and strip implant widths increase. Additionally to the default ATLAS zone, also Zone 2 (Wide Metal) satisfies the ATLAS ITk Strip specification. For bias voltages > 300 V the inter-strip capacitance is constant and does not depend on the radiation dose and type.

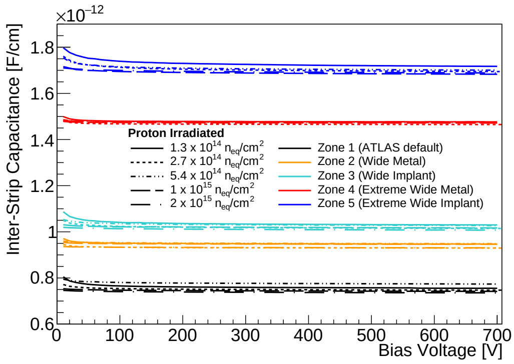

(a) Proton (KIT) irradiated.

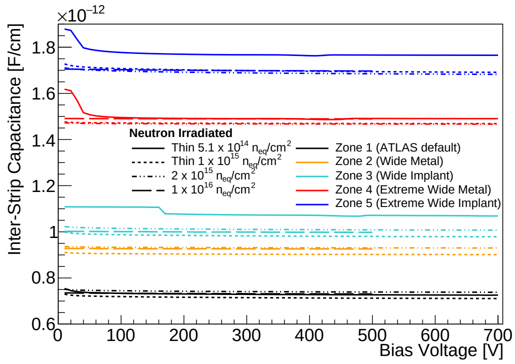

(b) Neutron (JSI) irradiated.

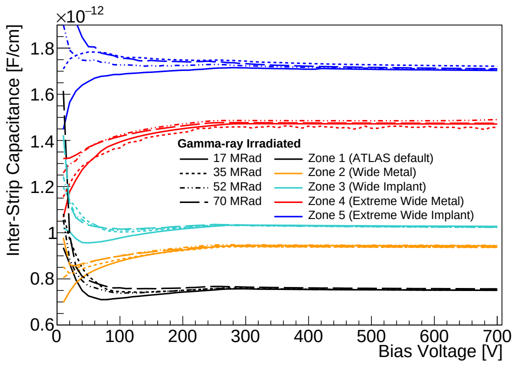

(c) Gamma-ray (UJP) irradiated.

Figure B.9: Inter-strip capacitance as a function of the bias voltage in the five zones of irradiated R&D mini-sensors. Different colors indicate the different zones and different line styles indicates the different radiation levels.

B.9 Additional Coupling Capacitance Results

Figure B.10 shows the coupling capacitance as a function of the bias voltage in the five zones of irradiated R&D mini-sensors. As in the results discussed in Section 5.2.2, the coupling capacitance depends primarily by the overlap width between the aluminum layer and the strip implant. All five zones satisfy the ATLAS ITk Strip specification. For most sensors the coupling capacitance is constant for bias voltages > 300 V and does not depend on the radiation dose and type.

For gamma-irradiated sensors the regions with a wide aluminum layer (Zones 2 and 4) exhibit a coupling capacitance about 20% larger with respect to measurements with non-irradiated and neutron- and proton-irradiated sensors. Moreover, the coupling capacitance measured in Zone 4 (Extreme Wide Metal) of gamma-irradiated R&D mini-sensors decreases as the voltage increases. These effects are related to the electron accumulation layer underlying the aluminum overhang, which acts as an additional coupling between the strip implant and the aluminum layer.

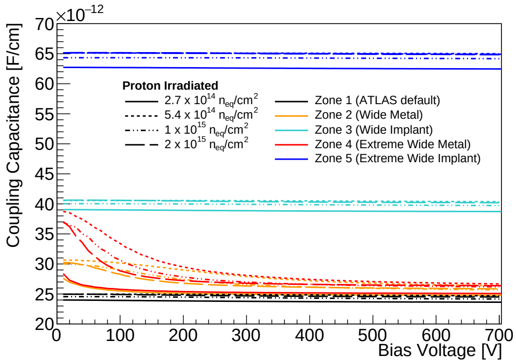

(a) Proton (KIT) irradiated.

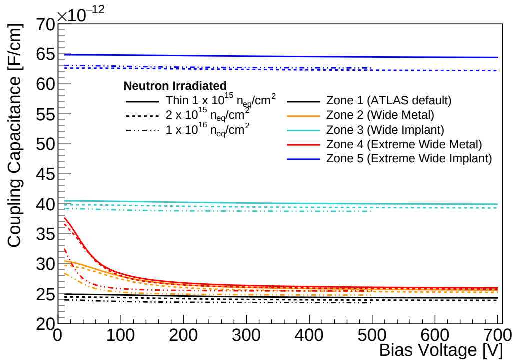

(b) Neutron (JSI) irradiated.

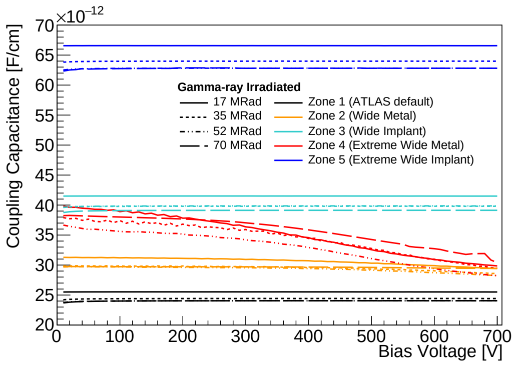

(c) Gamma-ray (UJP) irradiated.

Figure B.10: Coupling capacitance as a function of the bias voltage in the five zones of irradiated R&D mini-sensors. Different colors indicate the different zones and different line styles indicates the different radiation levels.

B.10 Additional Inter-Strip Resistance Results

The Figures in this Section show the inter-strip resistance measured in the five zones of non-irradiated and irradiated R&D mini-sensors. The measurements exhibit the same behavior as the results discussed in Section 5.2.2. It is observed that the increase of inter-strip resistance by the aluminum overhang is less pronounced in gamma-irradiated sensors subject to a low TID. The reason is that the lower the TID, the lower the density of the electron accumulation layer, therefore its depletion by the aluminum overhang plays a smaller role in the inter-strip resistance value.

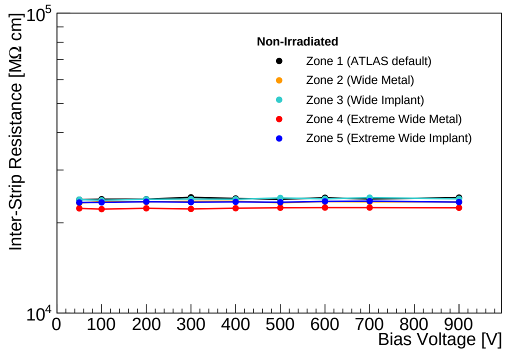

(a) Inter-strip resistance.

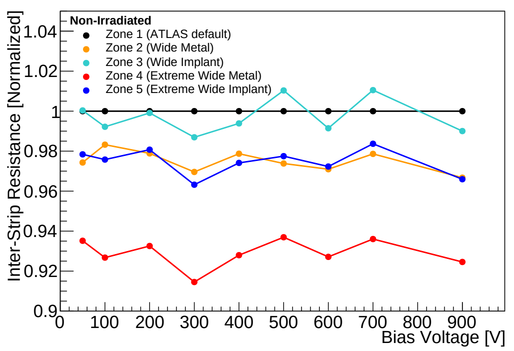

(b) Inter-strip resistance normalized to the values obtained in the default ATLAS zone.

Figure B.11: Inter-strip resistance as a function of the bias voltage in the five zones of a non-irradiated R&D mini-sensor.

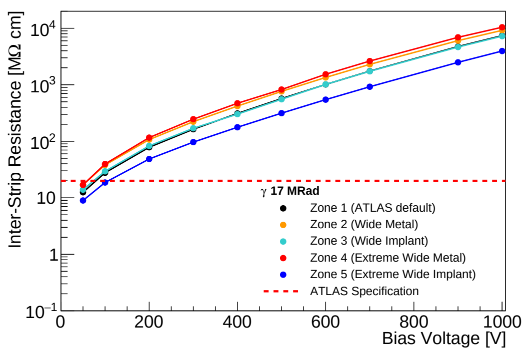

(a) Inter-strip resistance.

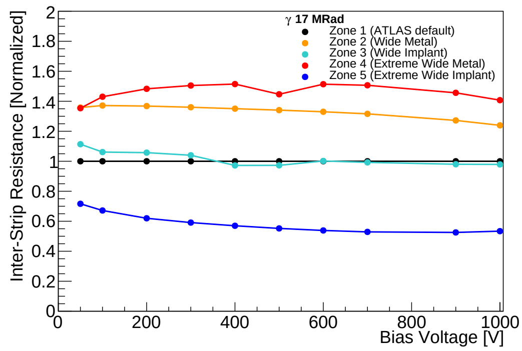

(b) Inter-strip resistance normalized to the values obtained in the default ATLAS zone.

Figure B.12: Inter-strip resistance as a function of the bias voltage in the five zones of an R&D mini-sensor irradiated with gamma-rays (UJP) at a TID of 17 MRad (170 kGy).

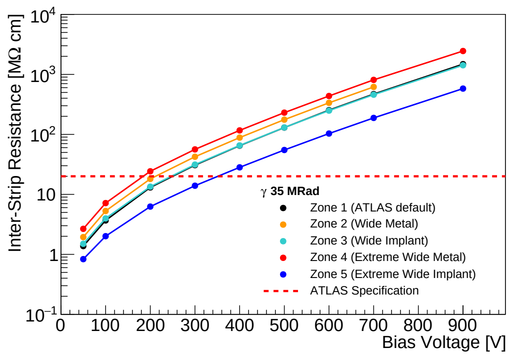

(a) Inter-strip resistance.

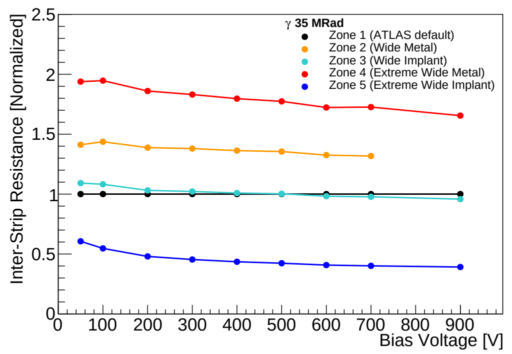

(b) Inter-strip resistance normalized to the values obtained in the default ATLAS zone.

Figure B.13: Inter-strip resistance as a function of the bias voltage in the five zones of an R&D mini-sensor irradiated with gamma-rays (UJP) at a TID of 35 MRad (350 kGy).

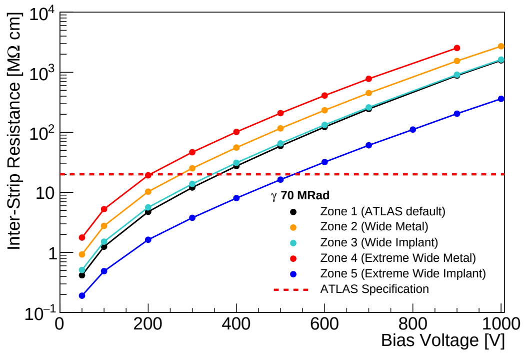

(a) Inter-strip resistance.

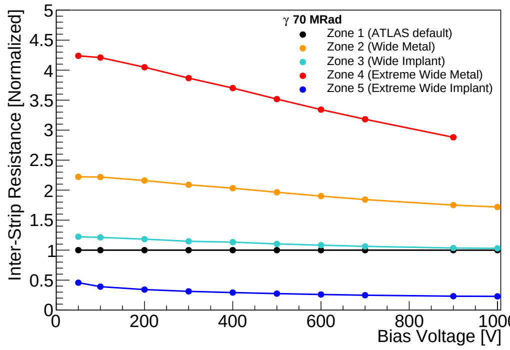

(b) Inter-strip resistance normalized to the values obtained in the default ATLAS zone.

Figure B.14: Inter-strip resistance as a function of the bias voltage in the five zones of an R&D mini-sensor irradiated with gamma-rays (UJP) at a TID of 70 MRad (700 kGy).

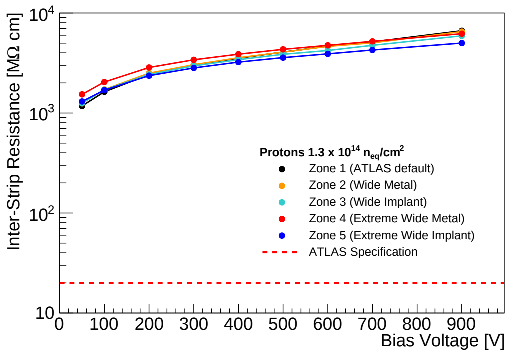

(a) Inter-strip resistance.

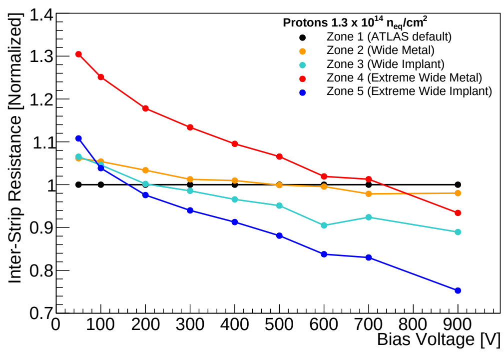

(b) Inter-strip resistance normalized to the values obtained in the default ATLAS zone.

Figure B.15: Inter-strip resistance as a function of the bias voltage in the five zones of an R&D mini-sensor irradiated with protons (KIT) at a NIEL fluence of $1.3 \times 10^{14}\,\mathrm{n_{eq}/cm^2}$.

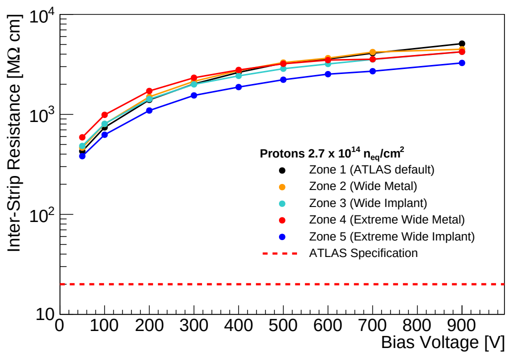

(a) Inter-strip resistance.

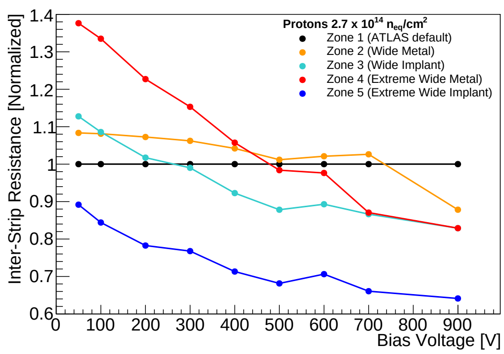

(b) Inter-strip resistance normalized to the values obtained in the default ATLAS zone.

Figure B.16: Inter-strip resistance as a function of the bias voltage in the five zones of an R&D mini-sensor irradiated with protons (KIT) at a NIEL fluence of $2.7 \times 10^{14}\,\mathrm{n_{eq}/cm^2}$.

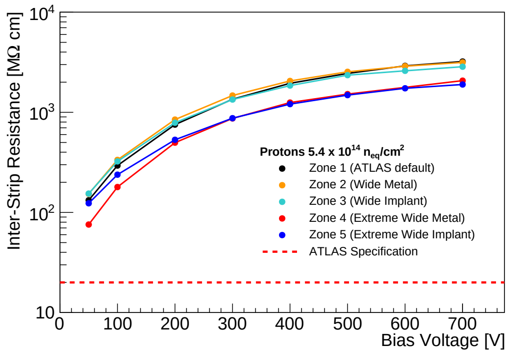

(a) Inter-strip resistance.

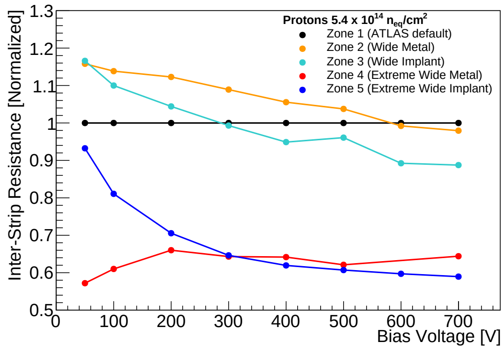

(b) Inter-strip resistance normalized to the values obtained in the default ATLAS zone.

Figure B.17: Inter-strip resistance as a function of the bias voltage in the five zones of an R&D mini-sensor irradiated with protons (KIT) at a NIEL fluence of $5.4 \times 10^{14}\ n_{eq}/cm^2$.

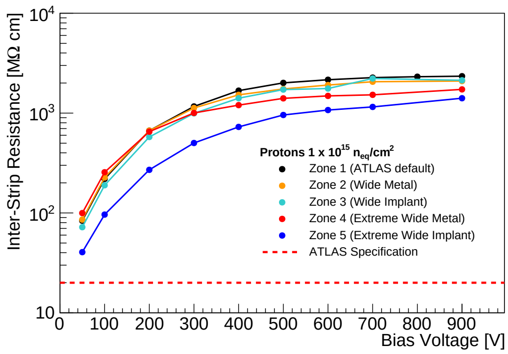

(a) Inter-strip resistance.

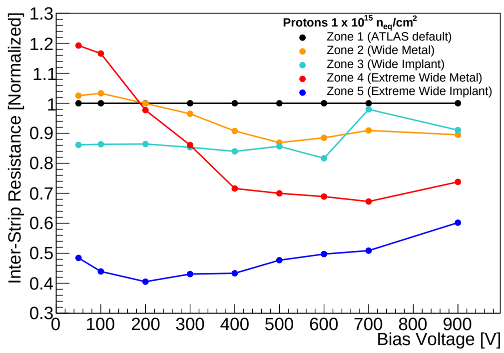

(b) Inter-strip resistance normalized to the values obtained in the default ATLAS zone.

Figure B.18: Inter-strip resistance as a function of the bias voltage in the five zones of an R&D mini-sensor irradiated with protons (KIT) at a NIEL fluence of $1 \times 10^{15}\ n_{eq}/cm^2$.

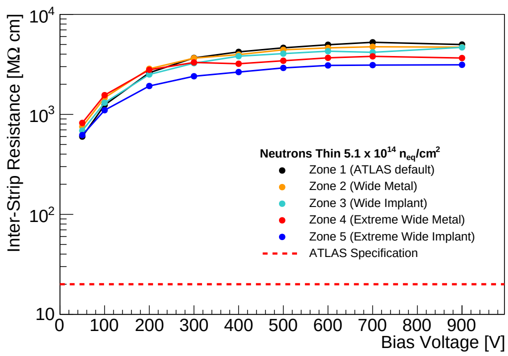

(a) Inter-strip resistance.

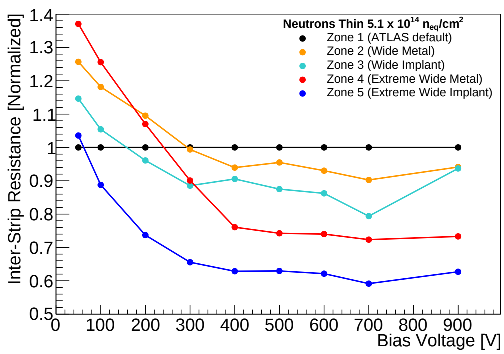

(b) Inter-strip resistance normalized to the values obtained in the default ATLAS zone.

Figure B.19: Inter-strip resistance as a function of the bias voltage in the five zones of an R&D Thin mini-sensor irradiated with neutrons (JSI) at a NIEL fluence of $5.1 \times 10^{14}\ n_{eq}/cm^2$.

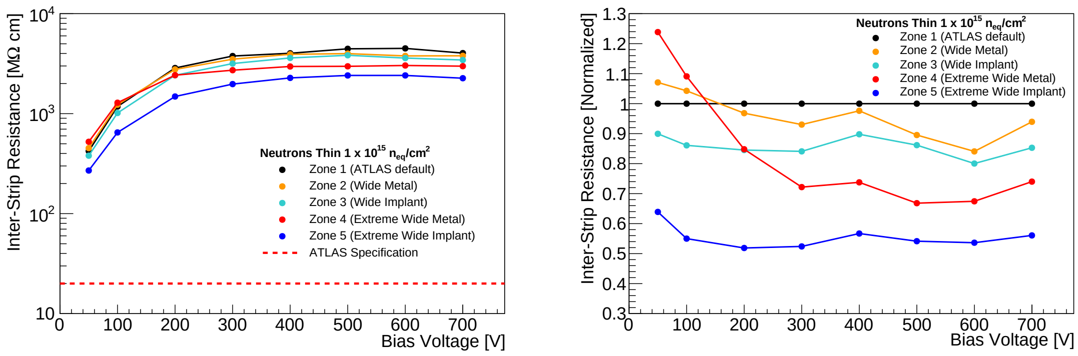

(a) Inter-strip resistance.

(b) Inter-strip resistance normalized to the values obtained in the default ATLAS zone.

Figure B.20: Inter-strip resistance as a function of the bias voltage in the five zones of an R&D mini-sensor irradiated with neutrons (JSI) at a NIEL fluence of $1 \times 10^{15}\ \mathrm{n_{eq}/cm^2}$.

B.11 Additional Test Beam Results

Figures B.21a and B.21b show the efficiency and cluster size as a function of the threshold for the second R&D Short Strip mini-sensor irradiated with protons (KIT) at a NIEL fluence of $1 \times 10^{15}\ \mathrm{n_{eq}/cm^2}$ (the leftmost sensor in Figure 5.14). Figures B.22 and B.23 show the same quantities for a non-irradiated and an irradiated R&D Short Strip mini-sensors operated with a bias voltage of 700 V. The measurements exhibit the same behavior of the results discussed in Section 5.3.1.

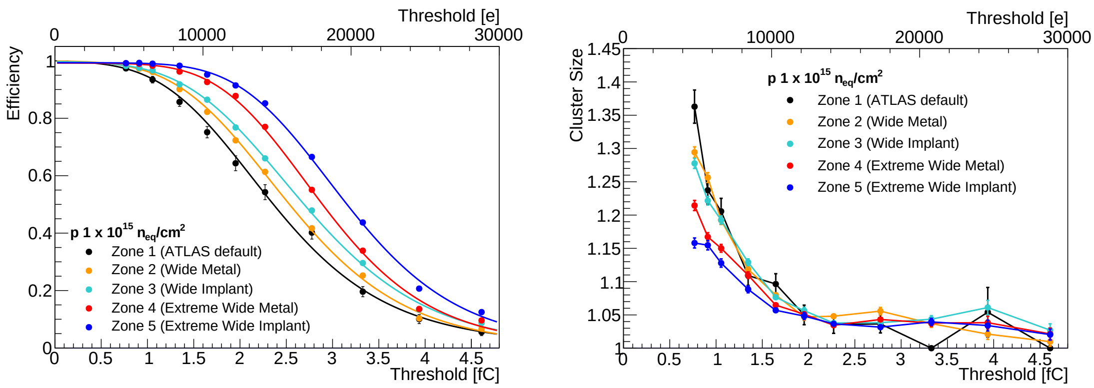

(a) Efficiency as a function of the threshold.

(b) Cluster size as a function of the threshold.

Figure B.21: Efficiency and cluster size as a function of the threshold in the five zones of the second R&D Short Strip mini-sensor irradiated with protons (KIT) at a NIEL fluence of $1 \times 10^{15}\ \mathrm{n_{eq}/cm^2}$ (the leftmost sensor in Figure 5.14).

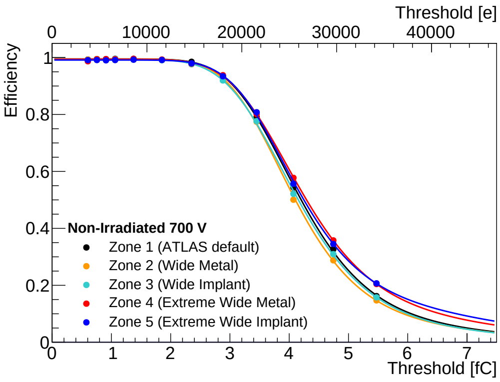

(a) Efficiency as a function of the threshold.

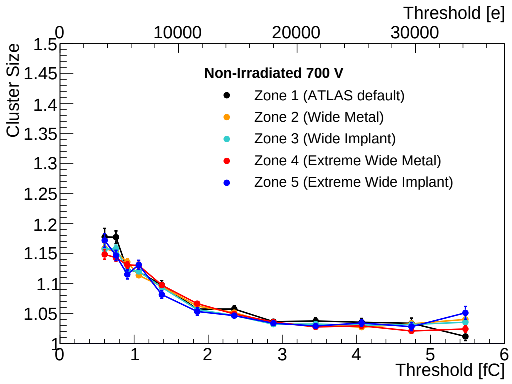

(b) Cluster size as a function of the threshold.

Figure B.22: Efficiency and cluster size as a function of the threshold in the five zones of the non-irradiated R&D Short Strip mini-sensor with a bias voltage of 700 V.

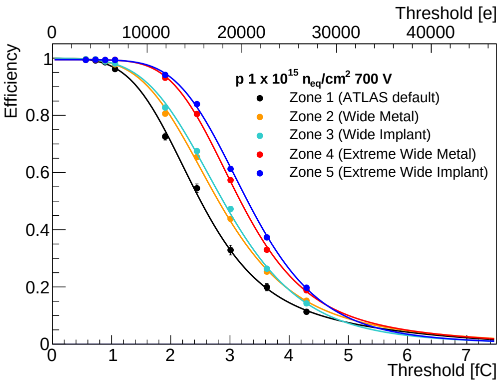

(a) Efficiency as a function of the threshold.

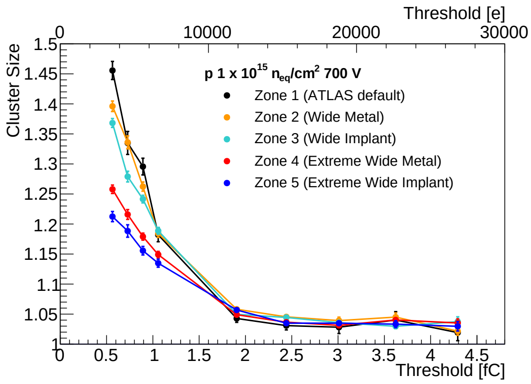

(b) Cluster size as a function of the threshold.

Figure B.23: Efficiency and cluster size as a function of the threshold in the five zones of the second R&D Short Strip mini-sensor irradiated with protons (KIT) at a NIEL fluence of $1 \times 10^{15}\,\mathrm{n_{eq}/cm^2}$ (the leftmost sensor in Figure 5.14) with a bias voltage of 700 V.

BIBLIOGRAPHY

[1] L. Evans and P. Bryant, "LHC Machine", *J. Instrum.*, vol. 3, no. 08, p. S08001, 2008.

[2] C. L. Smith, "Genesis of the Large Hadron Collider", *Philos. T. R. Soc. A*, vol. 373, no. 2032, p. 20140037, 2015.

[3] S. Holmes, R. S. Moore, and V. Shiltsev, "Overview of the Tevatron Collider Complex: Goals, Operations and Performance", *J. Instrum.*, vol. 6, no. 08, p. T08001, 2011.

[4] R. F. Schwitters, "Future hadron collider: the SSC", *AIP Conf. Proc.*, vol. 272, no. 1, pp. 306–320, 1992.

[5] ATLAS Collaboration, "The ATLAS Experiment at the CERN Large Hadron Collider", *J. Instrum.*, vol. 3, no. 08, p. S08003, 2008.

[6] CMS Collaboration, "The CMS Experiment at the CERN LHC", *J. Instrum.*, vol. 3, no. 08, p. S08004, 2008.

[7] ALICE Collaboration, "The ALICE experiment at the CERN LHC", *J. Instrum.*, vol. 3, no. 08, p. S08002, 2008.

[8] LHCb Collaboration, "The LHCb Detector at the LHC", *J. Instrum.*, vol. 3, no. 08, p. S08005, 2008.

[9] ATLAS Collaboration, "Observation of a new particle in the search for the Standard Model Higgs boson with the ATLAS detector at the LHC." *Phys. Lett. B*, vol. 716, pp. 1–29, 2012.

[10] CMS Collaboration, "Observation of a new boson at a mass of 125 GeV with the CMS experiment at the LHC." *Phys. Lett. B*, vol. 716, pp. 30–61, 2012.

[11] J. Pequenao, "Computer generated image of the whole ATLAS detector", CERN-GE-0803012, 2008.

[12] ATLAS Collaboration, “The ATLAS Inner Detector commissioning and calibration”, *Eur. Phys. J. C*, vol. 70, pp. 787–821, 2010.

[13] “The Inner Detector”. https://atlas.cern/discover/detector/inner-detector Accessed: 11-12-2019.

[14] ATLAS Collaboration, “Study of the material of the ATLAS inner detector for Run 2 of the LHC”, *J. Instrum.*, vol. 12, no. 12, p. P12009, 2017.

[15] ATLAS Collaboration, “ATLAS event at 13 TeV - 21 May 2015 - Run 265545 Event 5720351”, ATLAS-PHO-Event-2015-010, 2015.

[16] H. Pernegger, “The Pixel Detector of the ATLAS experiment for LHC Run-2”, *J. Instrum.*, vol. 10, no. 06, p. C06012, 2015.

[17] Y. Takubo, “The Pixel Detector of the ATLAS experiment for the Run2 at the Large Hadron Collider”, *J. Instrum.*, vol. 10, no. 02, p. C02001, 2014.

[18] G. Darbo, “Experience on 3D Silicon Sensors for ATLAS IBL”, *J. Instrum.*, vol. 10, no. 05, p. C05001, 2015.

[19] V. Cindro et al., “The ATLAS Beam Conditions Monitor”, *J. Instrum.*, vol. 3, no. 02, p. P02004, 2008.

[20] ATLAS Collaboration, “Luminosity determination in pp collisions at $\sqrt{s} = 8$ TeV using the ATLAS detector at the LHC”, *Eur. Phys. J. C*, vol. 76, p. 653, 2016.

[21] M. Mikuž et al., “The ATLAS beam conditions monitor”, in *Proceedings of 2007 IEEE NSS/MIC*, vol. 3, 2007, pp. 1914–1917.

[22] ATLAS Collaboration, “Operation and performance of the ATLAS semiconductor tracker”, *J. Instrum.*, vol. 9, no. 08, p. P08009, 2014.

[23] ATLAS Collaboration, “Workers assembling the ATLAS SemiConductor Tracker (SCT) at CERN”, ATLAS-PHO-ach-2015-029, 2015.

[24] K. Sedlak, “Macroassembly and performance of the ATLAS SCT barrels”, *Nucl. Instrum. Meth. A*, vol. 573, no. 1, pp. 280–282, 2007.

[25] ATLAS Collaboration, “Expected performance of the ATLAS experiment: detector, trigger and physics”, CERN-OPEN-2008-020, 2009.

[26] ATLAS Collaboration, “Performance of the ATLAS Transition Radiation Tracker in Run 1 of the LHC: tracker properties”, *J. Instrum.*, vol. 12, no. 05, p. P05002, 2017.

[27] J. M. Stahlman, "Commissioning and Performance of the ATLAS Transition Radiation Tracker with First High Energy pp and Pb-Pb collisions at LHC", *Phys. Procedia*, vol. 37, pp. 506–514, 2012.

[28] ATLAS Collaboration, "Particle Identification Performance of the ATLAS Transition Radiation Tracker", ATLAS-CONF-2011-128, 2011.

[29] R. Achenbach et al., "ATLAS level-1 calorimeter trigger", *J. Instrum.*, vol. 3, no. 03, p. P03001, 2008.

[30] N. Buchanan et al., "Design and implementation of the Front End Board for the readout of the ATLAS liquid argon calorimeters", *J. Instrum.*, vol. 3, no. 03, p. P03004, 2008.

[31] H. Wilkens, "The ATLAS Liquid Argon calorimeter: An overview", *J. Phys. Conf. Ser.*, vol. 160, p. 012043, 2009.

[32] D. Gillberg, "Performance of the ATLAS forward calorimeters in first LHC data", *J. Phys. Conf. Ser.*, vol. 293, p. 012041, 2011.

[33] A. M. Henriques Correia, "The ATLAS Tile Calorimeter", in *Proceedings of ANIMMA 2015*, 2015, pp. 1–7.

[34] D. Rousseau, "The ATLAS liquid argon calorimeter : test beam, installation and commissioning", in *Proceedings of 2007 IEEE NSS/MIC*, vol. 1, 2007, pp. 147–152.

[35] E. Diehl, "ATLAS Muon Detector Commissioning", in *Proceedings of DPF 2009*, 2009.

[36] ATLAS Collaboration, "Studies of the performance of the ATLAS detector using cosmic-ray muons." *Eur. Phys. J. C*, vol. 71, p. 1593, 2010.

[37] ATLAS Collaboration, "Measurements and interpretations of Higgs-boson fiducial cross sections in the diphoton decay channel using 139 fb of pp collision data at $\sqrt{s}$ = 13 TeV with the ATLAS detector", ATLAS-CONF-2019-029, 2019.

[38] ATLAS Collaboration, "Measurements of the Higgs boson inclusive, differential and production cross sections in the 4ℓ decay channel at $\sqrt{s}$ = 13 TeV with the ATLAS detector", ATLAS-CONF-2019-025, 2019.

[39] ATLAS Collaboration, "Measurement of the Higgs boson mass in the $H \to ZZ^* \to 4\ell$ and $H \to \gamma\gamma$ channels with $\sqrt{s}$ = 13 TeV pp collisions using the ATLAS detector", *Phys. Lett. B*, vol. 784, pp. 345–366, 2018.

[40] ATLAS and CMS Collaborations, "Combined Measurement of the Higgs Boson Mass in pp Collisions at $\sqrt{s} = 7$ and 8 TeV with the ATLAS and CMS Experiments", *Phys. Rev. Lett.*, vol. 114, p. 191803, 2015.

[41] ATLAS Collaboration, "Summary plots from the ATLAS Standard Model physics group". https://atlas.web.cern.ch/Atlas/GROUPS/PHYSICS/CombinedSummaryPlots/SM/ Accessed: 17-01-2020.

[42] B. Schmidt, "The High-Luminosity upgrade of the LHC: Physics and Technology Challenges for the Accelerator and the Experiments", *J. Phys. Conf. Ser.*, vol. 706, no. 2, p. 022002, 2016.

[43] HL-LHC Project, "Project Schedule". https://project-hl-lhc-industry.web.cern.ch/content/project-schedule Accessed: 21-03-2020.

[44] W. Herr and B. Muratori, "Concept of luminosity", in *Proceedings of the CERN Accelerator School 2003*, 2003.

[45] G. Apollinari et al., High-Luminosity Large Hadron Collider (HL-LHC): Technical Design Report V. 0.1, ser. CERN Yellow Reports: Monographs, 2017.

[46] P. Ferracin et al., "The HL-LHC Low-β Quadrupole Magnet MQXF: From Short Models to Long Prototypes", *IEEE Trans. Appl. Supercond.*, vol. 29, no. 5, pp. 1–9, 2019.

[47] ATLAS Collaboration, "Projections for measurements of Higgs boson cross sections, branching ratios, coupling parameters and mass with the ATLAS detector at the HL-LHC", ATL-PHYS-PUB-2018-054, 2018.

[48] A. Liss and J. Nielsen, "Physics at a High-Luminosity LHC with ATLAS", ATL-PHYS-PUB-2013-007, 2013.

[49] ATLAS Collaboration, "Technical Design Report for the ATLAS Inner Tracker Strip Detector", CERN-LHCC-2017-005, 2017.

[50] ATLAS Collaboration, "Expected Tracking Performance of the ATLAS Inner Tracker at the HL-LHC", ATL-PHYS-PUB-2019-014, 2019.

[51] A. Greenall, "ATLAS ITk short-strip stave prototype module with integrated DCDC powering and control", *PoS Proc. Sci.*, vol. TWEPP-17, p. 056, 2017.

[52] E. Villani et al., "HVMUX, a high voltage multiplexing for the ATLAS Tracker upgrade", *J. Instrum.*, vol. 12, no. 01, p. C01076, 2017.

[53] J. Dopke et al., "Lessons learned in high frequency data transmission design: ATLAS strips bus tape", *J. Instrum.*, vol. 12, no. 01, p. C01019, 2017.

[54] C. Wanotayaroj et al., “The End-of-Substructure (EoS) Card for the Strip Tracker Upgrade of the ATLAS experiment”, in *Proceedings of 2018 IEEE NSS/MIC*, 2018, pp. 1–3.

[55] ATLAS Collaboration, “The Silicon Microstrip Sensors of the ATLAS Semi-ConductorTracker”, *Nucl. Instrum. Meth. A*, vol. 578, no. 1, pp. 98–118, 2007.

[56] M. Ullán et al., “Ionization damage on ATLAS-SCT front-end electronics considering Low Dose Rate Effects”, *IEEE Trans. Nucl. Sci.*, vol. 49, no. 3, pp. 1106 – 1111, 2002.

[57] ATLAS Collaboration, “Radiation Simulation Public Results”. https://twiki.cern.ch/twiki/bin/view/AtlasPublic/RadiationSimulationPublicResults Accessed: 13-12-2019.

[58] ATLAS Collaboration, “Technical Design Report for the ATLAS Inner Tracker Pixel Detector”, CERN-LHCC-2017-021, 2017.

[59] W. R. Leo, Techniques for Nuclear and Particle Physics Experiments: A How to Approach. Springer, 1987.

[60] F. Hartmann, Evolution of Silicon Sensor Technology in Particle Physics. Springer, 2017.

[61] Wikipedia contributors, “p–n junction — Wikipedia, The Free Encyclopedia”. https://en.wikipedia.org/wiki/P%E2%80%93n_junction 2019, Accessed: 10-12-2019.

[62] C. Leroy and P.-G. Rancoita, Principles of radiation interaction in matter and detection. World Scientific, 2011.

[63] F. Cenna et al., “Weightfield2: A fast simulator for silicon and diamond solid state detector”, *Nucl. Instrum. Meth. A*, vol. 796, pp. 149 – 153, 2015.

[64] Particle Data Group, “Review of Particle Physics”, *Phys. Rev. D*, vol. 98, p. 030001, 2018.

[65] “ESTAR: Stopping Powers and Ranges for Electrons”. Http://physics.nist.gov/PhysRefData/Star/Text/ESTAR.html

[66] H. Spieler, Semiconductor Detector Systems, ser. Semiconductor Science and Technology. Oxford University Press, 2005.

[67] C. Jacoboni et al., “A review of some charge transport properties of silicon”, *Solid State Electron.*, vol. 20, no. 2, pp. 77–89, 1977.

[68] J. Becker, E. Fretwurst, and R. Klanner, “Measurements of charge carrier mobilities and drift velocity saturation in bulk silicon of <111> and <100> crystal orientation at high electric fields”, *Solid State Electron.*, vol. 56, no. 1, p. 104, 2011.

[69] S. Selberherr et al., “The evolution of the MINIMOS mobility model”, *Solid State Electron.*, vol. 33, no. 11, pp. 1425–1436, 1990.

[70] I. G. Kirnas et al., “Concentration dependence of the hall factor in n-type silicon”, *Phys. Status Solidi A*, vol. 23, no. 2, pp. K123–K127, 1974.

[71] J. Lin et al., “Theoretical analysis of hall factor and hall mobility in p-type silicon”, *Solid-State Electron.*, vol. 24, no. 9, pp. 827 – 833, 1981.

[72] W. Shockley, “Currents to Conductors Induced by a Moving Point Charge”, *J. Appl. Phys.*, vol. 9, no. 10, pp. 635–636, 1938.

[73] S. Ramo, “Currents Induced by Electron Motion”, *Proc. of the IRE*, vol. 27, no. 9, pp. 584–585, 1939.

[74] T. Eichhorn, “Development of Silicon Detectors for the High Luminosity LHC”, PhD thesis, Universität Hamburg, 2015.

[75] A. Chilingarov, “Temperature dependence of the current generatedin Si bulk”, *J. Instrum.*, vol. 8, no. 10, p. P10003, 2013.

[76] M. A. Vos et al., “Charge collection with binary readout from a test beam perspective”, ATL-INDET-2003-011, 2003.

[77] M. Moll, “Radiation damage in silicon particle detectors: microscopic defects and macroscopic properties”, PhD thesis, Universität Hamburg, 1999.

[78] A. Vasilescu and G. Lindstroem, “Displacement damage in silicon, on-line compilation”. https://rd50.web.cern.ch/niel/ Accessed: 12-06-2020.

[79] A. Junkes, “Influence of radiation induced defect clusters on silicon particle detectors”, PhD thesis, Universität Hamburg, 2011.

[80] R. Wunstorf, “Systematische Untersuchungen zur Strahlenresistenz von Silizium-Detektoren für die Verwendung in Hochenergiephysik-Experimenten”, PhD thesis, Universität Hamburg, 1992.

[81] G. Kramberger et al., “Effective trapping time of electrons and holes in different silicon materials irradiated with neutrons, protons and pions”, *Nucl. Instrum. Meth. A*, vol. 481, no. 1, pp. 297–305, 2002.

[82] N. Barlow, “Operation of the ATLAS semiconductor tracker”, *PoS Proc. Sci.*, vol. RD09, p. 004, 2009.

[83] J. Zhang, “X-ray Radiation Damage Studies and Design of a Silicon Pixel Sensor for Science at the XFEL”, PhD thesis, Universität Hamburg, 2013.

[84] T. Pöhlsen, “Charge Losses in Silicon Sensors and Electric-Field Studies at the Si-SiO_2 Interface”, PhD thesis, 2013, Universität Hamburg, 2013.

[85] G. Lutz, Semiconductor Radiation Detectors. Springer, 2007.

[86] A. Abdesselam et al., “The barrel modules of the ATLAS semiconductor tracker”, *Nucl. Instrum. Meth. A*, vol. 568, no. 2, pp. 642 – 671, 2006.

[87] Y. Unno et al., “Novel p-stop structure in n-side of silicon microstrip detector”, *Nucl. Instrum. Meth. A*, vol. 541, no. 1, pp. 40–46, 2005.

[88] Y. Iwata et al., “Optimal P-stop pattern for the N-side strip isolation of silicon microstrip detectors”, *IEEE Trans. Nucl. Sci.*, vol. 45, no. 3, pp. 303–309, 1998.

[89] T. Rohe, “Sensor concepts for pixel detectors in high energy physics”, in *Proceedings of PIXEL2002*, 2002.

[90] R. Diener et al., “The DESY II Test Beam Facility”, *Nucl. Instrum. Meth. A*, vol. 922, pp. 265–286, 2019.

[91] R. Alemany et al., “Summary Report of Physics Beyond Colliders at CERN”, CERN-PBC-REPORT-2018-003, 2019.

[92] “AIDA2020 Advanced European Infrastractures for Detectors at Accelerators – CERN”. http://aida2020.web.cern.ch/content/cern Accessed: 17-10-2019.

[93] I. Rubinskiy, “An EUDET/AIDA Pixel Beam Telescope for Detector Development”, *Phys. Procedia*, vol. 37, pp. 923 – 931, 2012.

[94] “EUDET-type beam telescopes”. https://telescopes.desy.de/ Accessed: 09-12-2019.

[95] J. Baudot et al., “First test results Of MIMOSA-26, a fast CMOS sensor with integrated zero suppression and digitized output”, in *Proceedings of 2009 IEEE NSS/MIC*, 2009, pp. 1169–1173.

[96] H. Jansen et al., “Performance of the EUDET-type beam telescopes”, *Eur. Phys. J. Tech. Instrum.*, vol. 3, no. 1, p. 7, 2016.

[97] D. Pitzl, Private Communication, 2019.

[98] M. Mager, “ALPIDE, the Monolithic Active Pixel Sensor for the ALICE ITS upgrade”, *Nucl. Instrum. Meth. A*, vol. 824, pp. 434 – 438, 2016.

[99] Y. Liu, Private Communication, 2019.

[100] M. Backhaus et al., "Development of a versatile and modular test system for ATLAS hybrid pixel detectors", *Nucl. Instrum. Meth. A*, vol. 650, no. 1, pp. 37–40, 2011.

[101] D. Cussans, "Description of the JRA1 Trigger Logic Unit (TLU), v0.2c", EUDET-MEMO-2009-04, 2009.

[102] P. Baesso, D. Cussans, and J. Goldstein, "The AIDA-2020 TLU: a flexible trigger logic unit for test beam facilities", *J. Instrum.*, vol. 14, no. 09, p. P09019, 2019.

[103] P. Ahlburg et al., "EUDAQ – A Data Acquisition Software Framework for Common Beam Telescopes", *J. Instrum.*, vol. 15, no. 01, p. P01038, 2019.

[104] R. Peschke, "Characterisation of the ATLAS ITK Strips Front-End Chip and Development of EUDAQ 2.0 for the EUDET-Style Pixel Telescopes", PhD thesis, Universität Hamburg, 2016.

[105] Y. Liu et al., "EUDAQ2—A flexible data acquisition software framework for common test beams", *J. Instrum.*, vol. 14, no. 10, p. P10033, 2019.

[106] "PS-IRRAD Proton Facility". https://ps-irrad.web.cern.ch/ Accessed: 28-09-2019.

[107] M. Glaser, F. Ravotti, and M. Moll, "Dosimetry assessments in the irradiation facilities at the CERN-PS accelerator", *IEEE Trans. Nucl. Sci.*, vol. 53, no. 4, pp. 2016–2022, 2006.

[108] L. Snoj, G. Žerovnik, and A. Trkov, "Computational analysis of irradiation facilities at the JSI TRIGA reactor", *Appl. Radiat. Isot.*, vol. 70, no. 3, pp. 483–488, 2012.

[109] "KIT – Proton Irradiation". https://www.etp.kit.edu/english/264.php Accessed: 28-09-2019.

[110] "UJP Praha – Terabalt". http://ujp.cz/en/terabalt/ Accessed: 01-10-2019.

[111] P. Allport et al., "Experimental Determination of Proton Hardness Factors at Several Irradiation Facilities", *J. Instrum.*, vol. 14, no. 12, p. P12004, 2019.

[112] M. Mikeštíková et al., "Electrical characterization of surface properties of the ATLAS17LS sensors after neutron, proton and gamma irradiation", *Nucl. Instrum. Meth. A*, vol. 983, p. 164456, 2020.

[113] V. Cindro, "World Irradiation Facilities for Silicon Detectors", *PoS Proc. Sci.*, vol. Vertex2014, p. 026, 2014.

[114] V. Cindro, “Transnational acces to TRIGA MarkII reactor at Jožef Stefan Institute, Ljubljana, Slovenia”, presented at the AIDA-2020 Third Annual Meeting, 2018.

[115] J.-O. Gosewisch, “Investigation of the interstrip isolation of p-type strip sensors”, presented at the 14th "Trento" Workshop on Advanced Silicon Radiation Detectors, 2019.

[116] EUTelescope Developers, “EUTelescope – A Generic Pixel Telescope Data Analysis Framework”. https://github.com/eutelescope/eutelescope

[117] T. Bisanz et al., “EUTelescope: A modular reconstruction framework for beam telescope data”, *J. Instrum.*, vol. 15, no. 09, p. 09020, 2020.

[118] “ILC Soft”. https://ilcsoft.desy.de/ Accessed: 15-10-2019.

[119] “Marlin”. https://ilcsoft.desy.de/portal/software_packages/marlin/ Accessed: 15-10-2019.

[120] “LCIO”. http://lcio.desy.de/ Accessed: 15-10-2019.

[121] “GEAR”. https://ilcsoft.desy.de/portal/software_packages/gear/ Accessed: 15-10-2019.

[122] V. Blobel, “A new fast track-fit algorithm based on broken lines”, *Nucl. Instrum. Meth. A*, vol. 566, no. 1, pp. 14–17, 2006.

[123] C. Kleinwort, “General broken lines as advanced track fitting method”, *Nucl. Instrum. Meth. A*, vol. 673, pp. 107 – 110, 2012.

[124] “GeneralBrokenLines”. http://www.desy.de/~kleinwrt/GBL/doc/cpp/html/ Accessed: 09-10-2019.

[125] S. Spannagel, “Test Beam Measurements for the Upgrade of the CMS Pixel Detector and Measurement of the Top Quark Mass from Differential Cross Sections”, PhD thesis, Universität Hamburg, 2016.

[126] “Millepede II”. https://www.terascale.de/wiki/millepede_ii/ Accessed: 11-10-2019.

[127] R. Brun and F. Rademakers, “ROOT: An object oriented data analysis framework”, *Nucl. Instrum. Meth. A*, vol. 389, no. 1, pp. 81–86, 1997.

[128] L. B. A. Hommels et al., “Detailed studies of full-size ATLAS12 sensors”, *Nucl. Instrum. Meth. A*, vol. 831, pp. 167–173, 2016.

[129] R. F. H. Hunter et al., “First bulk and surface results for the ATLAS ITk Strip stereo annulus sensors”, *Nucl. Instrum. Meth. A*, vol. 924, pp. 142–146, 2019.

[130] W. Lu et al., “Development of the ABCStar front-end chip for the ATLAS silicon strip upgrade”, *J. Instrum.*, vol. 12, no. 04, p. C04017, 2017.

[131] A.-L. Poley et al., “The ABC130 barrel module prototyping programme for the ATLAS strip tracker”, *J. Instrum.*, vol. 15, no. 09, p. P09004, 2020.

[132] A. J. Blue et al., “Test beam evaluation of silicon strip modules for ATLAS phase-II strip tracker upgrade”, *Nucl. Instrum. Meth. A*, vol. 924, pp. 108–111, 2019.

[133] “ITSDAQ Software”. https://gitlab.cern.ch/atlas-itk-strips-daq/itsdaq-sw Accessed: 22-05-2019.

[134] F. Campabadal et al., “Beam tests of ATLAS SCT silicon strip detector modules”, *Nucl. Instrum. Meth. A*, vol. 538, no. 1, pp. 384–407, 2005.

[135] Y. Unno et al., “Beamtest of nonirradiated and irradiated ATLAS SCT microstrip modules at KEK”, *IEEE Trans. Nucl. Sci.*, vol. 49, no. 4, pp. 1868–1875, 2002.

[136] J. Bernabeu et al., “ALIBAVA Silicon Microstrip Readout System for Educational Purposes”, *Nucl. Part. Phys. Proc.*, vol. 273-275, pp. 2563 – 2565, 2016.

[137] S. Spannagel et al., “Allpix^2: A modular simulation framework for silicon detectors”, *Nucl. Instrum. Meth. A*, vol. 901, pp. 164 – 172, 2018.

[138] Geant4 Collaboration, “Physics Reference Manual Release 10.6”, 2019.

[139] K. Hara et al., “Charge collection and field profile studies of heavily irradiated strip sensors for the ATLAS inner tracker upgrade”, *Nucl. Instrum. Meth. A*, vol. 831, pp. 181 – 188, 2016.

[140] A. Affolder et al., “Silicon detectors for the sLHC”, *Nucl. Instrum. Meth. A*, vol. 658, no. 1, pp. 11–16, 2011.

[141] V. Cindro et al., “Measurement of the charge collection in irradiated miniature sensors for the upgrade of the ATLAS phase-II strip tracker”, *Nucl. Instrum. Meth. A*, vol. 924, pp. 153 – 159, 2019.

[142] J. Kaplon, Private Communication, 2020.

[143] A. Abdesselam et al., “The Data acquisition and calibration system for the ATLAS semiconductor tracker”, *J. Instrum.*, vol. 3, no. 01, p. P01003, 2008.

[144] Z. Liang, “Performance and operation experience of the ATLAS Semiconductor Tracker”, *Int. J. Mod. Phys. Conf. Ser.*, vol. 31, p. 1460295, 2014.

[145] T. Akimoto et al., “Beam study of irradiated ATLAS-SCT prototypes”, *Nucl. Instrum. Meth. A*, vol. 485, no. 1, pp. 67 – 72, 2002.

[146] J. Dopke, “Re-timing testbeam data”, presented at the 4th Beam Telescopes and Test Beams Workshop, 2016.

[147] C. T. Klein, “Investigation of performance and the influence of environmental conditions on strip detectors for the ATLAS Inner Tracker Upgrade”, PhD thesis, University of Cambridge, 2019.

[148] C. Sawyer, Private Communication, 2020.

[149] K. Hara et al., “Charge collection study with the ATLAS ITk prototype silicon strip sensors ATLAS17LS”, *Nucl. Instrum. Meth. A*, vol. 983, p. 164422, 2020.

[150] S. Wonsak, “The ATLAS ITk Strip Detector System for the Phase-II LHC Upgrade”, *PoS Proc. Sci.*, vol. Vertex2019, p. 017, 2020.

[151] C. Sawyer, “The ATLAS ITk Strip Detector System for the Phase-II LHC Upgrade”, presented at the 15th "Trento" Workshop on Advanced Silicon Radiation Detectors, 2020.

[152] Tracker Group of the CMS Collaboration, “Impact of low-dose electron irradiation on n+p silicon strip sensors”, *Nucl. Instrum. Meth. A*, vol. 803, pp. 100 – 112, 2015.

[153] Y. Unno, “ATLAS17LS - Large-format prototype silicon strip sensors for the long-strip barrel section of the ATLAS ITk strip detector”, presented at the 12th International "Hiroshima" Symposium on the Development and Application of Semiconductor Tracking Detectors, 2019.

[154] A.-L. Poley et al., “Investigations into the impact of locally modified sensor architectures on the detection efficiency of silicon micro-strip sensors”, *J. Instrum.*, vol. 12, no. 07, p. P07006, 2017.

[155] A.-L. Poley, “Studies of adhesives and metal contacts on silicon strip sensors for the ATLAS Inner Tracker”, PhD thesis, Humboldt-Universität zu Berlin, 2018.

[156] D. Passeri et al., “Physical modeling of silicon microstrip detectors: Influence of the electrode geometry on critical electric fields”, *IEEE Trans. Nucl. Sci.*, vol. 47, no. 4, pp. 1468–1473, 2000.

[157] K. Ranjan et al., “Analysis and comparison of the breakdown performance of semi-insulator and dielectric passivated Si strip detectors”, *Nucl. Instrum. Meth. A*, vol. 495, no. 3, pp. 191–215, 2002.

[158] M. Bergholz, “Vergleich relevanter Parameter von Multipixelsensoren für Spurdetektoren nach Bestrahlung mit hohen Proton- und Neutronflüssen”, PhD thesis, Brandenburgische Technische Universität, 2015.

[159] M. Mikeštíková et al., "Study of surface properties of ATLAS12 strip sensors and their radiation resistance", *Nucl. Instrum. Meth. A*, vol. 831, pp. 197–206, 2016.

[160] E. Barberis et al., "Capacitances in silicon microstrip detectors", *Nucl. Instrum. Meth. A*, vol. 342, no. 1, pp. 90–95, 1994.

[161] M. Mikeštíková, Z. Kodek, and J. Št'astný, "Evaluation of Bulk and Surface Radiation Damage of Silicon Sensors for the ATLAS Upgrade", *PoS Proc. Sci.*, vol. Vertex2014, p. 050, 2015.

[162] D. Passeri et al., "Comprehensive modeling of silicon microstrip detectors", in *Proceedings of 1996 IEEE NSS/MIC*, vol. 1, 1996, pp. 118–122.

[163] R. Dalal et al., "Combined effect of bulk and surface damage on strip insulation properties of proton irradiated n^+-p silicon strip sensors", *J. Instrum.*, vol. 9, no. 04, p. P04007, 2014.

[164] S. Chatterji et al., "Analysis of interstrip capacitance of Si microstrip detector using simulation approach", *Solid State Electron.*, vol. 47, no. 9, pp. 1491–1499, 2003.

[165] D. Passeri et al., "Optimization of overhanging-metal microstrip detectors: test and simulation", *IEEE Trans. Nucl. Sci.*, vol. 48, no. 3, pp. 249–253, 2001.

[166] ATLAS Collaboration, "Beam-induced and cosmic-ray backgrounds observed in the ATLAS detector during the LHC 2012 proton-proton running period", *J. Instrum.*, vol. 11, no. 05, p. P05013, 2016.

[167] ATLAS Collaboration, "Comparison between simulated and observed LHC beam backgrounds in the ATLAS experiment at E_{beam} = 4 TeV", *J. Instrum.*, vol. 13, no. 12, p. P12006, 2018.

[168] ATLAS Collaboration, "A beam halo event of the ATLAS Experiment in 3D", ATLAS-PHO-EVENTS-2014-025, 2014.

[169] S. Gibson et al., "Beam-Gas Background Observations at LHC", in *Proceedings of IPAC 2017*, 2017, p. TUPVA032.

[170] ATLAS Collaboration, "Selection of jets produced in 13TeV proton-proton collisions with the ATLAS detector", ATLAS-COM-CONF-2015-024, 2015.

[171] ATLAS Collaboration, "Search for New Phenomena in Monojet plus Missing Transverse Momentum Final States using 10fb^{-1} of pp Collisions at $\sqrt{s}$ = 8 TeV with the ATLAS detector at the LHC", ATLAS-CONF-2012-147, 2012.

[172] R. Caminal Armadans, "Searches for monojets and monophotons with the ATLAS detector", *PoS Proc. Sci.*, vol. DIS2013, p. 119, 2013.

[173] ATLAS Collaboration, "Characterisation and mitigation of beam-induced backgrounds observed in the ATLAS detector during the 2011 proton-proton run." *J. Instrum.*, vol. 8, no. 07, p. P07004, 2013.

[174] P. Laycock et al., "ATLAS data preparation in run 2", *J. Phys. Conf. Ser.*, vol. 898, no. 4, p. 042050, 2017.

[175] F. Lasagni Manghi, "LUCID: The ATLAS Luminosity Detector", *PoS Proc. Sci.*, vol. ICHEP2018, p. 280, 2019.

[176] A. Duncan, "A search for top-antitop quark resonances with the ATLAS detector at the LHC", PhD thesis, University of Glasgow, 2019.

[177] J. Jeong, "The offline analysis on Beam Induced Background of all runs of 2016 in the ATLAS Semiconductor Tracker", ATL-COM-INDET-2017-047, 2017.

[178] ATLAS Collaboration, "Athena - The ATLAS Experiment's main offline software repository". https://gitlab.cern.ch/atlas/athena

[179] ATLAS Collaboration, "Non-collision backgrounds as measured by the ATLAS detector during the 2010 proton-proton run", ATLAS-CONF-2011-137, 2011.

[180] ATLAS Collaboration, "Beam backgrounds in the ATLAS detector during LHC loss map tests at $\beta^* = 40$ cm and $\beta^* = 80$ cm at $E_{\text{beam}} = 6.5$ TeV", ATL-DAPR-PUB-2017-001, 2017.

[181] R. Kwee-Hinzmann et al., "Machine-induced Background Simulation Studies for LHC Run 1, Run 2 and HL-LHC", CERN-ACC-2017-0025, 2017.

[182] R. Bruce et al., "Sources of Machine-Induced Background in the ATLAS and CMS Detectors at the CERN Large Hadron Collider", *Nucl. Instrum. Meth. A*, vol. 729, pp. 825–840, 2013.

[183] A. Abdesselam, "ATLAS SCT Endcap Module Production", ATL-INDET-PUB-2006-007, 2006.

[184] E. Yildirim, "Collected Charge and Lorentz Angle Measurement on Non-irradiated and Irradiated ATLAS Silicon Micro-Strip Sensors for the HL-LHC", PhD thesis, Universität Hamburg, 2016.

[185] J. Fernandez-Tejero et al., "Humidity sensitivity of large area silicon sensors: Study and implications", *Nucl. Instrum. Meth. A*, vol. 978, p. 164406, 2020.

[186] M. Mikeštíková, "Preliminary results of bulk damage study in ^{60}Co irradiated n-in-p silicon strip sensors", presented at the 34th RD50 Workshop, 2019.

[187] K.-H. Hoffmann, “Development of new sensor designs and investigations on radiation hard silicon strip sensors for CMS at the Large Hadron Collider during the high luminosity phase”, PhD thesis, Karlsruher Institut für Technologie, 2013.

Eidesstattliche Versicherung

Hiermit versichere ich an Eides statt, die vorliegende Dissertationsschrift selbst verfasst und keine anderen als die angegebenen Hilfsmittel und Quellen benutzt zu haben.

Die eingereichte schriftliche Fassung entspricht der auf dem elektronischen Speichermedium.

Die Dissertation wurde in der vorgelegten oder einer ähnlichen Form nicht schon einmal ineinem früheren Promotionsverfahren angenommen oder als ungenügend beurteilt.

Hamburg, den 27.04.2020

Edoardo Rossi

ACKNOWLEDGMENTS

I would like to thank Ingrid-Maria Gregor for her supervision and for making me part of DESY and ATLAS. I would like also to thank Erika Garutti for the advices and for the evaluation of this thesis and I would like to thank the member of the commission of the Disputation: Dieter Horns, Bernd Kniehl, and Christian Sander.

First, I would like to thank Yi Liu for always being willing to help and to reply technical questions on telescope, silicon, and China.
I would like to thank Luise Poley for her support and organization of the R&D sensors, and for her very useful advices.
I would like to thank the DESY ATLAS group for the help I received over the years. In particular, I would like to thank Sergio Diez, Dario Ariza for his tremendous support with shipments, Xiaocong Ai for her work on the test beam radial reconstruction, and Torsten Külper for the outstanding and patient help in the laboratory. A special thank goes to the very few smokers for the many daily breaks over the years: Ahmet Bayrak, Namgyun Jeong, and Roger Naranjo.
I would like to thank the ITk Strip test beam group for the many nights of Eurovision music, junk food, and countless thought-provoking surprises during data taking.
I would like to thank the ATLAS group in Zeuthen, which helped me many times and provided support in crucial aspects of the thesis. In decreasing height order (to the best of my recollection): Martin Renzmann, Marko Milovanović, Ingo Bloch, Dennis Sperlich, Thorsten Kuhl, Martin Stegler, Ben Brüers, Paul Kranz, and Sam Yanwing Ng.
During my work I received help from many people in the ATLAS Collaboration and unfortunately I can not mention everyone. To name a few, I would like to thank Jürgen Thomas and the RAL magic quartet (Jens, Craig Sawyer, Bruce Gallop, Peter Phillips).
Last but not least, I would like to thank the proofreader of the thesis for their insigtful advices: Andrew Blue, Emma Buchanan, Dopke, Ruchi Gupta, Christian Sander, Christian Scharf, and Marcel Stanitzki.

Finally, I would like to thank my family for all they did for me. In particular, I would like to thank my sister Beatrice and wish her good luck for her future!

Thank you!

The test beams at DESY and CERN and the irradiation at KIT were supported by the H2020 project AIDA-2020, GA no. 654168.